Multiscale approach of the stress-assisted oxidation of nickel-based superalloys : from strain localization to the onset of mechanochemical damage

Charles Romain

Université Fédérale

Toulouse Midi-Pyrénées

THÈSE

en vue de l'obtention du

DOCTORAT DE L'UNIVERSITÉ DE TOULOUSE

délivré par

IMT – École Nationale Supérieure des Mines d'Albi-Carmaux

---

présentée et soutenue par

Charles Romain

le 15 Décembre 2022

Multiscale approach of the stress-assisted oxidation of nickel-based superalloys: from strain localization to the onset of mechanochemical damage

---

École doctorale et discipline ou spécialité :

MEGEP : Génie mécanique, mécanique des matériaux

Unité de recherche :

Institut Clément Ader, UMR CNRS 5312, IMT Mines Albi

Directeurs de thèse :

Denis Delagnes, Professeur, IMT Mines Albi, Albi

Damien Texier, Chargé de recherche CNRS, IMT Mines Albi, Albi

Autres membres du jury :

Nathalie Bozzolo, Professeure, Mines Paris, Sofia Antipolis *(Présidente)*

Cécilie Duhamel, Professeure, MINES ParisTech, Evry *(Rapporteure)*

Eric Hug, Professeur, Université de Caen Normandie, Caen *(Rapporteur)*

Jonathan Cormier, Maître de conférences, ISAE-ENSMA, Chasseneuil en Poitou *(Examinateur)*

Clara Desgranges, Chargée de mission, CEA ISAS, Paris-Saclay *(Invitée)*

Stéphane Knittel, Expert revêtement et traitement de surface, SAFRAN Aircraft Engines, Corbeil-Essonnes *(Invité)*

Daniel Monceau, Directeur de recherche CNRS, ENSIACET, Toulouse *(Invité)*

Acknowledgements

This thesis project was originally made possible thanks to Damien Texier and Jonathan Cormier. Their mutual experience and friendship ensured perfect collaboration and supervision. The subject and founds research were oriented towards SAFRAN Tech company and SAFRAN Aircraft Engines with the help of Clara Desgranges and Stephane Knittel. Denis Delagnes completes such a first-choice supervision team with the role of official director. The project was founded by SAFRAN Tech and IMT Mines d'Albi.

My first thoughts go to Cécilie Duhamel and Eric Hug for their extensive and detailed review of my thesis work. I also greatly thank Nathalie Bozollo for having presided over my thesis defense, as well as Clara Desgranges, Stephane Knittel, Daniel Monceau and Jonathan Cormier for their participation in my jury. The thesis defense was a real pleasure to live thanks to all of you.

Daniel Monceau unofficially joined the supervision team, with a contribution to the progress meetings, but also performed oxidation experiments at the CIRIMAT laboratory. I highly thank all of them for their expertise but also their human and supervision skills. Our regular meetings were the fuel that kept me motivated all along those almost four years of project. A special mention of Damien's sense of humor is required, but also of Jonathan's fatherhood skills (sorry, Damien's sense of humor is unbeatable...), Daniel's pedagogy, Clara's response to emails (sorry for that joke) and positivism, Stéphane's analyze and availability, and Denis' kindness. I could not recommend more such a supervision team!

As with every Ph.D. project, many peoples were involved to ensure the project's success. The following list cannot be extensive, I am deeply for any forgotten person. I would like to particularly thank people from Safran tech (especially Aurélie Soula, Jean-Michel Franchet, Tom Sanviemvongsak and Daniel Galy) and people from Safran Aircraft Engine. I spend several hours/days/weeks on the jig machine at midival. I highly thank Eric Andrieu for making possible such a partnership. I also thank the midival team, and especially Romain Mouginot, Julien Milanese, and Jean-Baptiste . The SEM observations were performed at both the ICA-Albi laboratory and at Castaing UMR. I highly thank Karine Vieillevigne for her SEM formation and also the nice atmosphere of the Albi laboratory. As for the Castaing section, I especially thank Arnaud Proietti, and Claudie Josse for their anytime availability, kindness, and also the friendly working atmosphere. This mechanical project's success is highly dependent on the machining quality of specimens. PMP company, Pprime machining department, and Abdallah Bouzid from ICA-Toulouse laboratory were involved in the success of the different machinings performed. I highly thank them to ensure I have the best

conditions with high-precision specimens. As for the Pprime laboratory, I highly thank Jonathan Cormier for his involvement and supervision of the two experimental batches conducted.

As for the daily life of those four years of project, I would like to really thank all the Clement Ader Institute personnel. To be sure not to forget anyone from the laboratory, I will only give a warm but global thanks to all the technicians, engineers, researchers, and professors, but also to my Ph.D. and post-doctoral friends. A special mention to my regular carpoolers!

To end with, I would like to deeply thank my parents, step-parents, grandparents, and family for their support in this adventure. My last but not at least greetings goes to my partner during those almost four years, Clara, for her patience, support and understanding.

Summary

Résumé étendu de thèse en français

Introduction

Contexte

Les superalliages sont apparus à la fin des années 1920 avec la conception d'alliages de nickel-chrome durcis par vieillissement. Sir Frank Whittle, inventeur du moteur à turbine à gaz Whittle [1], a mis en évidence le besoin d'alliages durables et résistants aux hautes températures dans les années 1930 [2, 3]. Le premier superalliage γ/γ' nommé NIMONIC® alloy 80 a été conçu par L.B. Pfeil en 1941, dans l'entreprise Inco de Wiggin au Royaume-Uni. Il s'agit d'un alliage Ni-Cr auquel on a ajouté suffisamment d'Al et de Ti pour permettre la formation de la phase γ', phase relativement stable à haute température [4].

Les superalliages ont été grandement améliorés depuis, allant de l'ajout d'éléments chimiques pour cibler des propriétés spécifiques, aux procédés d'élaboration (coulé et forgé, métallurgie des poudres). L'évolution des alliages s'est faite conjointement aux évolutions de performance des moteurs aéronautiques. L'augmentation de la température d'entrée dans la turbine (TET) au fil des générations de moteurs est une preuve directe des progrès réalisés en termes d'alliages. Au cours des 70 dernières années, la TET est passée de 800 °C à 1650 °C. Une augmentation de la TET se répercute sur la température en service des matériaux, mais est également associée à une amélioration des performances du moteur, comme le montre la figure 1. Les considérations environnementales actuelles (émissions de CO_2 et de NOx) visant à limiter le réchauffement de la planète, associées à des questions financières (diminution de la consommation du moteur et du poids total), garantissent la pérennité et pertinence des améliorations d'alliage [5].

Les superalliages sont capables de fonctionner à haute température, c'est à dire au voisinage de leur point de fusion. Ils sont conçus pour offrir une excellente résistance mécanique à haute température, une résistance à la déformation par fluage et à la fatigue thermomécanique, et une résistance à la corrosion ou à l'oxydation [6]. Cet ensemble de caractéristiques rend les superalliages particulièrement adaptés aux sections chaudes des moteurs à réaction [7], telles que les étages de compression à haute pression, les chambres de combustion, ainsi que les aubes et les disques de turbine. Cette large gamme d'applications fait que les superalliages occupent jusqu'à 50 % de la masse d'un moteur.

Les propriétés mécaniques élevées des superalliages résultent de leur microstructure particulière. La matrice γ est renforcée par une ou plusieurs phases de durcissement (précipités γ' ($Ni_3(Al, Ti)$) dans l'alliage René 65, γ'' (Ni_3Nb) dans l'alliage 718, ou

durcissement interstitiel). Des phases non durcissantes, mais aussi des inclusions peuvent également être présentes dans le matériau (carbures, borures, phase η (Ni_3Ti), etc.). Le matériau de cette étude étant le René 65, seule la phase γ' et quelques autres inclusions non-métalliques sont d'intérêt et seront développées ultérieurement.

L'exposition de ces alliages à un environnement à haute température induit la formation d'oxydes au contact de l'oxygène (oxydation) ou d'un mélange de gaz de combustion et de pollution saline (corrosion). Le René 65 est un alliage chromino formeur dans sa gamme de température d'usage. Il a été conçu pour former une couche d'oxyde protectrice à la surface du matériau, la chromine Cr_2O_3, afin de réduire la cinétique d'oxydation en limitant le transport de l'oxygène ou de l'entité oxydée à travers la couche d'oxyde. Ces phénomènes induisent des modifications de la sous-surface dues à la consommation des entités chimiques menant à leur déplétion, localisées sous forme de gradient ou global. Bien que l'étendue de ces propriétés graduelles soit souvent négligeable par rapport aux dimensions des pièces structurelles aéronautiques (de quelques micromètres à une centaine de micromètres), la variabilité du comportement mécanique au sein de ce gradient thermo-mécano-chimique peut parfois conduire à un développement précoce de l'endommagement. C'est pourquoi la prédiction du comportement mécanique et de l'endommagement mécano-chimique local est de la plus haute importance du point de vue économique, sécuritaire et scientifique. Pour atteindre cet objectif, la caractérisation mécanique multi-échelle des propriétés usuelles (résistance à la traction, fatigue, fluage et fatigue de maintien) de ces matériaux à propriétés graduelles est essentielle, et ce, dans une large gamme de températures.

En raison de variations de propriétés importantes sur de faibles épaisseurs/profondeurs rencontrées dans les matériaux gradués, des techniques de caractérisation micromécanique sont nécessaires. Les techniques dites de mesure directe, c'est-à-dire donnant accès aux propriétés de traction, de fatigue et de fluage en utilisant des échantillons minces autoportants (quelques dizaines de micromètres d'épaisseur), ont l'avantage de donner accès à des quantités qui peuvent être utilisées directement dans les modèles numériques (en supposant des propriétés homogènes couche par couche). Outre les grandeurs "macroscopiques" mesurées par ces techniques de mesure dites directes sur des échantillons minces autoportants, une investigation spécifique de la surface par la mesure de champs cinématiques (technique de corrélation d'images photomécaniques à haute résolution) permet d'obtenir des informations locales sur les processus de déformation et d'endommagement à l'échelle de la microstructure suite à une exposition en atmosphère oxydante / réactive.

Objectifs

Le René 65, tout comme les superalliages polycristallins à base de nickel similaire (en termes de composition chimique, de microstructure et de génération d'alliages), exposé à des températures élevées, forme des oxydes externes et internes [8–11]. Pour l'oxydation interne, ces matériaux ont révélé une oxydation des précipités primaires γ', des joints de grains, mais aussi d'inclusions intermétalliques telles que TiN ou NbC. L'application de contraintes mécaniques sur ces éléments pré-oxydés se révèle comme étant des sites favorables à l'amorçage de fissures en traction, et particulièrement enclins à une rupture précoce sous l'effet de contraintes cycliques.

L'état métallurgique du René 65 peut évoluer et interagir, soumis à des contraintes mécaniques et thermiques. Govaere a signalé un effet de l'environnement sur la durée de vie en fatigue de l'alliage AD730^{TM}, avec des changements dans l'amorçage des fissures

et ses caractéristiques microstructurales associées. Des fissures intergranulaires ont été observées dans les joints de grains oxydés en sous surface lors d'essais de fatigue à haute température pour le scénario a), tandis que des nitrures ou des bandes de glissement persistantes (PSB) se fissurent sous vide ou lors d'essais de fatigue à basse température dans le scénario b), comme le montre la figure 2 [9]. Il est donc intéressant d'étudier les propriétés locales de ces couches impactées par l'environnement et leurs conséquences sur l'intégrité et le comportement du René 65.

Les principaux objectifs de cette thèse sont les suivants:

- Établir une base de données sur l'utilisation d'échantillons minces de micro-traction pour évaluer davantage les dégradations dues à l'exposition à des températures élevées.
- Identifier le comportement à l'oxydation du matériau. Quantifier les couches d'oxyde qui peuvent modifier les performances mécaniques du matériau. Quantifier mécaniquement les gradients affectés par l'oxydation.
- Évaluer l'effet de l'environnement sur les mécanismes d'endommagement lors d'essais de traction et de fatigue.
- Déterminer quelles caractéristiques et configurations microstructurales du René 65, et plus largement de superalliages γ/γ' à précipités primaires, sont plus susceptibles de rompre sous l'effet de contraintes à haute température en atmosphère oxydante.

Structure de la thèse

Ce manuscrit débute par une analyse documentaire des différents domaines nécessaires pour établir l'étude dans le **Chapitre** 1. Les superalliages à base de nickel sont d'abord présentés, suivis des conséquences de l'exposition à haute température à la surface et à coeur du matériau, des particularités de l'utilisation d'échantillons ultra-minces et des mécanismes de déformation et d'endommagement.

Le **Chapitre** 2 est consacré aux méthodes expérimentales employées, ainsi qu'à la caractérisation du René 65 en termes de microstructure et de propriétés mécaniques sur essais standards.

Le **Chapitre** 3 se consacre à l'exposition du matériau à haute température et ses conséquences sur la cinétique d'oxydation et l'évolution de la microstructure du René 65 en surface/sous-surface.

Le **Chapitre** 4 aborde la partie mécanique avec des essais de traction et de fatigue à température ambiante. L'utilisation d'échantillons ultra-minces est largement développée pour appréhender leurs particularités, suivie des conséquences de l'exposition à haute température sur le comportement à la traction et la durée de vie en fatigue.

Les **conclusions** finales sont données avant d'introduire quelques perspectives sur le travail effectué.

Contribution

Ce projet a été soutenu par SAFRAN-Tech, IMT mines d'Albi, et l'Agence Nationale de la Recherche (ANR) [ANR-18-CE08-0003 ; projet ANR-JCJC-COMPAACT financé par l'AAPG2018], et l'institut Pprime.

Ce projet de recherche a rassemblé les compétences et expertises complémentaires de l'institut Pprime, de SAFRAN-Tech et de SAFRAN Aircraft Engines, et de l'institut Clément Ader. Ce projet a également bénéficié de l'expertise en oxydation haute température du CIRIMAT.

Présentation des résultats expérimentaux

Chapitre 2: Matériau et méthodes expérimentales

Le chapitre 2 présente les moyens expérimentaux utilisés et développés en **partie** 2.1. Les différentes régions d'intérêt et de prélèvement dans le disque de turbine sont introduites en figure 2.1. Le René 65 a été caractérisé mécaniquement selon deux géométries différentes: a) des micro-éprouvettes de traction et b) géométrie cylindrique M12 standard, dont les plans sont donnés en figure 2.4 . Les micro-éprouvettes de traction permettent d'étudier le comportement mécanique de l'alliage sur une large gamme d'épaisseur (de 20 µm à 500 µm) de par leurs dimensions compatibles avec le processus d'amincissement (JIG présenté en section 2.1.3). Les essais mécaniques de traction et fatigue sur micro-éprouvette sont réalisés sur une INSTRON 5800 électo-mécanique. Le suivi de déformation introduit en section 2.1.4 est réalisé par corrélation d'images. Le protocole expérimental d'oxydation est donné dans la partie 2.1.5. La fin de la section est consacrée à la description des moyens expérimentaux d'observation et d'analyses.

Ce travail est basé sur l'observation de deux états métallurgiques du René 65: un état réception (AR) ainsi qu'un état proche solvus (AS). Ces deux états métallurgiques sont décris en termes de microstructure et propriétés en traction à température ambiante sur essais à géométrie standard dans la section 2.2. Le René 65 est un superalliage base nickel polycristallin durci par précipitation γ', comprenant des précipités primaires étagés en taille (γ'_I, γ'_{II}, γ'_{III}), caractérisés dans ces travaux par machine learning:

L'état AR révèle une microstructure bimodale en taille de grains et précipités primaires γ'_I comme démontré dans la figure 2.22. L'illustration de ces insertions de grains fins (FG) dans une matrice à grains moyens (MG) est donnée dans les figures 2.20-2.21 pour la taille de grains et dans les figures 2.25-2.26 pour la distribution en précipités primaires γ'_I. Ces analyses montrent une variation de ± 1 µm en taille de grains, pour une moyenne à 7.9 µm, ainsi qu'une variation de ± 0.5 µm en taille de précipités primaires γ'_I, pour une moyenne à 1.8 µm. Les précipités primaires γ'_{II} et γ'_{III} montrent une distribution homogène dans ces deux zones, avec une moyenne à 64 nm et 15 nm respectivement. Le comportement mécanique en traction, résumé dans le tableau 2.6, se révèle cohérent aux alliages base nickel polycristallins similaires.

L'état AS présente une taille de grains moyenne de 52.3 µm, une présence ponctuelle de précipités primaires γ'_I avec une taille moyenne de 1.6 µm. L'état de précipitation γ'_{II} et γ'_{III} est, lui, cohérent à l'état réception, avec des valeurs de 40 nm et 20 nm, respectivement.

Le résumé de ces valeurs, ainsi que les fractions surfaciques associées, est présenté dans le tableau 2.5. Les essais mécaniques de traction sur géométrie cylindrique standard sont détaillés dans la partie 2.2.3.

Des conclusions finales comprenant un résumé du chapitre sont données dans le résumé page 89.

Chapitre 3: Comportement à l'oxydation du René 65

Le chapitre 3 détaille le comportement du René 65 à haute température. Les évolutions métallurgiques à coeur du matériau sont présentées dans la première partie 3.2. La réactivité de surface du matériau est ensuite considérée, avec notamment son comportement à l'oxydation dans les parties 3.3 et 3.5. Les températures principales visées dans le cadre de cette étude sont de 700 °C et 800 °C. Des résultats complémentaires aux températures 650 °C, 900 °C, et 1000 °C sont également présentés.

Les évolutions microstructurales du René 65 sont caractérisées aux températures 650 °C, 700 °C, et 800 °C pour des durées d'exposition entre 10 h et 1000 h. Aucune évolution de taille de grain ni de précipités primaires γ'_I n'est observée aux trois températures. La précipitation γ'_{II} et γ'_{III} montre cependant des variations: les γ'_{II} diminuent en taille de 12 nm tandis que les γ'_{III} augmentent de 5 nm, et ce, dès les prémices d'exposition en températures (dès 10 h d'exposition). Les précipités primaires γ'_{III} voient une forte évolution avec une quasi complète dissolution pour les longues durées (600 h) à 800 °C comme reporté figure 3.6. Les statistiques détaillées du vieillissement métallurgique de l'état AR sont résumées dans le tableau 3.1. Le vieillissement métallurgique de l'état AS n'a pas été étudié.

La composition chimique du René 65 est déterminée dans le but de contrôler la cinétique d'oxydation en visant une oxydation sélective des éléments chimiques. La concentration et activité en chrome sous-jacente donnée au tableau 1.1 fait du René 65 un alliage chromino-formeur. Le René 65 présente donc une couche de chromine continue à la surface du matériau après exposition à 700 °C et 800 °C. Cette couche de chromine est surplombée d'ilots de TiO_2 rutile, révélateur des précipités primaires γ'_I et des joints de grains affleurants à la surface, comme illustré à la micrographie MEB-SE 3.7. L'évolution de la concentration en chrome en sous-surface du matériau a été étudiée dans la partie 3.3.1. En sous-surface, le René 65 développe de l'alumine que ce soit en inter- ou intra-granulaire, comme le montre l'analyse EDS de la figure 3.10. Les profondeurs d'alumine sont quantifiées indépendamment entre inter- et intra-granulaire, avec une profondeur d'oxydation plus importante aux joints de grains de par leur effet puits de diffusion en oxygène.

Le comportement à l'oxydation du René 65 a été quantifié en effectuant un suivi de gain de masse ex-situ. Sa cinétique suit une loi parabolique selon le modèle de Wagner à toutes les températures étudiées, comme illustré dans la figure 3.16. La contribution de la chromine et de l'alumine dans le gain de masse total a été mesurée à $70 \pm 4\,\%_{\text{wt}}$ et $30 \pm 4\,\%_{\text{wt}}$ respectivement.

L'état AS voit, quant à lui, une oxydation interne plus profonde, avec la formation d'alumine ponctuelle proche de la profondeur de formation d'alumine inter-granulaire. La couche de chromine externe se révèle peu adhérente au substrat comparativement à l'état AR.

Le René 65 présente également des phases inter-métalliques telles que des nitrures de titane. L'oxydation des nitrures est présentée en partie 3.6. Leur oxydation se révèle intéressante à étudier de par la forte expansion volumique qui en résulte. Les TiN forment du TiO_2 rutile. Cette formation de rutile entraine un effet de puits de diffusion d'oxygène avec une oxydation de leur sous-surface équivalente au matériau au contact de la surface.

L'épaisseur des échantillons, lors de cette étude, est comprise dans la gamme 20 µm à 500 µm. Un effet de taille sur les cinétiques d'oxydation est reporté à 700 °C et 800 °C. Les échantillons minces présentent une couche de chromine plus épaisse, une quantité

totale d'alumine plus importante, mais avec une profondeur d'intrusion plus faible, ce qui peut être observé dans les figures 3.29 à 3.31. Ceci conduit en un gain de masse plus important des échantillons minces comparé aux échantillons épais.

Des observations à la surface de coupons polis de biais mettent en lumière la distribution de l'oxydation interne (inter- et intra- granulaire), comme illustré aux figures 3.12 à 3.14. L'oxydation en sous-surface des nitrures de titane révèle une profondeur d'intrusion bien plus importante que l'oxydation intergranulaire sans nitrure de titane en surface.

Finalement, l'utilisation d'échantillons minces permet l'étude de l'oxydation post régime parabolique due à l'épuisement local (InCF) des entités chimiques impliquées dans le régime d'oxydation parabolique, *i.e.* le chrome. Le René 65 développe des spinelles de $CoCr_2O_4$ ou du NiO en raison de l'InCF du matériau. L'occurrence de l'InCF a été modélisée à partir de l'épuisement total du chrome dans la masse des échantillons et vérifiée expérimentalement dans la partie 3.8.

Chapitre 4: Comportement mécanique

Le chapitre 4 présente les résultats des essais mécaniques de traction et de fatigue sur micro-éprouvettes dans la gamme d'épaisseur 20 µm à 500 µm. Les essais sont réalisés sur différents états métallurgiques: AR, AR vieilli (700 °C et 800 °C - 200 h et 600 h), AR oxydé (700 °C et 800 °C - 200 h et 600 h), AS, AS oxydé (800 °C - 200 h et 600 h).

L'état réception démontre une évolution de la limite d'élasticité ($Rp_{0,2\%}$) due aux effets d'épaisseur en dessous de 100 µm, soit 12.5 grains dans l'épaisseur du matériau (transition multicristal à polycristal), comme illustré à la figure 4.3. La $Rp_{0,2\%}$ atteint une valeur de 1120 MPa sur échantillon épais, avec une diminution de 15.6 % sur échantillon fin. La contrainte à rupture et la ductilité évoluent de pair jusqu'à 500 µm, avec un taux d'écrouissage similaire, tel que présenté dans la figure A.1. L'observation des faciès de rupture démontre le caractère ductile du matériau aux figures 4.5 et 4.6.

Les évolutions de microstructure liées au vieillissement à 700 °C observées dans la partie 3.2 induisent une amélioration du comportement mécanique en traction. Ces résultats sont cohérents avec la théorie du durcissement par précipitation, avec une taille de précipités primaires γ'_{II} de 50 nm. La dissolution des précipités primaires γ'_{III} suite au vieillissement à 800 °C résulte en une diminution de la résistance du matériau en traction. La figure 4.9 résume le comportement mécanique du René 65 après vieillissement aux différents couples "températures - temps" de cette étude.

Les essais de traction sur état AR oxydé révèlent un effet bénéfique de l'oxydation, notamment sur éprouvettes minces, lorsque les couches d'oxydes sont fines (inférieures au micron pour la couche de chromine externe). Ceci est particulièrement visible sur la figure 4.14. Une augmentation d'épaisseur de la couche d'oxyde externe ainsi que de la pénétration d'alumine inter-granulaire induit une forte dégradation du comportement en traction, tel qu'illustré sur la figure 4.15. Ces effets sont particulièrement visibles sur les échantillons minces, de par l'exacerbation des effets de surface comparés aux effets de coeur. Des éprouvettes prélevées dans le gradient d'oxydation ont été testées mécaniquement, nommées grad Cr et grad Al, tel que présentées à la figure 4.16. Celles-ci apportent de premiers éléments concernant la contribution des couches d'oxydes à 700 °C et 800 °C sur le comportement mécanique. L'impact néfaste de l'oxydation est particulièrement visible à 800 °C pour les faibles épaisseurs (proche de 20 µm), comme présenté à la figure 4.18. Enfin, des observations en surface sur essais interrompus à

l'état oxydé montrent des prémices d'endommagement avec de la fissuration à proximité ou traversant les précipités primaires γ'_I, visible à la figure 4.24.

L'état AS est quant à lui révélateur du caractère quasi-monocristallin à multicristallin du fait du faible ratio nombre de grains par rapport à l'épaisseur de l'éprouvette. L'état AS oxydé démontre un abattement de propriétés mécaniques du même type que l'état AR oxydé, cependant exempt de transition quasi-monocristallin à multicristallin, comme observable à la figure 4.26.

L'impact des couches d'oxyde sur la dégradation du comportement mécanique en traction a été considéré dans la partie 4.6. Une perte de section utile équivalente à la perte de $Rp_{0,2\%}$ a été déterminée au niveau de l'intrusion d'alumine sur les éprouvettes les plus fines dans les conditions critiques d'oxydation.

Une étude de faisabilité sur des essais de fatigue sur éprouvettes minces est présentée en section 4.7.2. Le rôle des précipités primaires γ'_I affleurants à la surface, sous couvert des ilots de rutile, est révélé par corrélation d'images haute résolution à la figure 4.42. La distribution des primaires ainsi que les chemins de fissuration orientés préférentiellement à la sollicitation semblent être l'origine de la propagation de la fissuration. Ces zones sont d'autant plus présentes dans les régions à grains fins de par la plus faible taille de grains. Les TiN oxydés se sont également révélés candidats à la fissuration, avec une décohésion principalement à l'interface TiN-matrice.

Conclusions et perspectives

Conclusions

Ce projet vise à enrichir la compréhension des mécanismes d'endommagement associés à la sollicitation mécanique d'un superalliage polycristallin à base de nickel, le René 65, dans un environnement oxydant. Les couches affectées par l'oxydation, qu'elles soient homogènes et distribuées en surface, ou localisées aux joints de grains, peuvent induire des changements de comportement mécanique.

L'originalité du présent travail réside dans l'utilisation d'éprouvettes de microtraction ultraminces pour quantifier directement la couche affectée par l'oxydation en termes de comportement mécanique et de mécanismes d'endommagement.

René 65

Le superalliage à base nickel polycristallin René 65 est composé d'une microstructure bimodale, composée d'insertions de grains fins (FG) dans une matrice à grains moyens (MG), héritée de la solidification de la billette et/ou du résultat des opérations de forgeage. Les précipités γ'_{II} et γ'_{III} présentent cependant des caractéristiques similaires dans les deux régions malgré des variations mineures dans la taille des grains et de précipités γ'_I. La présence de particules intermétalliques (borures, carbures, etc.) est révélée, avec, en particulier, des nitrures qui ait pour effet de réduire la durée de vie en fatigue du matériau à l'état oxydé aux deux températures de pré-oxydation de 700 °C and 800 °C.

Une deuxième microstructure a été étudiée, à partir d'un traitement thermique proche du solvus, appelé AlbiSolvus (AS). Ce type de traitement thermique permet d'obtenir un matériau presque exempt de précipités γ' primaires, mais s'accompagne d'une augmentation de la taille des grains.

Effets de taille sur le comportement mécanique

Des échantillons ultraminces ont été utilisés dans ce projet pour mettre en évidence tout effet environnemental de la surface et de la sous-surface par rapport au comportement d'échantillons massifs. L'utilisation d'échantillons minces hérite d'effets de taille vis à vis du rapport entre l'épaisseur de l'échantillon et la taille des grains (t/d). Alors que le comportement des échantillons minces et le rapport t/d associé suscitent un vif intérêt dans la littérature sur des matériaux purs ou modèles (pour leurs connaissances théoriques et de modélisation bien connues), leur application aux matériaux industriels pose des défis à la fois techniques et technologiques.

Le comportement mécanique des éprouvettes minces de microtraction a été validé en les comparant à des essais cylindriques standard. L'étude des éprouvettes de microtraction a nécessité le développement de moyens de caractérisation adaptés, tant pour la réalisation des essais que pour le suivi du comportement.

Le comportement en traction de l'état AR du René 65 a été largement caractérisé dans la gamme d'épaisseur 20 µm to 500 µm correspondant à un rapport t/d de 2.5 to 60. Cette base de données a ensuite été considérée comme une référence pour comparer les conséquences de l'exposition à haute température sur le comportement mécanique. Le durcissement par précipitation du René 65 démontre l'influence mineure de l'épaisseur des échantillons sur l'écrouissage du matériau par rapport au nickel pur. Une diminution des propriétés de traction macroscopiques avec la réduction de l'épaisseur a révélé une transition de comportement multicristallin à polycristallin autour de 100 µm échantillons d'épaisseur (12,5 grains dans l'épaisseur). Une telle transition est révélatrice d'effets de surface libre par rapport au comportement polycristallin à coeur.

Le comportement à la traction de l'état AS a également été caractérisé dans la gamme d'épaisseur 20 µm to 500 µm correspondant à un rapport t/d de 0.4 to 10. La différence de rapport t/d induit un comportement quasi-monocristallin à multicristallin avec une transition autour de 100 µm (2 grains dans l'épaisseur). Une diminution de la contrainte pour une même déformation en traction a été observée dans l'état AS par rapport à l'état AR en raison de ses évolutions microstructurales intentionnelles.

La durée de vie en fatigue du René 65 a été étudiée en sollicitation de traction en utilisant des échantillons de microtraction similaires dans la gamme d'épaisseur 20 µm to 500 µm. Une diminution du nombre de cycles à rupture a été observée sur les échantillons de moins de 50 µm d'épaisseur.

Produits d'oxydation

Le comportement à l'oxydation du René 65 a été étudié (sans aucune sollicitation mécanique externe). L'oxydation isotherme sous air laboratoire suit un régime parabolique pour toutes les températures étudiées entre 650 °C and 1000 °C avec une activation d'énergie similaire à la chromine pure. La cinétique d'oxydation est en accord avec des types d'alliages similaires, *i.e.* superalliages à base de Ni formant de la chromine. L'oxydation conduit à la formation de plusieurs oxydes : une couche externe dense de chromine, des îlots de titane faiblement distribués recouvrant les précipités γ' primaires et les joints de grains, et de l'alumine intergranulaire, et ce, indépendamment de la température et de l'épaisseur de l'échantillon. La formation de spinelles se produit à des températures élevées, pendant de longues durées et sur des échantillons de faible épaisseur, ce qui entraîne des phénomènes de "Breakaway" local du fait de la rupture chimique intrinsèque. L'effet réservoir, c'est-à-dire les effets limités au volume, a été mis en évidence en utilisant des échantillons ultraminces jusqu'à 15 µm.

L'évolution microstructurale inhérente à l'exposition à haute température entraîne une altération de la surface et de la sous-surface avec des couches appauvries en chrome, en précipités γ' ainsi qu'en TCP, dont les profondeurs respectives ont été déterminées sur la base d'observations de section transversale afin d'établir l'influence des modifications de la sous-surface sur la réponse mécanique. L'impact de ce gradient microstructural en fonction de l'épaisseur de l'échantillon est intéressant pour l'analyse du comportement mécanique.

Un effet de l'épaisseur des échantillons sur la cinétique d'oxydation a été observé aux températures de 700 °C and 800 °C. Une analyse d'images systématique réalisée de façon conséquente a mis en évidence des variations d'épaisseur d'oxyde externe ainsi que de la surface équivalente d'alumine intergranulaire. Ces variations d'épaisseur sont responsables des variations de gain de masse mesuré. Les échantillons plus minces présentent une couche de chromine plus épaisse ainsi qu'une couche d'alumine équivalente plus épaisse, mais avec une profondeur de pénétration plus faible. La contribution de la couche externe de chromine et de l'alumine intergranulaire au gain de masse total a été quantifiée: 70 $\%_{\mathrm{wt}}$ dû à la couche externe d'oxyde. L'énergie d'activation extraite de l'oxydation globale du René 65 est conforme à la chromine pure.

La microstructure AS a révélé une oxydation principalement interne en raison de la fraction inférieure des joints de grains. L'oxydation intergranulaire est cependant présente, avec une profondeur d'intrusion inférieure au matériau AR. La chromine externe est affectée par rapport à l'état AR avec une faible adhérence à la surface du matériau.

Dégradation des propriétés mécaniques et amorçage de fissures dûs aux interactions environnementales en traction et fatigue

Le vieillissement global et l'impact de l'oxydation du René 65 ont été étudiés à des durées de 200 h et 600 h à 700 °C et 800 °C. Des évolutions de précipités γ' secondaires et tertiaires ont été observées aux deux températures jusqu'à 10 h de vieillissement, révélant une homogénéisation potentielle de la microstructure. Une telle homogénéisation induit une augmentation des propriétés de traction du matériau par rapport à l'état AR en raison de l'augmentation de la CRSS due au cisaillement des petits précipités γ' secondaires et des précipités γ' tertiaires plus grands. L'évolution microstructurale à 800 °C est beaucoup plus prononcée (*e.g.* dissolution des précipités γ' tertiaires), ce qui entraîne la perte des propriétés de traction et révèle un comportement similaire à l'état AR.

La couche de chromine externe semble accentuer le durcissement du matériau en limitant le mouvement des dislocations pour les couches d'oxyde minces, comme le montrent les échantillons oxydés à 700 °C. Les couches d'oxydes plus épaisses (plus de 1 µm) participent à la propagation des fissures surfaciques avec une potentielle interconnexion générant une déformation plastique cumulée élevée. La fissuration intergranulaire des joints de grains oxydés par l'alumine à proximité des précipités γ' primaires émergeant à la surface du matériau semble jouer un rôle important dans les processus d'endommagement. La région FG, où les précipités γ' primaires sont regroupés, présente une localisation des déformations résultant de fissures superficielles longues, mais peu profondes reliant les précipités γ'_I (rupture inter et intra γ'_I). La perte de comportement à la traction a été étudiée en termes de section efficace supportant les contraintes mécaniques. Les grains dont les joints sont complètement oxydés par la formation

d'alumine ne contribuent que très faiblement au comportement mécanique. Les échantillons minces oxydés mettent en évidence les conséquences du gradient microstructural et de la fragilisation sous-surfacique dans la couche affectée par l'oxydation.

Les nitrure de titane ont révélé une oxydation complète à 700 °C and 800 °C pour former du rutile TiO_2, associés à une expansion volumique importante. L'interface nitrure/matrice présente une cinétique et des produits d'oxydation similaires à ceux de la surface du matériau. Une telle interface est révélatrice d'un puits de diffusion de l'oxygène. Les fractographies de fatigue ont révélé la formation de fissures dans l'environnement du nitrure oxydé sous-surfacique. Les nitrures oxydés, de par leur décohésion à la matrice, mais aussi de par leurs dimensions importantes en surface et sous-surface par rapport à la microstructure, semblent contrôler la durée de vie en fatigue du René 65 à température ambiante.

Toutes ces conclusions sont basées sur la caractérisation du René 65 à température ambiante. Les conclusions sur les mécanismes d'endommagement qui réduisent la durée de vie du matériau ne sont valables que jusqu'à 550 °C. Un changement dans les mécanismes de déformation, et en particulier la contribution du précipité γ', pourrait induire des changements majeurs dans les processus d'endommagement, en particulier à partir des joints de macles $\Sigma 3$.

Perspectives

- L'abattement de la résistance à la traction résultant du processus d'oxydation du matériau n'a été considéré que comme une section non porteuse. Cette méthodologie discontinue pourrait être grandement améliorée en considérant une évolution graduelle des propriétés de traction depuis la surface du matériau jusqu'au comportement global.

- Tous les essais de fatigue et de traction de cette étude ont été réalisés à température ambiante. Les changements dans les mécanismes de déformation se produisant au-dessus de 550 °C, mais aussi les interactions mécanique-oxydation (PSB de fatigue pouvant favoriser le transport de l'oxygène, rupture de l'échelle d'oxyde externe protectrice) qui peuvent se produire pendant les essais à haute température peuvent induire des différences majeures par rapport aux conclusions dressées dans cette étude.

- Les propriétés mécaniques des échantillons extraits dans le gradient pour cibler une couche spécifique ont été limitées à l'élimination de la couche externe de chromine, comme indiqué dans la section 4.4.3. L'élimination de la couche intergranulaire affectée par l'alumine pourrait également être intéressante pour valider l'hypothèse d'une section non porteuse.

- Les observations MEB en coupe transversale ont révélé une couche en sous-surface dépourvue de γ', et notamment de γ'_I, mais également associé à un appauvrissement en précipités γ'_{II} et γ'_{III} au niveau des joints de grains. L'impact mécanique de ces couches en solution solide est à approfondir.

- L'effet de l'épaisseur sur la cinétique d'oxydation a été mesuré en termes de gain de masse et d'échelle d'oxyde. Des essais d'oxydation ATG pourraient améliorer la précision du gain de masse. La surveillance in situ des dimensions géométriques des échantillons pourrait également répondre à toute présence potentielle de fluage.

Introduction

Framework

The superalloys started their journey in the late 1920s with the design of age-hardened nickel-chromium alloys, without direct industrial application. Sir Frank Whittle, inventor of the Whittle gas turbine engine [1], highlighted the requirement of high-temperature resistant and durable alloys in the 1930s [2, 3]. The first γ/γ' superalloy named NIMONIC® alloy 80 was then designed by L.B. Pfeil in 1941, working at Inco's Wiggin facility in the United Kingdom. It consists of a Ni-Cr alloy with sufficient Al and Ti addition to enable γ' phase formation [4].

Superalloys have been greatly improved since, going from the addition of chemical elements to target specific properties, to elaboration processes (cast and wrought, powder metallurgy). Evolution on the alloys happened concomitantly to aero-engines performance requirements. The Turbine Entry Temperature (TET) increase over engine generations is a direct evidence of the progress made in terms of alloys. Over the last 70 years, the TET increased from 800 °C to 1650 °C. An increase in the TET reverberates on the in-service temperature of materials but is also associated with enhancing engine performances, as denoted in figure 1. Actual environmental considerations (*i.e.* CO_2 and NOx emissions) to limit global warming associated with financial matters (decrease engine consumption and global weight) ensure the alloy improvements are still relevant [5]. The European involvement is proven in several projects, notably through the Clean Sky project, in its version 2 with expected conclusions near 2024, and through the long-term project Flight Path ending in 2050 (reductions of: 75 % for CO_2, 90 % for NO_X, and 65 % of noise) [12].

Superalloys are a class of alloys with the ability to operate close to their melting point. They are designed to provide excellent mechanical strength at high temperatures (up to 80 % of their melting point), a resistance to creep deformation and thermo-mechanical fatigue, good surface stability, and a resistance to corrosion or oxidation [6]. This set of characteristics makes superalloys particularly suited for hot sections of jet engines [7], such as *e.g.* high-pressure compression stages, combustion chambers, and turbine blades and disks. Such a wide range of applications results in superalloys occupying up to 50 % in the mass of an engine.

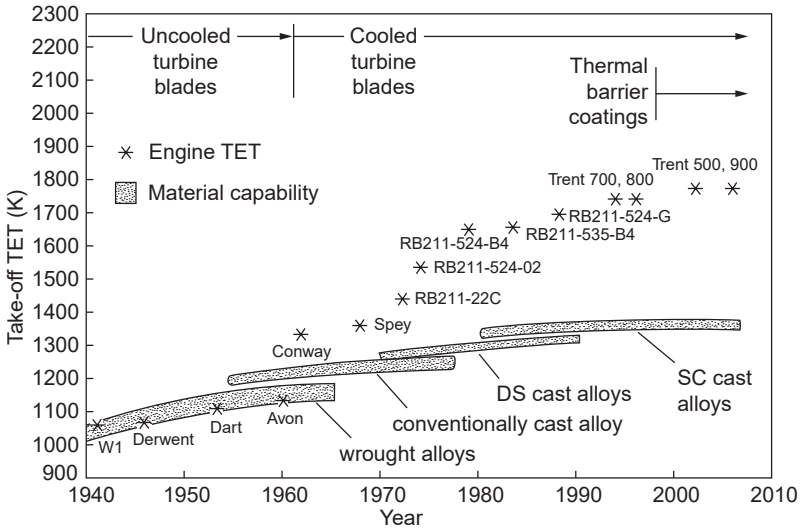

Figure 1: TET evolution in Rolls-Royce motors between 1940 and 2010 [2]

The high mechanical properties of superalloys arise from their particular microstructure. The γ matrix is strengthened by one or several hardening phases (γ' ($Ni_3(Al,Ti)$) precipitates in René 65 alloy, γ'' (Ni_3Nb) in Alloy 718, or interstitial hardening). Non-hardening phases can also be present: (δ (Ni_3Nb) in Alloy 718) but also inclusions (carbides, borides, η (Ni_3Ti) phase, etc.). The material of this study being René 65, only the γ' phase and some other non-metallic inclusions are of interest and will be further developed.

These initially homogeneous materials can see their properties evolve on the surface and sub-surface during their life due to surface reactivity (corrosion, oxidation) that progressively generates a gradient of chemical composition, microstructure, and properties. We then speak of materials with a gradient of properties that evolve over time. The exposure of such alloys to a high-temperature environment induces oxides formation from the contact with oxygen (oxidation) or to a mixture of combustion gases and salt pollution (corrosion) of the material entities. Superalloys are designed to form a protective oxide scale at the surface of the material to reduce the oxidation kinetic rate by limiting the transport of oxygen or of the oxidized entity through the oxide scale. Although the range of these graded properties is often negligible compared to the dimensions of aeronautical structural parts (from a few micrometers to a hundred micrometers), the variability of mechanical behavior within this thermo-mechanical-chemical gradient can sometimes lead to early damage development. For this reason, the prediction of mechanical behavior and local mechanical-chemical damage is of utmost importance for economic, safety, and scientific points of view. To achieve this objective, the multi-scale mechanical characterization of the usual properties (tensile strength, fatigue, creep, and dwell fatigue) of these materials with graded properties is essential, and this, over a wide range of temperatures.

Due to large variations in properties over small thicknesses/depths encountered in graded materials, micromechanical characterization techniques are necessary. The so-called direct measurement techniques, i.e., giving access to tensile, fatigue, and creep properties by using thin self-supporting (free-standing) samples (a few tens of micrometers thick), have the advantage of providing access to quantities that can be used directly in numerical models (assuming homogeneous properties layer by

layer). In addition to the "macroscopic" quantities measured by these so-called direct measurement techniques on thin self-supporting samples, a specific investigation of the surface by measuring kinematic fields (high-resolution photomechanical image correlation technique) would provide local information on deformation and damage processes at the microstructure scale.

Objectives

René 65, but also similar polycrystalline nickel-based superalloys (in terms of chemical composition, microstructure, and alloy generation) exposed at elevated temperatures forms both external and internal oxidation [8–11]. For the internal oxidation, these materials revealed oxidized primary γ' precipitates, grain boundaries, but also intermetallic inclusions such as TiN or NbC. Mechanical stresses onto these pre-oxidized features as been reported as favorable crack initiation sites under tensile loading and particularly prone to early failure under cyclic stresses.

The phases and microstructure can evolve and interact in the life of the mechanically and thermally stressed alloy. Govaere reported an environmental effect in the fatigue life of AD730^{TM}, with changes in crack initiation and its microstructural features associated. Intergranular cracking was observed in subsurface oxidized grain boundaries in high-temperature fatigue testing under ambient environment in scenario a), whereas nitrides or Persistent Slip Bands (PSB) cracking under vacuum or at low-temperature fatigue testing in scenario b), as depicted in figure 2 [9]. It is hence interesting to study the local properties of such environmentally-impacted layers and their consequences on the integrity and behavior of René 65.

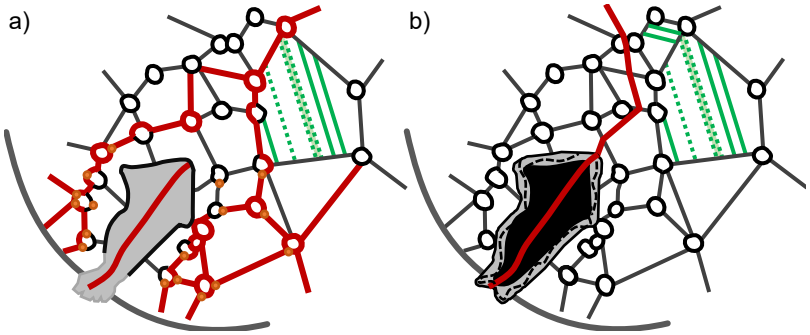

Figure 2: Crack initiation scenario under LCF fatigue testing in AD730^{TM} according to Govaere [9]

The primary purposes of this thesis are:

- Set a database on the use of thin micro-tensile specimens to further evaluate the impairments from the high-temperature exposure.
- Identify the oxidation behavior of the material. Quantify the oxide scales that may interact with the mechanical performance of the material.
- Mechanically quantify the oxidation-affected layers.
- Assess the environmental effect on the damaging mechanisms in tensile and fatigue testing.
- Determine which microstructural features and configurations are more prone to failure under high-temperature stresses on the materials.

Dissertation structure

This manuscript begins with a literature review of the various fields necessary to establish the study in **Chapter** 1. Nickel-based superalloys are firstly introduced, followed by the high-temperature exposure consequences, the particularities of the use of ultrathin specimens, and the deformation and damaging mechanisms of this class of alloys.

The **Chapter** 2 is devoted to the experimental methods employed in this framework, and René 65 characterization in terms of microstructure and standard mechanical properties.

The **Chapter** 3 focuses on the high-temperature exposure and its consequences on bulk and surface/sub-surface evolutions.

The **Chapter** 4 deals with mechanical investigations of room temperature tensile and fatigue tests. The use of ultrathin specimens is extensively developed to apprehend their particularities, followed by the consequences of the high-temperature exposure on the tensile behavior and fatigue life.

Final **conclusions** are given before introducing some perspectives on the work done and that remains to be done.

Contribution

This project was supported by SAFRAN-Tech, IMT mines d'Albi, and the Agence Nationale de la Recherche (ANR) [ANR-18-CE08-0003; ANR-JCJC-COMPAACT project funded from the AAPG2018]. Participation of the Pprime laboratory in the experimental works was also granted.

This research project gathered the expertise of Pprime institute, SAFRAN-Tech and SAFRAN Aircraft Engines, and the Clement Ader institute with complementary expertise from all sides. Additional expertise in oxidation matters was given by the CIRIMAT laboratory.

Figure 3: Contributors to this framework: SAFRAN-Tech, SAFRAN Aircraft Engines, Pprime Institute, Clement Ader Institute, ANR, CIRIMAT

Chapter 1

Bibliographic review

This chapter exposes the state-of-the-art available in the literature to apprehend the subject. This bibliographic review starts with γ/γ' Ni-based superalloys for turbine disks application presentation.

As Ni-based materials are designed to be employed at high temperatures, both metallurgical aging and oxidation-assisted evolution of the material are presented in the following section. The high-temperature exposure includes two distinct sections, with bulk evolution and surface reactivity (*i.e.* focused on oxidation matters).

Micro-mechanical thin specimens are employed during this project to exacerbate any surface effect from thickness reduction. An introduction to such specific mechanical characterization is then given.

The last section enlightens the deformation mechanisms, from bulk to oxidation-assisted cracking.

1.1 Superalloys

1.1.1 Cast and wrought γ/γ' Ni-based superalloys for turbine disks application

In-service temperature behavior of turbine disks

Turbine disks experience lower in-service temperatures than the TET due to their location out of the air flux. They are nevertheless designed to withstand temperatures up to 700 °C. The massive parts scale, the thermo-mechanical solicitations, and the cycling effect for each flight impose a complex design of the turbine disks. While the part located near the low-pressure turbine shaft sees moderate temperature, it experiences biaxial stresses (radial and tangential), requires to be burst resistant, and does not allow cracks formation. The part located at the rim, on the other hand, expects temperature up to 650 °C to 700 °C, it requires then sufficient environmental resistance and endures creep to avoid any geometrical looseness on turbine blades attached to the disk. A maximum of 0.5 % of plastic strain is allowed on turbine disks for such reasons [13].

The temperature during one cycle (*i.e.*, one flight) is not constant within the engine. Figure 1.1 depicts the temperature variations from take-off to landing. Two temperature maximums are obtained during the takeoff/climb and landing associated with the use of the reverse thrust. Airport regulations require aircraft to takeoff using the shortest distance and climb as fast as possible to minimize noise pollution and takeoff inside the limits of the track. The takeoff sequence then compels pilots to set the thrust commands at maximum (max thrust) thus inducing the maximum temperature in the engines. To the same extent, the use of reverse thrust allows aircraft to decelerate faster and liberate the track as soon as possible. Those parameters are significant in the design of the alloys composing turbine disks and their environmental behavior, as the maximal temperature will be seen during a few minutes at each flight/cycle.

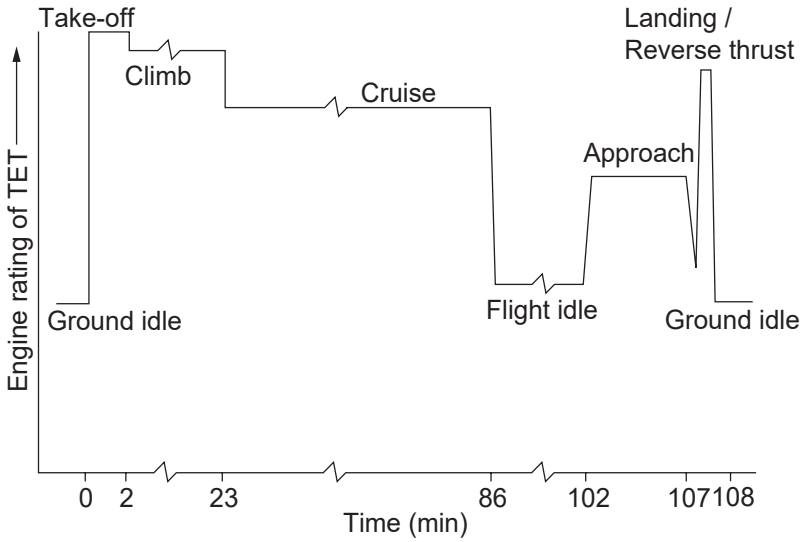

Figure 1.1: TET in usual commercial flight [2]

Let us apprehend now how the γ/γ' Ni-based superalloys are able to meet the specifications of turbine disks.

γ/γ′ microstructure

The γ matrix is FCC ordered, and the γ′ precipitates population (γ'_I, γ'_{II}, and γ'_{III}) are $L1_2$ ordered. The crystallographic structure of both phases is illustrated in figure 1.2. Several populations of γ′ precipitates are found, classified by sizes resulting from different times of coalescence, but also by location in the alloy, as depicted in figure 1.3.

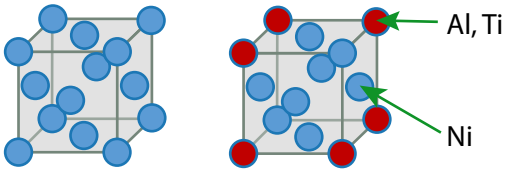

Figure 1.2: FCC (left) and $L1_2$ (right) structures

Primary γ′ precipitates (γ'_I) 1 µm to 10 µm, located preferentially along grain boundaries. They play a key role in the pinning of grain boundaries during the solutionizing treatment [14, 15]. This mechanism is called Smith-Zener pinning [16].

Secondary γ′ precipitates (γ'_{II}) 50 nm to 200 nm, located inside the grains in the γ matrix. Secondary precipitates are mainly responsible for the hardening of superalloys. γ'_{II} precipitates form during cooling or aging after the forging process. The size and morphology mainly vary depending on the cooling rate [17, 18].

Tertiary γ′ precipitates (γ'_{III}) 5 nm to 20 nm, located in the remaining matrix, preferentially along grain boundaries and primary γ′ precipitates [2, 19–21].

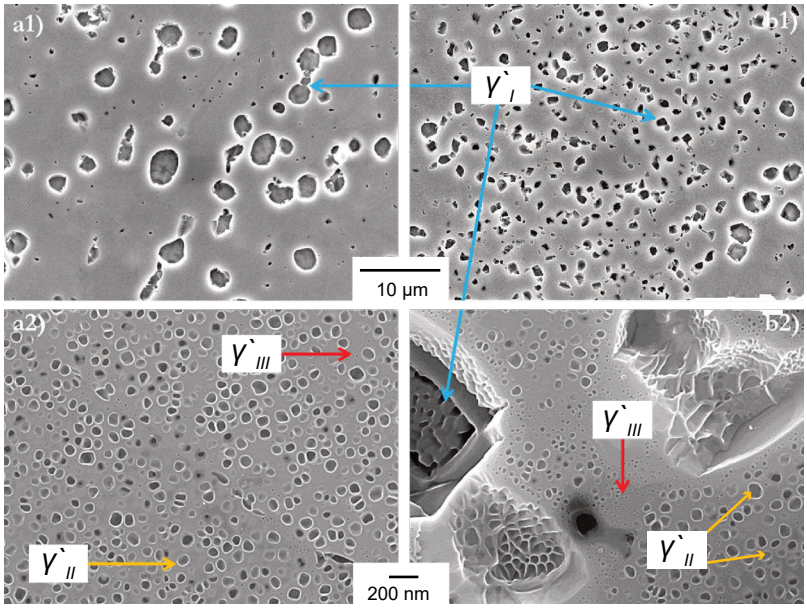

Figure 1.3: SEM-SE micrographs after chemical etching of different γ′ precipitates population [22]

Both γ and γ' phases present a low parametric misfit $\delta = 0.05\,\%$ at room temperature according to Wlodek in René 88DT [23]. The misfit reflects the parametric misfit between two phases according to equation 1.1. A low parametric misfit ensures then a proper matrix/precipitate coherency. The presence of a misfit induces, however, local elastic stresses and strain fields at the γ/γ' interfaces that contribute to the hardening of superalloys [24].

$$\delta = 2 \cdot \frac{a_{\gamma'} - a_{\gamma}}{a_{\gamma'} + a_{\gamma}} \tag{1.1}$$

with a_{γ} and $a_{\gamma'}$ respectively the lattice parameters of the γ and γ' phases.

The addition of aluminum, titanium, and tantalum entities in the composition of the alloys enables the hardening phase formation γ' [2]. Precipitates (γ'_{II} and γ'_{III}) allow the pinning of dislocations, dislocations pill up under solicitation resulting in hardening of the material [25]. The hardening phenomenon is nonetheless affected by the intrinsic strength of the γ' phase, the misfit, the volume fraction of γ' in the matrix, the morphology, distribution, and size of the γ' precipitates [26–28].

The misfit is expected to vary depending on the temperature because of the different thermal expansion coefficients from both γ and γ' phases, but also the Heat Treatment (HT) and the stresses applied during processing [29–33]. Beardmore has studied the influence of the fraction of γ' precipitates in Ni-based superalloys onto the 0.2 % yield stress as a function of the temperature, as resumed in figure 1.4 [25].

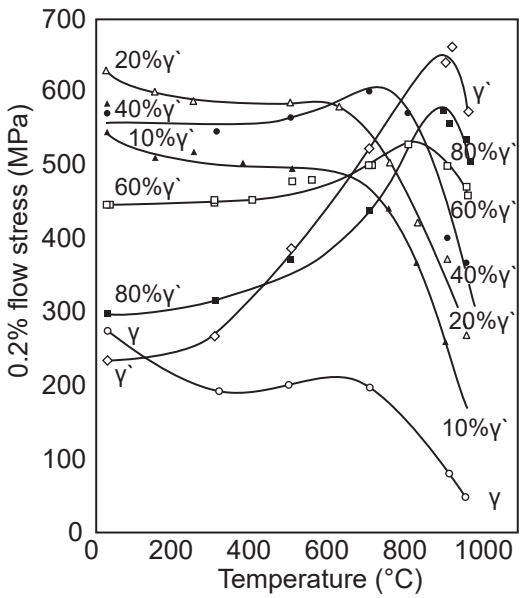

Figure 1.4: Yield stress (YS) evolution over the temperature depending on the γ' fraction [25]

Dimensional criteria

Turbine disks are designed to endure multiple types of mechanical stresses. Wessman resumed the characteristics expected for each type of solicitation [34]. This set of specifications is the foundation of γ/γ' Ni-based superalloys developments.

Tensile strength *Material ultimate strength determines disk burst characteristics, and yield strength determines the deflection of the disk under initial loading.*

Creep strength *The alloy must exhibit a predictable and minimal time-dependent deformation, such that clearances between the rotating blade tips and the case can be kept small for purposes of engine efficiency.*

Fatigue strength *Disks undergo mechanical and thermal stress cycles, and adequate fatigue strength and life are required to create parts with an economically viable service life.*

Fatigue crack growth rate *Once cracks in the material form, their propagation must be slow enough that the cracks can be found during periodic inspections, instead of causing catastrophic failures.*

Safety matters also play a role in the parts design criteria. A safety factor of at least 1.5 is applied on all aeronautic structures.

Turbine disk alloys are generally manufactured from polycrystalline superalloys. The grain size is optimized to maximize the combination of yield strength, resistance to fatigue crack initiation (both of which scale inversely with grain size), creep strength, and resistance to fatigue crack growth (which scale directly with it). Figure 1.5 summarizes the effect of grain size on the mechanical properties of turbine disks alloys. Turbine disks commonly present a dual microstructure, with large grains at the rim of the disk to optimize the creep resistance, and small grains at the core to optimize the fatigue behavior and minimize disk burst phenomena.

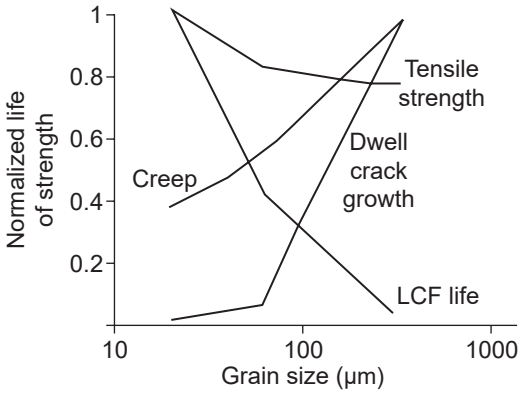

Figure 1.5: Schematic illustration of the important properties of turbine disk alloys and their dependence upon grain size [35]

1.1.2 René 65 alloy in the literature

René 65 alloys is a forged version of the René 88DT (powder metallurgy). This alloy was developed by General Electric and ATI Alvac (North Carolina). The forging process enables cost-effective production compared to powder metallurgy; the microstructure is, yet, more heterogeneous. Numerous studies (Laurence - *Pprime* [8, 15], Charpagne - *CEMES - Mines ParisTech, Pprime, UCSB* [22, 36], Heaney - *General Electric Aircraft Engines* [14], Terrazas, Bond *et al.* - *ATI Specialty Materials* [37], Wessman - *Pprime - SAFRAN* [34], Katsari - *McGill* [38]) have been carried out on the improvement of the microstructure homogeneity of René 65 in order to bring it closer to the René 88DT [39, 40].

Chemical composition

The chemical composition of René 65 is exposed in table 1.1, detailed between the γ matrix and γ' precipitates from Energy Dispersive Spectroscopy (EDS) analysis carried out by Charpagne [22]. René 65 is a complex combination of twelve elements, chosen for particular reasons from mechanical strength to environmental resistance. The pros and cons of each element are presented in figure 1.6.

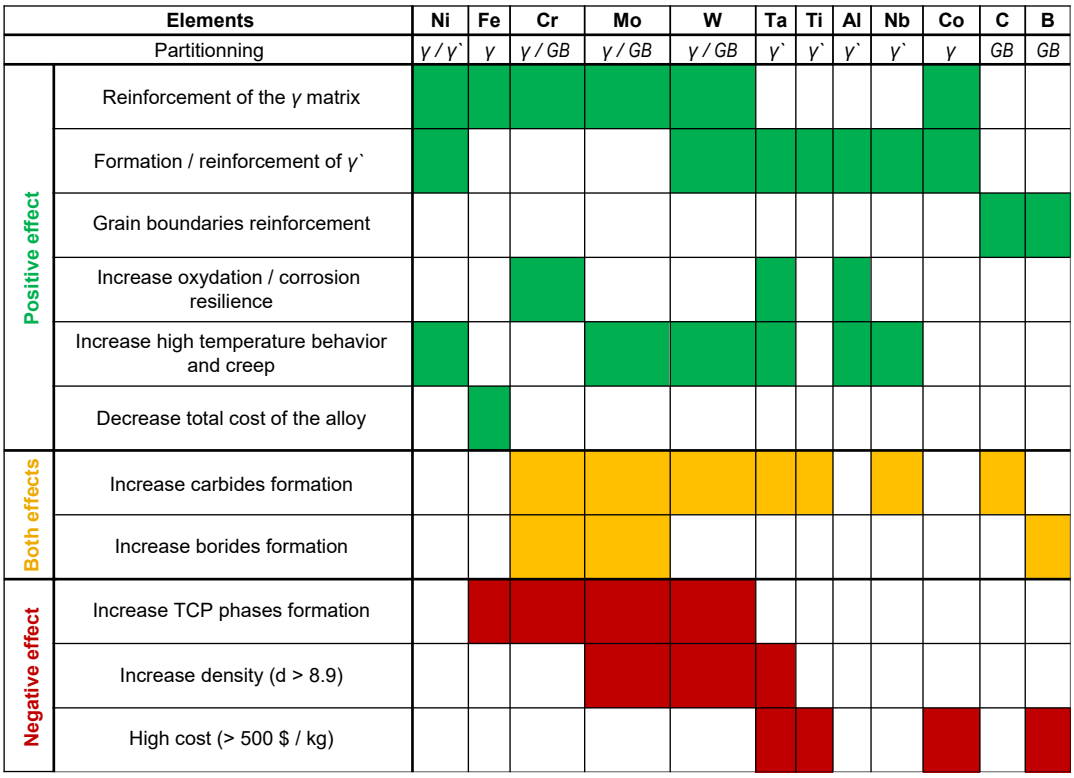

Figure 1.6: Pros (green) and cons (red) of alloying elements on R65. Elements in yellow can present beneficial or deleterious contributions to the alloy depending on the solicitation mode. Inspired from Thébaud and Bourdin [2, 7, 8, 41–47]

	Ni	Cr	Mo	W	Co	Fe	Nb	Ti	Al	Zr	B	C
René 65												
Global	Bal.	16.0	4.0	4.0	13.0	1.0	0.7	3.7	2.1	0.05	0.016	0.015
γ matrix	Bal.	17.9	3.6	2.9	14.3	0.9	0.3	3.6	1.6	–	–	–
γ'_I precipitate	Bal.	3.1	0.7	1.0	7.7	0.2	1.2	11.1	5.3	–	–	–
René 88DT												
Global	Bal.	16.0	4.0	4.0	13.0	–	0.7	4.1	1.8	–	0.015	0.03

Table 1.1: Chemical composition (% weight) of René 65 and René 88DT. Nominal composition of René 65 by Heaney [14], EDS analysis for phases composition by Charpagne [22], Nominal composition of René 88DT by Wlodek [23]

Microstructure and Phases

René 65 is a γ/ γ' polycrystalline superalloy with an area fraction of 35 % to 40 % of γ' phase. Such proportion of γ' precipitates expects René 65 to obtain its maximal elastic limit between 600 °C and 700 °C according to figure 1.4. The three populations of γ' precipitates are found in René 65 with characteristic sizes as follows:

Grain size 5 µm to 15 µm;

Primary γ'_I precipitates 1 µm to 3 µm;

Secondary γ'_{II} precipitates 20 nm to 70 nm;

Tertiary γ'_{III} precipitates 5 nm to 15 nm;

A large proportion of grains presents Σ3 coherent twin boundaries that occurred during the annealing process [8]. Lenthe *et al.* reported up to 46 % of Σ3 boundaries by 2D measurements and up to 70 % by 3D measurements of the total boundary length fraction in René 88DT using TriBeam tomography [48]. Twin boundaries are reported to affect the fatigue life of superalloys due to being a potential crack initiation site [49–52]. The proportion of Σ3 boundaries can be appreciated in the EBSD micrograph of grain boundaries in René 65 in figure 1.7 [34].

The microstructure of René 65 inherits heterogeneities from the forging process, as depicted in the EBSD map in figure 1.7. The alloy reveals a local dual microstructure constituted of zones with equiaxed grains (of 5 µm to 15 µm) embedded by fine grains bands (of 1 µm to 5 µm). The fine grains bands display very low grain misorientation due to the unrecrystallization of these regions.

EDS analyses reveal a significant proportion of chromium (up to 4 $\%_{wt}$) in primary γ' precipitates after 800 °C - 300 h aging treatments. Kontis *et al.* evidenced the presence of chromium and cobalt in primary γ' precipitates, in particular along dislocations inside the γ'_I, using Atom Probe Tomography (APT) reconstruction [45, 53, 54].

Other interstitial phases located in the γ matrix were revealed in René 65 by Bond *et al.* [40]:

Nitrides, TiN are characterized by a hexagonal or pentagonal shape, and size in the range of tens of micrometers. Nitrides can be enveloped by carbides / nitro-carbides. They exhibit a high Vickers hardness between 15 GPa and 35 GPa, Young's modulus (E) between 250 GPa to 580 GPa, a brittle behavior, and a face-centered cubic structure B1 [55].

Carbides, $MC - M_6C - M_{23}C_6$. Carbon, often present at concentrations up to $0.2\,\%_{\mathrm{wt}}$, combines with reactive elements such as titanium, tantalum, and hafnium to form MC carbides. M_6C and $M_{23}C_6$ are found along γ grain boundaries. Their formation occurs during processing or service. They are rich in chromium, molybdenum, and tungsten [2]. Carbides can act as crack initiation sites and thus play a deleterious effect on the fatigue behavior [56–58]. The addition of carbon is, nonetheless, required to increase the machinability of the alloy.

Borides, $MB - M_5B_2 - M_3B_2$. Boron can combine with elements such as chromium or molybdenum to form borides. They are preferentially located along γ grain boundaries. Their coalescence can increase the high-temperature ductility due to pinning of the grain boundaries by borides [44, 49].

TCP, $\sigma - \mu - Lavas...$. Topologically Close-Packed Phases (TCP) impact superalloys depending on the solicitation applied. They are generally undesirable, brittle phases that can form during the aging of the alloy. Laurence's observations on TCP formation in René 65 are resumed in the TTT (Time Temperature Transformation) diagram in figure 1.13. TCP phases are usually plates shaped, located along γ grain boundaries and close to γ'. Their brittle behavior negatively affects the mechanical properties (especially ductility and creep-rupture) as they act as crack initiation sites and tie up γ and γ' strengthening elements in a non-useful form [2, 58, 59].

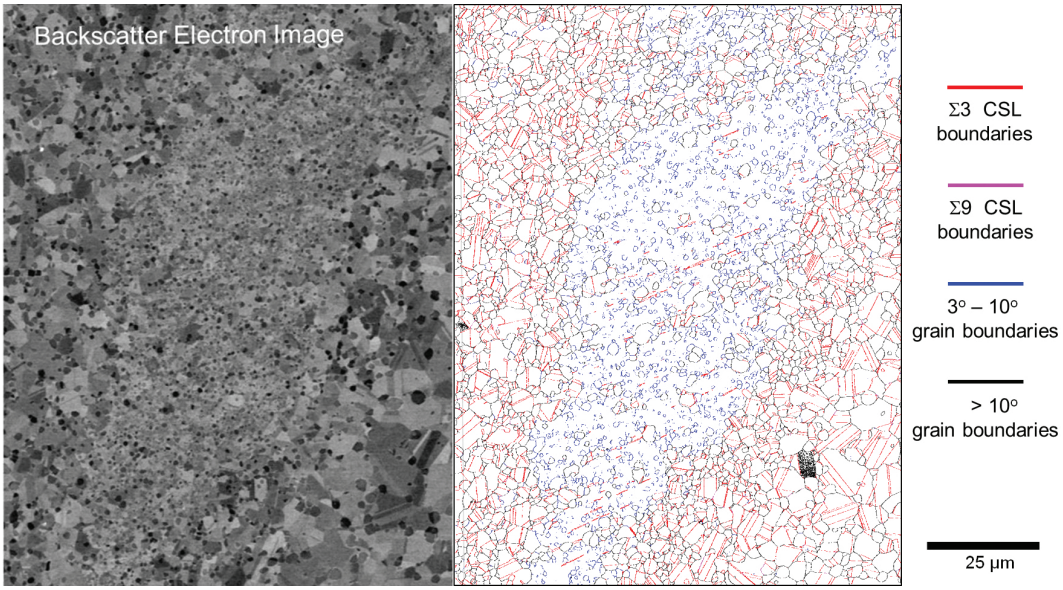

Figure 1.7: BSE and equivalent EBSD micrograph of René 65 by Wessman [34]

Mechanical Properties

The principal investigations conducted within this project only concern the tensile and fatigue behavior of René 65. The creep behavior is not in the present framework. The tensile behavior is of major concern since it is the most compatible with standard testing (available in the literature) to micro-mechanical testing. The tensile behavior is introduced first, followed by the fatigue behavior of René 65.

The two physical properties assessed in the tensile test are the Ultimate Tensile Strength (UTS - dimensioning criterion of disk burst during overspeed events of a turbine) and the Yield Strength (YS defined at 0.2 % of plastic strain - to minimize plastic deformation during service, which could cause blades and cases to rub together). The deformation mechanisms in René 65 are constant from room temperature to 550 °C (detailed in section 1.4.4), the material response is then in adequacy to the room temperature behavior minus the decrease in mechanical properties due to the increase in temperature. The mechanical properties of René 65 were first published by Heaney in 2014 [14], but more recent studies by Wessman and Laurence reported the René 65 mechanical properties [8, 34]. The room temperature YS of as-forged René 65 along with various aging conditions is summarized in figure 1.8.

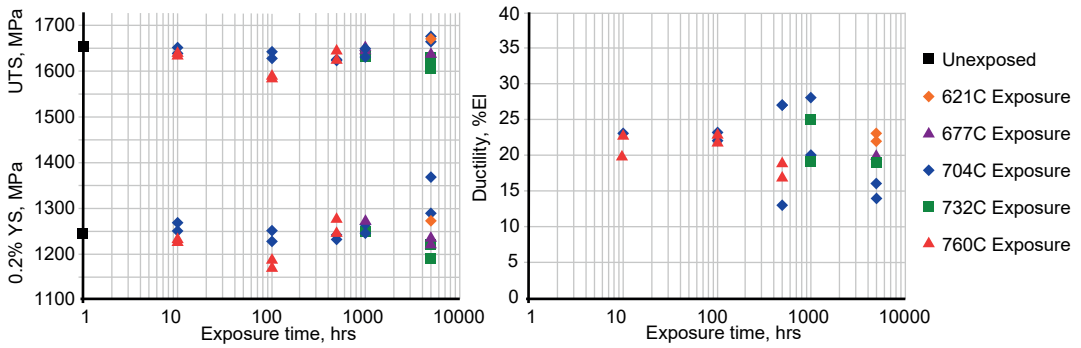

Figure 1.8: YS, UTS and ductility of René 65 at Room Temperature (RT) for as-forged and various static lab air aging conditions [34]

The YS measured by Wessman in the as-forged state is 1240 MPa [34]. René 65 exhibits a relatively stable YS for all aging conditions of Heat Treatment (HT) up to 1000 h except for Wessman's most elevated temperature of 760 °C.

The decrease in yield stress of René 65 over temperature in the range 20 °C to 760 °C is given in figure 1.9 [34]. 5 % decrease in YS is observed between 20 °C to 200 °C, whereas the YS is constant in the range 200 °C to 500 °C, to finally decrease with temperature increase above 500 °C. René 65 demonstrates similar YS behavior over the temperature as René 88DT but with 6 % to 8 % superior results. Figure 1.9 also reveals the higher performance of Alloy 718 at low temperatures but a faster decrease over the temperature. René 65 alloy outperforms alloy 718 from 500 °C with a slower decrease rate over temperature due to the different microstructures of the two alloys (γ'' phase in Alloy 718 is thermodynamically unstable above 650 °C).

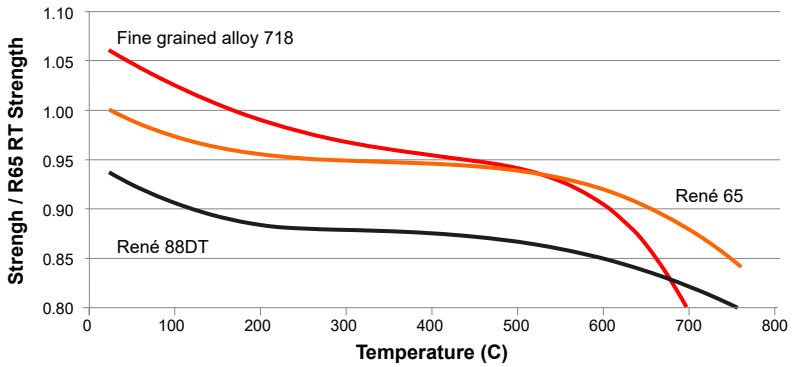

Figure 1.9: Tensile strength versus temperature of René 65 compared to René 88DT and fine-grained alloy 718 [34]

Standard heat treatment of René 65

The standard heat treatment applied to René 65 is a subsolvus solutionizing at 1065 °C for 1 h followed by a quench, and an aging at 760 °C for 8 h (see figure 1.10) [8].

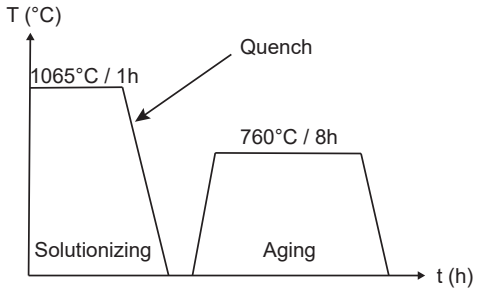

Figure 1.10: Standard heat treatment applied to René 65.

1.2 Metal evolution from heat exposure

The exposure to high temperatures generates modifications on the alloy, whether at the surface due to reactivity with the environment (thermally activated), or in the core with growth and stabilization of all the phases to reach thermodynamic equilibrium. The term high-temperature is rather controversial to use as it is materials dependent. Sahu and Navrotsky defined the term high-temperature to be "*the temperature above which the material is strongly chemically reactive in use*" [60].

The first section aims at defining the high temperature of René 65 studying its bulk microstructural evolution in the temperature range from 650 °C to 800 °C. The second section focuses on the interactions of René 65 with its environment, *i.e.* the surface reactivity phenomena.

1.2.1 Bulk aging phenomena

Microstructural evolutions

Microstructural evolution of René 65 exposed to temperatures from 700 °C to 925 °C for exposure times of 2 h to 4000 h were investigated in the works of Laurence and Wessman [8, 34]:

Grain size . Laurence exposed René 65 to heat treatments at temperatures of 750 °C, 800 °C, 850 °C and 900 °C at respective times of 1000 h, 1000 h, 500 h and 1000 h. EBSD analysis allowed the grain size evolution analysis. Figure 1.11 reveals no migration of grain boundaries and subsequently grain growth for all heat treatments performed. The overall average grain size was of 5 µm with 3 µm for unrecrystallized fine grains regions.

primary γ′ precipitates γ'_I . Similarly as the grain size, Laurence reported limited evolution of the primary γ′ precipitates from the same analysis. Long-term exposure heat treatments induced a slight decrease in area fraction of the primary γ′ precipitates, 8 % to 10 % were reported after 1000 h at 900 °C compared to the initial area fraction of 12 % to 14 %. No change in morphology was reported, and the spherical shape remained still.

Secondary precipitates γ'_{II} . Wessman and Laurence both agreed on the coarsening of the secondary precipitates. Such coarsening is thermally activated as denoted in figure 1.12, an increase in the temperature results in the small secondary precipitates dilution in favor of the large secondary precipitates growth. These evolutions are driven by the reduction of the interfacial energy and are named Ostwald ripening [61]. The increase of the exposure time at iso-temperature also leads to similar conclusions. Secondary γ′ precipitates coarsening is controlled via diffusion phenomena and follows an Lifshitz-Slyozov-Wagner (LSW) law (see equation 1.2) [62]. This assumption is valid for low exposure time (100 h) for temperatures above 850 °C or exposure time of up to 2000 h for temperatures lower than 850 °C. The constant value of the LSW law k is 17 $nm^3\,h^{-1}$ at 750 °C and 67 $nm^3\,h^{-1}$ at 800 °C according to Laurence [8]. The coalescence being diffusion governed, the activation energy Q was given by Laurence at a value of 349 $kJ\,mol^{-1}$ according to equation 1.3. No change in shape was reported, and the spherical shape remained still.

Tertiary precipitates $\gamma`_{III}$. Wessman reported no observation of tertiary precipitates in its investigations for aging heat treatment above 788 °C. For temperatures between 677 °C to 760 °C, the presence of such precipitates was reported for short exposure times closer to 760 °C (10 h) and longer times at lower temperature (thousands of hours at 677 °C). The $\gamma`_{III}$ dissolution supplies preferably $\gamma`$ entities (Al, Ti) to the coalescence of $\gamma`_{II}$ precipitates reported above.

$$r^3 - r_0^3 = k \cdot t \tag{1.2}$$

with r being the actual particle diameter, r_0 the initial particle diameter and t the exposure time.

$$k = k_0 \cdot \exp \frac{-Q}{R \cdot T} \tag{1.3}$$

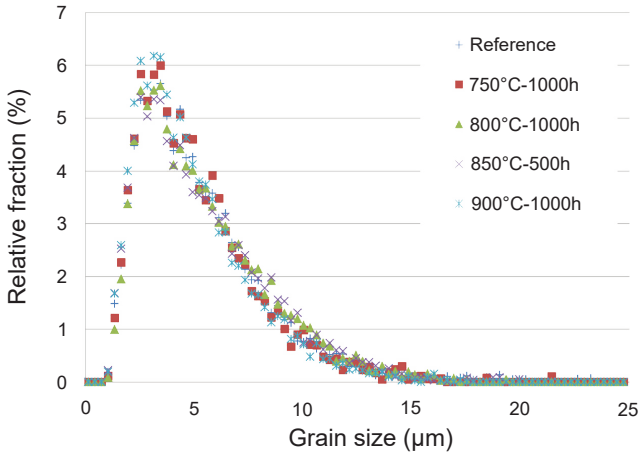

Figure 1.11: Grain size distribution in as-forged and aged René 65 [8]

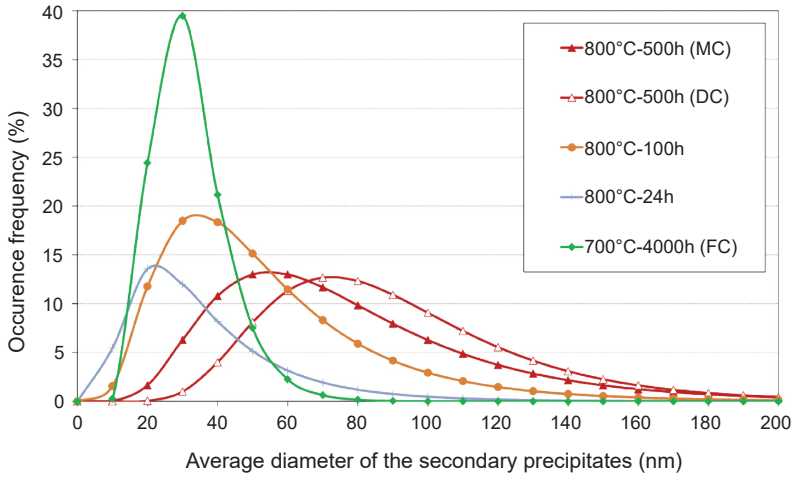

Figure 1.12: Secondary γ' precipitates coarsening due to 500 h aging heat treatment at different temperatures [8]

Phases formation

The high-temperature exposure of an alloy can not only modify the stable or metastable phases present at the initial state but micro-segregation/diffusion of elements can involve the development of additional phases. New phases forming in the bulk of the alloy resulting from heat exposure are summarized in figure 1.13. René 65, with a weight fraction of 4 % of molybdenum and tungsten, is prone to boride and TCP phase formation. Borides and TCP phases segregate close to primary γ' precipitates or along grain boundaries [8, 34].

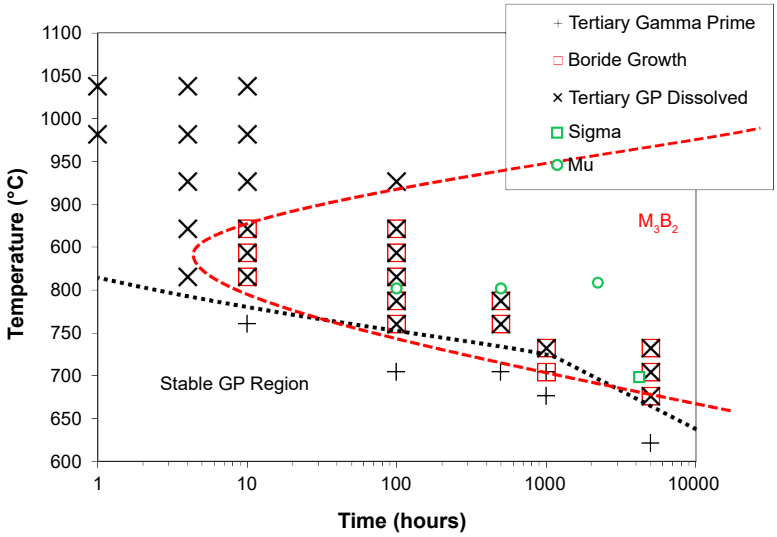

Figure 1.13: Time Temperature Transformation diagram of René 65 by Wessman [34]

1.2.2 Surface reactivity phenomena

Introduction

Exposing an alloy in service at high-temperature results in chemical reactions with the surrounding environment. Depending on the entities present at high-temperature (wet or dry air, combustion remainings or not, salts...), oxidation or corrosion of the surface can occur. This study focuses on the oxidation of René 65, the corrosion process will be excluded from the scope of the surface reactivity phenomena.

Ni-based superalloys, and consequently the René 65, contain aluminum and chromium able to promote the development of a self-protective oxide onto the surface when exposed to air at high-temperature [63]. Aluminum and chromium oxidize preferably due to their affinity with oxygen, the thermodynamic stability of their respective oxidized form with regards to their activity, and the partial pressure of reactants, accompanied by their favorable kinetics [64–66]. The Ellingham / Richardson diagram reports the relative thermodynamic stability (free energy of formation) for various oxides on pure elements as exposed in figure 1.14 [67]. The thermodynamic stability of oxides only predicts their formation. The kinetic rate influences which phases preponderate for a specific condition, as summarized in figure 1.15.

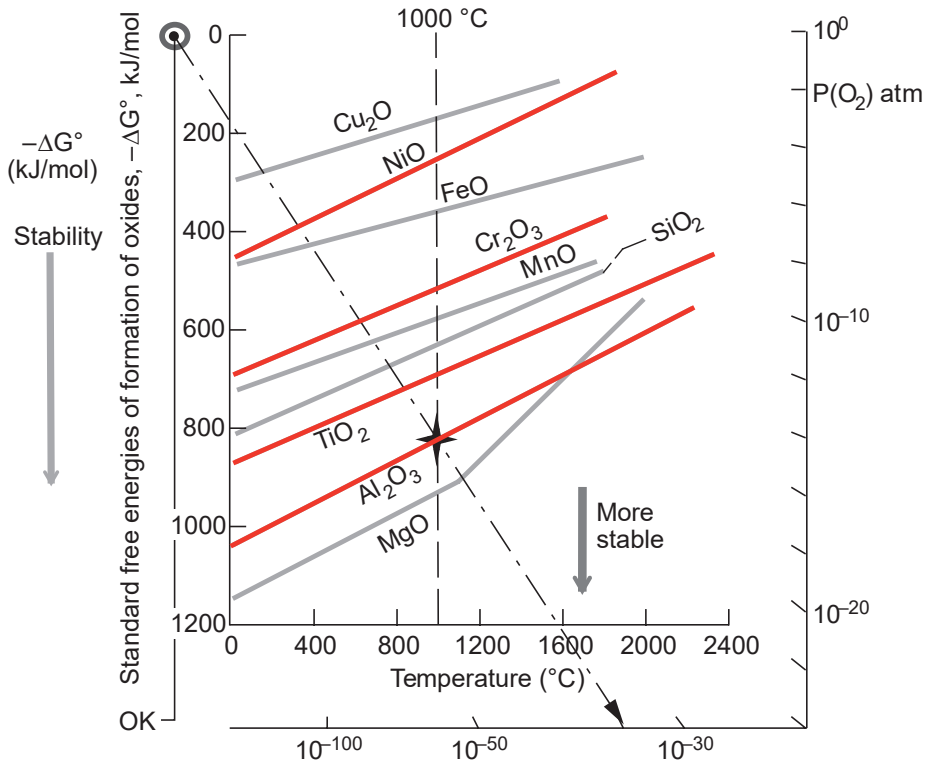

Figure 1.14: Modified Ellingham/Richardson diagram showing the relative thermodynamic stability (free energy of formation) of various oxides. The corresponding equilibrium gas composition can be found using the monograph by drawing a line from the focus point to the oxide curve at the temperature of interest and extending to the side axes for O_2 equilibrium pressure [67].

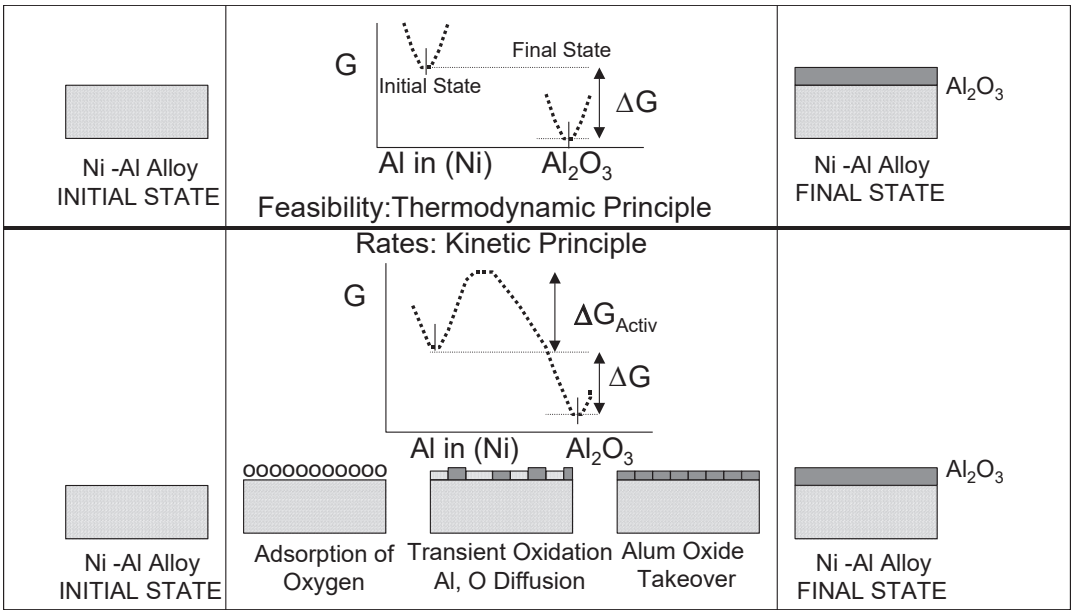

Figure 1.15: Illustration of the concept of activation energy from Bose [64]

The reaction required to form the oxide involves the oxidation of the metal element to a metal cation and the reduction of the oxygen to an anion as given by eq. 1.4.

$$\frac{2a}{b}M + O_2 = \frac{2}{b}M_aO_b \tag{1.4}$$

Where M is a pure metal or an oxidizable element of an alloy.

The location of the chemical reaction between the anion and the cation depends on the rates of the anions or cations diffusion through the formed oxide layer for diffusion-controlled oxidation. Diffusion mechanisms through a solid layer are thermally driven (Arrhenius law). Therefore, the oxidation kinetics and the consequences of oxidation on the microstructure and local chemistry of nickel-based superalloys are accelerated with increasing temperature for similar growth mechanism. The outer oxide layer can develop at two locations:

1. at the surface, *i.e.* at the "environment/external oxide" interface.

2. below the external oxide layer, *i.e.* at the "oxide/superalloy" interface.

As mentioned earlier, the reaction front, *i.e.* at the "environment/external oxide" interface or at the "oxide/superalloy" interface depends on the diffusion of anions and cations through the oxide layer. The growth rate of the oxide layer is governed by the kinetics of the fastest diffusing cation/anion through the oxide:

Anionic growth the oxide formation reaction takes place at the oxide/superalloy interface due to the faster diffusion of anions.

Cationic growth the reaction of oxide formation takes place at the interface environment/oxide due to the faster diffusion of metallic cations.

In the case of complex materials where different metallic elements of the superalloy are subject to oxidation, different external oxides (M_aO_b) can form, but internal oxides (B_aO_b) can also grow depending on the thermodynamic stability of element B, the concentration/activity of element B in the superalloy, the diffusivity of element B in the superalloy and the dissolution of oxygen in the superalloy. B_aO_b is necessarily thermodynamically more stable than M_aO_b oxide to form internally.

An oxide layer can be protective or destructive for the structure depending on its compacity, *i.e.* the presence of pores. The Pilling and Bedworth ratio, noted PBR and defined by the equation 1.5, allows to determine the continuous or discontinuous character of the oxide (continuous or not continuous oxide layer at the surface). A ratio between 1 and 2 leads to a continuous oxide layer; a ratio lower than 1 is symptomatic of a discontinuous layer on the surface (oxide gap on the surface generating oxygen diffusion wells) while a ratio higher than 2 leads to compressive/tensile stresses due to oxide formation likely to deteriorate the oxide layer (stresses in the oxide layer causing its potential damage and spallation). The notion of protective oxide comes into play when the external oxide scale acts as a barrier limiting the oxidation reaction, reducing the diffusion kinetics of the oxidant or the reductant due to an increase in oxide thickness with time. The oxide must therefore be stable, adherent, and compact, *i.e.* free of cracks and pores. A destructive oxide consists in diffusion wells that facilitate the oxidation

reaction. The kinetics of oxide formation is not reduced if the mean free path of gas molecules is higher than the size of the pores. Linear kinetics then results. [68–71]

$$PBR_{alloy} = \frac{V_{oxide}}{xV_{metal}} \tag{1.5}$$

Where V is the molar volume of the oxide and the metal and x is the number of metal atoms in an oxide molecule.

Wagner's kinetic rate theory

The kinetic rate of an external oxide layer can be modeled through different mathematical laws: logarithmic, linear, parabolic, cubic, etc. The parabolic model, following the assumption of Wagner's model, corresponds to the oxidation kinetics of AD730^{TM} according to the work of Thébaud, to RR1000 according to Encinas-Oropesa, and more generally to the oxidation kinetics of most of the Ni-based superalloys in the temperature range from 600 °C to 800 °C [2, 10, 41, 72]. A parabolic regime induces mass gain to follow the equation 1.6.

$$\Delta m^2 = k_w \cdot t \tag{1.6}$$

Where Δm represents the mass gain per unit area at time t and k_w the parabolic rate constant from mass measurements. It is common to describe k_p (from oxide scale measurement) by an Arrhenius relation as the k_p is a temperature-dependent constant:

$$k_p = k_0 \cdot \exp \frac{-E_a}{R \cdot T} \tag{1.7}$$

Where k_0 is a material constant, E_a is the activation energy, R is the perfect gas constant and T is the temperature (in K).

For the external oxidation mechanisms, the activation energy is similar to that of the fastest diffusing ion through the oxide layer. The Arrhenius diagram in figure 1.16 illustrates the parabolic rate constant of different nickel-based superalloys as a function of temperature [73–75].

Wagner's theory of oxidation kinetic relies on several restrictive hypotheses [76–78]:

- The oxide layer is compact, planar, and adherent to the planar substrate;
- The kinetic rate limiting parameter of the process is the diffusion of ions through the oxide layer;
- Thermodynamic equilibrium is established at the interfaces and any point in the oxide layer;
- The oxide is close to stoichiometry;
- Local charges phenomena at the interfaces are neglected because of a sufficiently thick oxide layer.

In reality, modeling the oxidation kinetics by a parabolic law is not valid over the whole life of the oxidation cycle. In the early stages, called the transient regime, the oxidation kinetics as well as the nature of oxides and the oxidation mechanisms can differ. Oxides observable at the surface may find their origins in such transient regime

[79]. A complete parabolic law taking into account not only the parabolic regime but the transitory regime was developed by Monceau and Pierraggi in equation 1.8 [80].

$$t = A + B\Delta m + \frac{1}{k_P}\Delta m^2 \tag{1.8}$$

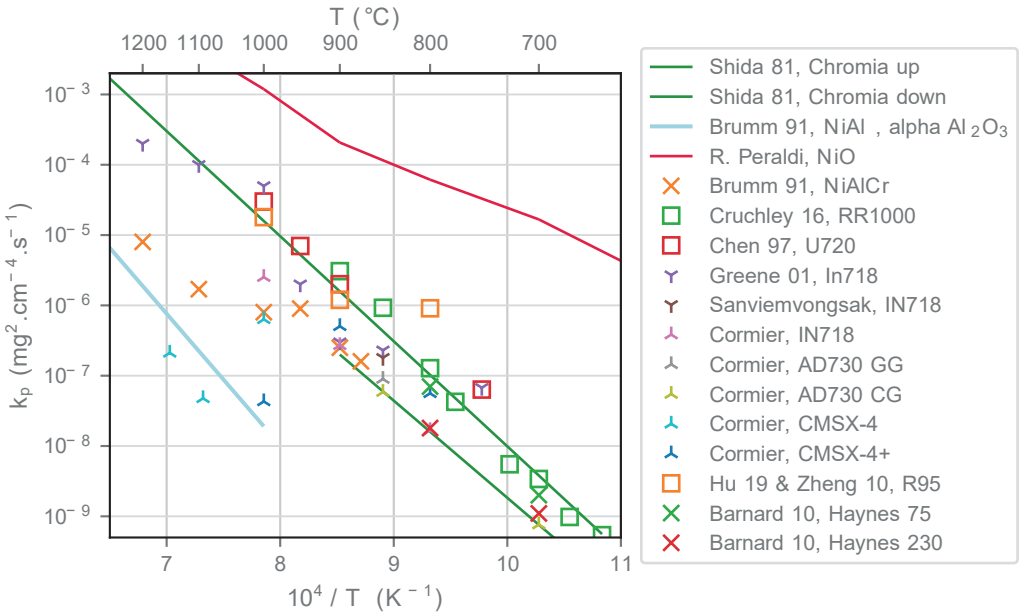

Figure 1.16: Arrhenius diagram for the parabolic rate constant of different Ni-based superalloys along with pure oxides [79, 81–88]

Sub-surface metal evolution during oxidation

The formation of oxide on the surface by the reaction of alloying elements with oxygen leads to the sub-surface consumption of these alloying elements. The consumption of these elements creates a chemical gradient between the core and the surface of the material, which induces migration phenomena by diffusion to balance the chemical composition. Fick's laws account for this flow of chemical species through the material (Fick's law: equation 1.9) [70].

$$J = -D \cdot \nabla c \tag{1.9}$$

Where D is the diffusion coefficient of each species in the superalloy, of dimension $[D] = L^2/T$, usually expressed in $cm^2\,s^{-1}$. The flux J is expressed in number of particles or number of moles per unit area per unit time (corresponds to a flux density, commonly abbreviated flux).

The entities flux is microstructure dependent as described below [89]:

- Intragranular diffusion: diffusion in volume via punctual defects of the crystal lattice, gaps in particular.
- Intergranular diffusion: diffusion along grain boundaries.
- Diffusion along the dislocation lines.

In the temperature range from 20 °C to 800 °C, the diffusion kinetics varies between the different microstructural elements, the grain boundaries are the entities showing the fastest diffusion, followed by the dislocations and finally the diffusion in the volume: $D_{gb} > D_{dislo} > D_{volume}$. Such microstructural dependency on diffusion kinetics has a major effect on the oxidation kinetics. For instance, Bataillou reported several orders of magnitude in the parabolic rate constant in chromia forming alloys [90].

Models taking into consideration microstructural features and vacancies in the oxidation kinetics such as EKINOX developed by Desgranges aim for a better understanding and modeling of oxidation impact on the sub-surface [90–95].

From intrinsic chemical failure to breakaway mechanisms

The elements involved in surface or sub-surface oxidation are consumed to feed the oxidation reactions. Chemical failure is about to happen in the case of a dense oxide layer produced by selective oxidation for high-temperature and long-term exposure of the alloy [65]. The entities' consumption is then faster than their replenishment via atom diffusion to the metal/oxide interface due to a depleted area or a diffusion barrier formation. Two types of chemical failure are possible:

MICF mechanically induced chemical failure the protective oxide layer was to spall or crack and the solute concentration of the oxidizing element is too low to re-form the protective layer, leading to the formation of a non-protective oxide scale (faster oxidation growth for instance) but no apparent mass gain increase from such non-protective oxide scale.

InCF intrinsic chemical failure the oxidizing element that forms the protective layer becomes progressively depleted as the oxide scale increases in thickness. The concentration and so activity of the element involved in the protective oxide scale (Cr_2O_3 or Al_2O_3) decreases below other entities involved in mixed oxide formation ($NiAl_2O_4$ for instance). The mixed oxidation formation is not protective but no significant mass gain increase is revealed due to diffusion limitations from the intact protective oxide scale [96].

Breakaway oxidation occurs cyclically or monotonically depending on the depletion profile and diffusion kinetics of the oxidized entities. A fast diffusivity of the oxidized elements can lead to the entire thickness of the part being depleted, whereas a slow diffusivity can lead to a local depletion profile. A cyclic breakaway is the result of a local depletion profile with concomitant oxidation from protective and non-protective oxide scales regarding the ratio of chemical entities available at the oxidation interface. The breakaway mechanism is associated with linear to exponential mass gain due to the formation of non-protective oxides [97–99]. InCF can therefore produce no mass gain kinetic increase due to the protectiveness of the parabolic regime oxide scale onto the diffusivity of breakaway related entities through such scale [96, 100].

Oxidation of René 65 and similar alloys

Data on the oxidation of René 65 are very limited in the literature. Nickel-based superalloys contain sufficient aluminum and chromium to form at least an external oxide of chromium at intermediate temperature and alumina at high temperature due to the high thermodynamic stability of these oxides. In addition, very stable internal oxides, such as alumina, can develop at intermediate/high temperatures resulting in an oxidation-affected layer of thickness greater than the external oxide layer thickness.

Due to the complex chemical composition of these superalloys and the microstructural heterogeneities of alloys similar to René 65 (primary γ' precipitates, etc.), other external oxides can be formed. Because of its chemical composition, René 65 is likely to develop chromia (eq. 1.10), alumina (eq. 1.11), and titania (eq. 1.12).

$$2\frac{2}{3}Cr + O_2 = \frac{2}{3}Cr_2O_3 \tag{1.10}$$

$$2\frac{2}{3}Al + O_2 = \frac{2}{3}Al_2O_3 \tag{1.11}$$

$$2\frac{1}{2}Ti + O_2 = \frac{2}{2}TiO_2 \tag{1.12}$$

Similar studies, notably by Thébaud and Malacarne (see figure 1.17) on AD730^{TM} [41, 101], Németh and Chateau on Udimet720Li [102, 103], Cruchley and Encinas-Oropesa on RR1000 [10, 82], show a continuous development of an outer chromia oxide layer on the surface, as well as internal alumina spikes, located along grain boundaries and in primary γ' precipitates surroundings, in the temperature range from 600 °C to 800 °C.

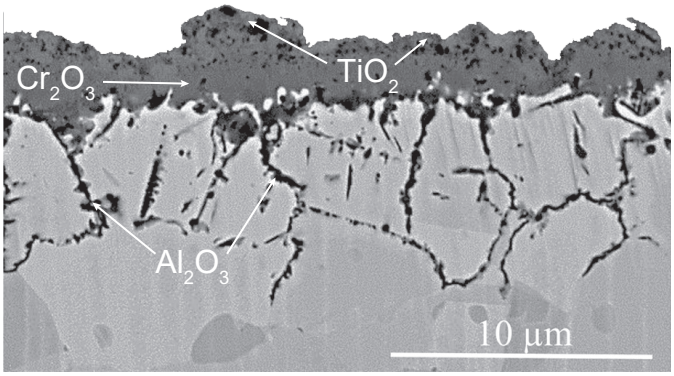

Figure 1.17: Cross-sections from samples of AD730^{TM} oxidized during 10 000 h at 700 °C [101]

External oxidation A concomitant sprouting of TiO_2 and Cr_2O_3 in the form of a mixed layer develops until the establishment of the parabolic oxidation regime, creating a homogeneous and continuous Cr_2O_3 layer in contact with the substrate.

Internal / intergranular oxidation Intergranular Al_2O_3 was also observed by Thébaud and Malacarne on AD730^{TM}. Malacarne reported the intergranular oxidation to be responsible for 30 % of the total gain mass [101].

Figure 1.18 schematically illustrates the oxidation processes of AD730^{TM} in the presence of grain boundaries according to Thébaud: (a) being the microstructure before oxidation, (b) being the transitory regime, (c) and (d) the parabolic regime [41]. This step-by-step oxidation mechanism is in agreement with Malacarne *et al.* observations on AD730^{TM} as denoted in figure 1.17.

Govaere and Malacarne performed EDS analysis on the oxidized surface of AD730^{TM} revealing insights on the presence of emerging primary γ' precipitates onto the oxidation kinetics and products. Primary γ' precipitates reported a thicker chromia layer and the pronounced presence of alumina [9, 104].

Stinville *et al.* reported the impact of the higher grain boundary diffusivity with grain boundary oxidation above the external scale of chromia in René 88DT as denoted in figure 1.19 [105].

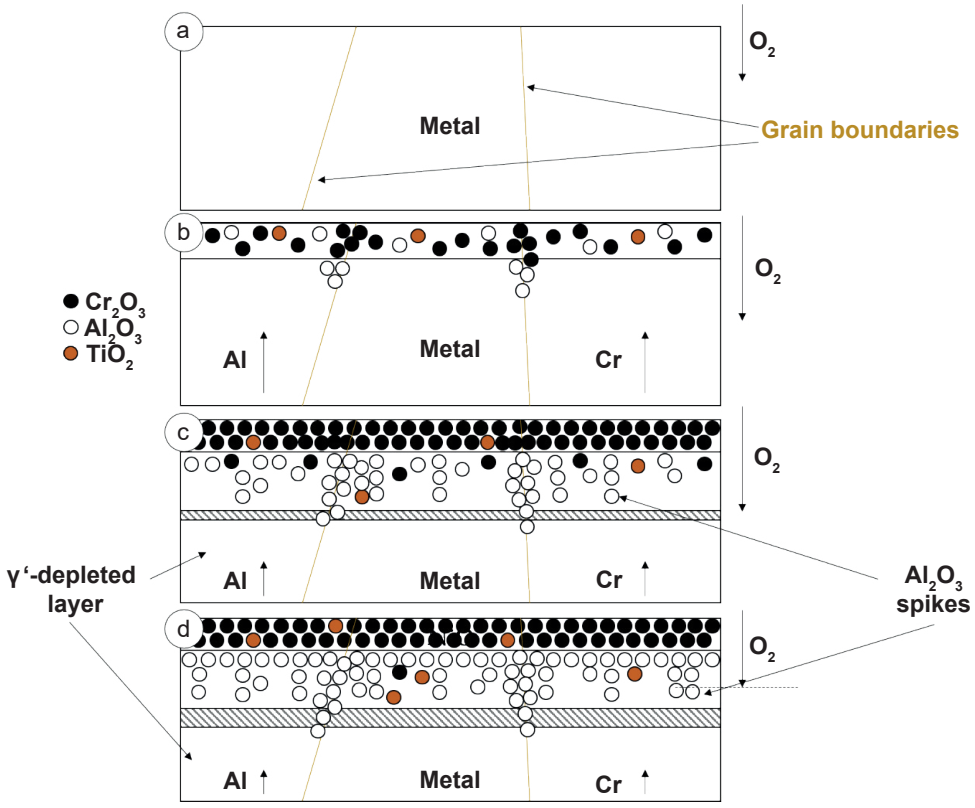

Figure 1.18: Schematic representation of oxidation process in AD730^{TM} at intermediate temperatures [41]

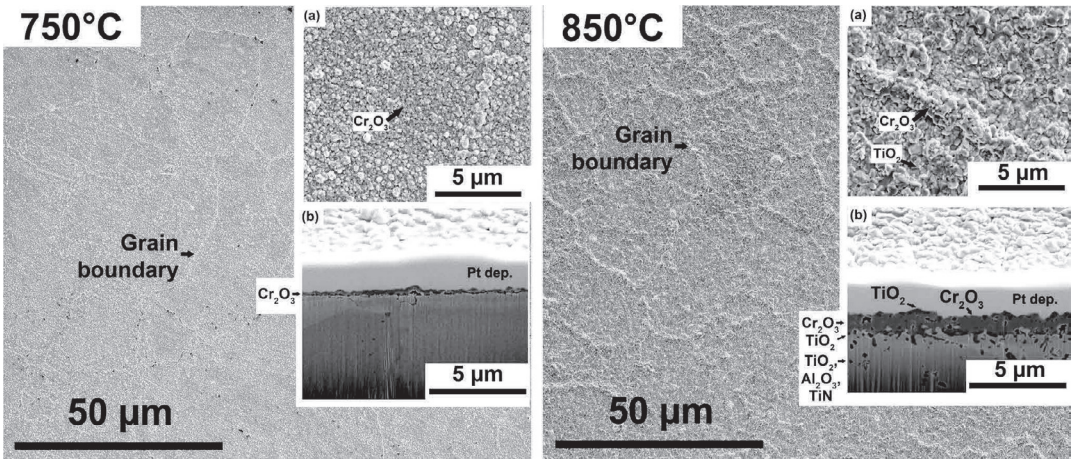

Figure 1.19: Surface and FIB cross-section micrographs of René 88DT oxidized at 750 °C and 850 °C revealing grain boundary oxidation [105]

Non-metallic phases' oxidation

Nitrides at the surface of the metal with direct contact to oxygen may oxidize to titania TiO_2 in the temperature range 650 °C to 1000 °C according to equation 1.13 [106–110]. Nitrides oxidation results in strong volume expansion, resulting in tensile/compressive stress generation that can favor crack initiation. The carbide transformation equation is given in equation 1.14. Oxidation of the nitrides results in the release of nitrogen in the matrix. The 900 °C parabolic rate constant k_p of nitrides oxidation was reported in the magnitude of $3.0 \times 10^{-8}\,\mathrm{kg^2\,m^{-4}\,s^{-1}}$ [111] against $4.9 \times 10^{-11}\,\mathrm{kg^2\,m^{-4}\,s^{-1}}$ in AD730^{TM} [41].

$$TiN + O_2 = TiO_2 + \frac{1}{2}N_2 \tag{1.13}$$

$$TiC + 2O_2 = TiO_2 + CO_2 \tag{1.14}$$

The titania TiO_2 formed adopts two crystallographic structures depending on the temperature. Below 700 °C, the anatase structure prevails, above 700 °C the rutile structure is dominant (as denoted by figure 1.20).

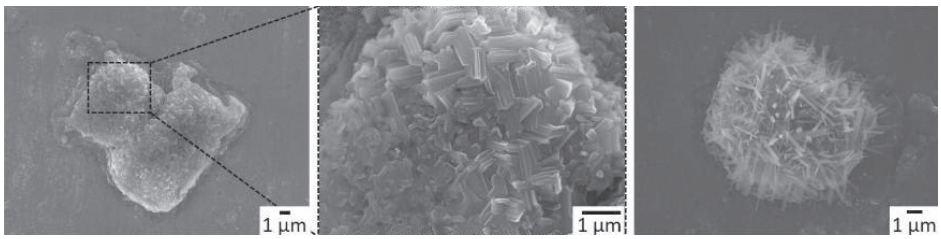

Figure 1.20: SEM-SE micrograph of TiN oxidized at 700 °C during 24 h observed by Govaere [9]

1.3 Size effect on the mechanical and oxidation behavior

René 65 is expected to have interaction with air that influence the first micrometers at the surface, as exposed in the previous section 1.2.2. Such thin layers present at the surface may impair the mechanical behavior according to the solicitation modes and environmental interactions seen by engine parts during their in-service life. The surface and sub-surface degradation/evolution may play a key role in the damaging processes of the alloy. The use of thin specimens, in the same length magnitude as the microstructural/chemical gradient, would allow the characterization of the local properties of a such gradient. This section focuses then on the use of thin specimens.

The different concepts introduced so far demonstrate the usefulness of discretizing the gradient of properties (mechanical, chemical, microstructural, etc.) in order to characterize each layer of the gradient. The representative thicknesses underlying the different phenomena in the range of temperatures/times intended are the following, as depicted in figure 1.17:

Oxidation from micrometers to ten micrometers.

Depletion zone from the micrometer to the ten micrometers.

Grain size height micrometers.

1.3.1 Particularities on the use of thin specimens

Mechanical tests on thin products are sensitive to the surface-to-volume ratio, and, moreover to the reduction of the specimen section. A high surface-to-volume ratio, *i.e.* of thin specimens, favors surface effects (free surface, surface diffusion, oxidation, reduction of surface tension, etc.). The use of thin products is rather controversial because of the small volumes tested, especially in the case of high-temperature testing of metallic materials. The effects inherent to the use of thin specimens are listed in the literature: [112–114], with a look at the ratio of specimen thickness to average grain diameter for polycrystalline materials: [115–120].

The use of microtensile specimens raises questions about the minimum representative elementary volume of analysis due to the low number of grains in the thickness. For a sample to be representative of the material's mechanical behavior, the threshold is set as the representative volume element (RVE), with sufficient size to provide an appropriate homogenized behavior. This point leads to investigating the number of grains contained in the specimens' thickness for a given polycrystalline material. For the specimen geometry employed within this framework, a 20 µm-thick specimen provides a 0.04 mm^2 section with 1 to 3 grains in thickness for an ASTM 10 grain-sized alloy but hundreds of thousands of grains in the 2 mm wide and 5 mm long gage region (developed in section 2.1.2). As RVE is questionable in the thickness of the specimens and animates the scientific community disagreements on the use of micro-mechanics, the gage volume of the thinnest sample fulfills RVE requirements in terms of material considerations and elastic behavior.

The mechanical behavior of a thin specimen varies according to the ratio "specimen thickness / average grain diameter" (t/d). This ratio delimits three domains, a monocrystalline behavior for a value of t/d below 1, a multicrystalline behavior for values of t/d in the range 1 to 10, a polycrystalline for high values of t/d [114, 121, 122].

This phenomenon was illustrated by Texier on In718 with a polycrystal to multicrystal transition of two grains in the thickness [115]. Keller concatenated several values of t/d ratio from the literature, depending on the material and its microstructure. The critical value of t/d of the polycrystal to multicrystal transition is within the range 2 grains to 30 grains in the section of the material. Keller's work evidenced a transition value in the range 1 to 4 in a high-purity polycrystalline nickel alloy, as denoted in figure 1.21 [120]. Low values of t/d revealed a drop in ductility, yield strength, and maximum stress at failure.

The multicrystal to polycrystal transition seems intrinsic to the material. Miyazaki attributes this transition to the microstructure and to the stacking fault energy of the dislocations [123]. These surface effects induce a stress gradient of about 30 % between core and surface grains, according to TEM results performed by Keller *et al.* on pure nickel and validated by a finite element model of crystal plasticity, as depicted in figure 1.21 [124, 125]. Surface softening is a combination of several effects. Couret studied the elementary mechanisms of deformation by *in-situ* TEM testing: [126]

- The zero stress field in the boundary condition imposes an image force on the dislocations at the free surface, which attracts the dislocations to a distance at the surface less than the mean free path [126].
- Annihilation of dislocations parallel to the surface, which causes a decrease in the density of dislocations. The emergence of these dislocations prevents the formation of dislocation dipole and thus the strain hardening related to multiple slips and the formation of a dense network of dislocations [127].

Maximization of the oxidation impact on the microstructure for reasonable oxidation duration requires specimens as thin as technologically possible. A reduction in specimen thickness results in greater involvement of surface effects than volume effects, and thus exacerbates any oxidation-affected layer.

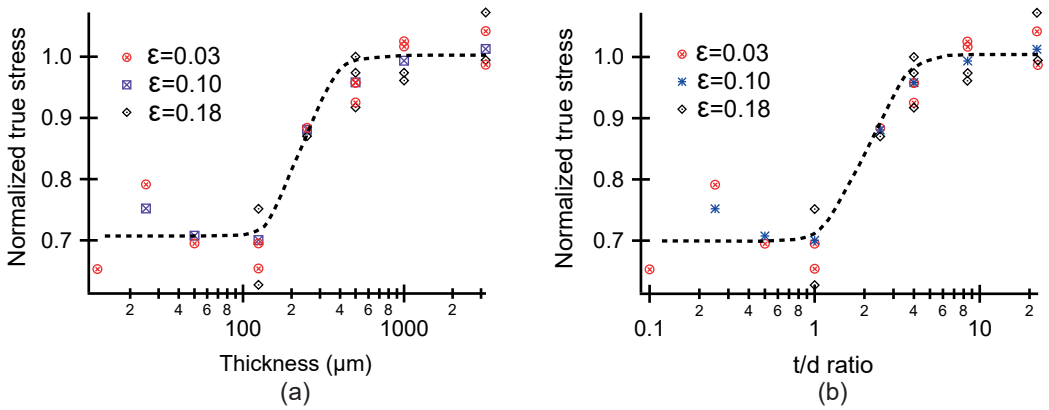

Figure 1.21: Evolution of the normalized stress by the stress of the thickest sample for different strain levels, as a function of the thickness (a) and t/d ratio (b) [120]

1.3.2 Microstructural effect in the use of thin specimens

Figure 1.22 compares the yield strength of two microstructures (solid solution and precipitation hardened) for three grain sizes (CG = coarse grains, MG = medium grains, FG = fine grains) on Alloy 718. The multicrystalline to polycrystalline transition in the solid solution was obtained for a t/d ratio around two on all grain sizes. The precipitation-hardened specimens have a transition around 150 µm for all three grain sizes. The yield strength of the three grain sizes shows a variation of 20 % for the precipitation-hardened material versus 33 % for the solid solution. These results expose the impact of the precipitates on the elastoplastic transition and draw particular attention to the results of this project (René 65 being precipitation-hardened).

The results of mechanical tests for René 65 should not be dependent on the sampling area for mechanical tests on the non-aged state (the variation in grain size can be significant in the case of only one grain in the thickness of the specimens, thus influencing the fraction of grain boundaries present in the specimen). Microstructural evolutions due to aging at high-temperature result in the formation of a sub-surface primary γ' precipitates depleted layer. Such a solid-solution layer may induce mechanical behavior variability within the microstructural gradient, as the bulk is excepted to behave similarly to the precipitation-hardened specimens. Moreover, the intensity in planar slip from a precipitation-hardened to a solid solution-hardened microstructure may differ. At macroscopic iso-strain, a solid solution Alloy 718 exhibits more emergent slip bands on the surface compared to a hardened Alloy 718. Hardened alloy demonstrates significantly more pronounced slip bands in intensity but with fewer bands (fewer slip bands in number results in higher slip activity to accommodate the plastic strain) [13].

The present study focuses on the oxidation of René 65 and its mechanical impact. The presence of a homogeneous, adhesive, and continuous external oxide layer at the material surface may affect the free surface phenomena. An oxide layer can restrain the dislocation escape by acting as a microstructural barrier. This is particularly true in the case of thermo-mechanical-chemical coupling of materials with graded properties/microstructure.

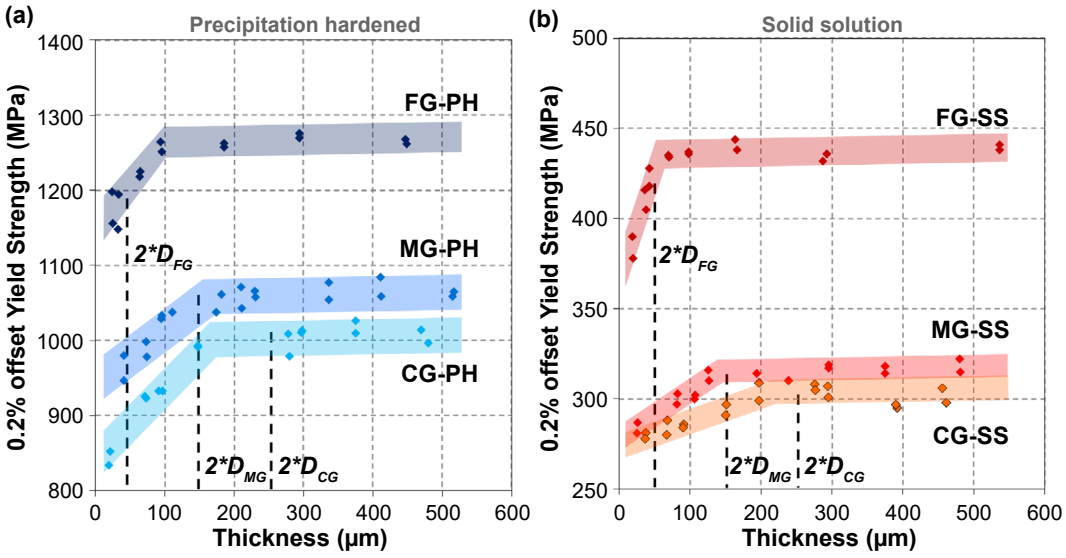

Figure 1.22: Influence of the microstructure on the yield stress of Alloy 718 thin specimens [128]

1.3.3 Small scale specimens preparation and testing

Several methods allow to obtain the local properties of a material up to high-temperature:

- Nanoindentation [129–131], micropillars [132], microcantilevers aim at the local mechanical properties of nanocrystalline materials or of a grain / bi-crystal in order to investigate the fundamental mechanisms of the dislocations dynamics [133, 134].
- Tensile or bending on micro-tube / micro-specimens [135–139] allows to obtain mechanical properties from a representative elementary volume, able to take into account the presence of defects or microstructural barriers (precipitates, grain boundaries, free surface) [112, 113, 122, 140, 141].

The main focus of this project is the use of thin specimens with a minimum thickness of 20 µm. Several techniques are listed in the literature to design micro-mechanical specimens:

- Ion Abrasion [142].
- Lithographic techniques [143, 144].
- Focused Ion Beam (FIB) Ion Abrasion [145–150].
- TriBeam with femtosecond laser [151].
- Xe+ plasma FIB [152].
- Photochemical machining [153].
- 3D Micro Milling [133, 154].
- Electrochemical stamping (EDM: Electric discharge Machine) coupled with tripod polishing [135, 136, 139, 155, 156]. This latter method is implemented in this work.

1.4 Ni-based superalloys behavior and environmental interaction

Understanding the multi-scale relation of the ins and outs involved in the damaging of Ni-based superalloys drives the research community. A better understanding of the processes implicated in the failure of alloys helps to design parts and materials accordingly. The life span of parts is also more accurately predicted by considering environmental phenomena.

Polycrystalline materials

Polycrystalline materials are, by definition, composed of several grains having various crystallographic orientations. The plastic deformation within the grains induces irreversible deformations with the sliding of the densest planes (in terms of atoms density) {111} planes along the <110> direction for FCC structure (using Miller indices). The incompatibility of crystallographic orientation from neighboring grains under mechanical loading generates geometric dissimilitude. The continuity of stresses and strains on both sides of the grain boundaries may impose the simultaneous activation of several sliding systems. Such mechanism induces the presence of dislocation named GND (Geometrical Necessary Dislocation) according to Ashby (see figure 1.23) [157].

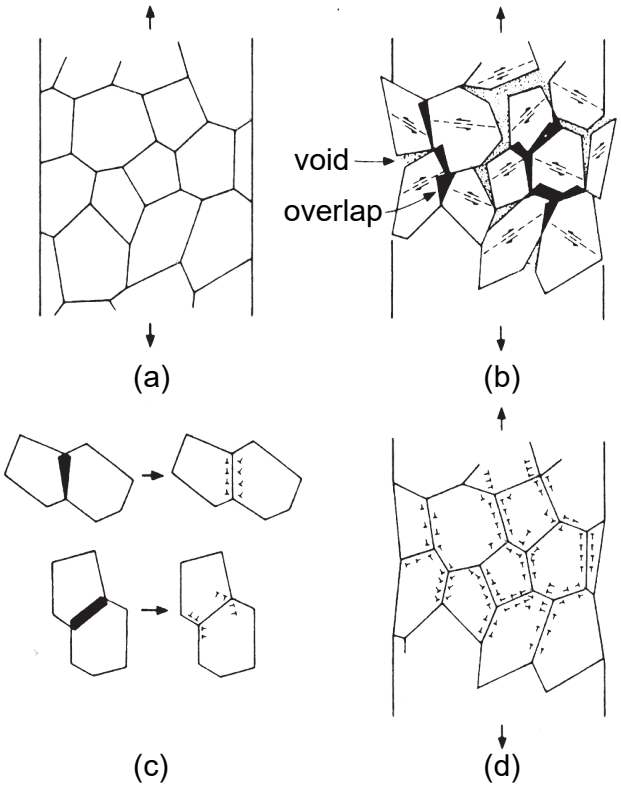

Figure 1.23: If each grain of a polycrystal, shown at (a), deforms uniformly, overlaps and voids appear (b). These can be corrected by introducing geometrically-necessary dislocations, as shown at (c) and (d) [157]

1.4.1 Tensile behavior

Grain size impact

The microstructure presented in section 1.1.2 and more particularly the figure 1.7 demonstrates the variability in size and shape of the grains present in René 65, and generally in polycrystalline materials produced by forging. The diversity of grain size leads to different mechanical behaviors in tension, fatigue, and creep. The yield stress of a polycrystalline material is related to the grain size by the Hall-Petch relation equation 1.15 [115, 158–160]

$$\sigma_c = \sigma_0 + \frac{k}{\sqrt{d}} \tag{1.15}$$

Where σ_c is the critical stress above which a polycrystalline material undergoes macroscopic plastic deformation, σ_0 is the component of the uniaxial tensile yield strength due to lattice friction and the presence of dislocations in the undeformed crystal, k is a constant related to the material, and d is the average grain diameter.

The value of σ_0 depends on the thermo-mechanical history of the material which modifies the initial dislocation density but also evolves during the activation of the multiple and deviated slip events causing a high degree of strain hardening due to the formation of a dense network of dislocations [115, 121]. Sondhi reported a k value of $400\,\mathrm{MPa}\,\mu\mathrm{m}^{-1/2}$ in René 88DT [34].

Bain *et al.* studied a duplex microstructure of U720Li (composed of large and small grains, obtained by solution heat treatment at a temperature close to the γ' solvus). Finer grains seem to drive the tensile properties. A duplex microstructure, thus, has monotonic tensile properties close to a microstructure composed exclusively of fine grains [161]. A fine grain size helps to increase the number of grain boundaries, thus promoting strain-hardening and material YS and UTS increase. Goff compared the impact of grain size and γ' precipitation state on the monotonic tensile properties of U720 at high-temperature; grain size is a second-order parameter compared to the γ' precipitation state [46].

γ' contribution

The γ' precipitates are the hardening phase of the nickel-based superalloys as they prevent dislocation motion through the crystal lattice. Such a mechanism directly contributes to the high yield strength of the material, and thus to its tensile properties. Not only the size but distribution is of importance in optimizing the alloy's mechanical properties. Vaunois *et al.* concluded that interparticle spacing is predominant to precipitate size and volume fraction in U720Li alloy strengthening [26].

The intragranular precipitate size, and in particular the γ'_{II} precipitates, has an impact on the tensile deformation mechanisms. Wessman modeled the evolution of the YS on René 65 through dislocation mechanism highlighting the effect of γ'_{II} size on the contribution of each mechanism, compared to experimental results, as illustrated in figure 1.24. Studies conducted on U720 Li and René 88DT confirm the precipitates-dislocations relationship [19, 26, 28]. Both figures 1.24 and 1.25 emphasize the higher resistance to shear of thinner secondary γ' precipitates. It is nonetheless true up to an optimal value below which, precipitates become shearable by dislocations.

The γ'_{III} precipitates, located in the matrix lanes, also have an impact on the yield strength. The ideal size according to Billot corresponds to the one that induces the transition between the shear mechanism by weakly coupled pairs of dislocations and

the shear mechanism by strongly coupled pairs (close to 40 nm for U720, close to 15 nm for RR1000 in figure 1.26) [162, 163].

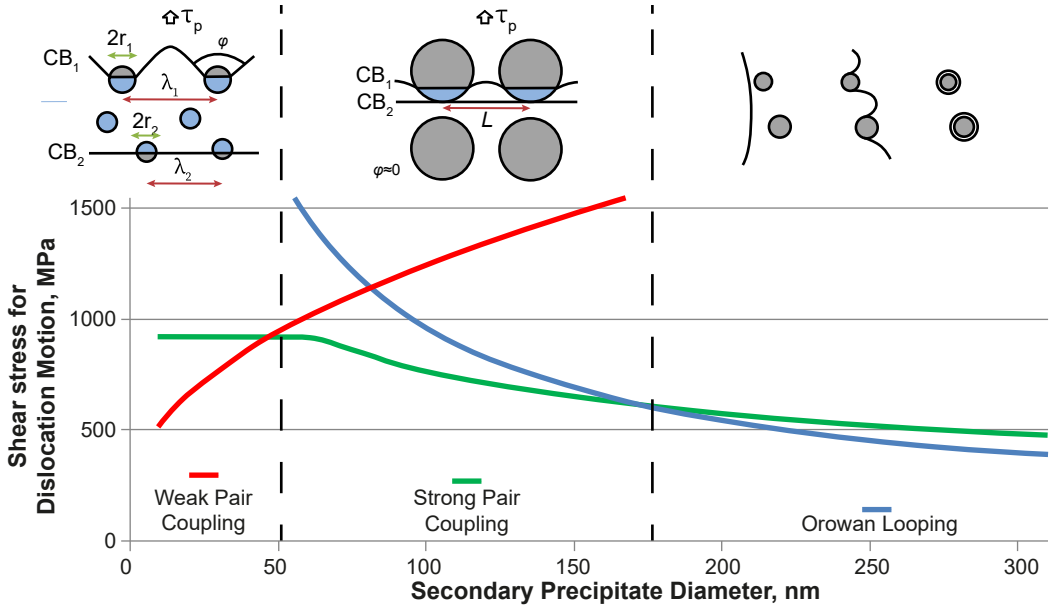

Figure 1.24: Shear stress for dislocation motion and equivalent precipitate crossing mechanism as a function of secondary precipitate size in René 65 [34, 163–165]

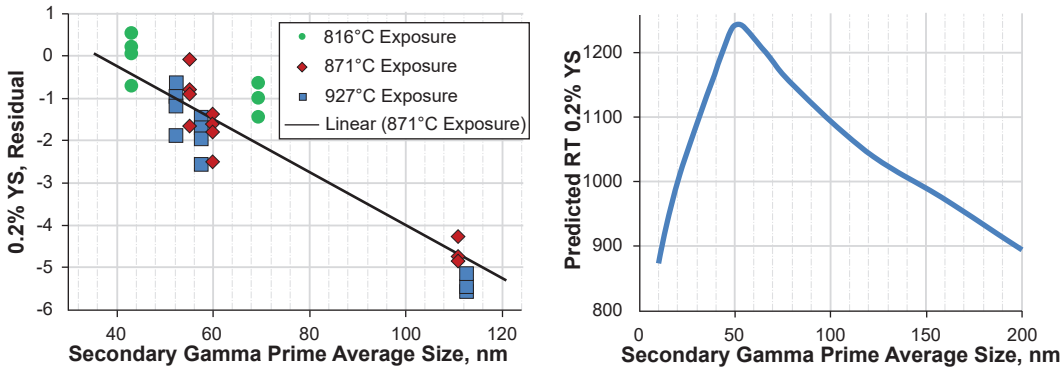

Figure 1.25: Experimental and predicted YS as a function of the secondary precipitates size in René 65 [34]

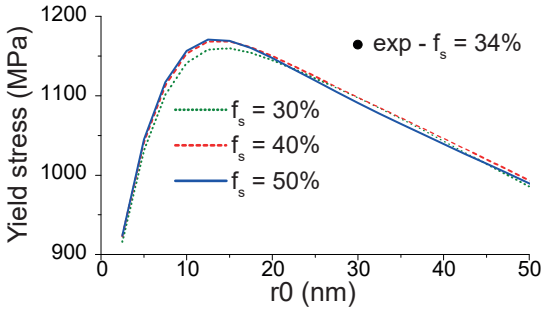

Figure 1.26: YS as a function of the tertiary γ' precipitates' size in RR1000 [163]

1.4.2 Fatigue behavior

Mechanical stresses of pure fatigue type are strongly related to the yield stress of a material. The fatigue behavior of nickel-based superalloys is generally studied along two main axes: the fatigue behavior at imposed deformation (total plastic strain control, monitoring of the stress evolution) and the cracking behavior (monitoring of the cracking rate).

Crack initiation

Different crack initiation mechanisms can be found in polycrystalline Ni-based superalloys depending on their microstructure, solicitation mode, and environment. Damages are known to mainly appear in the surface of René 65-like alloys for the high stress-strain domain of the LCF solicitation as denoted in figure 1.27 [166]. The presence of defects, inclusions, pores or roughness may act as local strain concentrators. Localization of the plastic deformation may also be revealed in the form of Persistent Slip Bands (PSB) at the origin of irreversible surface reliefs. In the absence of a defect, different damage modes can be observed, as illustrated in figure 1.28 by the work of Mineur on austenitic stainless steel of type 316L [167].

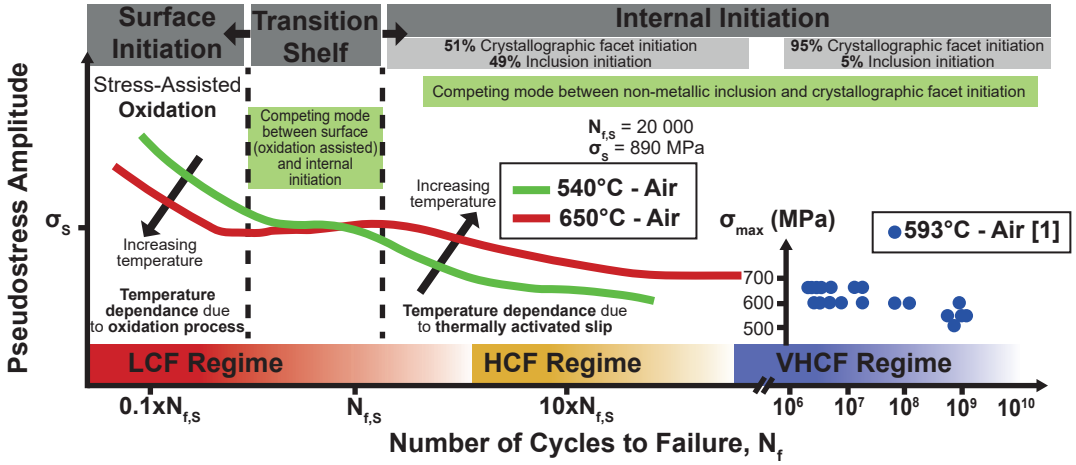

Figure 1.27: Synthesis of the parameters affecting the initiation mechanisms and durability of René 88DT for temperatures between 540 °C to 650 °C in LCF (0.5 Hz and 1 Hz), HCF (1 kHz) and VHCF (20 kHz) [166]

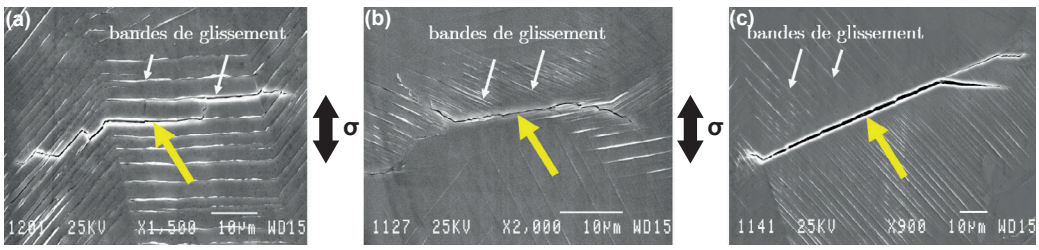

Figure 1.28: Fatigue crack initiations (marked by yellow arrows) on an austenitic 316L stainless steel ($\Delta\varepsilon_p/2 = 2.10^{-3}$, 20 °C, air, tests interrupted at 20 % Nf): intragranular along slip bands (a), and intergranular at general grain boundaries (b) and twin boundaries (c) [167]

Larrouy, Genée, and Pineau reported mostly intergranular initiation mode for U720 Li at intermediate temperatures (20 °C to 500 °C), through micro-volumes due to the interactions between PSBs and grain boundaries [13, 52, 168]. Billot *et al.* studied the impact of large grains in a duplex microstructure of U720 Li on crack initiation. These large grains represent preferential initiation sites [162]. Stinville *et al.* observed more precisely the role of twin boundaries in intergranular initiation mode. Grains are said favorably oriented once the three following conditions are met [169, 170]:

- a high Schmid factor in the twin and the parent grain for slip systems parallel to the {111} planes.
- a high elastic modulus discrepancy from the twin to the grain.
- an elongated twin boundary (linked to a large grain by extension).

1.4.3 Deformation mechanisms

Two major phenomena emerge in the literature regarding the crossing of precipitates by dislocations: shear and Orowan bypass. The prevalence of each phenomenon arises from the type and intensity of solicitation, the spatial distribution, and the size of secondary and tertiary γ' precipitates, but also the temperature.

Figure 1.24 combines the different crossing modes: (a) weakly coupled dislocation pair shear; (b) strongly coupled dislocation pair shear; (c) Orowan bypass; with a transition between the different mechanisms.

Orowan bypass

The bypass mechanism is composed of a perfect dislocation bending across the precipitate, leaving an Orowan loop around the precipitate after withdrawing. The shear must be above the Orowan stress given in equation 1.16.

$$\tau_{Orowan} = \frac{\mu b}{2r}\sqrt{f_v} \tag{1.16}$$

where μ is the shear modulus, b is the norm of the Burgers vector, r is the mean particle radius, and f_v their volume fraction.

Precipitates shearing

The stresses required for shearing γ' precipitates in the case of weakly coupled and strongly coupled dislocations in the case of mono-modal γ' precipitate distributions are given by the equations 1.17 and 1.18, respectively [163].

$$\tau_p^{Weak} = \frac{\gamma_{APB}}{2b}\left(\left(\frac{6\gamma_{APB}rf_v}{2\pi T_{ten}}\right)^{1/2} - f_v\right) \tag{1.17}$$

where γ_{APB} is the antiphase boundary energy of the precipitates in the {111} planes, and T_{ten} is the line tension.

$$\tau_p^{Strong} = \frac{\gamma_{APB}l_1}{2bL} = \sqrt{\frac{3}{2}}\left(\frac{\mu b}{\pi^{3/2}}\right)\frac{f_v^{1/2}}{r}\sqrt{\frac{2\pi\gamma_{APB}r}{\mu b^2} - 1} \tag{1.18}$$

where l_1 length of the leading dislocation segment active in shear, L is the average interparticle distance, μ is the shear modulus, b is the Burger vector.

1.4.4 Temperature involvement

Temperature impacts the mechanical properties by involving different plastic deformation mechanisms at the dislocation scale. Figure 1.29 illustrates three temperature ranges that have been identified on several single crystal superalloys [171]. Laurence describes the three temperature-dependent domains [8]:

20 °C to 550 °C Plastic deformation is mainly controlled by the shearing of the γ' precipitates. The perfect matrix dislocations dissociate into partial dislocations creating stacking faults. The stacking faults interfere with the dislocation movement, which contributes to increasing the material strength. This mechanism is activated at room temperature and progressively disappears with temperature increase, which leads to a progressive decrease of the yield strength [171].

550 °C to 750 °C The dissociated dislocations a$< 110 >$ adopt a Kear-Wilsdorf lock configuration in the γ' phase leading to an increase of the YS by deviated cross-slip in the cubic plane, favoring the hardening [172, 173].

Over 750 °C The bypass deformation mechanism of precipitates becomes preponderant. At these temperatures, the smaller intragranular precipitates coalesce or dissolve, thus increasing the interparticle distances, which favors precipitate bypass rather than shear. As a result, dislocations can move more easily, leading to a drop in yield strength.

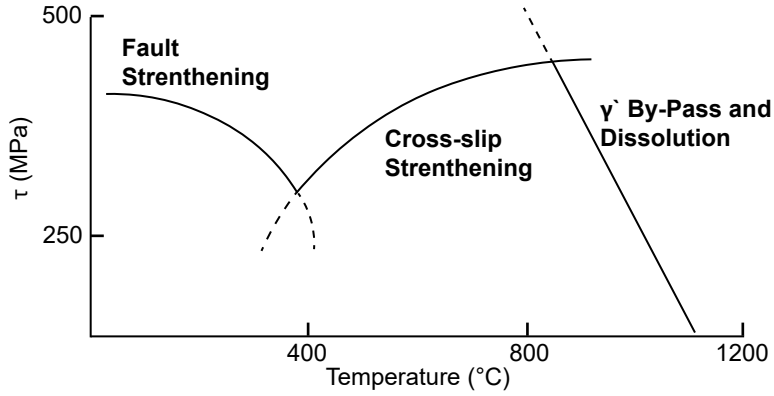

Figure 1.29: Temperature dependent plastic deformation mechanism for superalloy γ-γ' [171]

Temperature also impairs the ductility of the material. A drop was observed in monotonic tensile tests at (700 °C) by different authors on several superalloys (U720, Alloy 718 and RR1000) [11, 102, 174]. Not only the ductility but initiation mechanism are temperature dependent. Stinville et al. showed that in HCF an increase in temperature leads to longer lifetimes as denoted in figure 1.27 [175]. The formation of new slip systems arises with the temperature increase leading to lower localization of plasticity and thus longer crack initiation duration. In contrast, this trend is not observed in LCF due to oxidation-assisted damage mechanisms.

Not only the deformation mechanisms can be temperature dependent, but the material can also evolve with temperature increase.

Microstructural aging effect on the mechanical performances

Laurence studied the impact of TCP phase formation on the 700 °C creep and fatigue-holding behavior on René 65 aged at 800 °C. Their impact on the durability and viscoplastic behavior was highlighted by an increase in strain rates for creep and fatigue-holding solicitations. Figure 1.30 reveals such a phenomenon, but also the impact of precipitate size γ'_{II} and γ'_{III} on the creep properties of Rene65. Increasing the size of γ'_{II} precipitates leads to a slight increase in creep rates and ductility of the material. The occurrence of TCP phases combined with the presence of γ'_{III} precipitates is of first order on creep rate variations [8].

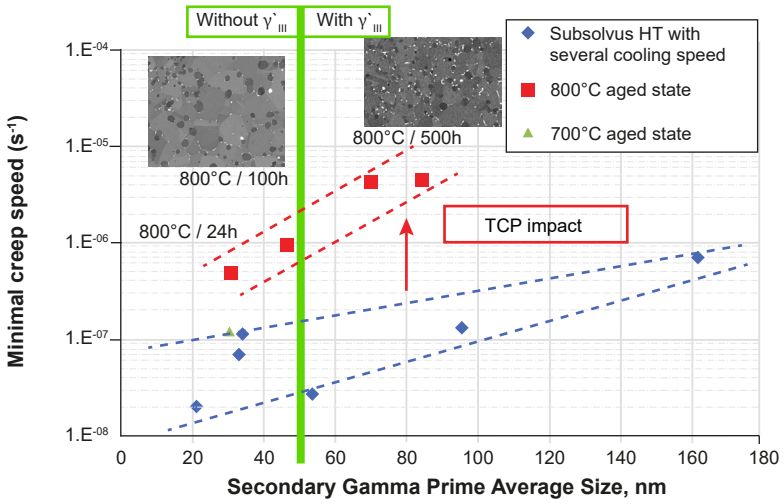

Figure 1.30: Impact of the over aging time at 800 °C on the minimum creep rate at 700 °C/800 MPa on René 65 [8]

1.4.5 Environmental impact on the mechanically solicited alloy

Oxidation is commensurably able to affect the mechanical behavior, by impacting the initiation site or the crack propagation, but also the mechanical behavior.

Mechanical impact onto the oxide scales

Oxides scales adopt a brittle behavior since their maximal tensile strain tends to be inferior to 1 %. The external oxide layers, if adherent and coherent to the substrate, are then cracking prematurely compared to the material. Considering a fracture mechanic approach, the oxide scale cracking is expected to initiate from a surface or sub-surface defects of such layer. The critical stress for scale failure to occur with a known defect size can be calculated using equation 1.19 [176]. Plane tensile stresses are assumed to be predominant in the oxide scale.

$$\sigma_c = \frac{K_{1c}}{f\,(\pi a)^{1/2}} \tag{1.19}$$

where σ_c is the critical stress to failure, K_{1c} is the critical stress intensity factor, f is a defect geometry factor ($f = 1.12$ for a surface notch, 1.0 for an embedded defect, and $f = 0.64$ for a semi-circular defect of radius c) and a is the defect size (half the length of

a defect or radius if circular). The failure strain of the oxide scale can also be modeled using a similar approach [177]:

$$\varepsilon_c = \frac{K_{1c}}{f E_{ox} (\pi a)} \tag{1.20}$$

where E_{ox} is the Young's modulus of the oxide, and ε_c is the critical strain to failure.

Hancock *et al.* modeled the presence and synergy of a multitude of neighboring small defects which can also be significant in the failure of the oxide scale [178].

The oxide scale cracking is dependent on applied stress onto the substrate if adherence of both is assumed [179]. The oxide layer thickness is also involved with the decrease in the required tensile strain to cracking with oxide thickness increase, as depicted in figure 1.31 [180].

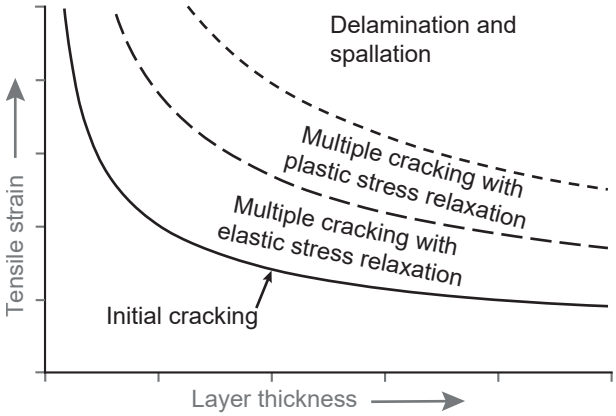

Figure 1.31: Schematic failure mode map for oxides tested in tension showing the different stages of the failure process [180]

Oxidation of cracks

Oxides can cyclically form at the crack tip due to the intake of oxygen through the mechanically solicited crack. This phenomenon named SAGBO (Stress/Strain Accelerated Grain Boundary Oxidation) depends on the temperature and the applied stress. A sequence of oxide cracking / spallation exposes the crack tip to the environment leading to a fast oxidation rate and an increase of the crack propagation rate [181–183]. Dynamic Embrittlement (DE) is another potentially damaging mechanism explaining the environmental effects on crack propagation. DE consists of oxygen diffusion into the grain boundary or ahead of the crack tip (several atomic layers characteristic length), thus lowering the grain boundary cohesion involved in the increase of crack growth rate [184–186].

Evans *et al.* concluded that oxide formation such as NiO, Cr_2O_3, TiO_2 and Al_2O_3 are more likely to form rather than oxygen penetrating along the grain boundary reducing cohesion [181]. Nemeth *et al.* proposed a diagram to model the crack tip oxidation of alloy U720Li, as denoted in figure 1.32 [11].

A schematic diagram of the oxidation morphology of a layered crack tip oxide in the thermodynamic sequence of NiO, Cr_2O_3, and Al_2O_3 is presented in (a). (b) and (c) present the schematic diagram of the oxidation morphology observed in alloy 720Li at a γ-grain boundary and at a primary γ'-interface. An external NiO layer is formed at the intergranular crack with an inner layer $NiCr_2O_4$. Oxygen diffusion results in the formation of Cr_2O_3 subscale, and Al_2O_3 is dissolved within this subscale before

a continuous Al_2O_3 layer is formed. The primary γ′-interface shows internal Al_2O_3 formation.

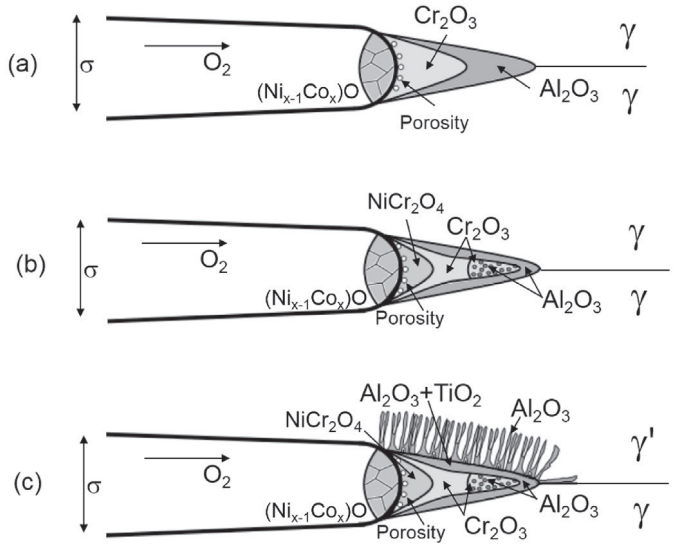

Figure 1.32: Schematic diagram of the oxidation morphology of a layered crack tip oxide [11]

Mechanical solicitation and oxidation interactions

Stinville's *et al.* work on the fatigue behavior of Ni-based superalloys (especially René 88DT) revealed some insights into the fatigue/environmental interactions. Figure 1.33 summarizes observations and modeling of spinel formation located at the surface of slip bands in the regions surrounding preferably orientated twin boundaries along the {111} planes. Slip bands form due to the accumulation of dislocations, thus favoring the diffusion transport of Ni and Co species at the surface from serial cracking of the oxide. The formation of non-protective porous Ni and Co oxides above the chromia layer is then made possible. Oxygen also diffuses inward producing chromia or alumina spike ingress and eventually leading to crack formation [105].

Figure 1.33 exposes a René 88DT sample after 79 % of expected fatigue lifetime tested in the HCF regime at 650 °C shows oxide spikes forming at the surface in (b). FIB-SEM cross-sections show the oxide spikes formed nearby a twin grain boundary at the surface in (c). An oxide spike forming at the surface is observed by SEM STEM imaging in (d). Energy dispersive x-ray spectroscopy maps of the oxide spike are shown in (e, f, g, h). Schematic representation of the oxide spike formation along twin boundaries in (a) [105].

Pang *et al.* evidenced the oxidation consequences of the fatigue behavior of RR1000 and AD730^{TM} with intergranular crack propagation. Oxidized grain boundaries are more prompt to crack initiation and propagation [187–190].

Oxidized thin specimens particularities

The use of microtensile specimens to exacerbate any surface effect from the oxidized layers arises with side effects. The consumption of entities involved in the oxidation phenomena can achieve bulk depletion leading to InCF of the specimens, as demonstrated by Texier *et al.* in MCrAlY coatings [96]. Thin specimens associated with oxidation

can then induce a reservoir effect from the specimens' thickness decrease, as depicted in figure 1.34.

Thin specimens are less likely to MICF and oxide spallation compared to thick specimens. The external stresses generated by the oxide scale are likely to accommodate the resulting strains, as reported via Orosz *et al.* [191], Duan *et al.* [192] and Texier *et al.* [96].

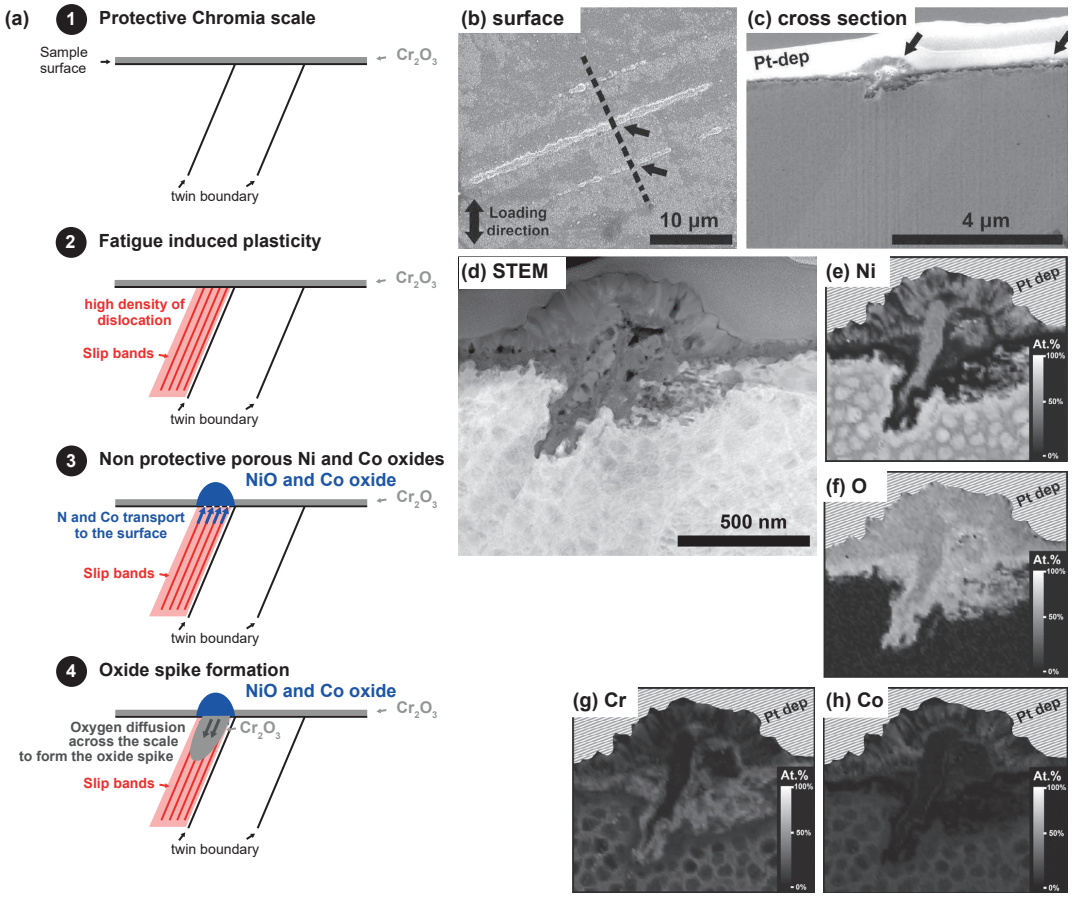

Figure 1.33: A René 88DT sample after 79 % of expected fatigue lifetime tested in the HCF regime at 650 °C, various observations and schematic of spinel formation [105]

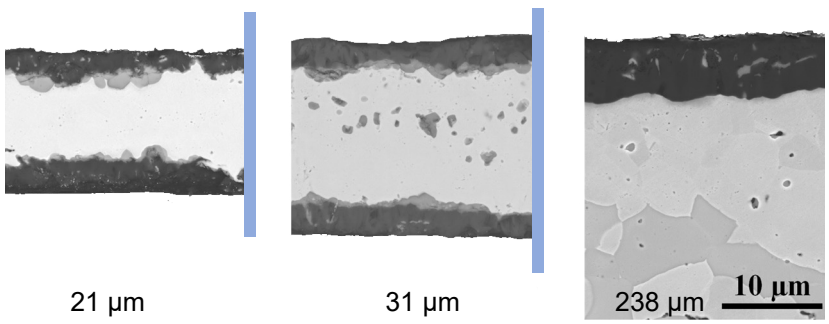

Figure 1.34: InCF on MCrAlY coating on three samples thicknesses after oxidation at 1150 °C during 250 h [96]

Intermediate conclusion

The γ/γ' polycrystalline material for turbine disk application René 65 is composed of a three-precipitates population structure related to the material thermal history. Intermetallic particles (borides, carbides, nitrides) are also found in the solutionized heat-treated René 65 (named As-Received in this framework, abbreviated AR).

The high-temperature exposure induces bulk changes but also alters the surface and sub-surface of the material due to the reactivity with the environment. The surface of René 65 expects chromia and titania formation, while intergranular alumina forms in the sub-surface. Grain boundaries are revealed from oxidation due to their diffusion shortcut path role.

The LCF regime, associated with the stress-assisted oxidation mechanisms, expects surface initiation of the material. The relatively thin oxidation-impacted layers impose the use of thin specimens to quantify the impairments and damages induced by their presence. A gentle grinding technique is employed to thin specimens down to 20 µm of thickness, but with a gage area high enough to be representative of a polycrystal behavior. Specifications on the use of thin specimens having a t/d ratio (total thickness versus grain size) close to 1 are to be studied in René 65 to dissociate any effect from the environment on the mechanical behavior to any thickness effects (YS decrease reported in the literature).

This project intends to quantify the microstructural evolutions from the high-temperature exposure, at the surface/sub-surface, but also in the bulk of the material, to apprehend their impact on the mechanical behavior and damaging processes. The surface and sub-surface evolutions are to be extensively characterized to apprehend any potential impact on the mechanical impairments.

Chapter 2

Material and experimental methods

Chapter 2 presents the different experimental techniques employed within this framework and describes the microstructure of the material in its reference state.

Part 2.1 is devoted to the technical means (thinning methodology, mechanical means developed, and analysis of the results) and protocols implemented to characterize the microstructural evolutions and oxidation consequences.

Part 2.2 exposes the microstructural characteristics of the material employed in this project: the nickel-base superalloy γ/γ' René 65. Two metallurgical states are to be investigated: As-Received (AR) and Albi-Solvus (AS) conditions. These initial states are to be employed as a reference for the remaining of this work.

2.1 Experimental methods

2.1.1 Regions of interest within the materials preform

Two microtensile specimens areas and one oxidation coupons area were extracted from the materials preform, as illustrated in figure 2.1. A three-axis coordinate system is employed to further locate the material characterizations: RD (Radial Direction), FD (Forging Direction), and TD (Tangential Direction). The choice of the three extraction zones has been based on service conditions:

Core Zone (CZ) representative of the metallurgical conditions at the core of the material; this zone will be used for the extraction of mechanical specimens.

Flank Zone (FZ) representative of the metallurgical conditions close to the flank of the material; this zone will be used for the extraction of mechanical specimens.

Oxidation Coupon (OC) located close to FZ to obtain similar metallurgical conditions; this zone will be used for the extraction of oxidation coupons.

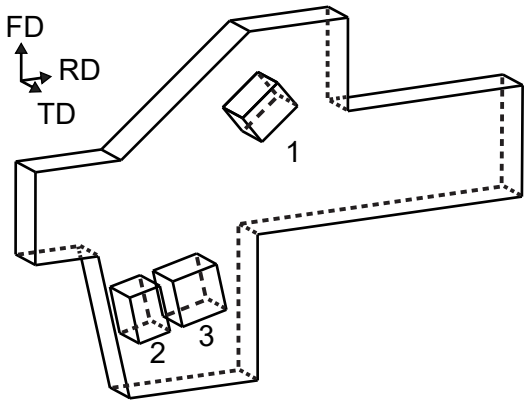

Figure 2.1: Cross section of the high-pressure turbine disk post heat treatments, pre-machining. Regions of interests 1 and 2: mechanical samples; 3: oxidation samples

2.1.2 Mechanical testings

Mechanical specimen geometries

The two solicitation modes investigated during this project are tensile and fatigue testing. Tensile tests were only conducted at room temperature using an adapted geometry from Texier in [193] as depicted in figure 2.2 a). Such geometry ensures respect for the following requirements for microscale tensile testing to be statistically representative of polycrystalline materials: limited overall size to comply with the thinning limitations, sufficient gage length to fulfill RVE requirements, strain distribution leading to plasticity and necking concentrated in the specimen's gage (figure 2.3). FEM simulation of the microtensile geometry was performed using Abaqus CAE with the following parameters: E=234 GPa, ν=0.34, hex C3D8R mesh, plastic behavior from true strain and stress measurements, display of the PEEQ (Equivalent Plastic Strain). The normalized tensile tests were performed on M12 cylindrical SAFRAN geometry as denoted in figure 2.2 b.

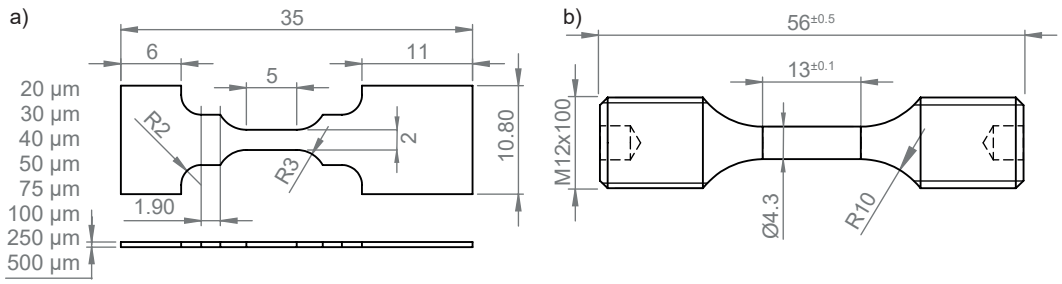

Figure 2.2: a) Microtensile specimen geometry and dimensions (mm) with corresponding thicknesses (µm) after thinning. b) M12 cylindrical normalized tensile specimen geometry

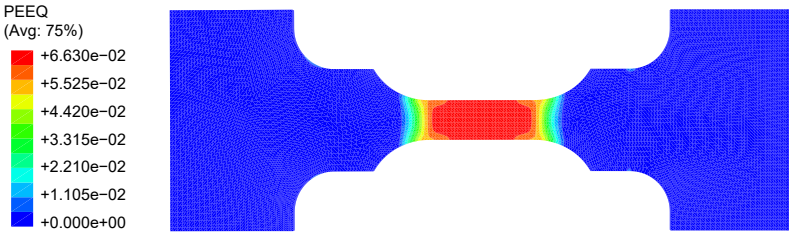

Figure 2.3: FEM simulation of the microtensile specimen revealing the equivalent plastic strain along the gage zone

Fatigue tests were conducted on two specimens' geometries depending on the fatigue bench and experiment purpose. The microtensile specimen geometry setup was used for room temperature LCF (figure 2.2). A second geometry was designed to perform high-temperature fatigue to further extract microtensile specimens in the specimen's gage. Figure 2.4 presents the fatigue specimen for HT pre-aging (in solid contours) and illustrates the extraction location of microtensile specimens (in dash contours). This pre-aging aims to characterize the mechano-chemical coupling occurring during fatigue testing at elevated temperature / low cycle stress levels in comparison with the oxidation test.

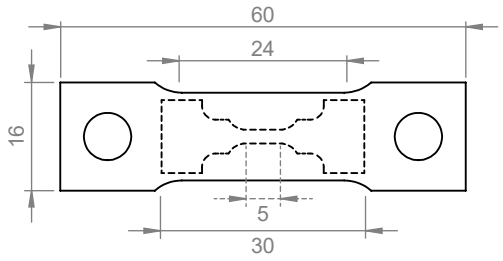

Figure 2.4: Fatigue specimen geometry for high-temperature fatigue aging (in mm)

Microtensile tests at room temperature

The specimen preparation method chosen to thin down material with high geometrical tolerance restricts the size of the samples (see the thinning section 2.1.3). Texier designed this microtensile specimen geometry from past experience with limited-size

specimens. The 2 mm × 5 mm gage is designed to comply with RVE requirements (see section 1.3.1) but concedes with the thinning operation down to final specimen thicknesses of 20 µm.

INSTRON 5800 electromechanical testing machine was adapted to receive the thin microtensile specimens' geometry through a custom-built tension rig. The design was performed by Q. Sirvin and D. Texier (see figure 2.5). The tensile jaws are adapted to the microtensile specimen geometry (complementary shape to the head of the sample up to the first radius) and were machined using Ni-based material to withstand high-temperature testing. An additional SCAIME load-cell (0.5 kN or 5 kN, depending on the samples' thickness) was serially used to improve the resolution of the load measurement and subsequently, the strength response to better characterize the mechanical behavior of the material. The SCAIME-load cell is connected to an acquisition bench via a National instrument NIDAC. Full-field kinematics fields were performed via an optical image correlation bench synchronized with the SCAIME load-cell through the NIDAC. Local strain fields as well as macroscopic strains were calculated from the displacement map using a VIC 2D + Python companion. The DIC technique is further detailed in section 2.1.4. All tensile tests were performed at a cross-head displacement rate of $5 \times 10^{-3}\,\mathrm{mm\,s^{-1}}$ corresponding to a total strain rate of $1 \times 10^{-3}\,\mathrm{s^{-1}}$ up to failure.

Thin microtensile specimens were mounted on the tensile bench with an applied pre-stress of 30 MPa to 100 MPa (depending on the specimen's thickness) to ensure perfect contact with the grips. Alignment of the tensile rig was performed using a shim when tightening the blockers. Tensile specimens heads like spacers of different thicknesses were used to ensure alignment with the tensile line core and avoid any plastic deformation of the specimens' fillets.

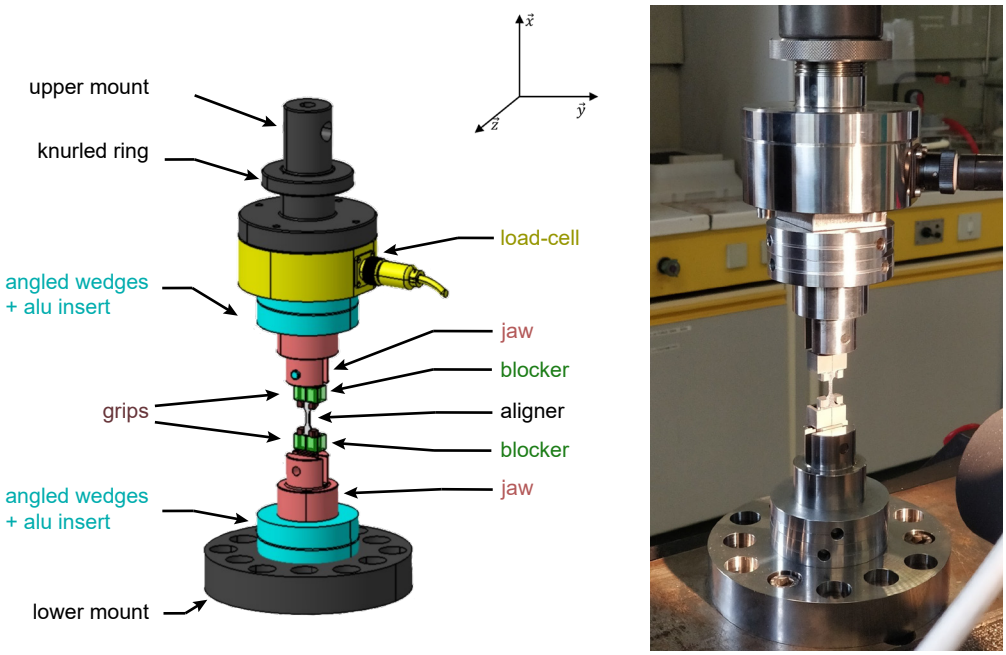

Figure 2.5: Schematic of the tensile rig and picture during a tensile test

Normalized tensile specimens were tested using a hydraulic INSTRON 8862 equipped with a contact extensometer for strain monitoring at the same strain rate as microtensile specimens ($\dot{\varepsilon} = 10^{-3}\,\mathrm{s^{-1}}$).

Fatigue tests

Room temperature LCF tests on thin samples were performed with the same custom-built rig of the INSTRON 5800. Such setup and specimen geometry only allow tension/tension fatigue. The stress ratio (defined in eq. 2.1) was then chosen at a value of $R_\sigma = 0.2$. The LCF tests were displacement driven with minimum and maximum strength targets as a limit condition. The tests were not deformation-driven due to technical restrictions. LCF is defined by high mechanical stresses, at the onset of plastic deformation; the LCF tests were thus carried out at $0.95\% \cdot Rp_{0.2}$. As for microtensile testing, strains were obtained through an image correlation bench. A python script was developed to allow synchronization of the image correlation bench and load acquisition line through a Transistor-Transistor Logic (TTL) signal generated by a function generator (0 V to 5 V low current logic circuit). The python script ensures the image acquisition operates only at predefined cycles during the test. Details on the image correlation setup are given in section 2.1.4.

$$R_\sigma = \frac{\sigma_{min}}{\sigma_{max}} \tag{2.1}$$

Interrupted tensile and fatigue tests

Tensile and fatigue interrupted tests were performed to investigate damaging and strain premises on the surface of specimens.

Tensile tests were interrupted at several plastic strain levels from 0.2 −% to 5 −%. Regions Of Interest (ROI) were monitored via optical or SEM microscopy before and after loading. Such an ROI was identified thanks to the geometric distance to the specimens' edges and the identification of the primary γ' precipitates at the surface.

Fatigue tests were interrupted at predefined cycles (1, 10, 100, 1000, 5000 and 10 000 cycles) on pre-oxidized specimens. Temperature / time couples investigated are the followings: 700 °C for durations of 200 h and 600 h and 800 °C for duration of 200 h. SEM-SE and BSE mappings of 1.2 mm × 1.2 mm were performed prior to testing (but after pre-oxidation) and at each cycle interruption for microscopic DIC strain monitoring (detailed in section **??**). The large dimensional mapping was realized via an image stitching of x1500 magnification SEM micrographs (resolution of 41 nm/px) composed of a 10 x 10 micrographs grid with 10 % overlap to a total dimension of 18 000 x 18 000 pixels. Identification of the strains was performed by comparing before and after mechanical testing stitched micrographs via the OpenCV disopticalflow library.

Experimental data processing

Raw data from the NIDAC acquisition bench and DIC bench were post-treated via a python script. Stresses and strains signals containing numerical noise from the acquisition bench, smoothing of the signals was then realized for all tests. The smoothing was performed by the LOWESS function from statsmodel non-parametric python library [194] based on robust locally weighted regression and smoothing scatter plots from Cleveland [195]. This algorithm was chosen for its fitting on inflection points and capacity of non-parametric data (strains and stresses are temporally sampled, and the stress versus strain signal sampling interval is then not constant). Examples of raw and smoothed data are presented in figure 2.6.

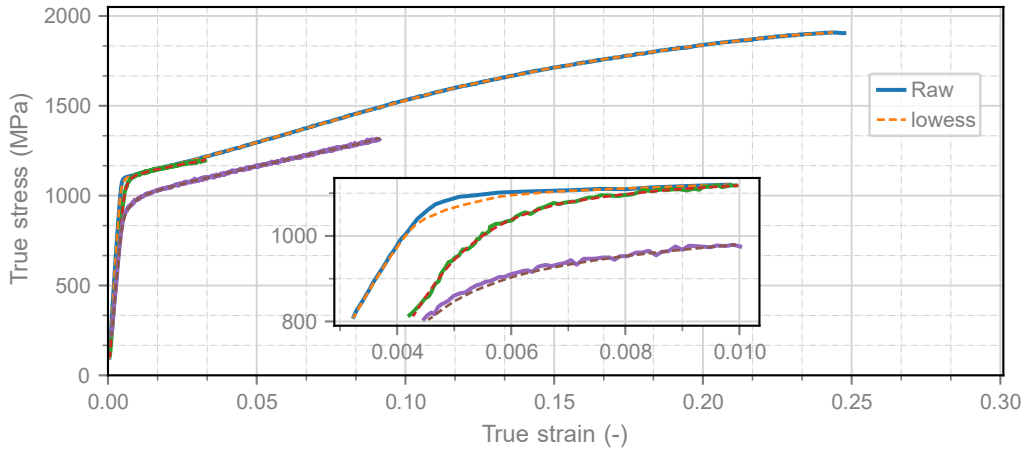

Figure 2.6: Fitting of the LOWESS function (dashed lines) onto raw tensile data (full lines)

2.1.3 Thin microtensile specimen preparation

The thinning technique is based on a commercial solution (JIG PP5 from Logitech, mainly used for geologic matter), modified and optimized in order to prepare metallic samples. The input conditions for such a device are to respect the parallelism of the sample and to control the grinding thickness. The precision JIG is depicted in figure 2.7. Microtensile specimens are glued onto a rectified circular glass via a thermo-fusible wax from agar scientific (high hardness and strength, shear-resistant, dissolved in acetone, and low melting point are its benefits). The sticking operation of the samples represents one of the most sensitive parts of the thinning process. The glue thickness has to be as thin as possible not to interfere with the parallelism and to provide maximum shear strength. The sticking process is fully performed by hand and offers no possible automation (see figure 2.8b for an example of microtensile specimen distribution and figure 2.8c for oxidation coupons). The rectified glass is then stuck at the center of the JIG via a vacuum network (see figure 2.7, the vacuum system can be seen in the background with dark circular patterns). The JIG is constituted of two main parts linked by a sliding connection. The outer ring sets the planeness of the system and is used as a reference for the thickness approximation of the material removal. The inner ring receives the rectified glass on the other side of the samples.

The material removal of the samples is monitored via a micrometer continuously giving the relative thickness from the inner ring to the outer ring. The reduced surface of the samples compared to the outer ring surface in addition to the very hard material used for the outer ring surface compared to the samples ensures the exactness of the micrometer information. The outer ring consumption is assumed negligible compared to the sample one. This assumption is verified for relatively low grinding times (maximal grinding speed of 100 µm for 20 min). The complete grit paper sequence described below is then optimized to avoid any grit paper repetition in the sequence. The JIG is finally positioned onto the grit paper through a frame, with two bearings as a guidance system. The JIG is positioned nearly tangent to the external circumference of the grit paper, differences in the relative speed from the inner and the outer of the grit paper induce the JIG to rotate according to its own axis. This consequence is actually beneficial

to the homogeneity of the material removal of the samples. A conventional grinding sequence is:

1. All sides are manually polished to the surface finish P2400/1000 grit.

2. Slight manual grinding of the faces to remove any machining (EDM) affected layer. This part is important to avoid any residual stresses from the machining process to cause bending of the samples while grinding when using the JIG. This manual grinding is performed using P320/240 grit.

3. Grinding of the first face through the JIG process up to P2400/1000 grit. One JIG process can grind up to three microtensile specimens with respect to the symmetry on the positioning of the sample onto the rectified glass (see figure 2.8b). The grinding complies with the following sequence:

    - 15 min at P600/360 grit. Objective of 100 µm material removal.
    - 15 min at P1200/600 grit. Objective of 80 µm material removal.
    - 20 min at P2400/1000 grit. Objective of 20 µm material removal.

4. Unmounting of the samples from the rectified glass via ultrasonic acetone bath for 20 min. A complete cleaning sequence is performed to remove any remaining wax (ultrasonic acetone followed by ultrasonic ethanol). Measurement of the sample thickness at different locations. Sticking process on the second face *i.e.* the polished side. Extra care is taken to minimize scratches at the surface but maintain the planeness.

5. Grinding of the second face following the same sequence of grit papers with an adaptation of the time for each paper to reach the final thickness.

The relationship between the time of grinding and the material removed depends on the hardness and machinability of the material, the pressure applied, and the total specimen surface to shrink. A preliminary study was performed to estimate the time-material removal relationship (in addition to the JIG micrometer). The external ring suffers analogously to specimens from material removal due to contact with the grinding paper; the micrometer gives the difference from the microtensile specimens to the external ring material removal.

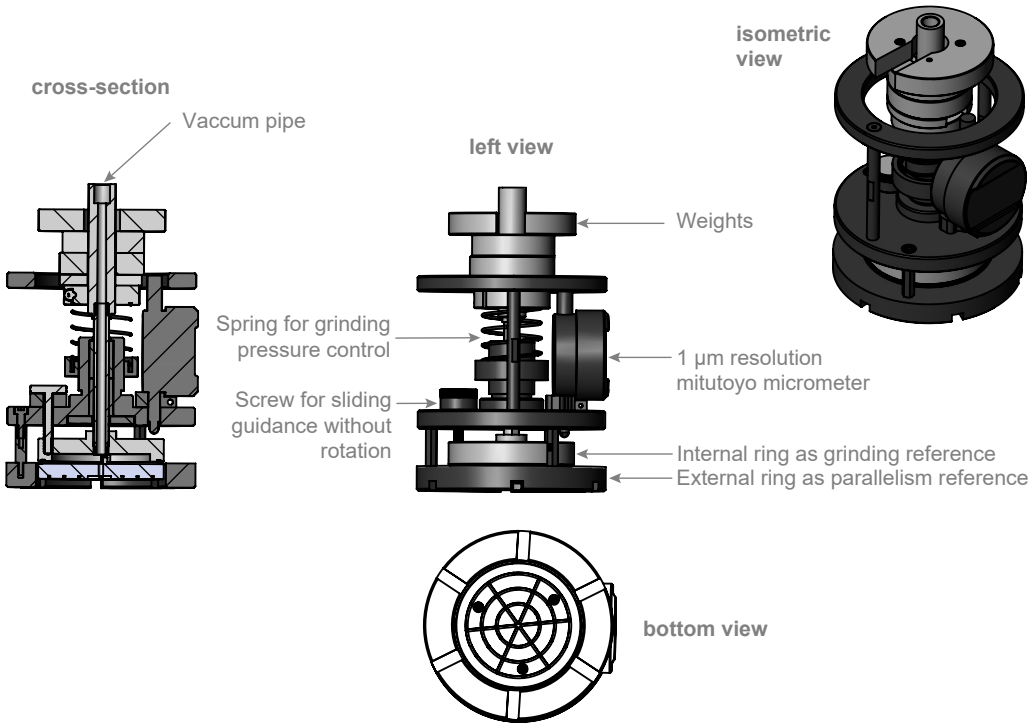

Figure 2.7: Schematic illustration of the home-built JIG for thinning preparation

(a) JIG device, JIG support, and associated grinding machine

(b) Positioning of the microtensile specimens on the rectified glass attached under the JIG

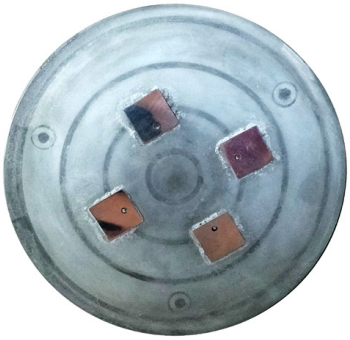

(c) Positioning of the oxidation coupons on the rectified glass attached under the JIG

Figure 2.8: Precision JIG and sticking of the samples under the JIG thinning device

2.1.4 Digital Image Correlation setup and parameters

Macroscopic strain monitoring

The use of tiny specimens prevents classic contact extensometry techniques. The gage length is not appropriate and the compliance of thin microtensile specimen is inadequate with the extensometer weight and clamping. Contactless methods appear as an interesting alternative, especially the Digital Image Correlation (DIC) technique for full-field kinematics measurements and visual extensometer [196].

Pictures of the sample are taken according to a step time (every 100 ms to 500 ms) during the tensile test. A speckle was manually applied on one of the specimens' faces (black droplets on a uniform white background, see figure 2.9). Such speckles allow pattern identification and so tracking of the surface of specimens. Regular pictures allow the tracking of the local and global displacement field through the use of DIC algorithms (VIC commercial software [197]). The pictures are synchronized with the load input (from the NIDAC), giving the strains and stresses of the tensile test as the final output.

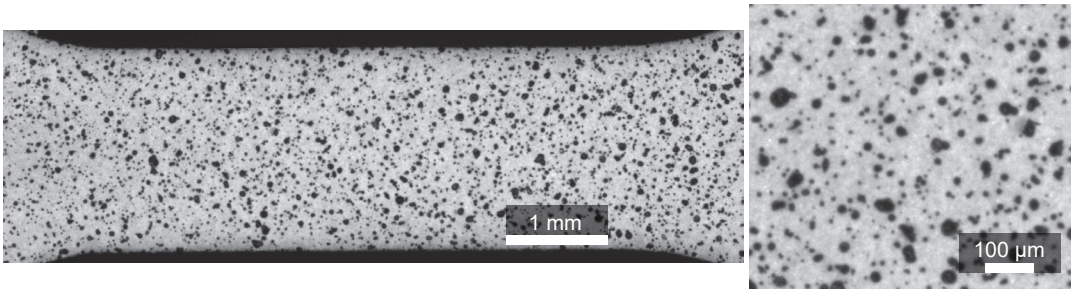

Figure 2.9: DIC painted speckle on tensile and fatigue specimens

The equipment used for this section is a BASLER acA2440-75um camera (5 MP) coupled with a non-corrected Sigma 105 mm f2.8 DG MACRO lens. The NIDAC from national instruments is a NI USB-6009.

The speckle and optical bench are set up accordingly to the physical length to be quantified. In this framework, macroscopic strains are the first assessment desired. Microscopic strains are also of interest for plasticity localization investigation. The 2 mm × 5 mm gage dimensions require then a speckle in the micrometer range and an optimized camera setup (lens focal, camera sensor in size and resolution).

The first step in the optical bench installation consists in acquiring the resolution of the camera (correspondence from physical distance to pixels). The CMOS sensor of the camera has to be planar and parallel to the specimen to limit distortions. Distortion and resolution ($4\,\mu m\,px^{-1}$) were estimated via a developed python code. The algorithm is the following:

1. Align the camera and the tensile specimen using a bubble leveler.
2. Calibrate the lens and camera vertically and horizontally using a ruler. The horizontal picture is presented figure 2.10. The resolution, alignment, and distortion are then computed via the following methods:
3. Each millimeter on the ruler is represented by a line (vertical black lines in figure 2.10). Those lines are detected by plotting the sum of the gray levels for each column of pixels versus the pixels' indent. The discrete plot is interpolated

using the python Scipy interpolate library [198] as depicted in figure 2.11a (discrete plot (blue dots) and its interpolation (orange line)). A manual entry is necessary to set the minimum gray level threshold for peak detection as denoted by the red horizontal line in figure 2.11a.

4. The output gives the pixel/size resolution of the image along with the distribution of the millimeter lines in the camera plan, as shown in figure 2.11b and figure 2.11c. The distribution is modeled by a cubic function to apprehend the spatial distortion. One can observe on both orientations (vertical and horizontal ruler) a cubic distribution of the millimeter, which reveals the geometrical aberration of the optical system. The gap from each extremity of the picture informs about the parallelism of the camera from the samples (on a second order, it informs about the distortion of the lens). The camera position can be adapted to minimize this difference.

5. The distributions for both vertical and horizontal calibration are used to compute a corrective matrix to improve the picture accuracy in order to minimize the geometrical aberrations.

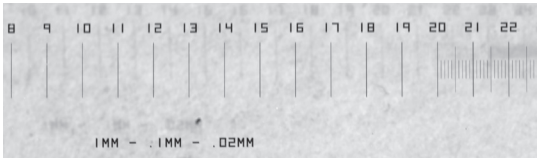

Figure 2.10: Camera calibration using a ruler

Once the pictures were corrected from any geometrical default (if a correction is judged necessary), the commercial software VIC 2D was used to compute the strain fields from each sequence of pictures (one per test). The parameters of the DIC algorithm are the following:

- Size of the subset: twice the size of the largest black droplet (usually around 75 pixels of subset width).
- Step size of a quarter of the subset size.
- Interpolation of type Gaussian with optimized 8 passes for sub-pixel accuracy (each pixel within the subset is center-weighted, and the passes give the interpolation order of spline).
- Normalized squared differences as correlation criteria and 5×5 subset decay kernel matrix (minimum available).
- All pictures are compared to the original one (the first picture, methodology named non-incremental). In the case of non-convergent computation of the image n (impossibility to correlate with the reference picture 1), it is compared to its $n-1$ one (incremental methodology); all $n+i$ remaining pictures are then compared to this $n-1$ picture but refer the initial displacements and strains of picture 1. Such methodology is named exhaustive search.

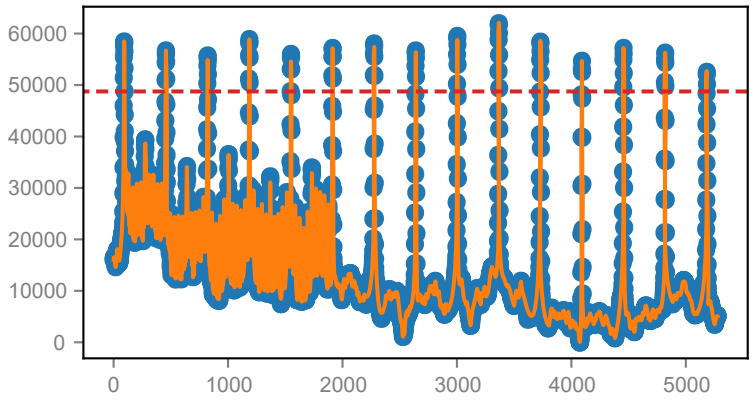

(a) Python code to manually select the threshold (red dotted line) for millimeter pikes detection through the diagram of gray-level versus pixel indents

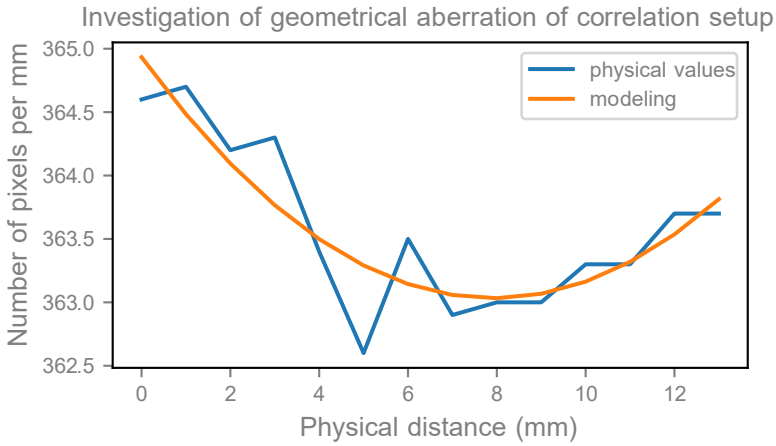

(b) Distortion and geometrical aberration estimation from the horizontal ruler picture. Resolution along the ruler giving the horizontal number of pixels (y-axis) per millimeter (x-axis)

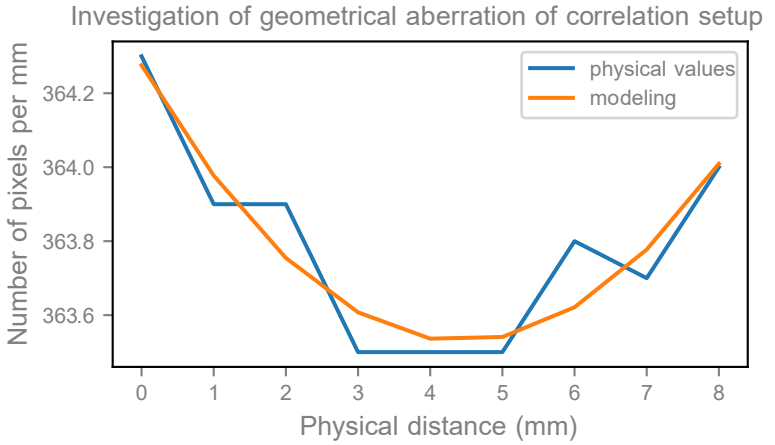

(c) Distortion and geometrical aberration estimation from the vertical ruler picture. Resolution along the ruler giving the vertical number of pixels (y-axis) per millimeter (x-axis)

Figure 2.11: Optical bench validation algorithm results

Strain and section determination

The DIC parameters are of 79 px square subset size separated from each other by 21 px (step size) as given in figure 2.12 (the three red squares are representative of the subset and step size, both values are optimized regarding the resolution of the pictures and the size of the speckle). The green rectangle in figure 2.12 informs on the area of interest used for the DIC computation, the gage area is longitudinally shrunk of up to 0.5 mm to minimize any influence of the radius onto the strain measurements.

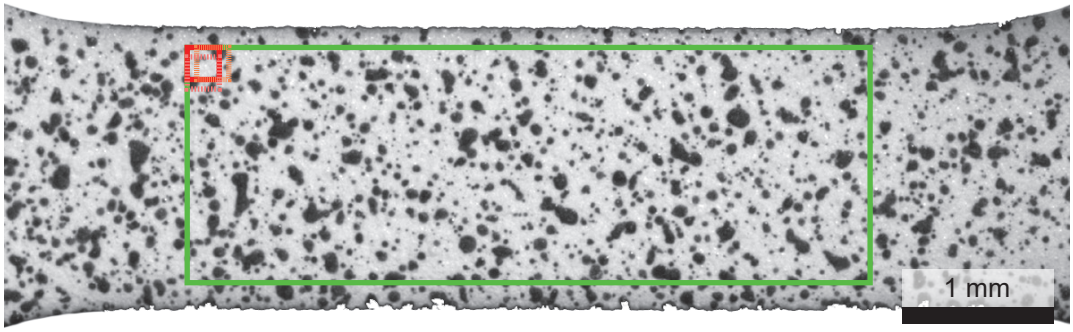

Figure 2.12: Specimen gage with speckle and area of interest for DIC computation (green rectangle for DIC computation, red squares for subset and step size illustration)

The YS defined by 0.2 % offset plastic strain is depending on the strain computation methodology. Whereas, in a perfectly flat and thick specimen, strains are supposed to be homogeneous in the entire specimen gage; strain distribution in thin specimens is much more sensitive to any parallelism default (down to the micrometer). A 2 µm-variation in 20 µm thick specimen represents a 10 % variation which can completely influence the strain distribution within the specimen gage. Such an investigation is directly connected to the section of the specimen taken into account for stress determination:

The underlying issue from strain computation is: **does the mean value of the strains correctly describes the strain distribution in the specimen gage or does the maximal value suit best ?**

The maximal value of strain is to be directly correlated to the planeness of specimens but also to the section chosen to compute the stresses from the strength measurement. The maximal strain is supposed to be located at the minimal thickness of the specimen for non-textured materials. Contact extensometry provides only the average strain between the two points of contact with the specimen. A similar methodology to contact extensometry via DIC technique is following the displacement of two regions in the specimen gage, which induces a mean value of the strain between those two regions, *i.e.* an optical extensometer. The two strategies from mean and maximal strain are to be discussed in appendix C.

Common customs and practices in material testing are to only take into account the minimal value of thickness from a sequence of at least 3 measurements at different locations on the gage. Within this framework the thickness was measured at three locations (one in the center, and one close to each radius of the specimen), with at least 2 sequences, using a micrometer. The micrometer used does not provide local measurement as the cylindrical measuring rod has a diameter of 1 mm. Each value measured is then the maximal value of the specimens' thickness in this 0.78 mm^2 area.

Taking into consideration that the minimal value of thickness results in a maximal value of stress, the mean value of thickness thus results in the mean stress.

Before discussing the impact of both strain and stress determination, let us introduce first René 65 AR room temperature tensile behavior for various specimen thicknesses. The strain given in all the stress-strain curves below takes into account the mean value of the strain resulting from the DIC computation on the specimen's gage associated with the mean stress (using the mean value of thickness).

2.1.5 Oxidation procedures

Coupons for oxidation tests with dimensions of 10 mm × 15 mm were extracted from a forged piece via electrical discharge machining (OC zone from figure 2.1, geometry given in figure 2.13). Samples were further drilled (ϕ 1.5 mm) for holding during oxidation tests. Samples with thicknesses ranging from 15 µm to 500 µm with thickness deviations less than 2 µm were obtained by mechanical polishing using a precision polishing jig up to P2400 grit (following the methodology described in section 2.1.3). Sides were manually polished up to the same surface finish without the intention to create any fillets to smooth the coupons' edges.

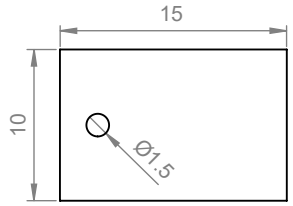

Figure 2.13: Schematic illustration of the Oxidation Coupons (OC) (dimensions in mm)

The final dimensions (after polishing, primary ultrasonic ethanol, and drying cleaning) were measured via a LEXT OLS5000 confocal microscope for length and width to allow surface computation through edge detection algorithms (OpenCV python library [199]). The confocal requirement arises from a potential bending of thin samples due to accommodation of the stresses generated by formation of the oxides for high-temperature exposure of the material (thin samples accommodate due to their low stiffness/high flexibility). Thickness was measured via a 1 µm-precision micrometer on a 5-point grid. OC were finally cleaned following a sequence constituted by: ultrasonic acetone immersion (10 min), air drying, ultrasonic ethanol (20 min), and final air drying). Samples were then weighted for initial mass measurement. Isothermal oxidation was performed in static lab air in a Nabertherm furnace. Oxidation samples were suspended via platinum wires during oxidation tests (see figure 2.14 for microtensile specimens pre-oxidation, identical to the oxidation coupons suspension method). OC were suspended by the drilled hole, and microtensile specimens were held at the head fillets (larger one). The oxidation temperature/time couples performed are presented in table 2.1. Microtensile specimens followed the oxidation temperature/time couples presented in table 2.2.

	10 h	30 h	50 h	100 h	160 h	200 h	300 h	600 h	1000 h
650 °C	x	x				x		x	x
700 °C	x		x		x		x	x	x
800 °C	x	x		x		x	x	x	
900 °C				x			x		
1000 °C				x			x		

Table 2.1: Oxidation of OC times and temperatures investigated

	200 h	600 h
700 °C	x	x
800 °C	x	x

Table 2.2: Oxidation of FZ and CZ (microtensile specimens) times and temperatures investigated

Samples were introduced in the hot furnace and air-quenched after oxidation interruption. The temperature was monitored via two K-type thermocouples positioned at different locations inside the furnace, one being in contact with the samples.

Mass gain measurements were evaluated via a Sartorius MC5 with a 2 µg accuracy.

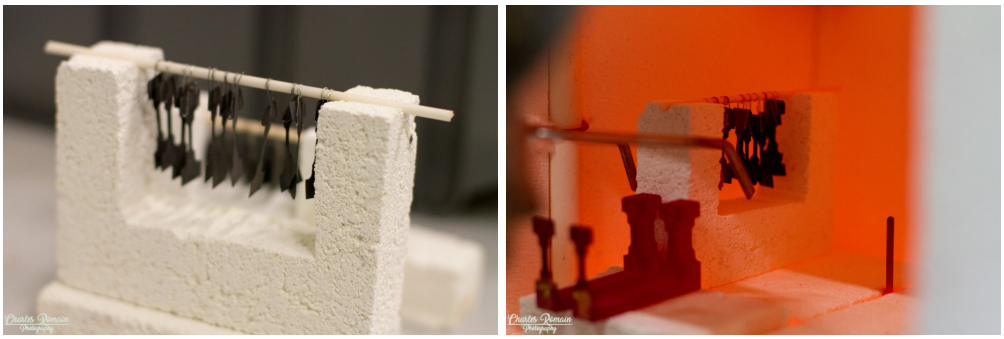

(a) **(b)**

Figure 2.14: Supports on microtensile specimens oxidation. (a) out of the furnace. (b) in the furnace

2.1.6 Specimen preparation for observation

The following methodology was used to prepare the samples for scanning electron microscopy (SEM) observation:

- 5 min SiC paper grinding P320 - water cleaning
- 2 min SiC paper grinding P600 - water cleaning
- 2 min SiC paper grinding P1200 - water cleaning
- 2 min SiC paper grinding P2400 - water cleaning
- 2 min SiC paper grinding P4000 - water cleaning

- 5 min Diamond paste grinding 6 µm - 5 min ultrasonic water then ethanol bath cleaning.
- 5 min Diamond paste grinding 3 µm - 5 min ultrasonic water then ethanol bath cleaning.
- 2 x 15 min final polishing with colloidal silica suspension (OP-S) 0.04 µm - 10 min ultrasonic water then ethanol bath cleaning.

An additional vibratory polisher sequence was added for EBSD or high-magnification SEM analysis. Such a procedure ensures removing the residual surface hardening remaining after any mechanical rotary polishing, to improve the crystallographic contrast for SEM-BSE observation. Vibratory polishing was performed for durations from 2 h to 4 h using 0.04 µm OP-S or 0.1 µm alumina suspensions. The OP-S induces a minor etching of γ' precipitates which can result in an imperfect planeness of samples, alumina grinding is then preferred if a perfect planeness is required.

Grinding of samples was performed using a semi-automatic Buehler automet 250 grinding machine. Thin and oxidized samples were mounted in a low shrinkage, low viscosity epoxy resin (Struers epofix) to allow semi-automatic grinding and protect the brittle external oxide layer from spalling. Unoxidized or large specimens were hot mounted in conductive Bakelite. SEM observation requires samples to be conductive, a carbon deposit of a few nanometers was deposited on the mountings using a Leica EM ACE600 to improve the conductivity of the resin.

Chemical etching for SEM-SE observation

Chemical etching to dissolve γ' phase was ensured using aqua regia (67 $\%_{vol}$ of HCl and 33 $\%_{vol}$ of HNO_3) diluted at 33 $\%_{vol}$ in distilled water. The etching was performed between 5 s to 8 s to especially dissolve emerging γ'. Such a procedure highlights the γ' phase via SEM-SE observation due to the topographical difference between the two phases, as depicted in figure 1.3.

2.1.7 Grinding methodologies

Two different methodologies were employed to observe the subsurface evolution of the material:

Cross-section: Samples are generally held in a cold or hot mounting resin before the grinding sequence. Such methodology ensures high-resolution observation of the subsurface evolutions but with a limited number of elements (low statistical representation).

Wedge polishing: Samples are fixed on the JIG rectified glass with a controlled tilt (using a thickness-controlled wedge) to allow wedge grinding up to the desired finish surface. The tilt is measured afterwards via CONFOCAL microscopy. The micrographs are then overlayed with iso-depths lines determined via the tilt measurement (red lines in the right figure 2.15). The surface finish using such methodology can be altered due to oxide spallation, but the statistical representation of wedge-polishing samples is beyond comparison with cross-section polishing.

Figure 2.15: Subsurface observation methodologies: left: cross-section cutting and grinding / right: wedge coupon grinding

2.1.8 Observation and analysis techniques

Confocal microscope

Laser Scanning Confocal Microscope (LSCM) is a contactless 3D observation metrology system. The optical source is focused thanks to a pin-hole to perform a 3D scan of the sample surface via conservation of the maximal intensity onto the Airy diagram for each point scanned. The subnanometric resolution allows surface roughness and area, line profile, film thickness, step height measurements, and more.

Confocal microscopy was performed using an Olympus LEXT OLS 5100 in order to record the developed area and perimeter of the specimens. Such LSCM is based on a 405 nm monochromatic source. Standard optical microscopy only alloys the projected measurements (parallel to the captor). The three-dimensional developed area finds its interest in thin samples measurement as their low stiffness can induce involuntary bending due to asymmetry in residual stresses within the samples. Asymmetries are to occur due to slight differences in oxidation behavior for both of the samples' faces, but also due to the mechanically strained hardened surface, or heredity from the forging process (as depicted in figure 2.16).

Confocal files were analyzed using the Gwyddion software [200]. The .lext extension allows the support of Olympus files onto Gwyddion and therefore onto python.

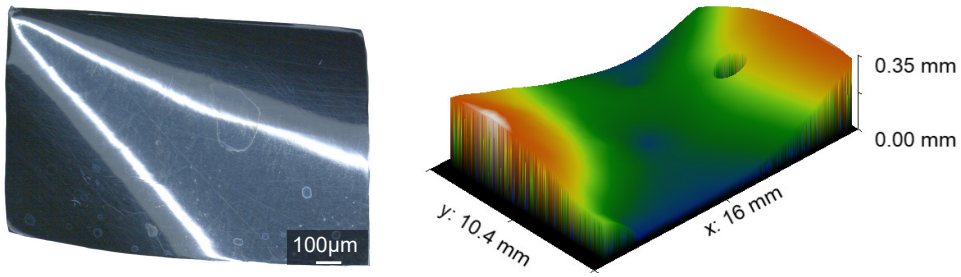

Figure 2.16: Natural bending of coupons that randomly happens on thin samples after thinning due to internal or mechanical grinding residual stresses

Scanning electron microscope (SEM)

SEM observation relies on electron and material interactions. A gun (field emission gun (FEG) in this case) projects electrons onto the surface of the material. Detectors capture the matter response via secondary electrons (SE), back-scattered electrons (BSE), or X-photons (EDS). SE reveals topographical contrast which is relevant in phase quantification after chemical etching using image analysis (developed in section 2.1.9). BSE reveals chemical and crystal-orientation contrast that is relevant in phase and grain identification.

A field-emission gun scanning electron microscope (FEG-SEM) Nova NanoSEM 450 from THERMOFISHER SCIENTIFIC was used to acquire SE and BSE micrographs

and fractographs that are to be presented in this framework. The settings preferably for each observation mode are:

BSE 15 kV - spot 4.5 (FEI notation representing the probe current), magnification in the range x150 to x10 000, working distance 5 mm.

SE 5 kV - spot 2.5, magnification in the range x80 to x500 000 (high magnification in immersive mode), working distance 5 mm for high resolution, 10 mm for fractographs.

SEM micrographs were analyzed using several softwares: Fiji ImageJ2 bundle [201]; python and especially the OpenCV [199], scipy [202], and skimage [198] libraries; and the commercial software Aphelion V3.

Energy-Dispersive Spectroscopy (EDS)

EDS observations were performed using a SEM-FEG JSM 7800F Prime from JEOL equipped with an EDS SDD X-Max 80 mm^2 detector from Oxford Instruments. EDS analysis relies on the qualitative quantification of X photons to identify the matter's chemical entities. Such methodology is of interest in the identification of entities involved in the oxide layers but provides a resolution in the micrometer range and so a first-order quantitative chemical composition (ratio from identified entities). The experimental parameters are of 15 kV to 20 kV to have access to the α ray of René 65 elements (except for light elements such as Carbon and Boron), and a probe current optimized for maximization of X photons signal but acceptable spatial resolution.

High-resolution EDS analyses were realized on a SEM-FEG FEI HELIOS 600i equipped with a DX Aztec Advanced SDD X-Max 80 mm^2 from Oxford Instruments.

EDS spectrograms were deconvolved using the Oxford (AzTec) and EDAX suite, final exportation was realized using the hyperspy python library [203].

Electron Back Scattered Diffraction (EBSD)

EBSD analysis is based on the Kikuchi band identification which depends on the crystallographic orientation of the diffractive grains. Such an analysis then reveals the grains' characteristics via the crystallographic disorientation from neighboring grains. EBSD analysis was performed on a FEG-SEM JEOL JSM 7100F TTLS LV equipped with an EBSD CMOS Symmetry S2 from Oxford Instruments.

The similarities in diffraction patterns from γ and γ' phases do not ensure crystallographic disorientation identification between the two phases only based on the Kikuchi band. EDS analysis is then coupled to EBSD as slave information to identify the primary γ' precipitates by their difference in chemical composition. This method was applied in the following EBSD maps but results in the degradation of the phases' delimitation spatial resolution due to the EDS interaction bulb (in the micrometer order).

EBSD maps were corrected by EDS analysis using the python library DefDAP [204] for EDS signal extraction and phase identification based on relevant chemical entities for phase differentiation. EBSD maps were then analyzed using the Matlab toolbox MTEX [205]. Grain boundaries were identified for misorientations superior to 3°, and twin boundaries were identified in the range 59.5° to 60.5°.

Focused Ion Beam (FIB)

FEG-SEM-FIB technique allows controlled machining of the samples' surface and sub-surface through an ion beam in a SEM chamber (sub-micro-metric resolution). The SEM is given a second column for ion extraction. Abrading the surface up to the sub-surface coupled with standard SEM observations enable local cross-sectional observation at specific region identified from surface observation. 3D reconstruction was performed from serial FIB sectioning and SEM-BSE micrographs using the Avizo software. Such methodology is of interest in assessing postmortem microstructural features involved in crack initiation and propagation. FIB analysis was performed on a FEG-SEM FEI HELIOS 600i equipped with a Tomahawk ionic column. 3D EDS mapping is also made possible with such a device.

X-ray diffraction (XRD)

Oxidation products resulting from the high-temperature exposition were identified via X-ray diffraction (XRD). XRD allows the identification of the crystallographic structure by assessing the diffractive angles (pic position) of the different phases constitutive of the alloy correlated to predefined diffractograms. The pic intensity deconvolved according to each phase diffractogram quantitatively provides information on their chemical composition. XRD analyses were carried out using a X'PERT-PANALYTICAL from PHILIPS with a $Cu - K\alpha$ radiation (λ=1.54 Å), covering a range of angles (2θ) from 15° to 100° with a step size of 0.033° for 1 h of total exposure duration.

2.1.9 Image analysis

Image analysis on SEM micrographs for phase quantification was performed through several methodologies.

Conventional image analysis for chemically etched surfaces on SE-SEM micrographs. γ' phases (γ'_I, γ'_{II}, γ'_{III}) are identified via the software Aphelion V3.2 by running the following script: median filter (kernel 3x3), Gaussian filter (kernel 5), adaptative threshold (low value for phases identification, high value for phases boundary determination), opening, hole fill, closing. Such an algorithm increases phase segmentation with a similar threshold. Extraction of the γ' sizes and distribution was performed via a python script.

Conventional image analysis requires contrasted micrographs to enable phases identification (distinctive gray levels from the different phases for identification), and the chemical etching has then to be perfectly realized (sufficient dissolution of emerging γ' precipitates but no etching of non-emerging γ' precipitates). Figure 2.17-a) denotes a discernible gray level from the γ' to γ phases. Figure 2.17-b) does not provide a discernible gray level for conventional image analysis thresholding requiring advanced identification techniques.

The long post-treatment time required by the Aphelion software (manual adjustment for each micrograph of the thresholds, of the elements' sizes...) combined with limitations on the quality of the input micrograph has led to deep learning image analysis developments.

Deep learning-based image analysis when conventional image analysis fails at phase segmentation on SEM-SE micrographs but also for grain size estimation from SEM-BSE micrographs.

SEM-SE micrographs (see e.g 2.17-c), revealed a white halo surrounding γ' phase due to edge effect from the topography generated by the negative etching of the precipitates and accentuated by the secondary electron mode (interaction pear). Such a halo is difficult to take into account in conventional image analysis but proved to be compatible with deep-learning image segmentation.

SEM-BSE micrographs were analyzed to segment the grains without considering twin boundaries. Such methodology is not possible in conventional image analysis, even if shape factors (twin boundaries presents straight line in SEM micrographs) can be of help in their identification. A deep learning image segmentation algorithm was trained using SEM-BSE and EBSD maps comparisons. EBSD allows grain boundaries segmentation based on their crystallographic orientation, twin boundaries are then easily excluded from grain boundaries.

The deep learning algorithm for image segmentation developed in this study relies on medical image segmentation algorithms, especially the DC-Unet model [206]. The extended algorithm for both SEM-SE and SEM-BSE segmentation is developed in appendix E.

2.1.10 Statistical representation of grains and precipitates diameters

All the statistical summaries of the results given in section 2.2 are presented using boxplot graphical distribution representation. It is based on the key numbers: the minimum and maximum ($Q1-1.5\cdot IQR$ and $Q3+1.5\cdot IQR$), the first and third quartile $Q1$ and $Q3$ (25 % and 75 %), and the median, with IQR being the interquartile range, as denoted in figure 2.18. The mean value is to be represented by a circle above the boxplot. Gaussian distribution can also be included to comply with standard statistical representation.

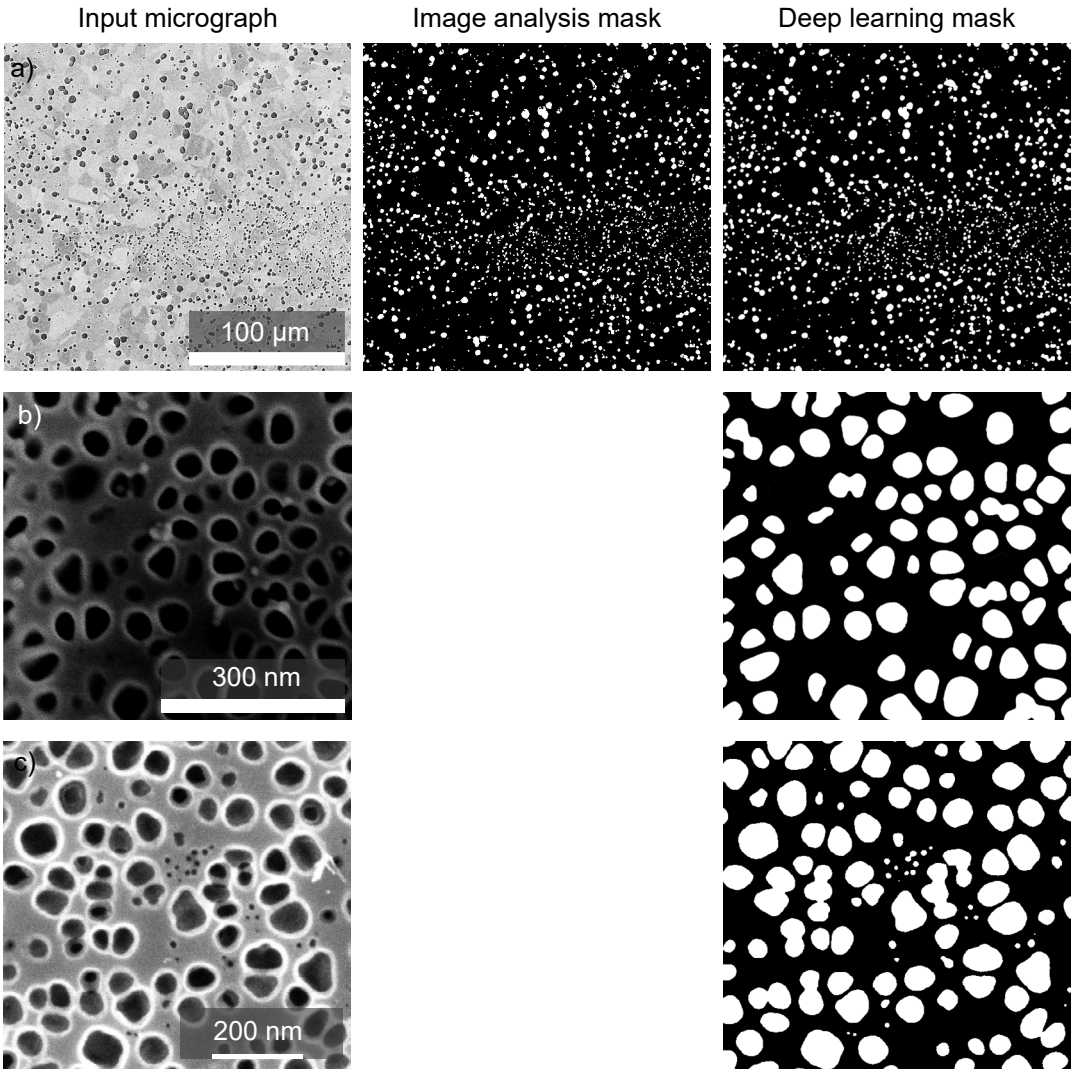

Figure 2.17: Example of image segmentation for a) discernible γ' from γ phases; b) not easily discernible phases via conventional image analysis. c) SEM-SE micrograph demonstrating the white halo delimiting γ' particles due to SE edge effect

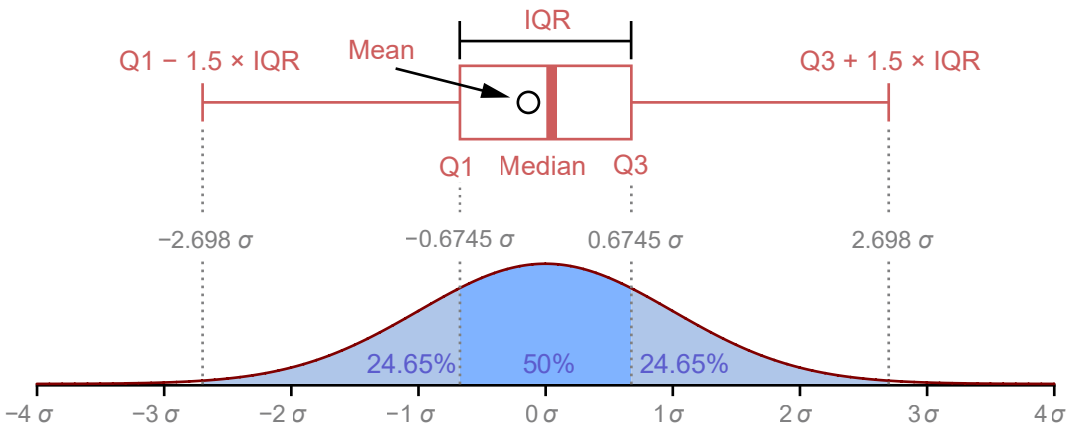

Figure 2.18: Boxplot definition versus Gaussian distribution

2.2 René 65

Two different microstructures are analyzed in this study: the As-Received (AR) and the Albi-Solvus (AS) metallurgical state. The AS state received heat treatments to diminish the fraction of primary γ' precipitates, thus revealing the impact of the γ'_I on the oxidation behavior but also the mechanical response of the material.

Both states are to receive mechanical characterization and oxidation using microtensile specimen and oxidation procedures given in section 2.1.2 and section 2.1.5 respectively. This section aims at a fine microstructural characterization of both states to validate the thin samples versus material compliance (number of grains versus thinner targeted specimen thickness)

The three extraction zones are to be characterized to investigate potential microstructural evolution in each zone. René 65 being forged, anisotropy in the microstructural features (grains size, morphology, and direction) can be observed, and all directions are then investigated as well.

2.2.1 As-received microstructure

Grain size distribution

In terms of mechanical properties, the grain size influences the tensile, fatigue, and creep behavior as depicted in figure 1.5. The thickness of microtensile specimens is designed according to the grain size in order to optimize the grain size over thickness ratio. Such a ratio leads to the multicrystal-to-polycrystal transition. The oxidation behavior is also grain size dependent due to the differences in oxygen diffusivity from the bulk of the grains to the grain boundaries, especially for internal oxidation. A larger grain size diminishes the ratio of grain boundaries.

The microstructure of René 65 is complex, *i.e.* constituted of grains and γ'_I. Both microstructural features have similar morphology (equiaxed but γ'_I being slightly smaller), and diffraction patterns but differ in chemistry. Therefore, the dissociation of grains from γ'_I in fine microstructures such as René 65 requires advanced mapping methods as EBSD alone does not allow differentiation of the almost coherent phases from the matrix to the primary γ' precipitates. But primary γ' precipitates vary from the matrix by their chemical composition ($Ni_3(Al, Ti)$, structure $L1_2$). The idea is therefore to take this difference into account, through coupling EDS and EBSD techniques as described in section 2.1.8. The EDS corrected EBSD map for Oxidation Coupon (OC) extraction region on as-received conditions with twin-boundary considered as a specific grain boundary is presented in figure 2.19.

The three extraction zones were quantified in grain size, as exposed in figure 2.20 based on the analysis of at least 2000 grains. The mean grain size of the parent grain, *i.e.* exempt of twins, is 7.8 µm, 8.0 µm and 7.9 µm for the core, coupon, and flank zone respectively. Maximal value and distribution of grain size were also revealed to be similar for the three extraction regions with maximal values of 33.5 µm, 30.9 µm and 31.1 µm.

Figure 2.20 gives two representations of the grain size with boxplot representation on the left and cumulative distribution plot on right. The cumulative distribution plot is smoothed via kernel density estimation function from the python seaborn library. The boxplot representation is explained in section 2.1.10.

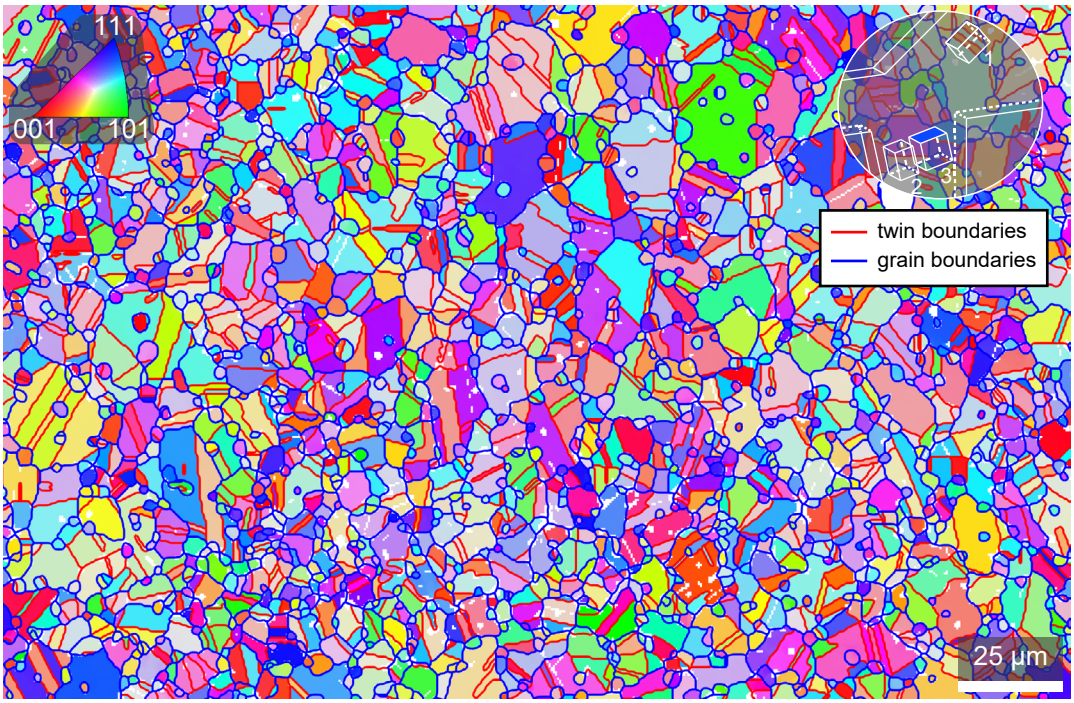

Figure 2.19: EBSD map on as-received OC extraction region

The microstructure presents fine grains (FG) and medium grains (MG) regions as depicted in figure 1.7. FG from MG region was dissociated and separately quantified on the OC zone. Minor grain size variations were reported from the two regions as summarized in figure 2.21. The FG from the MG region distinction was manually evaluated on the EBSD map. Mean grain size varies from 6.6 µm to 8.5 µm on the FG and MG respectively, with an overall mean value of 7.8 µm. The maximal value of grain size was reported at values of 17.8 µm and 26.2 µm for FG and MG regions.

The results in figure 2.20 demonstrate the heterogeneous microstructure of René 65 despite FG inclusion in an MG matrix. Minor variation from the two regions (FG and MG), resulting from the forging process, in the magnitude of the thinner specimens (20 µm) is still to be reminded for mechanical testing analysis.

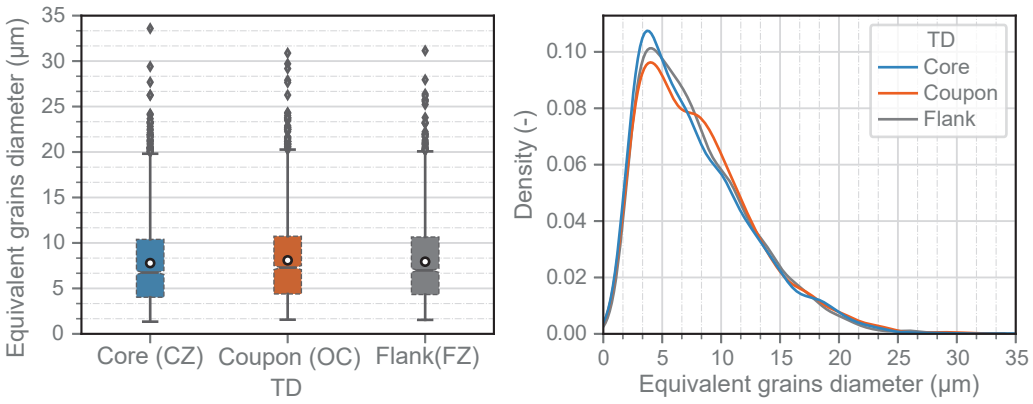

Figure 2.20: Distribution and mean value of the grain size equivalent diameter (µm) on the three extraction regions

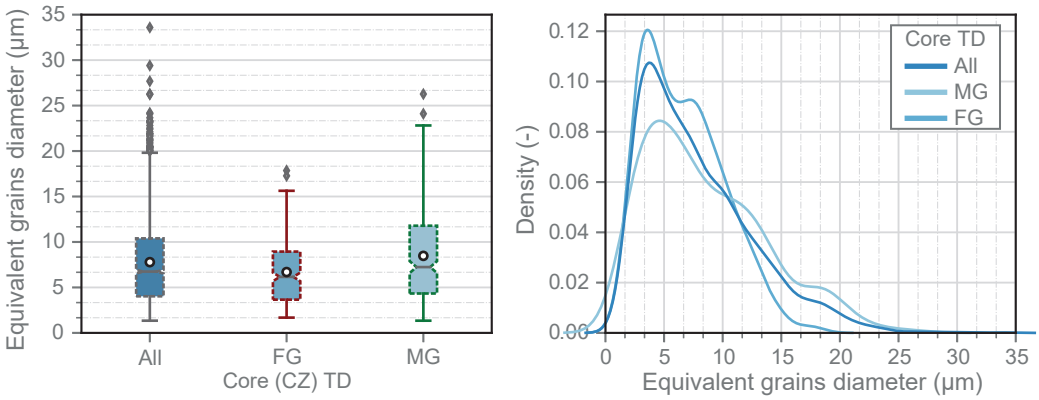

Figure 2.21: Distribution and mean value of the grain size equivalent diameter (µm) on the core region with distinction of FG to MG

γ' precipitates size and spatial distribution

γ' precipitates, hardening phase of René 65, have been reported responsible for the high mechanical properties up to high-temperature as described in section 1.1.1. The size and spatial distribution of the three γ' precipitates populations are then of interest.

Primary γ' precipitates can be revealed by segmenting SEM-SE micrographs as presented in figure 2.22 for magnification x250. Figure 2.22 reveals γ'_I population size regions (FG surrounded by a green box, and MG surrounded by a red box), with a focus on each region. Distinction from FG to MG was performed manually on SEM-SE micrographs as reported in figure 2.23 and a stitching on SEM x150 magnification micrographs in the tensile gage specimens on figure 2.24. The green color for the FG region and red color for the MG region is to be employed in all the statistical graphs that distinguish the two regions.

The two grain size regions (FG and MG) are to be specifically detailed on all extraction zones (FZ, CZ, OC). The *overall* or *all* region denominations refer to micrographs composed of both regions (up to x500 magnification). The ratio from FG to MG being variable, the *overall* region is only valid for micrographs presenting both FG and MG regions.

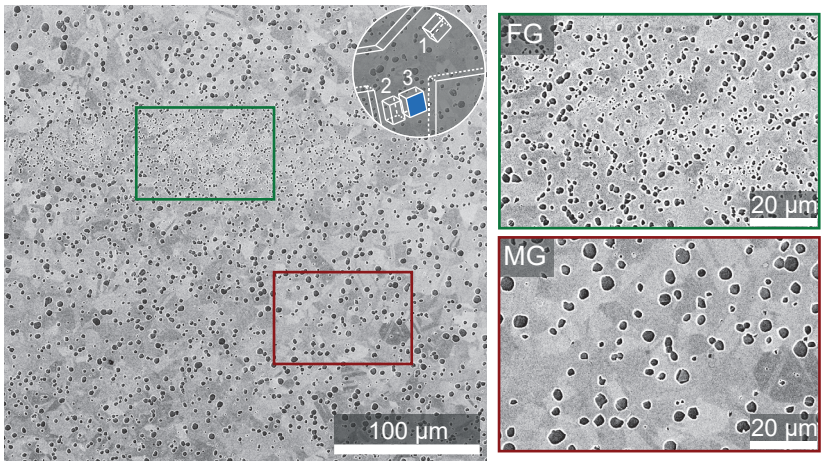

Figure 2.22: SEM-SE micrograph of as-received OC region x250. Focus on each extraction zone (FG and MG), highlighting the primary γ' precipitates

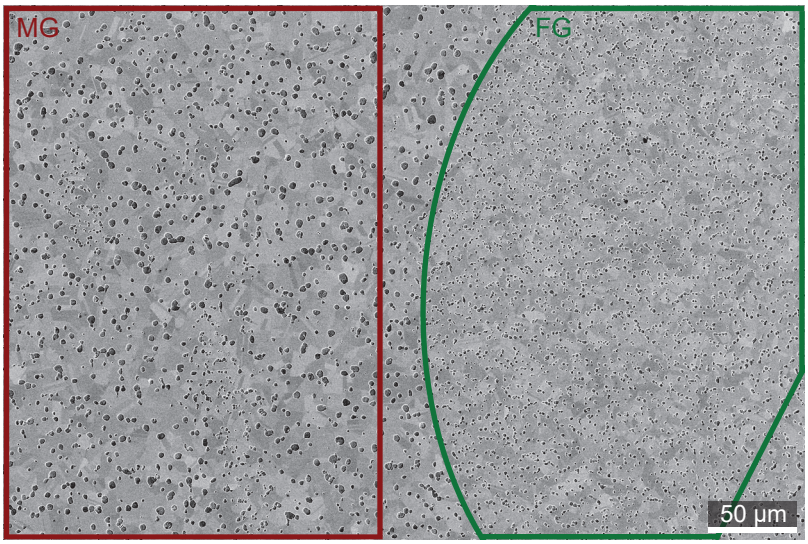

Figure 2.23: SE micrograph of as-received coupon region x250 Manual selection of FG and MG regions

Figure 2.24: SEM stitching from x150 magnification micrographs, differentiation from FG (green) and MG (red) regions

Primary γ' precipitates were quantified in the core region as presented in figure 2.25 from FG to MG and overall regions in the three orientations (along each plane normal to the axis TD, RD, FD, referred directly by the axis name from now on). The mean value is respectively of 2.03 µm, 1.93 µm and 1.98 µm for the RD, TD, and FD axis. MG reported 0.38 µm larger equivalent diameter than the overall average, FG reported 0.58 µm smaller equivalent diameter. The maximal value in equivalent diameter was reported 2 µm smaller from FG to MG.

All directions reveal a similar equivalent grain size with less than 0.1 µm variation in mean grain equivalent diameter. Significant variations from the MG and FG regions were reported with up to 0.6 µm but should reveal a trivial impact on the mechanical properties. The grain boundaries fraction is nevertheless impacted by such variations from both regions and should be reminded of the oxidation behavior of René 65.

Figure 2.26 exposes the equivalent diameter of primary γ' precipitates for all extraction zones (OC, FZ, CZ) in all directions. OC and CZ exhibit similar isotropic sizes for overall, FG, and MG regions. The FZ exhibits slightly lower precipitate size

in two of the three directions investigated (0.5 µm below). The average primary γ' precipitate size on all SEM-SE micrographs is 1.96 µm, 2.32 µm for MG, and 1.39 µm for FG. The surface proportion of emerging primary γ' precipitates is 11.8 %.

The primary γ' precipitates see significant evolution to the grain size from FG to MG region. The FG region, composed of finer grains, reveals finer primary γ' precipitates. The primary γ' precipitates are responsible for grain boundary pinning, a finer population agrees with finer grain size. However, the fraction of primary γ' precipitates is similar for both regions (FG and MG, 1.1 % variation with higher value for MG region) leading to a higher number of precipitates but smaller for the FG region.

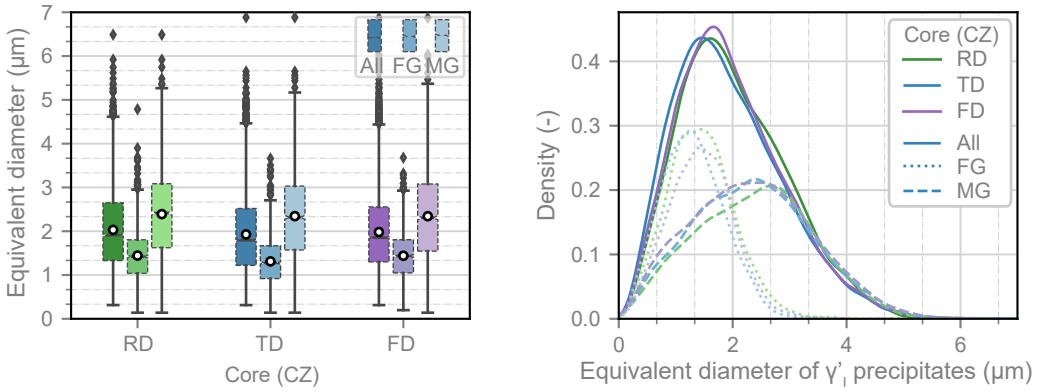

Figure 2.25: Size distribution of γ'_I and differentiation from FG to MG microstructures

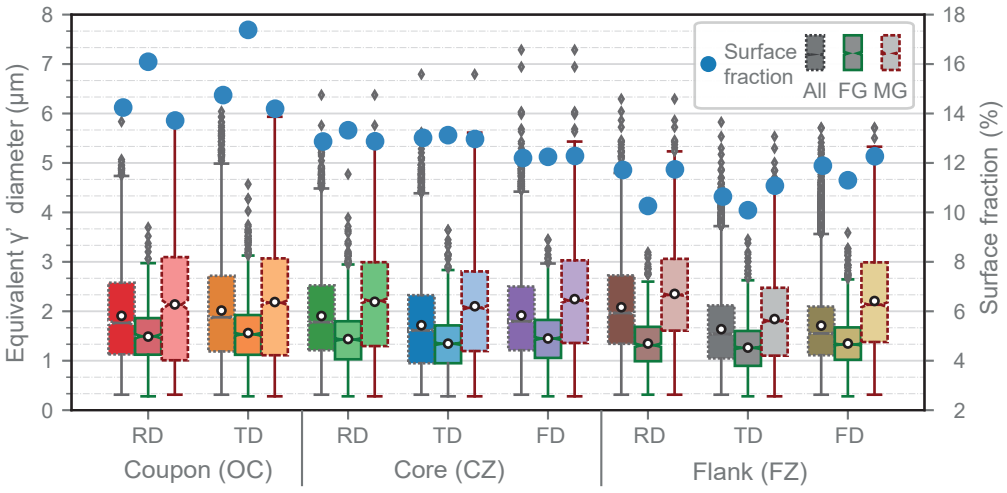

Figure 2.26: Spatial distribution of γ'_I in the different extraction locations

γ'_{II} and γ'_{III} precipitates statistics were computed onto both MG and FG regions using x20 000, x50 000, and x100 000 magnification SEM-SE micrographs. Micrographs at magnification higher than x500 are located only in one region (FG or MG) due to their restricted field of view (6.3 µm Horizontal Field of View (HWF) for x20 000 magnification micrographs, 846.8 nm HWF for x150 000 magnification micrographs).

The measurement uncertainty from x250 magnification SEM micrograph is set to one pixel on the radius of primary γ' precipitates detection. The resolution of such a

magnified micrograph leads to 0.48 µm uncertainty in the diameter. The experimental uncertainty of the secondary and tertiary precipitates is of 6 nm on the equivalent diameter from x20 000 and x50 000 magnification micrographs.

Secondary precipitates γ'_{II} can be revealed by segmenting SEM-SE micrographs as presented in figure 2.27 for magnification x50 000. γ'_{II} size distribution are presented in figure 2.28 with similar graph structure as figure 2.26 for zones, regions and orientations. OC and CZ exhibit similar γ'_{II} size with an average size of 64.0 nm for the FG and 63.3 nm for the MG. FZ reveals a lower average size to the same extent as γ'_{I} with 10 nm decrease in equivalent diameter. The proportion of secondary precipitates γ'_{II} is of 35.3 %.

Tertiary precipitates γ'_{III} varies from 12.4 nm to 16.8 nm with a mean value of 14.7 nm. No clear variation is observed from the three zones nor the three directions. The proportion of primary γ' precipitates γ'_{III} is of 1.45 %.

All the values of mean, maximal, and fraction of the three γ' precipitates in all regions and zones are summarized in table 2.3.

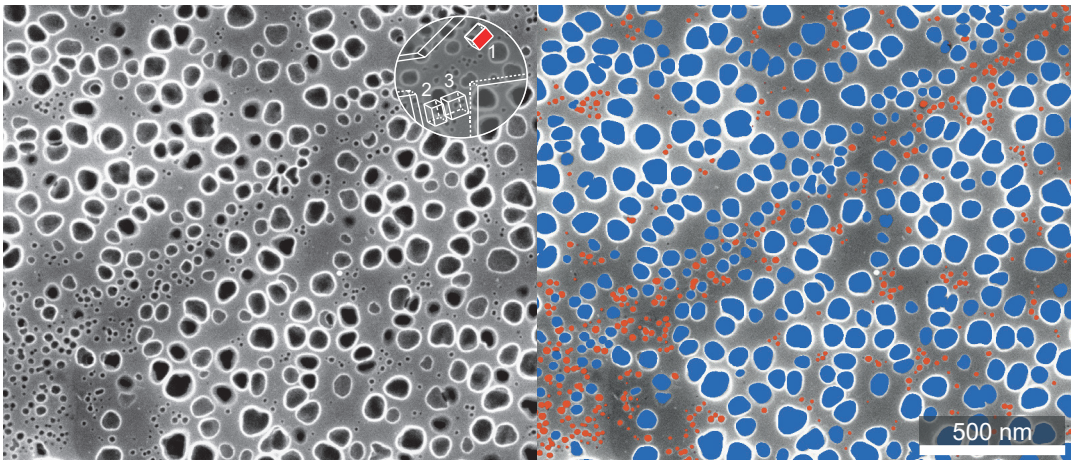

Figure 2.27: SEM-SE micrograph of as-received OC region at x50 000 magnification. Highlight of the primary γ' precipitates γ'_{II} and γ'_{III}

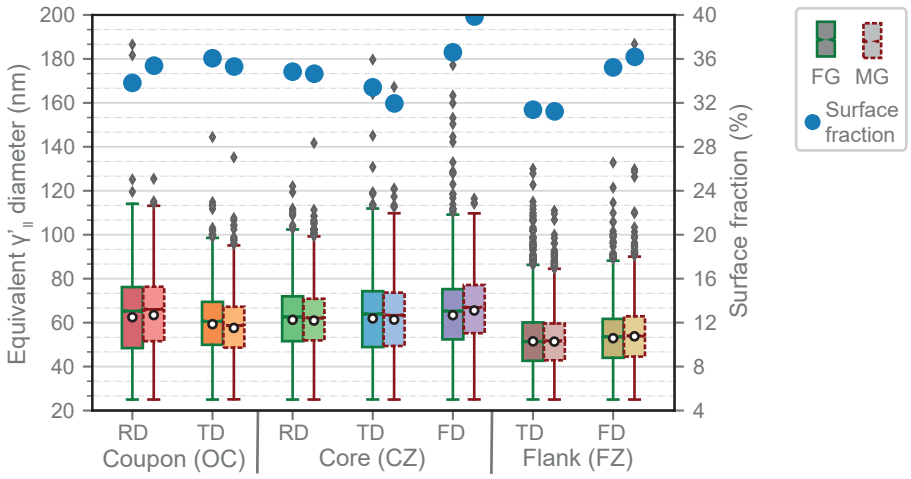

Figure 2.28: Spatial distribution of γ'_{II} in the different extraction locations

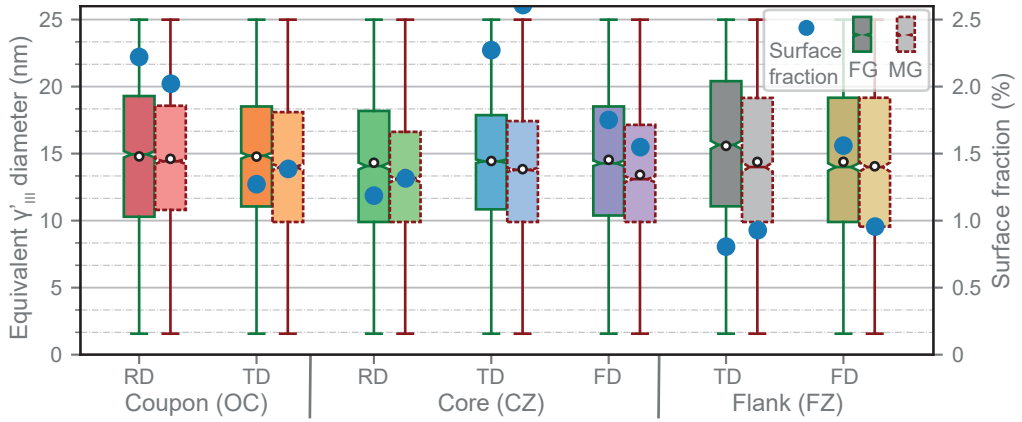

Figure 2.29: Spatial distribution of γ'_{III} in the different extraction locations

		Coupon (OC)		Core (CZ)			Flank (FZ)		
		TDFD	RDFD	TDFD	RDFD	TDRD	TDFD	RDFD	TDRD
γ'I precipitates	Mean (μm)								
	All	1.9	2.0	1.9	1.7	1.9	2.1	1.6	1.7
	FG	1.5	1.6	1.4	1.3	1.4	1.3	1.3	1.3
	MG	2.1	2.2	2.2	1.9	2.2	2.4	1.8	2.2
	Max (μm)								
	All	5.8	6.0	6.4	6.8	7.3	6.3	5.8	5.7
	FG	3.7	4.6	4.8	3.6	3.5	3.2	3.5	3.6
	MG	5.8	6.0	6.4	6.8	7.3	6.3	5.5	5.7
	Fraction (%)								
	All	14.2	14.7	12.9	13.0	12.2	11.7	10.6	11.9
	FG	16.1	17.4	13.3	13.1	12.2	10.3	10.1	11.3
	MG	13.7	14.2	12.9	13.0	12.3	11.7	11.1	12.3
γ'II precipitates	Mean (nm)								
	FG	62.4	59.3	61.3	61.5	63.3	-	51.5	52.9
	MG	63.4	57.6	61.0	61.4	65.5	-	51.4	53.8
	Max (nm)								
	FG	186.5	144.4	122.0	179.7	182.3	-	130.0	132.8
	MG	125.4	135.2	141.7	167.2	116.4	-	110.9	186.8
	Fraction (%)								
	FG	33.8	36.1	34.8	33.4	36.6	-	31.4	35.2
	MG	35.4	35.3	34.7	31.9	39.9	-	31.2	36.2
γ'III precipitates	Mean (nm)								
	FG	14.8	14.8	14.3	14.4	14.5	-	15.6	14.4
	MG	14.6	14.1	13.5	13.8	13.4	-	14.4	14.1
	Max (nm)								
	FG	25.0	25.0	25.0	25.0	25.0	-	25.0	25.0
	MG	25.0	25.0	25.0	25.0	25.0	-	25.0	25.0
	Fraction (%)								
	FG	2.2	1.3	1.2	2.3	1.8	-	0.8	1.6
	MG	2.0	1.4	1.3	2.6	1.5	-	0.9	1.0

Table 2.3: Statistics summary of all γ' precipitates on AR state

Influence of primary γ' precipitates on the grains size and γ'_{II}- γ'_{III} precipitates. The primary γ' precipitates fraction being constant for both regions (FG and MG), minor to no variation in γ'_{II} and γ'_{III} precipitates fraction is observed (no release of γ' entities in the matrix to form γ'_{II} and γ'_{III} precipitates).

The two René 65 extraction zones FZ and CZ mechanically investigated exhibit minor differences in terms of γ'_{I}, γ'_{II}, γ'_{III} precipitates. γ'_{II} and γ'_{III} precipitates being of first order in the material hardening (as described in section 1.1.1), the minor variations in γ'_{II} and γ'_{III} sizes consequences are to be monitored on a first manner. The oxidation coupon (OC) zone exhibits similar grain and γ' precipitation sizes as the CZ zone for both FG and MG regions.

Nitrides size and spatial distribution

Nitrides (TiN) particles are located preferably in the MG region as depicted in the micrograph 2.30. Mean and maximal values for equivalent diameter were obtained on the analysis of two gage specimens (2 mm × 5 mm area) via stitching of SEM-BSE micrographs at magnification x150 (same specimen gage presented in figure 2.24 for FG and MG regions distinction). Nitrides reveals an average diameter of 7.6 µm with a maximal value of 15.0 µm and a proportion of 10.8 nitrides/mm^2. Such proportion lead to between 200 nitrides to 250 nitrides at the surface of microtensile specimens (depending on the specimen's thickness). Those statistics are summarized along with carbides statistics in table 2.4.

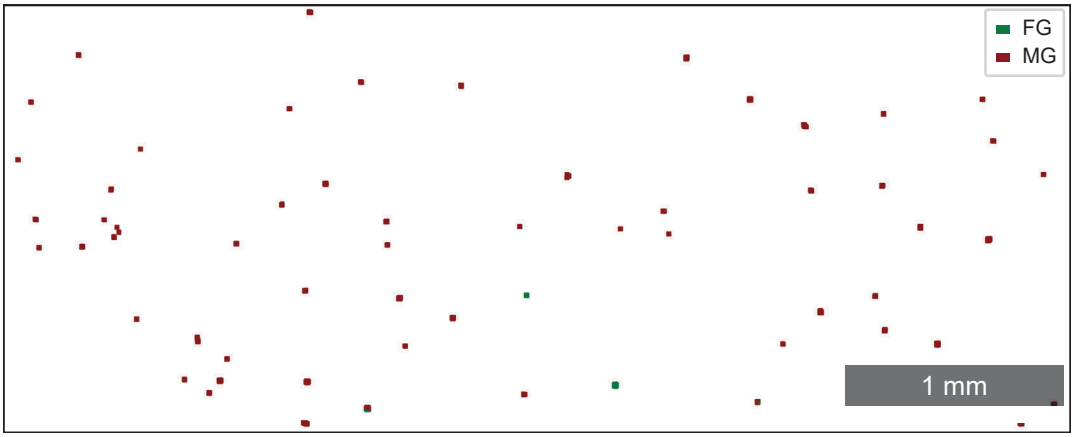

Figure 2.30: Nitrides identification (dilated for visualization) in a 2 mm × 5 mm microtensile specimen gage. Distinction from MG (red) to FG (green) region

Carbides size and spatial distribution

Carbides particles are also concentrated in MG region as depicted in the micrograph 2.31 (11.3 % in the FG region for 88.7 % in the MG region). Micrograph 2.31 correspond to figure 2.24 microtensile specimen gage. Carbides reveal similar fiber drawing as the MG and FG distribution present in figure 2.24. Fiber paths can also be identified in micrograph 2.31 resulting from the forging process. Carbides revealed a mean value of 2.5 µm with a maximal value of 7.6 µm. The proportion of carbides is of 421.6 carbide/mm^2, located preferentially along grain boundaries.

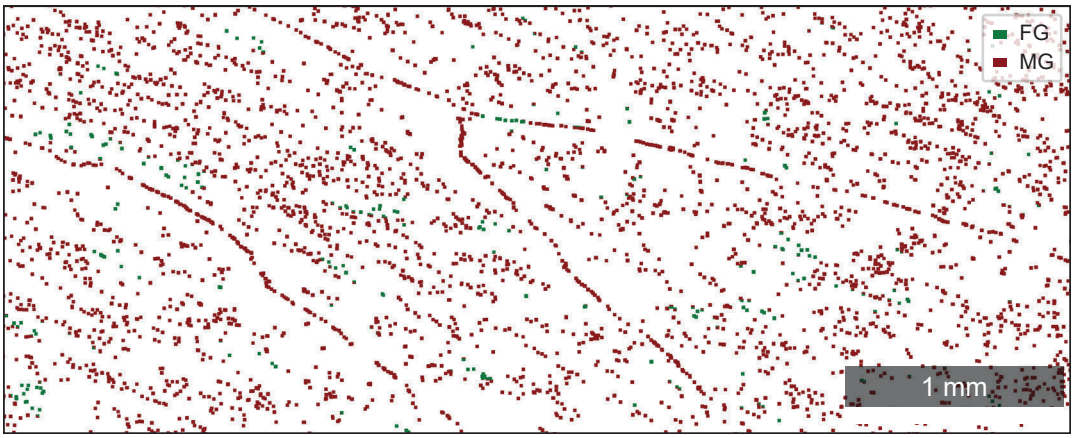

Figure 2.31: Carbides identification (dilated for visualization) in a 2 mm × 5 mm microtensile specimen gage. Distinction from MG (red) to FG (green) region

	Nitrides	**Carbides**
Mean (µm)	7.6	2.5
Max (µm)	15.0	6.8
Proportion (number/mm^2)	10.8	421.6
Fraction		
FG (%)	6.3	11.3
MG (%)	93.7	88.7

Table 2.4: Nitrides and carbides statistics from two micro-tensile specimens gage analysis

Phases identification of the AR state

Two phases were identified via XRD analysis of the as-received state of René 65 as denoted in figure 2.32. This diffractogram is further used as a reference for the identification of new phases developed during oxidation tests and aging treatments. The two phases identified are γ as Ni and γ' as $Ni_3(Al, Ti)$. Carbides and nitrides were not identified due to their low volume fraction and size in the material whereas transverse micrographs revealed their presence.

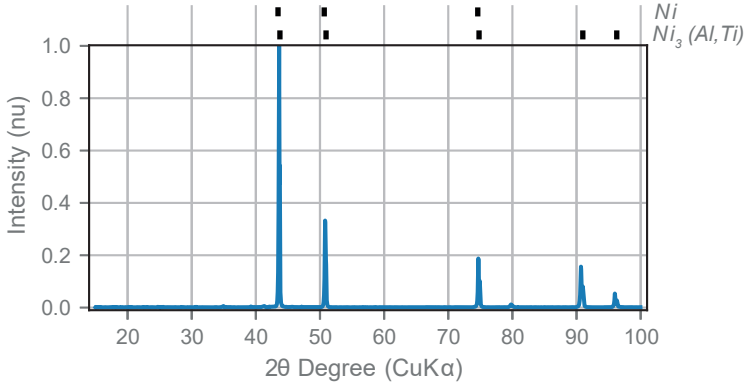

Figure 2.32: XRD diffractogram of as-received state

Phases chemical entities distribution

The partitioning in chemical entities between γ, γ′, and TiN phases in the AR metallurgical state is exposed in figure 2.34 and figure 2.35. The SEM-BSE micrograph corresponding to both EDS regions is presented in figure 2.33. High color intensity on both EDS figures for all chemical entities is indicative of higher chemical concentration. Figure 2.34 confirms the composition of primary γ′ precipitates with a high fraction of Ni, Al, and Ti. Nitride particles reveal a high fraction of Ti and N at their core, with a punctual presence of Al and O for the nitride presented in figure 2.35. Those particles also exhibit a thin NbC envelope. Such envelop detection was not detected in the SEM-BSE micrograph 2.33. A small carbide can be identified on both SEM-BSE micrograph 2.33 and SEM-EDS figure 2.35. Carbides are composed of heavy elements such as Mo and W, but also lighter elements such as Cr, Fe, Co, and Nb as depicted in figure 2.35.

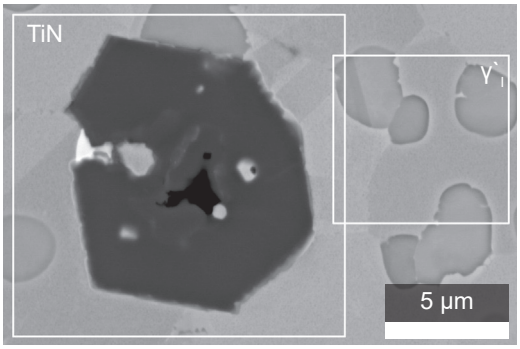

Figure 2.33: SEM-BSE micrograph of the SEM-EDS regions exposed in the two previous figures

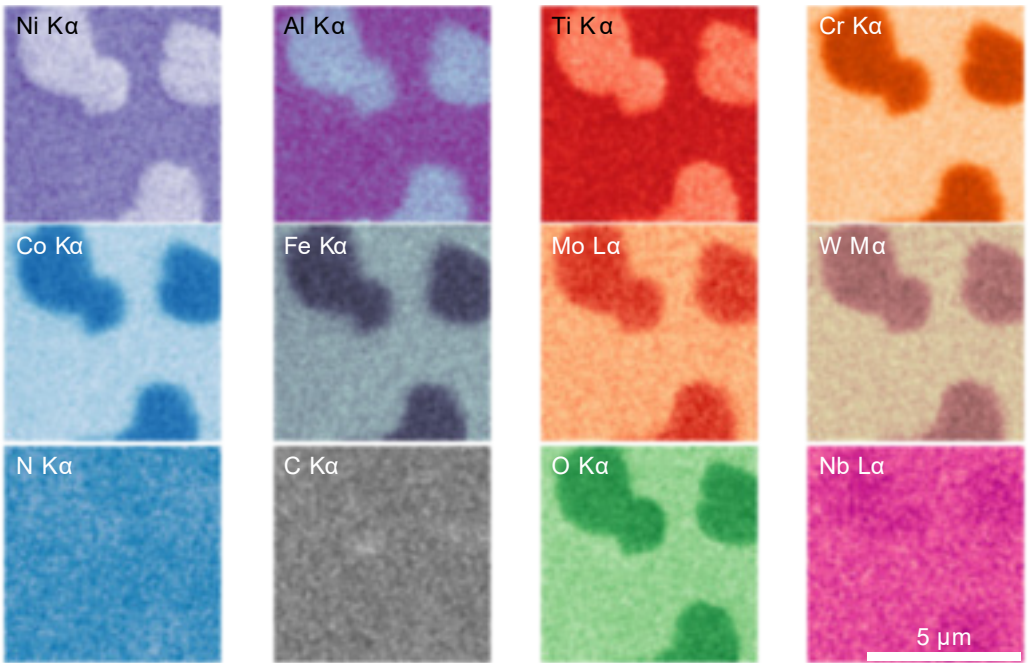

Figure 2.34: EDS maps of the main entities present in the phases γ and γ′ of AR state René 65

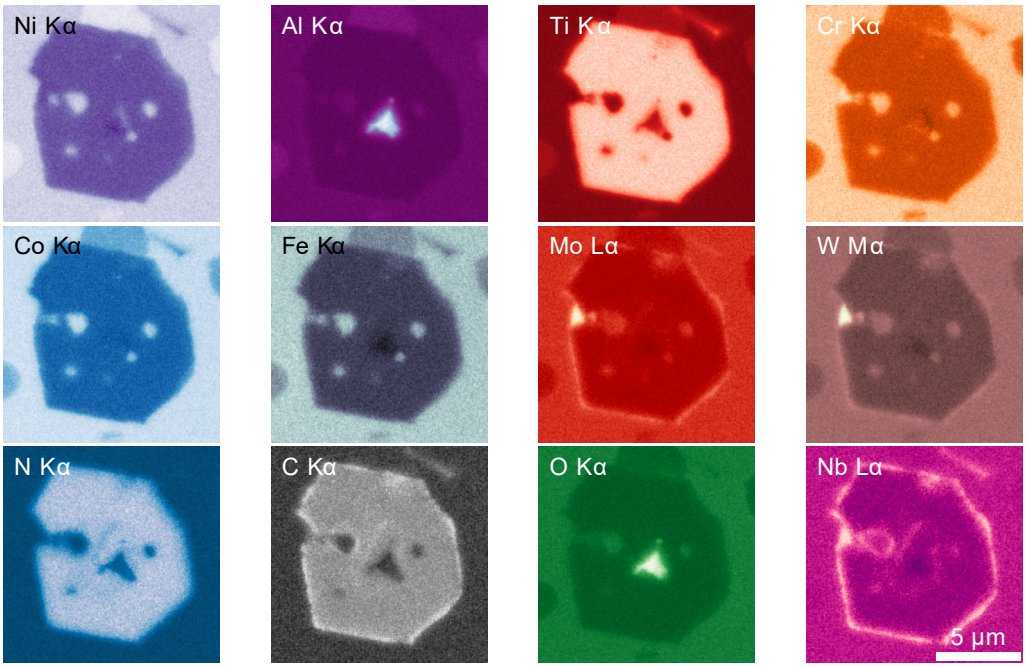

Figure 2.35: EDS maps of the entities present in the TiN phase of AR state René 65

2.2.2 AlbiSolvus microstructure

The characterization of the AlbiSolvus (AS - close to solvus) heat-treated samples microstructure characterization is presented in the section below. The heat treatment applied to René 65 to obtain AS metallurgical state was 1010 °C during 1 h (air quenched) followed by 760 °C during 8 h (air quenched). A similar methodology of characterizations as the AR state was performed.

Grain size distribution

The grain size of AS state was quantified from EBSD analysis, as depicted in figure 2.37. It presents an average diameter of 52.3 µm with a maximal size of 203.5 µm (figure 2.36).

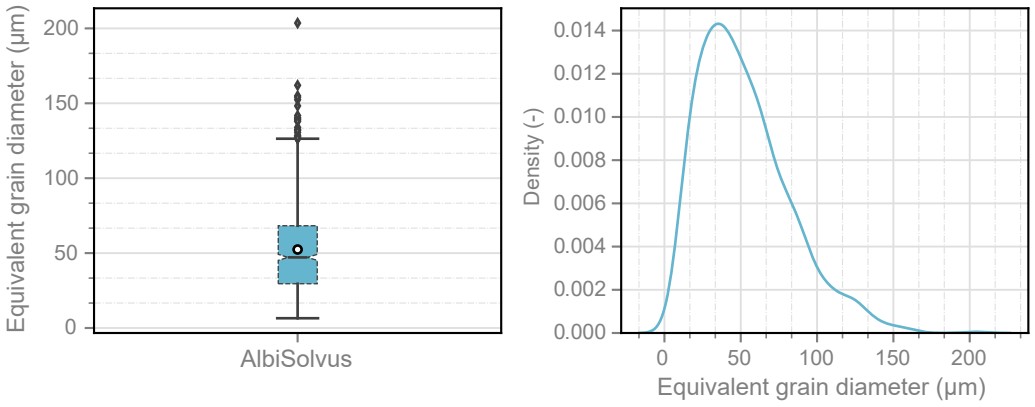

Figure 2.36: Distribution and mean value of the grain size equivalent diameter (µm) of the AS state

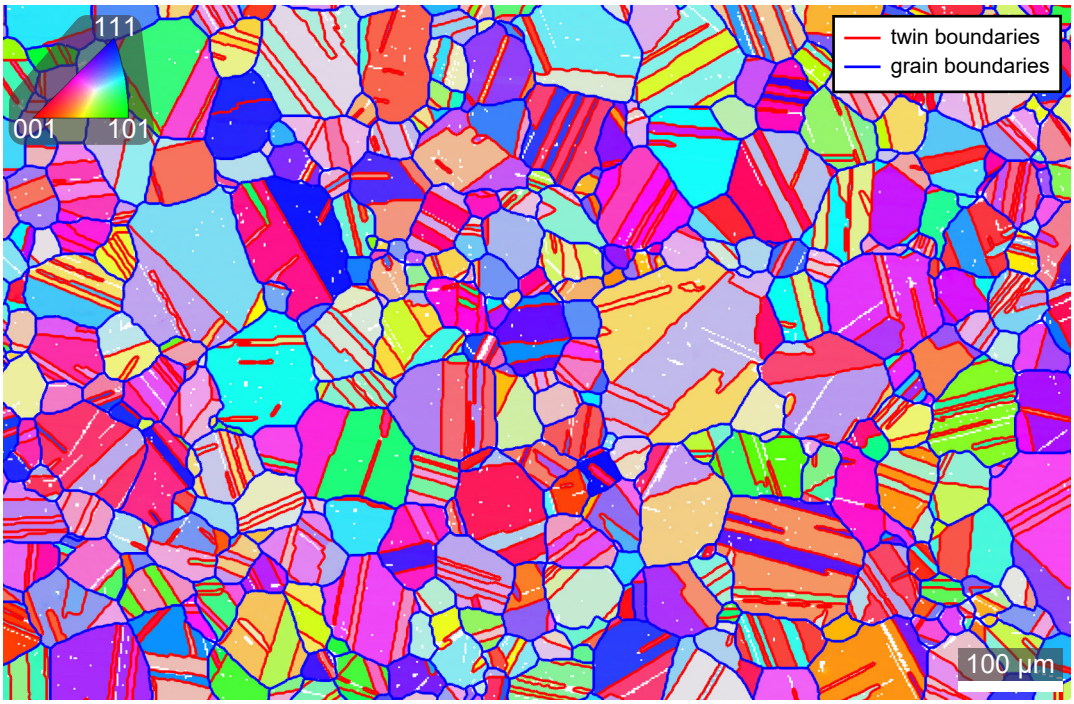

Figure 2.37: EBSD micrograph of AS state at magnification x150 revealing the grain size

γ' precipitates size distribution

γ' precipitates are estimated using SEM-SE micrographs at magnification x150, x250 and x500 after aqua regia chemical etching (figure 2.38) for γ'_I precipitates, and x20 000, x50 000, and x150 000 SEM-SE micrographs for γ'_{II} and γ'_{III} precipitates (figure 2.39).

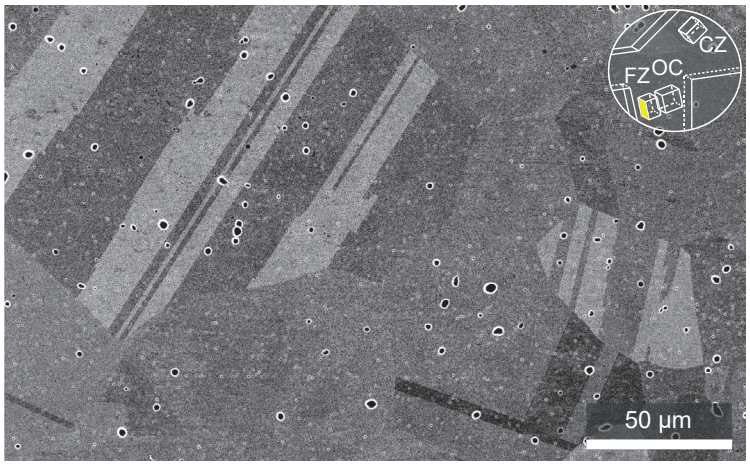

Figure 2.38: BSE micrograph of AS state at magnification x250. Exhibition of primary γ' precipitates

Statistics on the γ' precipitates: remaining primary γ' precipitates reveals a mean diameter of 1.6 µm and a volume fraction of 0.89 %. The secondary γ' precipitates reveal a mean diameter of 40.3 nm and a volume fraction of 30.0 %. As for γ'_{III} precipitates:

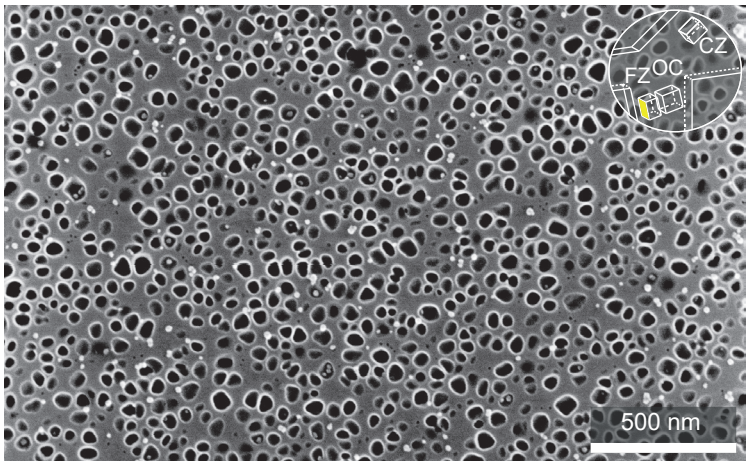

Figure 2.39: BSE micrograph of AS state at magnification x50 000 Exhibition of secondary and tertiary precipitates γ'_{II} and γ'_{III}

a mean value of 19.7 nm with a volume fraction of 1.2 %. The size distribution of the three precipitates populations is presented in figure 2.40

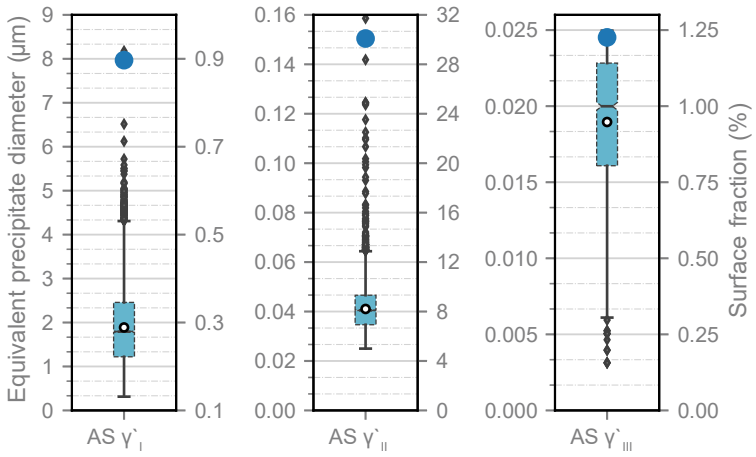

Figure 2.40: Distribution and mean value of the equivalent precipitates diameter (µm) for the three precipitates population of the AS state

Conclusions on AS precipitation: the AS microstructure contains more γ'-forming entities (Ti and Al) embedded in the γ matrix due to the lower size and surface faction of the three precipitates populations compared to the AR state.

Primary γ' precipitates γ'_I are 0.40 µm smaller and 10 % area fraction less in the AR state compared to AR.

Secondary γ' precipitates γ'_{II} revealed a 20 nm decrease in equivalent diameter and 5 % in area fraction.

Tertiary γ' precipitates γ'_{III} are slightly bigger with 5 nm increase in size but equivalent area fraction.

The overall area fraction of γ' phase is then lower than the AR state (44 % on the AR state compared to 32 % on the AS state).

γ'_{III} precipitates form preferably along grain boundaries and γ'_I precipitates, as depicted on figure 2.27. Results on the γ'_{III} precipitates, especially area fraction, are then dependent on the location of the micrograph (close to γ'_I precipitates or in the middle of the grains).

	AR			AS		
	mean	max	fraction (%)	mean	max	fraction (%)
Grain size	7.9	31.8	-	52.3	203.5	-
γ'_I (µm)	1.8	7.3	10.6	1.6	2.5	0.9
γ'_{II} (nm)	56	200	31.8	40	160	30.1
γ'_{III} (nm)	14	25	1.5	20	25	1.2

Table 2.5: AR and AS grain size and γ' precipitates statistics

The results in grain size are below typical supersolvus heat treatments, indicative of a sub-supersolvus state. This assumption is confirmed by the presence of primary γ' precipitates in figure 2.38, pinning grain boundaries by Zenner mechanism, and so limiting the exponential growth of the grain size.

The AS state is to be mechanically characterized in tensile solicitation mode within this framework. Evolution on the grain size (Hall-Petch effect), but also on the γ' precipitates should induce changes in the tensile behavior. The oxidation behavior is also to be influenced by such evolution due to reservoir effect of the γ' precipitates and differences in grain boundaries fraction leading to a decrease of the global diffusivity of entities involved in the oxidation process.

2.2.3 Tensile behavior of AR and AS states

Reference tensile behavior on standardized specimens

Room temperature tensile tests were conducted on standardized tensile specimens to validate the largest thickness (500 µm) microtensile specimen adequacy. The tensile behavior of standardized specimens on the AR and AS states are summarized in figure 2.41 and table 2.6. Table 2.6 exposes the major material features extracted from a tensile test:

YM: the Young Modulus is the modulus of elasticity in tension representative of the stiffness of the material.

YS: the Yield Stress corresponding to 0.2 % of plastic strain.

UTS: the Ultimate Tensile Stress is the maximal true stress of the test.

Ductility: is the maximal elongation.

	YM (GPa)	YS (MPa)	UTS (MPa)	Ductility (%)
AR	207.1	1149	2028	26.6
AS	210.8	1105	1909	22.5

Table 2.6: Standardized tensile tests results on AR and AS states

AR state reveals higher YS, UTS, and ductility than the AS state. Figure 2.41 points out the changes in the elastic-to-plastic transition from both states, with a more progressive transition for AS state and a decrease in YS. Considering the microstructural evolution from both states in terms of grains and γ' precipitates, the mechanical behavior is still relatively similar. The material is very slightly sensitive to the grain size, and so to the Hall-Petch relation, the fraction and size of γ'_{II} and γ'_{III} being first order parameters on the room temperature tensile properties as reported on similar Ni-based superalloys by several authors [8, 34, 41, 207].

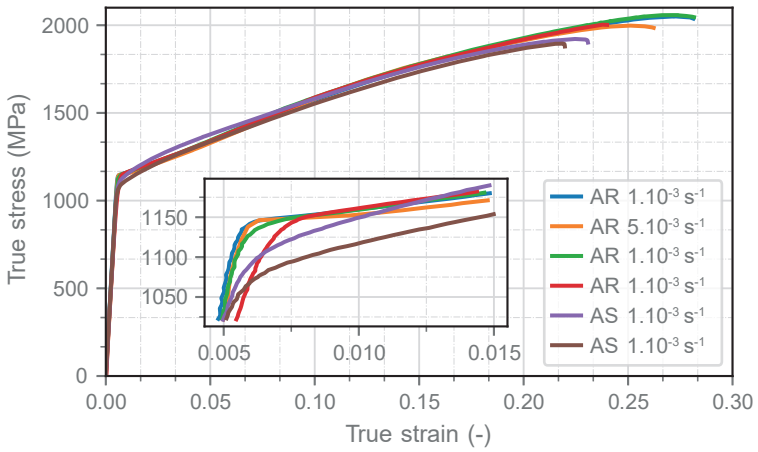

Figure 2.41: True stress versus true strain curves of standardized tensile tests for AR and AS metallurgical states. Investigation of deformation speed at $1 \times 10^{-3}\,\mathrm{s}^{-1}$ and $5 \times 10^{-3}\,\mathrm{s}^{-1}$ on AR specimens

Microtensile specimens behavior on the different extraction zones

The tensile behavior of the two extraction zones FZ and CZ was characterized for 500 µm thick microtensile specimens as depicted in figure 2.42 (thickest microtensile specimen investigated). Three microtensile specimens were tested per condition. The FZ exhibits a YS of 1121 MPa, an UTS of 1920 MPa and a ductility of 0.25. The CZ only differs on the YS with a value of 1101 MPa. The minor variations in microstructure from the two zones result in minor variations of the true stress vs true strain response of the material. The FZ, with slightly lower secondary γ' precipitates size, sees a 20 MPa increase in YS (1 % increase). Such minor variations reveal a homogeneous tensile behavior from both extraction zones. No differentiation from both zones is to be performed on all tensile tests within this framework.

Microtensile validation from standardized specimens

The two specimen geometries (microtensile and standardized) tensile behavior are presented in figure 2.43. The standardized specimens exhibit a 40 MPa increase in YS, a 100 MPa increase in UTS and a 0.1 higher ductility compared to the mean AR properties. The higher ductility and UTS may come from the circular shape of the standardized specimens (no sharp edges leading to premature damage of the specimen). The variation in YS can be observed on the true strain vs true stress data in figure 2.43 with a more progressive elastic-to-plastic transition for microtensile specimens. The work hardening is in agreement on both geometries. Finally, a change in YM is observed

from both geometries, with 40 GPa increase for the microtensile geometry (210 GPa for standardized to 250 GPa for microtensile specimens). Such changes in YM were not investigated but might arise from the DIC technique for strain monitoring.

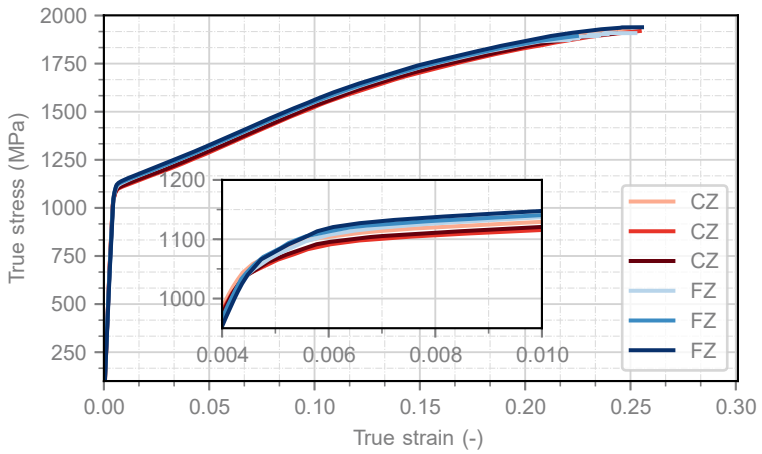

Figure 2.42: Stress strain curves of 500 µm thick specimens of the two extraction zones CZ and FZ

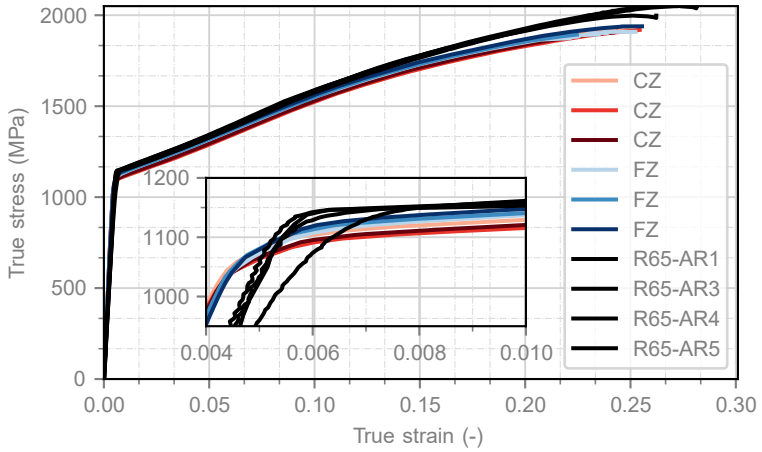

Figure 2.43: Stress strain curves of 500 µm thick specimens of the two extraction zones CZ and FZ compared to the standardized specimens

Outline

The As-Received metallurgical state demonstrates the followings conclusions:

- René 65, due to its forged manufacturing process, demonstrates two distinctive but similar microstructures regardless of the extraction regions. A medium grain (MG) microstructure with fine grains (FG) insertions. Both regions reveal minor differences in terms of grain size, but also in the three γ' precipitates populations.
- An equivalent grain diameter (without considering twin boundaries) of 6.6 µm to 8.5 µm on both regions (FG and MG, respectively). The 95 % maximal grain

diameter of both regions reports values of 15.6 µm and 22.8 µm on the FG and MG regions, respectively.

- primary γ' precipitates demonstrate an overall equivalent diameter of 1.96 µm and a area fraction of 11.8 %, with a variation from both regions of 1 µm in equivalent diameter.
- Secondary precipitates reveal a similar size distribution for both regions (MG and FG) with a mean equivalent diameter of 63.3 nm and an area fraction of 35.3 %.
- Similar conclusion on the tertiary precipitates with an average equivalent diameter of 14.7 nm and an area fraction of 1.45 %.
- The material, with its three extraction zones, demonstrates a similar microstructure for both CZ and OC zones but reveals noticeable variations in the secondary and tertiary precipitates populations from the FZ zone ($\gamma'_{II,CZ} \approx \gamma'_{II,OC} < \gamma'_{II,FZ}$).
- Nitrides are present at the surface of the material with an average diameter of 7.6 µm with a maximal value of 15.0 µm and a proportion of 10.8 nitrides/mm^2. Nitrides are preferably located in the MG region. The important dimensions of nitrides compared to all other microstructural features question their impact on the lifespan of the material. Govaere particularly studied their impact on the fatigue life of turbine disk alloys [9].
- Carbides and borides are much more present in the material, especially close to grain boundaries, mainly in the MG matrix.
- Both extraction zones mechanically investigated (FZ and CZ) demonstrate a minor superiority of the FZ zone, principally of the YS.
- Tensile tests on standard cylindrical specimens were performed at room temperature to set the reference compared to the microtensile specimens' design. Both designs demonstrate a similar behavior with minor superiority over the standard design.
- A close to solvus version of René 65 was processed and named AlbiSolvus. The mean grain size is of 52.3 µm. The precipitates populations demonstrate the following properties: a punctual presence of primary γ' precipitates (0.89 % of area fraction) of similar equivalent diameter, 10 nm smaller secondary precipitates with 30 % of area fraction and 5 nm larger tertiary precipitates of area fraction 1.2 %.
- Both AR and AS states tensile behavior vary in terms of YS, UTS, and ductility. The AS state exposes a similar tensile strain-hardening but with a more progressive elastic-to-plastic transition, and a premature failure compared to the AR state, leading to the tensile properties drop.
- René 65 is insensitive to the deformation speed in the range ($1 \times 10^{-3}\,s^{-1}$ to $5 \times 10^{-3}\,s^{-1}$) from the standard tensile tests.

Chapter 3

Oxidation and aging of René 65 at high-temperature

Chapter 3 is devoted to the study of microstructural aging, surface oxidation, and sub-surface metal evolution of René 65.

After introducing the oxidation conditions (time - temperature) and sample thicknesses targeted in this framework, the bulk evolutions *i.e.* the microstructural aging are investigated. The following sections of this chapter are then focused on surface reactivity phenomena. The oxidation products and kinetics are investigated in **section** 3.3. The impact of emerging primary γ' precipitates and TiN particles onto the oxidation products and kinetics are then of interest. The Albisovlus metallurgical state oxidation behavior is introduced in **section** 3.5. Samples thickness effect on the oxidation kinetics and mechanisms is investigated in **section** 3.7. The long-term exposure to high-temperature leading to breakaway or intrinsic chemical failure mechanisms is finally addressed in **section** 3.8.

3.1 Introduction

This chapter aims at quantifying the high-temperature exposure impact on the surface, subsurface, and bulk evolutions of René 65. The objectives are not an extensive study of oxidation of René 65, but revealing where the oxidation takes place and its consequences onto the surface and subsurface microstructure. The motivation behind this chapter is the fine quantification of such microstructural evolutions to further explain any mechanical behavior variation from the aged and pre-oxidized René 65 specimens in the **chapter** 4.

Bulk evolutions due to the high-temperature aging were substantially quantified in the work of Laurence for temperatures 750 °C, 800 °C, 850 °C and 900 °C with heat-treatment durations up to 2000 h in laboratory air [8]. The material in the present study is then to be quantified in terms of microstructure and phases evolutions at temperatures of 650 °C and 700 °C due to the lack of data in the literature (even so minor variations are expected). The temperature 800 °C, despite some data present in the literature, is also quantified. A large range of oxidation duration is performed with emphasis on the mechanically investigated durations of 200 h and 600 h.

This study is interested in the evolution related to the oxidation of René 65, but temperatures lower than 650 °C require over-aging heat-treatment durations not easily achievable in the framework of a thesis. R. Malacarne, in his thesis (12/2021, *SAFRAN Tech - IJL* [104]), focuses more particularly on the very long-term oxidation of the René 65. The diffusion of the chemical entities becomes particularly interesting to study for temperatures from 800 °C, the diffusion of chromium being one decade faster at 800 °C compared to 700 °C.

The temperature 650 °C is investigated only in terms of oxidation kinetics and products. Emphasis is carried out on the temperatures 700 °C and 800 °C as aging and oxidation impact are mechanically investigated in this framework. An additional review at 900 °C and 1000 °C is performed as extreme oxidation conditions.

3.2 Bulk microstructural evolutions (aging)

The high-temperature exposure of René 65 might lead to microstructural evolutions in the volume, far from the oxidation-affected layers. This section aims at quantifying such bulk evolution. It is organized similarly to the As-Received (AR) and AlbiSolvus (AS) states quantification in **section** 2.2: characterization of the grain size distribution and the three populations of γ' precipitates for each Heat-Treatment (HT). The AR results on the corresponding zone (OC) in the same direction (TD) are represented as horizontal lines in the boxplot graphs (colored lines for Q1, median and Q3 values, black line for mean value).

3.2.1 Grain size distribution

The grain size was extracted from EBSD analysis using the same methodology as described in section 2.1.8 and section 2.2.1 for γ'_I partitioning and analysis parameters. The results displayed in figure 3.1 reveal only the longest HT durations investigated: 200 h, 600 h and 1000 h at 650 °C | 288 h, 600 h and 1000 h at 700 °C | 100 h, 200 h and 600 h at 800 °C.

Regardless of the temperature and duration of heat treatment, the results reveal no grain size evolution from the AR state as depicted in figure 3.1. The maximum deviation being less than 1.5 µm with the 300 h at 700 °C mean and median values (mean value of 7.18 µm and 8.32 µm, median value of 6.06 µm and 7.42 µm for respectively AR state and 300 h at 700 °C heat treatment). Such variation may arise from the ratio of FG and MG regions being different for each EBSD map. No particular attention was paid to prioritizing any of the two regions (FG and MG) during the acquisition of the EBSD maps. Figure 3.1 reveals no grain size evolution compared to the AR state on all the temperatures investigated for each longer duration. The study of shorter heat treatment duration is then not relevant.

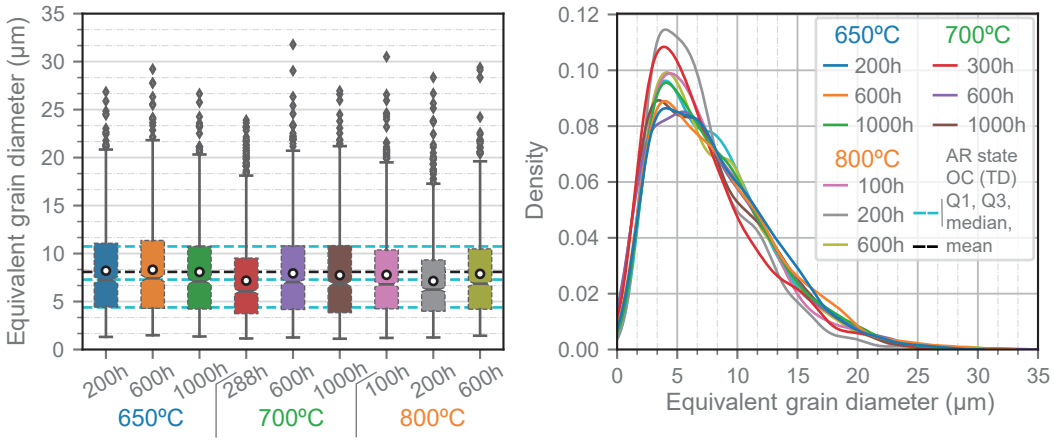

Figure 3.1: Grain size distribution on the 3 longest heat treatment durations for temperatures 650 °C, 700 °C and 800 °C. Boxplot representation on the left and probability density plot on the right

3.2.2 γ' precipitates size and spatial distribution

Primary γ' precipitates

Primary γ' precipitates statistics were computed using x250 and x500 magnification SEM-SE micrographs after chemical etching using aqua regia. The primary γ' precipitates were identified via deep learning techniques on one or two micrographs per condition (each micrograph is about to 2000 γ'_I precipitates). The AR primary γ' precipitates statistics on the equivalent region (OC, TD direction) are represented via red lines (Q1, median, and Q3) and black line (mean) for the overall micrograph (FG and MG regions mixed).

No to minors evolution in primary γ' precipitates equivalent diameter was observed, as depicted in figure 3.2. The HT duration of 10 h and 30 h at 650 °C was computed on x500 micrographs being focused on the FG region. The overall boxplot is then centered on the FG region leading to a decrease down to 1 µm in equivalent diameter. The FG and MG emphasis is, however, in agreement with the AR state, and so are the longer HT duration statistics.

It is worth noting that no evolution of γ'_I precipitates size was accompanied by no evolution of the grain size for the temperature-time window investigated in the present work.

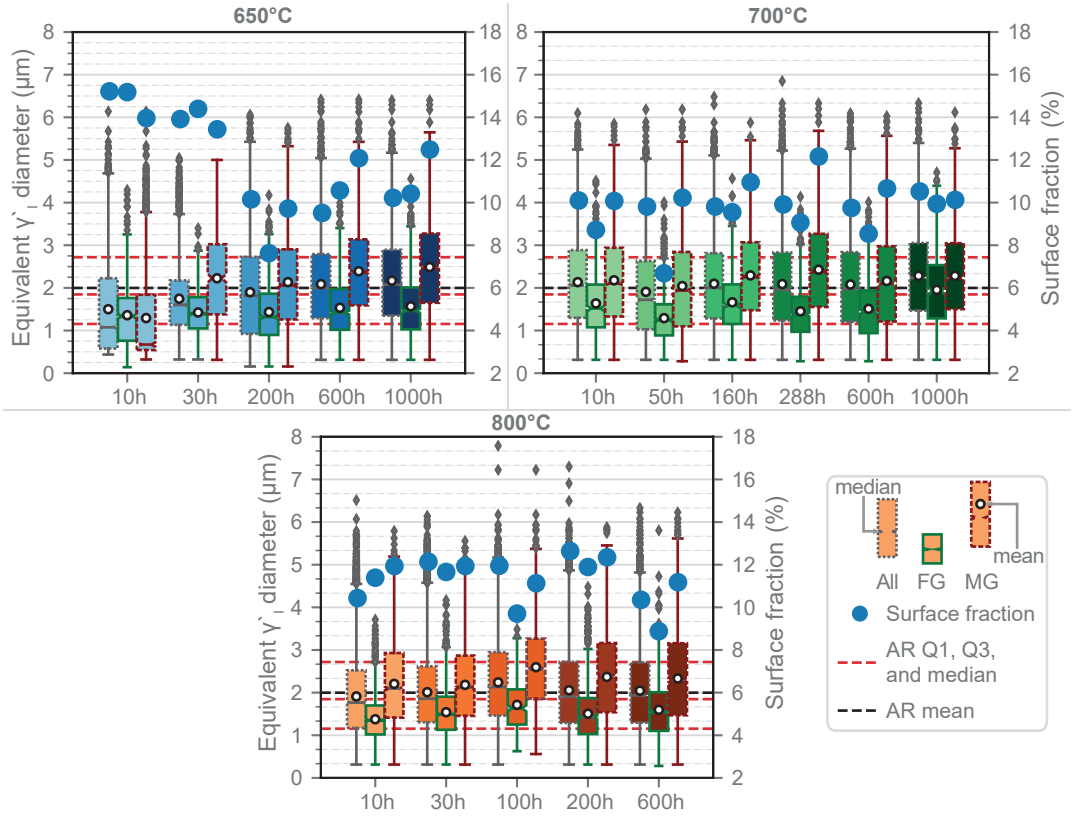

Figure 3.2: primary γ' precipitates equivalent diameter and area fraction for all HT durations and temperatures (650 °C, 700 °C and 800 °C)

Secondary γ' precipitates γ'_{II}

γ'_{II} equivalent diameter was computed from x20 000 and x50 000 magnification SEM-SE micrographs with at least two micrographs per region (FG and MG) for each condition. The size transition between γ'_{II} and γ'_{III} precipitates was estimated at 25 nm based on the bimodal distribution. The results in secondary γ' precipitates' equivalent diameter and area fraction for the temperatures 650 °C, 700 °C and 800 °C on all heat treatment duration are presented in figure 3.3.

The statistics in area fraction of γ'_{II} precipitates are highly dependent on the location of the SEM micrograph due to the lack of secondary precipitates along grain boundaries and in the primary γ' precipitates vicinity.

At 650 °C, the behavior of the secondary precipitates γ'_{II} on all duration experienced a 10 nm decrease in equivalent diameter ($\Delta\phi = -10\ nm$) compared the AR state for both FG and MG regions. The area fraction of secondary precipitates is also impaired with up to 13 % decrease. A reduction in equivalent diameter from 62 nm to 50 nm with an average of 4000 precipitates per micrograph induces a area fraction evolution from 35 % to 22.8 %. The reduction in equivalent diameter is then mainly responsible for the area fraction drop observed. The exposure to 650 °C, even at the onset of heat treatment duration of 10 h, leads to shrinkage of the secondary precipitates. γ'-gene elements are then released into the matrix or into primary γ' precipitates without noticeable evolution of their size. No evolution is to be observed between all heat treatment duration from 10 h to 1000 h at 650 °C. Such secondary precipitates evolution since the onset of HT but stable on all longer durations might be caused by incomplete solutionizing HT of René 65 in the AR state. Exposure to high-temperature induces then the material homogenization.

Microstructural evolutions at 700 °C reveals to be similar to the one at 650 °C for all heat treatment durations. René 65 exhibits a secondary precipitates average equivalent diameter of 51.3 nm with a area fraction of 25 %. The variation in size also agrees with the variation observed in area fraction.

René 65 exposed at 800 °C exhibits coarsening of the secondary precipitates from 100 h of heat treatment. Such coarsening follows the Lifshitz-Slyozov-Wagner (LSW) relationship defined in equation 1.2, as demonstrated by Laurence and Wessman for René 65 [15, 34]. The rate constant computed from figure 3.3 is 63 $nm^3\,h^{-1}$. It is in good agreement with Laurence's observations with a rate constant value of 67 $nm^3\,h^{-1}$. The decrease in the area fraction of the 600 h HT duration accompanied by the increase in size of secondary γ' precipitates are signs of smaller precipitates dissolution supplying larger precipitates for coalescing. The evolutions of secondary precipitates should be reminded in the mechanical behavior analysis (chapter 4).

γ'_{II} precipitates are slightly smaller for HT of 10 h regardless of the temperature compared to the AR state. Then the precipitates size evolution depends on the temperature/time window.

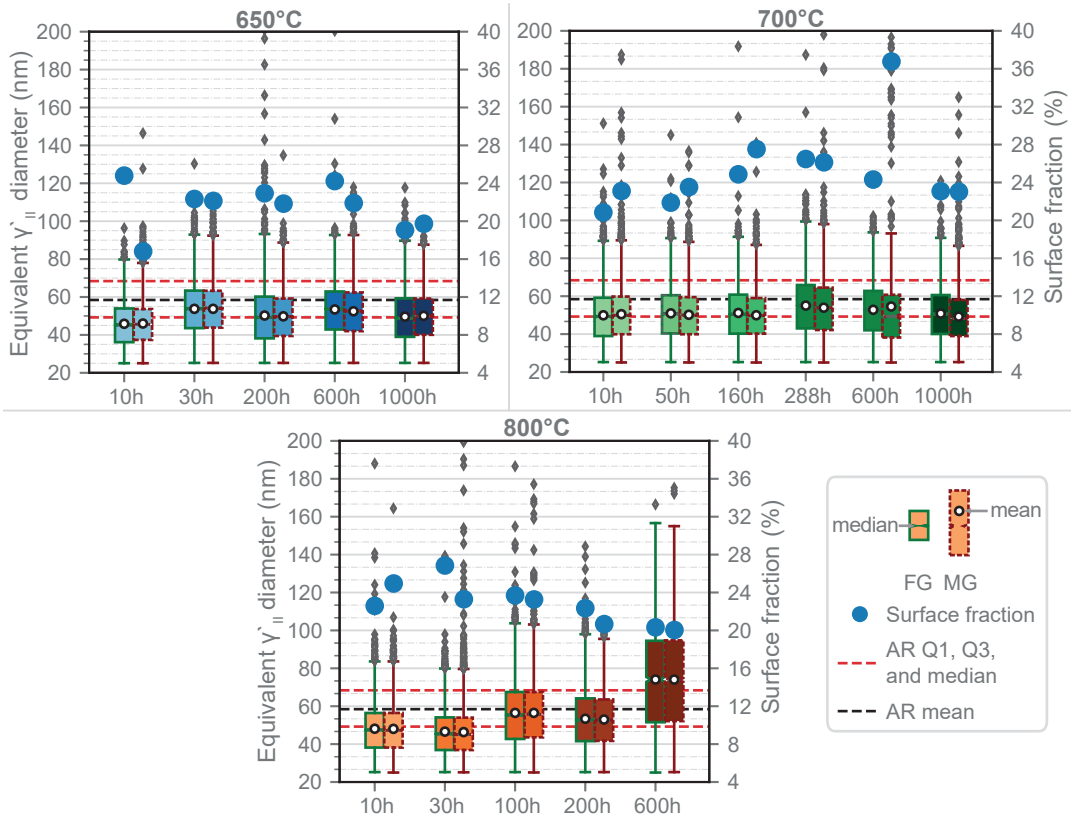

Figure 3.3: Secondary γ' precipitates equivalent diameter and area fraction on all HT duration for temperatures 650 °C, 700 °C and 800 °C

Tertiary γ' precipitates γ'_{III}

γ'_{III} were identified on x50 000 SEM-SE micrographs with emphasis on the location of the micrograph. Tertiary γ' precipitates are located preferably along grain boundaries and in the primary γ' precipitates neighboring (*i.e.* where secondary precipitates are less or not present).

The statistics in area fraction and equivalent diameter for γ'_{III} precipitates are then dependent on the location of the SEM micrographs. For reliable statistical analysis, at least 1000 microstructural features are required, which would represent 10 micrographs per region on each condition. The statistics in γ'_{III} precipitates' equivalent diameter are still given in figure 3.5 but the results are established on a 200 precipitates to 300 precipitates analysis.

The resolution of SEM-SE micrographs at this magnification is of 3 nm/px, a confidence margin for tertiary precipitates detection of 1 px onto the radius gives a measurement deviation of ±6 nm onto the diameter. Such uncertainty on particles being up to 25 nm in equivalent diameter set a relative error of up to 24 %. The statistics in tertiary precipitates are then to be considered semi-quantitative. The SEM-SE micrographs of figure 3.4 and figure 3.6 are presented to graphically evaluate the tertiary precipitates evolution close to the primary γ' precipitate. Identification and classification from γ'_{II} to γ'_{III} (red diamond for γ'_{III}) are also given.

700 °C heat treatment impacts the area fraction of tertiary precipitates as depicted in micrographs 3.4. γ'_{III} precipitates area fraction decreases from 1.7 % after 10 h of HT to 0.6 % for 1000 h HT duration. Such drop is supported by the SEM-SE observations in figure 3.4 with fewer tertiary precipitates surrounding a primary γ' precipitate while the increase in HT duration.

Aging at 800 °C affects the γ'_{III} precipitates as early as 10 h of heat treatment with 44 % fewer precipitates than the AR state. γ'_{III} precipitates area fraction decreases from 1 % after 10 h HT duration to 0.3 % for 600 h HT duration. A very low area fraction can be observed for HT durations above 100 h, with γ'_{III} free regions in figure 3.6 after 600 h at 800 °C.

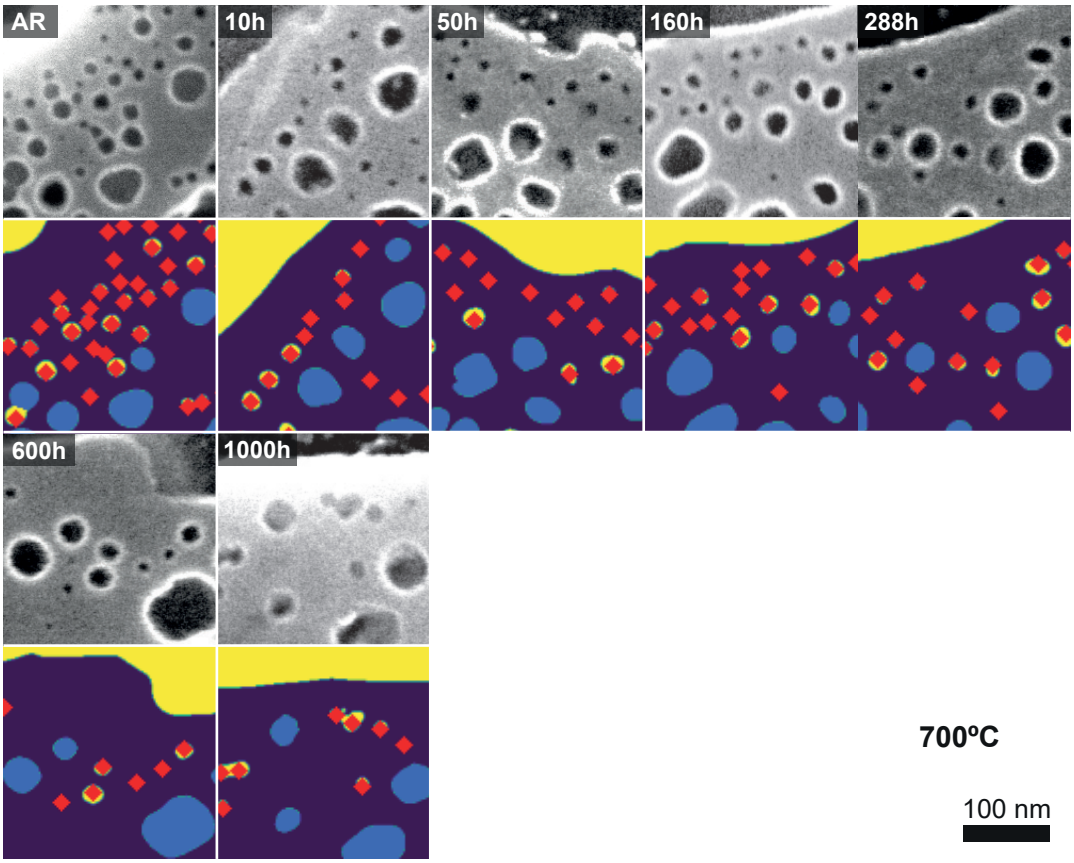

Figure 3.4: SEM-SE micrographs in the vicinity of primary γ' precipitate to emphasize tertiary precipitates for temperature 700 °C for all HT durations. Corresponding image analysis mask, with identification of tertiary precipitates via red diamonds

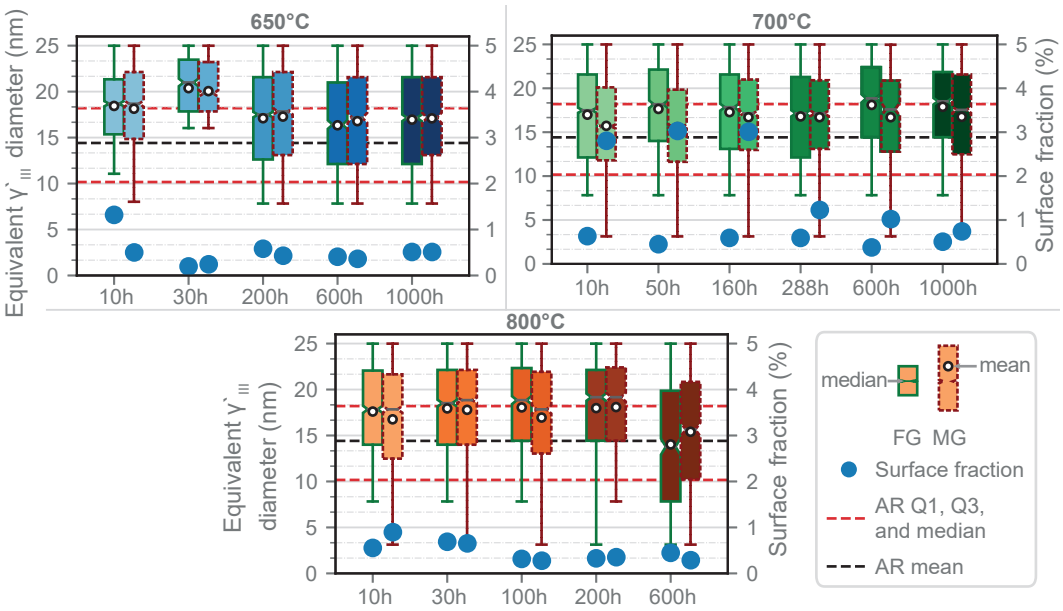

Figure 3.5: Tertiary precipitates γ'_{III} equivalent diameter and area fraction on all HT durations for temperatures 650 °C, 700 °C and 800 °C

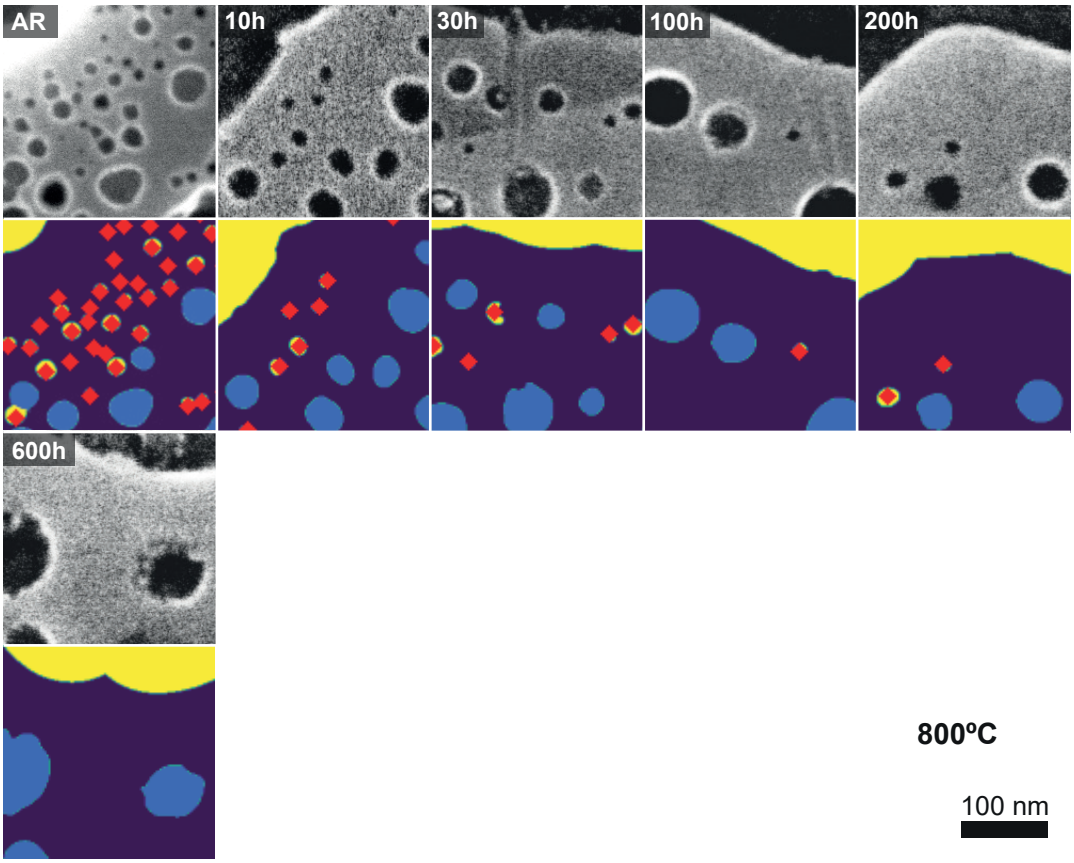

Figure 3.6: SEM-SE micrographs in the vicinity of primary γ' precipitate to emphasize tertiary precipitates for temperature 800 °C for all HT durations. Corresponding image analysis mask, with identification of tertiary precipitates via red diamonds

		650C				700C						800C			
		10h	30h	200h	600h	1000h	10h	50h	160h	288h	600h	1000h	10h	30h	100h	200h	600h
γ`I precipitates	Mean (µm)																
	All	1.5	1.7	1.9	2.1	2.2	2.1	1.9	2.1	2.1	2.1	2.3	1.9	2.0	2.2	2.1	2.0
	FG	1.4	1.4	1.4	1.5	1.6	1.6	1.3	1.7	1.5	1.5	2.0	1.4	1.5	1.7	1.5	1.6
	MG	1.3	2.2	2.1	2.4	2.5	2.2	2.0	2.3	2.4	2.2	2.3	2.2	2.2	2.6	2.4	2.3
	Max (µm)																
	All	6.1	5.0	6.1	6.4	12.1	8.7	6.2	6.5	6.8	6.1	6.3	6.5	6.1	7.8	10.9	10.5
	FG	4.3	3.4	4.2	4.0	4.6	4.5	4.0	4.6	4.1	4.0	4.7	4.7	4.2	3.7	4.5	5.8
	MG	6.1	5.0	5.8	6.4	6.4	5.9	6.2	5.9	6.3	6.0	6.1	5.8	5.6	7.2	5.9	6.2
	Fraction (%)																
	All	15.2	13.9	10.2	9.5	10.2	10.1	9.8	9.8	9.9	9.8	10.5	10.4	12.1	12.0	12.6	10.4
	FG	15.2	14.4	7.6	10.6	10.4	8.7	6.7	9.5	9.1	8.5	9.9	11.4	11.7	9.7	11.9	8.9
	MG	14.0	13.4	9.7	12.1	12.5	10.1	10.2	11.0	12.2	10.7	10.1	11.9	11.9	11.1	12.3	11.2
γ`II precipitates	Mean (nm)																
	FG	45.7	53.8	49.9	53.2	49.6	49.6	50.9	50.9	54.8	52.8	50.8	48.1	46.2	55.8	53.3	74.0
	MG	46.0	53.8	49.8	52.5	50.1	50.3	50.2	49.9	53.8	52.5	49.1	47.9	46.2	56.1	52.9	74.1
	Max (nm)																
	FG	96.3	130.3	196.4	154.0	117.7	151.2	145.1	191.8	187.4	102.3	120.9	188.0	139.2	186.6	144.3	166.5
	MG	146.4	105.4	134.8	117.9	96.7	187.5	136.6	140.9	198.0	196.6	164.9	164.4	199.4	177.1	103.9	175.3
	Fraction (%)																
	FG	24.8	22.3	22.9	24.2	19.1	20.8	21.9	24.9	26.5	24.3	23.1	22.6	26.8	23.7	22.3	20.3
	MG	16.8	22.1	21.9	21.9	19.7	23.1	23.5	27.5	26.1	36.8	23.0	24.9	23.3	23.3	20.7	20.0
γ`III precipitates	Mean (nm)																
	FG	18.4	20.4	17.1	16.3	17.0	17.0	17.6	17.3	16.8	18.1	17.9	17.6	17.9	18.1	18.0	14.0
	MG	18.1	20.1	17.3	16.8	17.1	15.7	15.6	16.7	16.7	16.7	16.7	16.8	17.8	17.0	18.1	15.4
	Max (nm)																
	FG	25.0	25.0	25.0	25.0	25.0	25.0	25.0	25.0	25.0	25.0	25.0	25.0	25.0	25.0	25.0	25.0
	MG	25.0	25.0	25.0	25.0	25.0	25.0	25.0	25.0	25.0	25.0	25.0	25.0	25.0	25.0	25.0	25.0
	Fraction (%)																
	FG	1.3	0.2	0.6	0.4	0.5	0.6	0.4	0.6	0.6	0.4	0.5	0.6	0.7	0.3	0.3	0.4
	MG	0.5	0.2	0.4	0.4	0.5	2.8	3.0	3.0	1.2	1.0	0.7	0.9	0.7	0.3	0.4	0.3

Table 3.1: Statistics summary of γ′ precipitates on aged states at temperatures 650 °C, 700 °C and 800 °C

Analysis

The following conclusions were evidenced from the study of the aged thin microtensile specimens:

- No grain size evolution is observed on all the temperatures investigated (650 °C, 700 °C and 800 °C) up to the maximal HT durations of 1000 h, 1000 h and 600 h, respectively.
- No evolution of the primary γ' precipitate γ'_I equivalent diameter and area fraction for all HT conditions. The consistency in γ'_I precipitates, known for the pinning of grain boundaries, is related to the invariability in grain size.
- The secondary precipitates γ'_{II} demonstrate 10 nm reduction in equivalent diameter from the very beginning of the HT on all temperatures (650 °C, 700 °C and 800 °C). Such a decrease in equivalent diameter results in the corresponding decrease in the area fraction. The secondary precipitates demonstrate a stable size and area fraction for temperatures of 650 °C and 700 °C up to 1000 h of HT. The 800 °C HT reveals an increase of the secondary precipitates' size with the HT duration on the order of 63 $nm^3\,h^{-1}$ according to the LSW law. Such increase is particularly visible on the 600 h HT, coupled with a decrease in the area fraction, signs of smaller secondary precipitates dissolution.
- The tertiary precipitates γ'_{III} detection is suffering a lack of SEM micrographs resolution but still demonstrates the constant size and area fraction for the temperatures of 650 °C and 700 °C up to 1000 h of HT, but with an increase in size from the AR state. The SEM-BSE micrographs reveal larger evolution with a decrease in area fraction close to primary γ' precipitates. The 800 °C demonstrates similar behavior on low HT durations but decreases in size and volume fraction with HT duration. The SEM-BSE micrographs expose the complete dissolution of the tertiary precipitates close to the primary ones.

The constant grain size and consequently primary γ' precipitates size observed from the aging HT up to the most critical condition of 800 °C-600 h are in agreement with Laurence's observations in René 65 [8]. Laurence observed that the granular skeleton of Rene 65 is preserved during thermal aging, whatever the duration applied (up to 2000 h at 900 °C). Such conclusions were also supported by Charpagne on low HT durations in René 65 [22].

The secondary γ' precipitates' evolutions were modeled via an LSW law with similar results in terms of growth rate compared to the observations and computation of Laurence and Wessman on René 65 [8, 34].

3.3 Oxidation products and kinetics

The following section aims at characterizing the oxidation products and microstructural evolutions developed on the surface and sub-surface of René 65. The two temperatures investigated in this section are 700 °C and 800 °C, corresponding to the tensile and fatigue specimens oxidation temperatures with emphasis for both temperatures on the oxidation duration of 200 h and 600 h.

3.3.1 Oxidation products on mechanically investigated oxidation conditions

External surface oxidation products

SEM-EDS analyses reveal a high concentration of Ti above primary γ' precipitates and along grain boundaries; whereas the intragranular surface exhibits a high concentration of Cr, as depicted in figure 3.7 an exposure of 200 h at 700 °C in air. XRD analysis allows identification of TiO_2 rutile and Cr_2O_3 topping the René 65 after oxidation at 700 °C and 800 °C for both oxidation durations of 200 h and 600 h, as given in the diffractograms in figure 3.8.

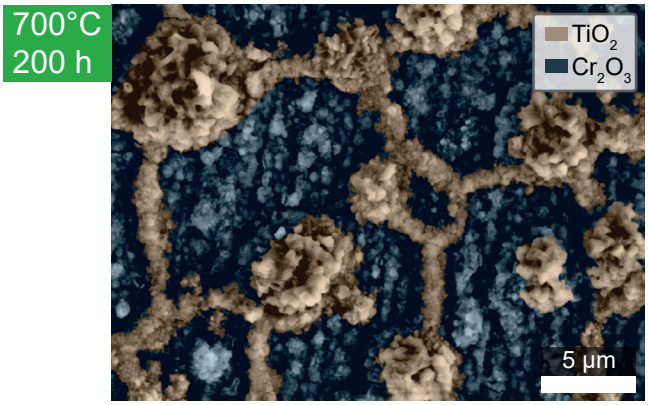

Figure 3.7: SEM-SE micrograph of René 65 at the surface after oxidation at 700 °C during 200 h with EDS analyses of Ti and Cr elements as overlay. Identification of the oxides in presence of both SEM-EDS and XRD analysis

The increase in oxidation time and temperature results in TiO_2 rutile and Cr_2O_3 diffraction peaks rise as exposed in the diffractograms in figure 3.8. The volume, and so the thickness of diffractive matter is almost constant (depending on the density of the scales). An increase in oxide scale thickness results in an increase of the oxide scale versus bulk matter ratio and so diffraction of the oxide planes being more intense. Such phenomena are even more accentuated in the case of XRD curves being normalized (each pattern is divided by its most intense diffraction peak).

Similar oxidation products are reported via XRD and EDS analyses for the oxidation conditions at 700 °C and 800 °C during 200 h and 600 h of exposure. The increase in oxidation duration and/or temperature mainly induce growth of the chromia layer compared to the titania islets.

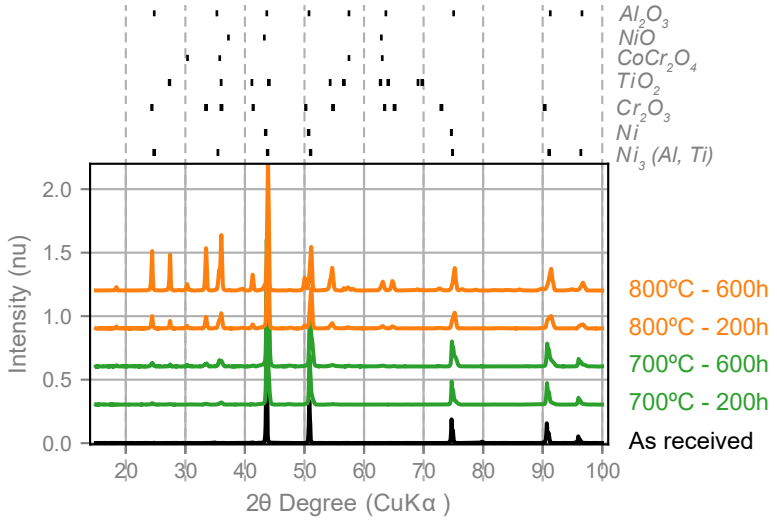

Figure 3.8: XRD diffractogram of René 65 in the AR state and oxidized at 700 °C and 800 °C during 200 h and 600 h. Equivalent structure identified for each predominant intensity peak

External oxidation impact on sub-surface integrity

Surface reactivity with the environment induces formation of an outer oxide layer composed of TiO_2 and Cr_2O_3, as described in section 3.3.1. The formation of an external oxide layer drives the surface and sub-surface modifications due to the selective element consumption required to feed the growth of the external oxide scale. The external Cr_2O_3 formation then leads to a sub-surface-depleted Cr-layer. Such depletion in chromium was quantified on SEM-EDS line profiles given in figure 3.9 for each oxidation condition.

The chromium concentration (given in $\%_{wt}$) is microstructure dependent due to the low concentration of chromium in primary γ' precipitates compared to the two-phase matrix (as detailed in table 1.1). Figure 3.9 exposes the maximal value for 7 to 10 line profiles recorded with a distance going from 5 µm to 10 µm from each other with 1 µm to 2 µm discretization step in depth between each spectrum point on a line. The maximal value is of interest due to the neglecting of Cr concentration drops when crossing primary γ' precipitates from their lower chromium concentration.

Figure 3.9 unveils the depletion profile of chromium after 200 h to 600 h of exposure in air at 800 °C with depletion thicknesses of approximately 10 µm and 15 µm respectively. The depletion thickness was considered as the distance between the metal/oxide interface (estimated via the mean curve) and return to 99 % of the nominal Cr concentration exposed in table 1.1. The depletion profile follows an *erf* function according to Fick's second law of diffusion for a semi-infinite solid given in equation 3.1.

$$\frac{C(x,t) - C_0}{C_s - C_0} = \frac{1}{2}\left[1 - erf\left(x/2\sqrt{Dt}\right)\right] \tag{3.1}$$

with x being the depletion scale thickness of the oxidized element, D its diffusion coefficient in the metal, C its concentration (C_0 the initial concentration, C_s the oxide / metal interface concentration, and $C(x,t)$ the concentration at distance x from the oxide / metal interface at time t), and t the oxidation time.

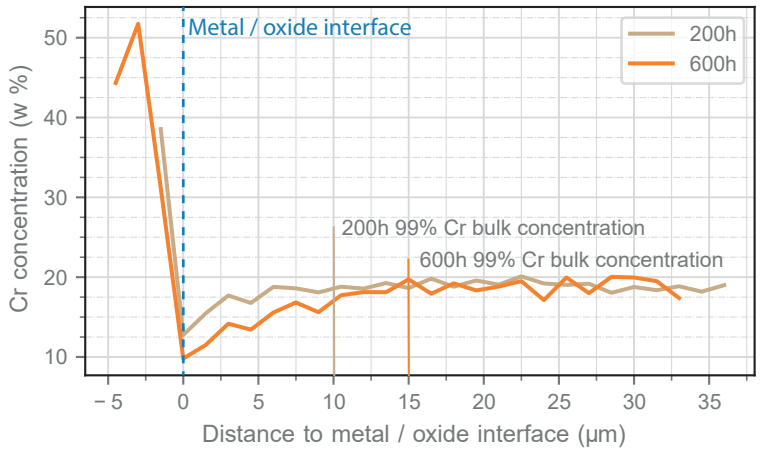

Figure 3.9: SEM-EDS lines profile of the Cr concentration ($\%_{wt}$) beneath the metal / oxide interface after oxidation at 800 °C during 200 h and 600 h

The external oxide thickness was calculated via the mass gain of samples at values of 1.59 µm and 2.75 µm for oxidation duration of 200 h and 600 h at 800 °C, respectively to figure 3.9 oxidation conditions. Cross-sectional observations using SEM micrographs confirmed the calculated oxide thickness, *i.e.* 1.5 ± 0.4 µm and 2.7 ± 0.4 µm for the 200 h and 600 h exposure respectively (exposed later in figure 3.29). The oxide scale is then relatively small compared to the depletion depth in Cr. The oxide/metal recession ξ_m is dependent on the thickness of oxide formed ($\xi_m = \xi / PBR$), and the oxide scale-alloy interface movement is slow compared to alloy diffusion. Such a hypothesis enables diffusion within the alloy to be treated as a semi-infinite case as given in equation 3.2.

$$N_{Cr}^{i} = \frac{N_{Cr}^{0} - \left(\frac{\pi k_c}{D}\right)^{\frac{1}{2}}}{1 - \left(\frac{\pi k_c}{D}\right)^{\frac{1}{2}}} \tag{3.2}$$

with N_{Cr}^{i} the mole fraction of chromium at the metal/oxide interface, N_{Cr}^{0} the initial mole fraction of chromium in the alloy, k_c the corrosion rate constant relative to the metal recession of the alloy.

The oxide scale thickness was estimated using the parabolic rate constant k_w established from mass gain using Wagner's equation 3.3 [70].

$$\xi^2 = \left(\frac{\Omega}{3M_o}\right)^2 \left(\frac{\Delta M}{S}\right)^2 = \left(\frac{\Omega}{3M_o}\right)^2 \cdot k_w t \tag{3.3}$$

with ξ being the depletion depth, b being the stoichiometric coefficient defined in equation 1.4, and Ω the molar volume.

The diffusion coefficient of chromium in the volume was then computed via equation 3.4 using the mole fraction at the metal/oxide interface at oxidation duration t: N_{Cr}^{i} and the initial mole fraction of chromium N_{Cr}^{0} in the alloy.

$$D = \frac{\pi \xi^2}{2tPBR^2} \left(\frac{1 - N_{Cr}^{i}}{N_{Cr}^{0} - N_{Cr}^{i}}\right)^2 \tag{3.4}$$

The diffusion coefficient of Cr in René 65 was then estimated taking into consideration the maximal and minimal values encountered from the 7 to 10 SEM-EDS line profiles on each oxidation condition (800 °C during 200 h and 600 h). Presenting both methodologies intend to give a diffusion window from the experimental SEM-EDS analysis. The results of chromium diffusion coefficient computation are given in table 3.2. The results expose almost 1 decade of diffusion coefficient range. The high deviation observed in the maximal N^i_{Cr} consideration arises from the local presence of primary γ' precipitates crossing the SEM-EDS path.

Oxidation condition	Minimal N^i_{Cr}	Maximal N^i_{Cr}
800 °C - 200 h	4.4 $\%_{at}$	10.7 $\%_{at}$
800 °C - 600 h	6.6 $\%_{at}$	13.7 $\%_{at}$
Cr diffusion coefficient	$1.8 \pm 0.4 \times 10^{-12}$ cm^2 s^{-1}	$9.6 \pm 6.7 \times 10^{-12}$ cm^2 s^{-1}

Table 3.2: Chromium diffusion coefficient computation from minimal and maximal values of chromium concentrations at the oxide/metal interface

The diffusion coefficient of Cr in Ni at 800 °C was found in the literature with values in the range 4.6×10^{-14} cm^2 s^{-1} to 1.07×10^{-13} cm^2 s^{-1} [70, 208–210]. Such difference in the diffusivity order of magnitude might come from a higher diffusivity of Cr at grain boundaries for our fine grain microstructure. The literature values report mainly volume diffusion of chromium into nickel, or with large grain size for experimental measurements, leading to a low fraction of grain boundaries. The effective diffusion presently estimated from the experimental profiles represents the concomitant diffusion of Cr in the volume and at grain boundaries according to $D_{eff} = D_v(1-f) + D_{gb}f$ (D_v being the volume diffusivity, D_{gb} the grain boundary diffusivity, and f the grain boundary fraction). Considering both phase's diffusion results then in a faster diffusion D_{eff} due to $D_{gb} >> D_v$ (10^4 to 10^6).

The external formation of TiO_2 does not induce intragranular titanium depletion but is accompanied by a sub-surface-depleted layer from primary and secondary precipitates. The γ' precipitates participation, and especially the role of γ'_I, to the oxidation processes are to be further detailed in section 3.4. Both chromium and titanium consumption are expected to contribute to the γ' destabilization.

Sub-surface / internal oxidation products

Figure 3.10 presents a SEM-EDS analysis of the sub-surface qualitative chemical entities distribution 2 µm to 3 µm beneath the metal/oxide interface (obtained via wedge polishing using the JIG detailed in section 2.1.3). Aluminum and oxygen are concentrated along grain boundaries but also punctually inside the grains after exposure for 600 h at 800 °C as exposed in figure 3.10. More generally, internal and intergranular oxidation with the formation of alpha alumina Al_2O_3 oxide for all the exposure times is evidenced for all the tests performed at 700 °C and 800 °C for durations of 200 h and 600 h.

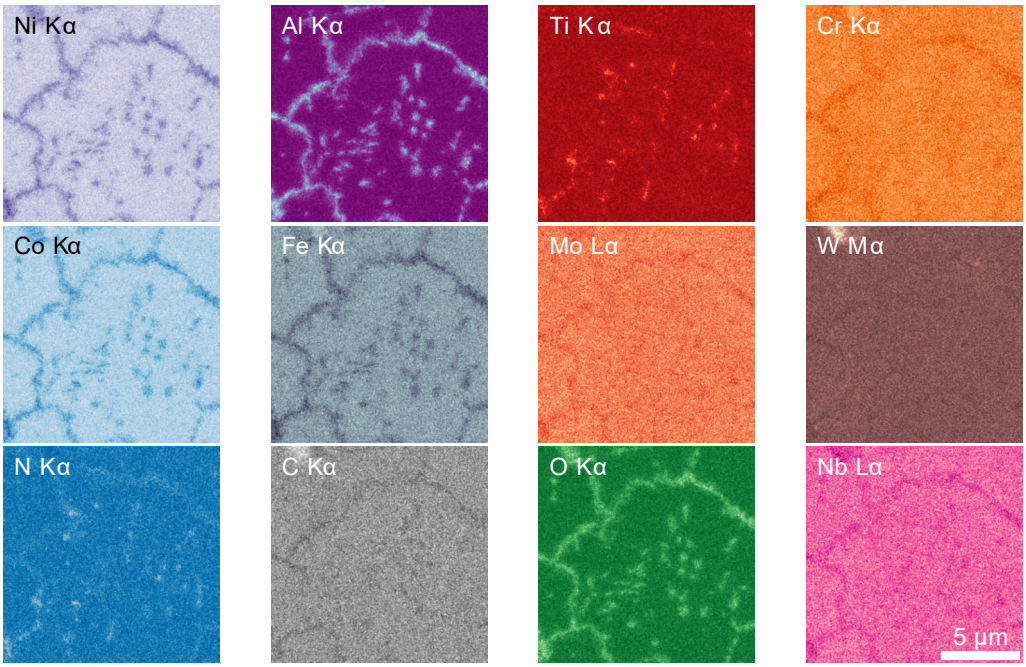

Figure 3.10: SEM-EDS sub-surface analysis from wedge polished sample located 2 µm to 3 µm below the metal / oxide interface of René 65 after oxidation at 800 °C during 600 h

The intergranular and internal oxidation were quantified in terms of depth using wedge polished samples at the surface as illustrated in figure 3.11 and figure 3.12 for 700 °C during 200 h to 600 h respectively and figure 3.13 and figure 3.14 for 800 °C during 200 h to 600 h respectively. The wedge created at the surface of oxidized samples was performed by sticking oxidation coupons using a 50 µm wedge under one edge of the coupon. The grinding angle on the wedged polished samples was measured using a laser scanning CONFOCAL microscopy with Gwyddion as data processing software. The SEM-BSE mapping was performed on x 1500 magnification micrographs (10x12 micrograph stitching). Residual polishing scratches are sadly observed due to the removal of the external chromia layer up to the finishing stages of the grinding sequence and acting as polluting particles.

Figure 3.11 to 3.14 reveal intergranular alumina penetration depths of 2.0 ± 0.5 µm, 3.0 ± 0.5 µm, 6.0 ± 0.5 µm and 7.5 ± 0.5 µm for oxidation conditions of 700 °C during 200 h to 600 h and 800 °C during 200 h to 600 h respectively. The intergranular oxidation front is microstructure dependent with variations from FG to MG regions as depicted in figure 3.13. The FG region, with a smaller grain size, reveals up to 2 µm deeper intergranular oxidation at 800 °C - 200 h due to the higher grain boundary fraction (FG region present between 4 µm and 7 µm deep at the top the micrograph).

	700 °C		800 °C	
	200 h	600 h	200 h	600 h
Intergranular alumina	2.0 ± 0.5 µm	3.0 ± 0.5 µm	6.0 ± 0.5 µm	7.5 ± 0.5 µm
Internal alumina	-	-	3.5 ± 0.5 µm	5.5 ± 0.5 µm

Table 3.3: Internal and intergranular alumina penetration depths

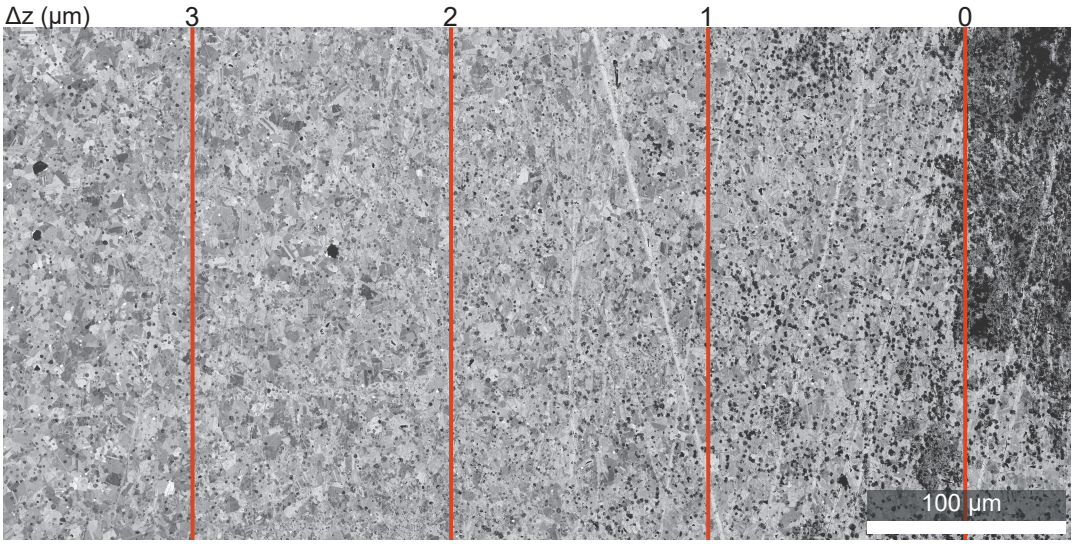

Figure 3.11: SEM-BSE observation of a wedge polished oxidation coupon to reveal the sub-surface oxidation impact at 700 °C during 200 h

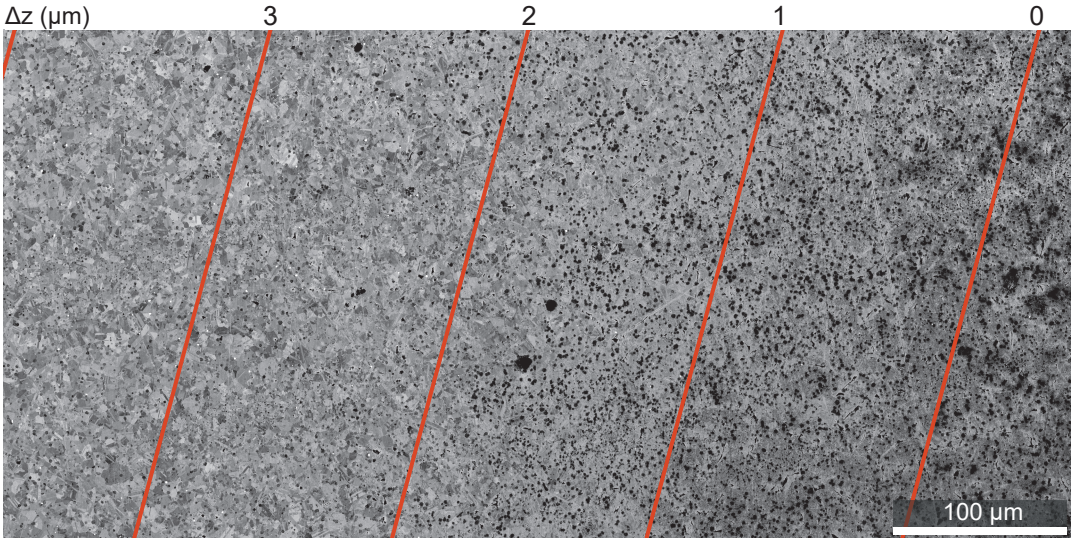

Figure 3.12: SEM-BSE observation of a wedge polished oxidation coupon to reveal the sub-surface oxidation impact at 700 °C during 600 h

Internal oxidation at 700 °C is concentrated inside and at the neighborhood of primary γ' precipitates. Involvement of the primary γ' precipitates in the oxidation phenomena is to be developed in section 3.4.

Internal oxidation penetration is also evidenced after oxidation at 800 °C in figures 3.13 and 3.14 with depths of 3.5 ± 0.5 µm and 5.5 ± 0.5 µm for oxidation durations of 200 h to 600 h respectively. The penetration depth of the internal oxidation is inferior to the intergranular oxidation on the two investigated duration. The supply of oxygen via diffusion phenomena is mainly caused by grain boundaries (due to the higher diffusion coefficient at least a decade faster than in the volume). The faster movement of oxygen in grain boundaries then leads to a deeper presence of oxygen close to grain boundaries than in the volume and so to deeper alumina formation.

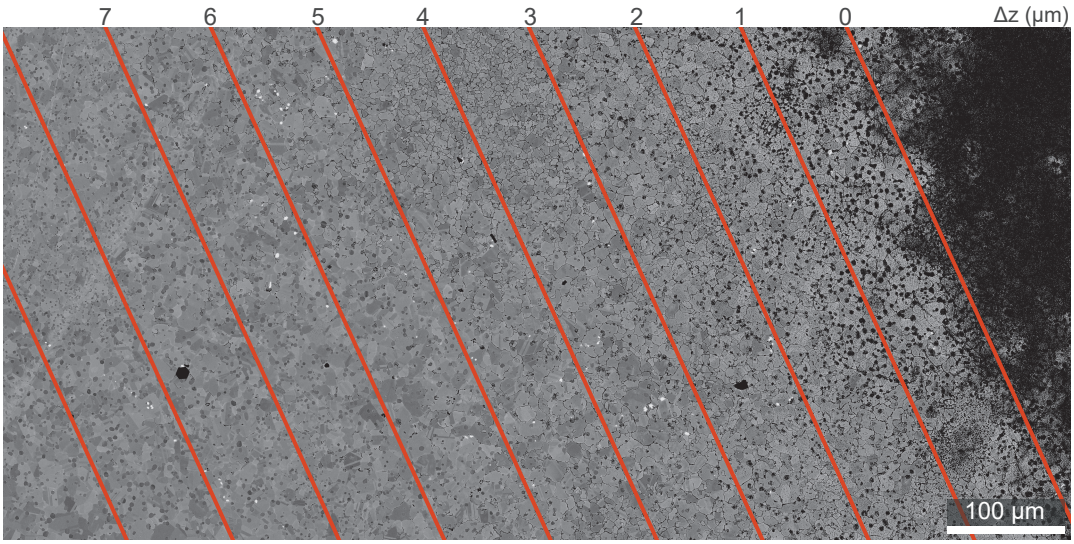

Figure 3.13: SEM-BSE observation of a wedge polished oxidation coupon to reveal the sub-surface oxidation impact at 800 °C during 200 h

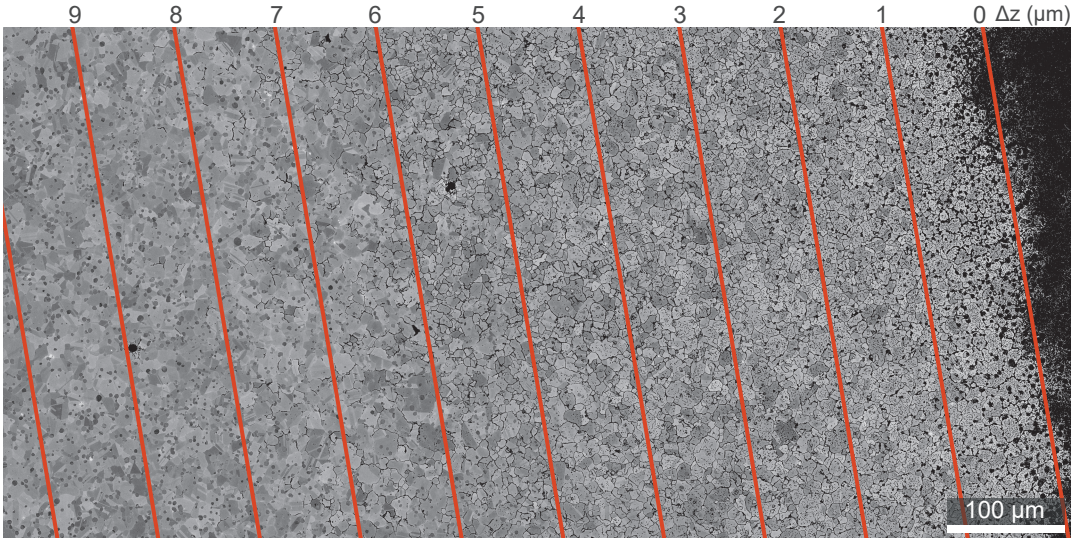

Figure 3.14: SEM-BSE observation of a wedge polished oxidation coupon to reveal the sub-surface oxidation impact at 800 °C during 600 h

3.3.2 Oxidation investigation at 700 °C and 800 °C

Microstructural evolutions due to oxidation at 700 °C for all durations are reported in figure 3.15a. The low surface reactivity is revealed with the formation of a sub-micrometric to micro-metric upper chromia and/or titania layer for oxidation durations up to 1000 h. Titania is usually located above the chromia layer in the presence of emerging primary γ' precipitate at the surface even for low oxidation durations (present after 10 h). Titania forms in the early stages of oxidation and is still growing in the chromia parabolic oxidation regime.

At 800 °C, figure 3.15b exposes a thicker and dense chromia layer topping the surface of the samples. The presence of primary γ' precipitates at the surface results in a relatively thicker and local oxide layer of titania for the two lower oxidation duration (10 h and 30 h). discontinuities in the oxide thickness are then visible for the early stages of oxidation. The chromia layer yet reveals a continuous thickness with the increase of the oxidation duration. All oxidation durations reveal similar intergranular alumina, with depth increasing with oxidation duration.

The maximal intergranular alumina penetration depth was reported at values of 6 µm and 8 µm on the 200 h and 600 h exposure at 800 °C from the SEM-BSE micrographs presented in figure 3.15b. Such results demonstrate similar results from the wedged samples. The wedged samples allow statistical representation of the underlying microstructure.

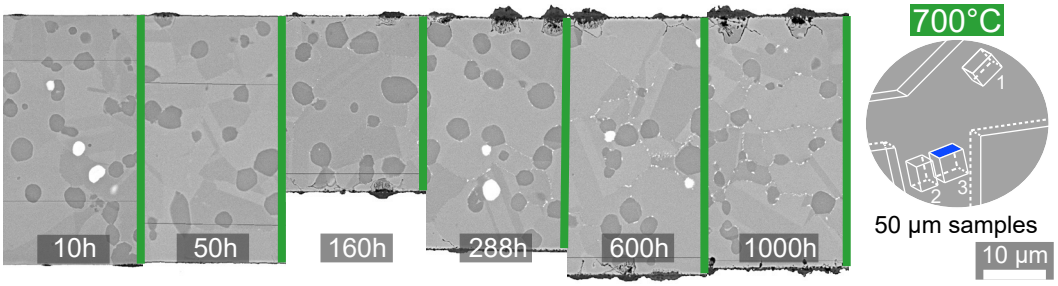

(a) SEM-BSE micrographs of 50 µm-thick samples oxidized during 10 h, 50 h, 160 h, 288 h, 600 h and 1000 h at 700 °C

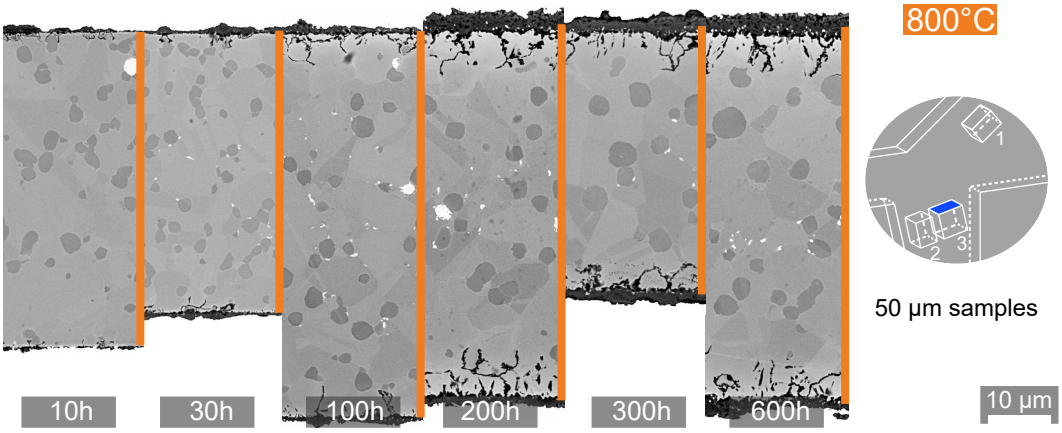

(b) SEM-BSE micrographs of 50 µm-thick samples oxidized during 10 h, 30 h, 100 h, 200 h, 300 h and 600 h at 800 °C

Figure 3.15: SEM-BSE cross-sectional observations. The green (700 °C) and orange (800 °C) lines represent the initial thickness of the samples, prior to oxidation

Oxidation kinetics: mass gain evolution

The mass changes recorded for samples of thickness 500 µm for all oxidation duration investigated in the temperature range of 650 °C to 1000 °C are reported in figure 3.16. The mass gain kinetic was modeled via a parabolic law as given in dashed lines in figure 3.16. The oxidation behavior follows then a parabolic law in agreement with Wagner's theory (see equation 1.6) [77, 78]. The measurement incertitude is approximately 2 % to 3 % for all oxidation tests. The parabolic rate constant values are summarized in table 3.4. The low reactivity for the 650 °C temperature exposes the oxidation transient regime impact. Simple approximation via eq. 1.6 does not take into account the transient oxidation mass gain as revealed by the high mass gain values for short-term oxidation duration compared to the parabolic modeling.

Temperature	650 °C	700 °C	800 °C	900 °C	1000 °C
Parabolic rate constant ($mg^2\,cm^{-4}\,s^{-1}$)	1.98×10^{-10}	2.11×10^{-9}	1.50×10^{-7}	2.17×10^{-6}	1.67×10^{-5}
R^2 ((%)	88.9	98.1	99.1	99.8	98.6

Table 3.4: Parabolic rate constant of René 65 from mass gain evolution on all investigated temperatures

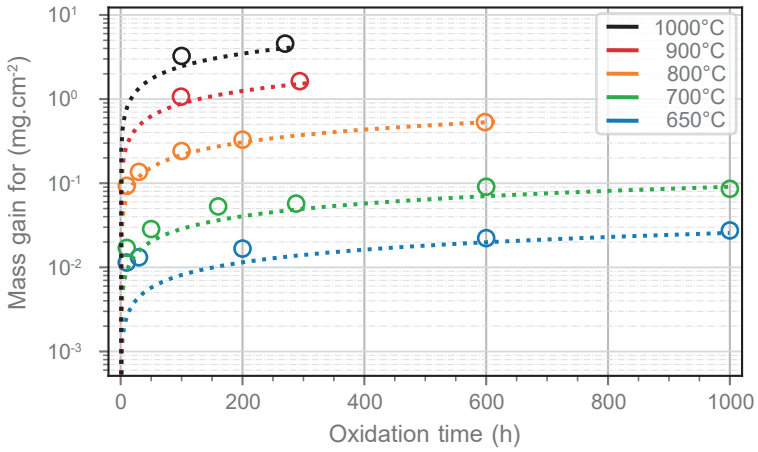

Figure 3.16: Mass grain ($mg\,cm^{-2}$) versus time (h) at temperatures of 650 °C, 700 °C, 800 °C, 900 °C and 1000 °C for 500 µm-thick samples. Circles represent experimental values, lines are parabolic law fitted to the experimental data according to $(\Delta m/S)^2 = kp \cdot t$

Oxidation kinetics: contribution of the oxides layers

The contribution of the external chromia layer and the intergranular alumina onto the mass gain was estimated via segmentation of the oxides in cross-sectional SEM-BSE micrographs for different oxidation conditions at 800 °C (due to the ease of oxide scale identification resulting from sufficient thickness developed compared to lower temperatures). The equivalent thickness for each oxide scale was estimated via the total area of oxide present in the SEM micrograph to an equivalent homogeneous oxide layer (rectangle of an area being equal to the total area of oxide identified, as depicted in

figure 3.17). Such methodology is inspired by the work of Sanviemvongsak and then Malacarne [104, 211]. The mass gain was then estimated via equation 3.5.

$$\frac{\Delta m}{S} = \xi \frac{3M_O}{\Omega} \tag{3.5}$$

with $\frac{\Delta m}{S}$ the mass gain over the surface in contact with the environment(wet surface), ξ the oxide scale thickness, y the stoichiometric balance of the oxidation reaction, Ω the molar volume of the oxide.

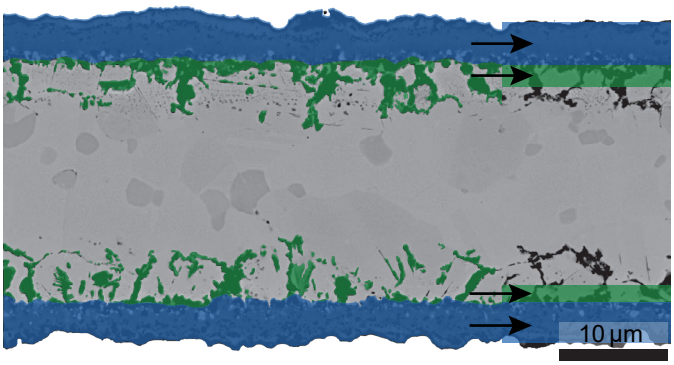

Figure 3.17: Sample of initial thickness 20 µm oxidized at 800 °C during 600 h. Equivalent oxide scale thickness of alumina and chromia estimated from equal area

The results in measured versus estimated via oxide thickness ξ mass gain at 800 °C are presented in figure 3.18. The cumulative mass gain from alumina (purple line) and chromia (brown line) is compared to the experimentally measured mass gain (black line). The contribution of alumina to the total mass gain cannot be ignored as the average participation is about of $30 \pm 4\,\%_{wt}$ on the mass gain and 25 % on the parabolic rate constant from all oxidation duration. Such results are in agreement with the work of Malacarne on René 65 and AD730^{TM} [104].

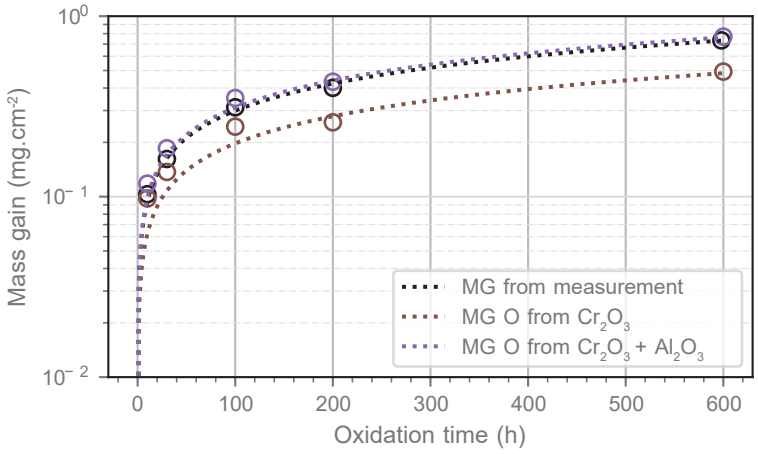

Figure 3.18: Mass gain from experimental measurement (black) versus oxygen contribution from alumina (purple) and chromia (brown) formation on a 500 µm-thick sample

Oxidation kinetics: activation energy

The Arrhenius plot of René 65 (according to equation 3.6) compared to similar alloys and pure oxide kinetics is presented in Fig. 3.19. The total mass gain (alumina + chromia) is taken into account. This graph highlights the predominant role of the chromia reaction in the oxidation product. René 65 oxidation kinetics complied with pure chromia formation kinetics as revealed by Shida's observations [88].

$$k_P = k_0 \cdot \exp^{\left(\frac{-Q}{R \cdot T}\right)} \tag{3.6}$$

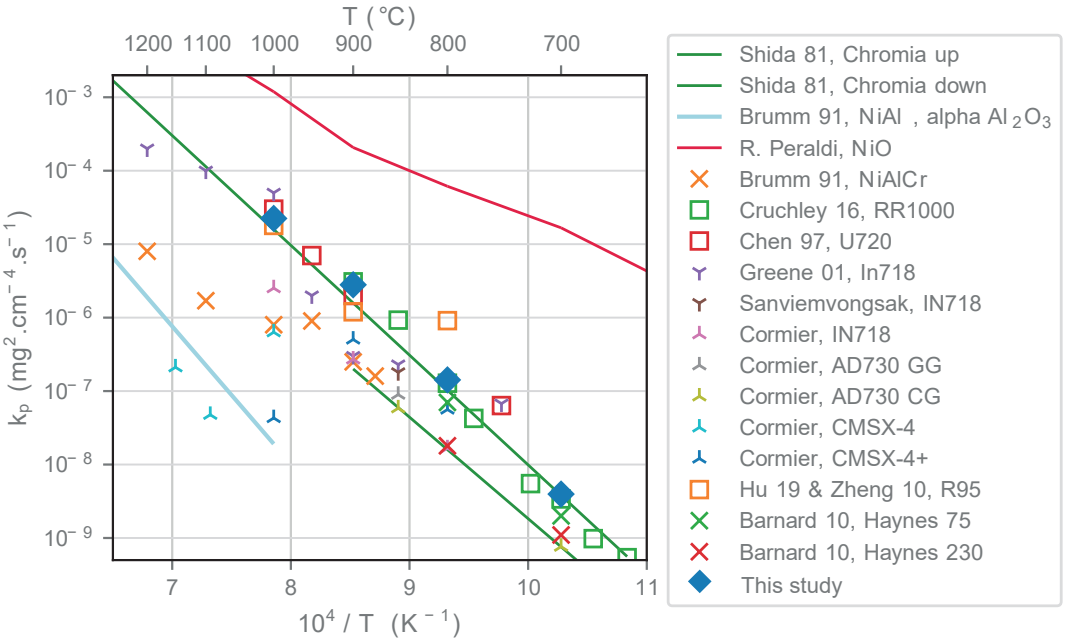

Figure 3.19: Arrhenius diagram comparing René 65 to analog metals and pure oxides. k_p computation from $\left(\frac{\Delta m}{S}\right)^2 = k_p \cdot t$ [79, 81–88, 211]

Analysis

The outlines from the oxidation products and kinetics of René 65 are the followings:

- René 65 develops a continuous adherent external chromia layer on all the mechanically investigated oxidation conditions (700 °C and 800 °C - 200 h and 600 h). A volume depletion of chromium is observed on the sub-surface grains to supply the chromia reaction. Rutile TiO_2 develops above the chromia layer, topping the emerging primary γ' precipitates and the grain boundaries.
- sub-surface oxidation demonstrates internal and intergranular oxidation with alumina formation.
- Materials oxidized at 800 °C exhibit a homogeneous and continuous external chromia layer.
- The oxidation kinetics follow a parabolic law in the temperature range of 700 °C to 1000 °C. The transient regime in the 650 °C oxidation HT demonstrates similar initial mass gain from the 700 °C but rapidly a parabolic law of rate constant two decades slower than of the 700 °C one.
- The mass gain is due to the formation of both the chromia layer and of the intergranular alumina with a contribution in the total mass of 70 % and 30 %, respectively. The chromia layer includes both chromia and titania formation. The internal alumina was not revealed in the SEM cross-sectional micrographs due to the grinding sequence. Its contribution to the total mass gain was then not evaluated.
- René 65 oxidation activation energy reveals values similar to pure chromia.

René 65 demonstrates oxidation products similar to concurrent alloys, as reported by Cruchley on RR1000 [212], Thebaud, Govaere, and Mrozowski on AD730^{TM} [9, 41, 213], Malacarne on René 65 and AD730^{TM} [101, 104]. Such alloys are designed to form chromium as a major protective external oxide. The presence of the external chromia layer supported by the overall activation energy of the oxidation process close to pure chromia agrees with the definition of René 65 being a chromia-forming alloy.

The contribution of the alumina to the total mass gain was also observed by Malacarne on both René 65 and AD730^{TM} with similar proportions [104]. Such proportions demonstrate a lower contribution (5 % and 15 %) of the intergranular alumina formation onto the total mass gain of samples compared to previous studies (Cruchley on RR1000, Chen on Udimet 720, Gabb and Sudbrack on other alloy classes [73, 83, 214, 215]).

3.4 Contribution of the γ′ precipitates onto oxidation

γ′ precipitates populations are mainly composed of aluminum, titanium, and nickel as given in table 1.1. Primary γ′ precipitates emerging at the surface react differently than the matrix to the contact of oxygen at elevated temperatures. The concentration and so the activity of aluminum and titanium, especially for primary γ′ precipitates (due to their size comparable to the grain size and in the observation/characterization means range) induce the formation of titania and alumina.

According to Ellingham / Richardson diagram exposed in figure 1.14, and assuming the aluminum and titanium concentrations in primary γ′ precipitates from SEM-EDS analysis in table 1.1 (11.1 $\%_{wt}$ Ti and 5.3 $\%_{wt}$ Al), the emerging primary γ′ precipitates are expected to develop external titania oxide and internal alumina oxide, as depicted in figures 3.20 and 3.21. Internal from external oxide formation is governed by kinetic matters (Ti diffusion being faster), but also thermodynamic matters (the low aluminum concentration in the material leading to its low activity).

Alumina oxide development is reported in figure 3.20 and figure 3.21 for oxidation at 700 °C and 800 °C respectively for duration of 10 h, 200 h and 600 h. The slower oxidation rate at 700 °C compared to 800 °C impacts the alumina formation. Alumina forms mainly through intraprecipitate spikes as reported up to 600 h at 700 °C. Increasing the temperature to 800 °C leads to the formation of a dense alumina oxide in place of the former precipitate. Once the aluminum available in the primary γ′ precipitates is completely consumed in the alumina reaction, the alumina forms particularly intergranularly. Diminution of the oxidation temperature is known to favor internal oxidation [70].

The formation of intergranular and internal alumina implies the consumption of aluminum. The low aluminum concentration in the matrix (1.6 $\%_{wt}$) compared to primary γ′ precipitates (5.3 $\%_{wt}$) according to table 1.1, sees the consumption of aluminum in the γ′ to enable the alumina reaction. Such phenomenon is experimentally observed in figures 3.13 and 3.14 with the absence of intragranular secondary precipitates down to the internal alumina front and deficit in intergranular primary γ′ precipitates down to the intergranular alumina oxidation front. Both temperatures demonstrate the contribution of the primary γ′ precipitate to the sub-surface oxidation, with oxidation being mainly initiated in such particles before finally progressing through the grain boundaries.

Titania formation is observed above the chromia layer as a result of the transient oxidation regime. Primary γ′ precipitates act as a titanium reservoir that supplies the titania formation. Development of the chromia layer decreases the mobility of titanium to the chromia / titania or chromia / environment interface which induces the development of titania at the sub-surface for long-term oxidation as shown for temperatures of 700 °C and 800 °C in figure 3.20 and figure 3.21.

Chromium is also present in the primary γ′ precipitates leading to the development of a chromia layer as depicted in all SEM micrographs 3.20 and 3.21. The low chromium concentration (3.1 $\%_{wt}$, 3.2 $\%_{at}$) in γ'_I is not supposed to develop such chromia scale by itself. For both temperatures, SEM micrographs reveal nevertheless a larger chromia scale above primary γ′ precipitates than above the matrix. γ'_I are mainly located in grain boundaries surroundings, short-cut diffusion path of chromium through the grain boundaries may explain such chromia development. Cruchley demonstrated the particular effect of grain boundaries onto the external oxide kinetic (chromia formation)

with an acceleration of the constant rate k_p above grain boundaries between 76 % to 145 % in RR1000 alloy between 700 °C and 800 °C.

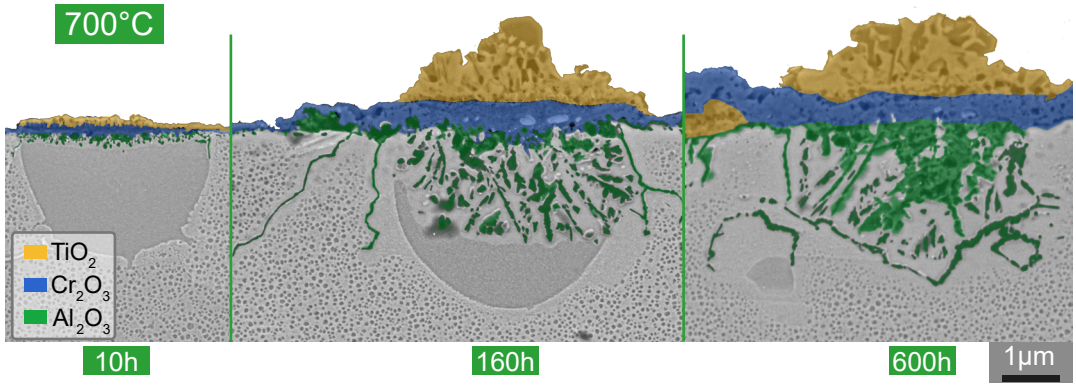

Figure 3.20: SEM-BSE micrographs of an oxidized γ'_I emerging at the surface after oxidation at 700 °C during 10 h, 160 h and 600 h

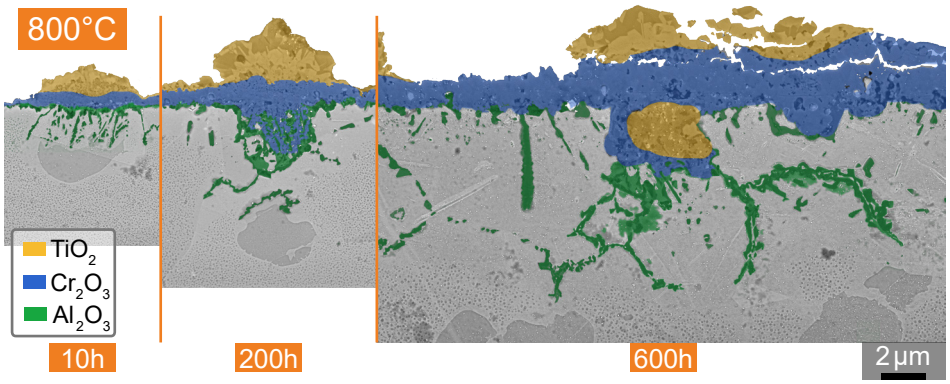

Figure 3.21: SEM-BSE micrographs of an oxidized γ'_I emerging at the surface after oxidation at 800 °C during 10 h, 200 h and 600 h

Analysis

The study of emerging primary γ′ precipitates oxidation process points out the following particularities:

- Rutile titania islets form on top of the emerging primary γ′ precipitates. The presence of rutile is also found above the emerging grain boundaries.
- The secondary and tertiary precipitates located in the grain boundary vicinity observe a depleted area, the sign of precipitates dissolution, participating in the surface supply of titanium to form rutile.
- Both intergranular and internal alumina are found at the sub-surface of René 65 on the mechanically investigated oxidation. The 700 °C temperature mainly reveals intraprimary γ′ precipitate oxidation associated with thin intergranular alumina spikes with similar penetration depth. The 800 °C oxidation exposes fully oxidized emerging primary γ′ precipitates, intragranular alumina punctures, and mainly intergranular alumina spikes.

3.5 AlbiSolvus metallurgical state oxidation

The AlbiSolvus metallurgical state 800 °C oxidation behavior was characterized using wedged-polished coupons, as presented in figure 3.22 and figure 3.23 for oxidation durations of 200 h and 600 h, respectively. The AS state demonstrates internal and intergranular alumina. The internal oxidation reveals penetrations depths of 2.0 ± 0.5 µm and 5.0 ± 0.5 µm on the oxidation durations of 200 h and 600 h, respectively. The intergranular oxidation reveals penetrations depths of 3.0 ± 0.5 µm and 6.0 ± 0.5 µm on the oxidation durations of 200 h and 600 h, respectively.

The external chromia layer was not characterized in terms of scale thickness in the AS state but revealed very low adherence to the substrate, as depicted in the SEM fractograph analysis exposed in the mechanical chapter in figure 4.29.

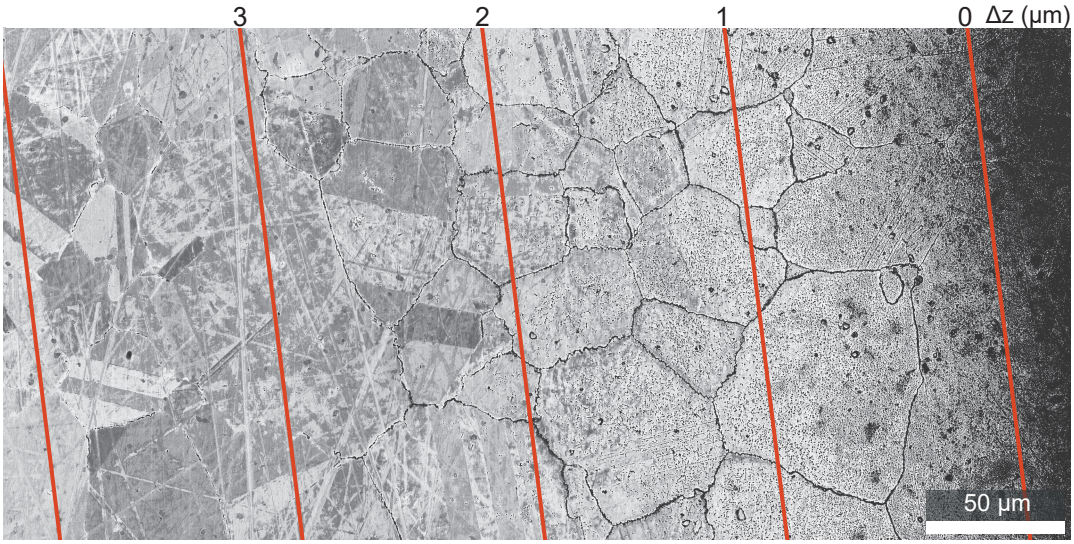

Figure 3.22: SEM-BSE observation of a wedge polished oxidation coupon to reveal the sub-surface oxidation impact of AS state at 800 °C during 200 h

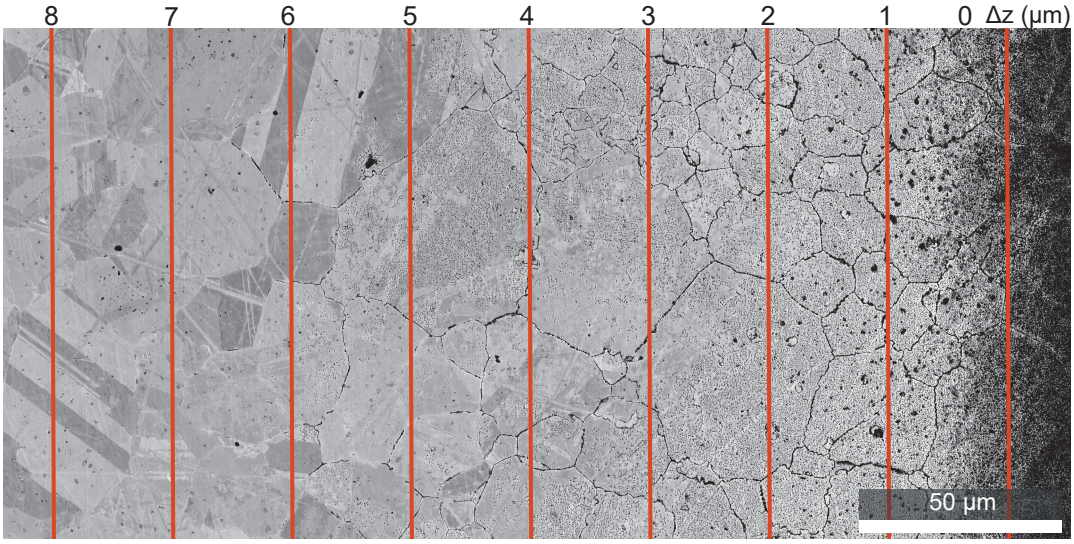

Figure 3.23: SEM-BSE observation of a wedge polished oxidation coupon to reveal the sub-surface oxidation impact of AS state at 800 °C during 600 h

Analysis

The following conclusions were evidenced from the oxidation of the AS state at 800 °C during 200 h and 600 h:

- The AS state demonstrates similar oxidation products at 800 °C compared to the AR state. The penetration depths in internal and intergranular alumina revealed lower values compared to the AR-oxidized state.

The oxidation at 800 °C on the AS state demonstrates a different oxidation kinetic from the AR-oxidized state with a 2 µm decrease in intergranular penetration depths, and 0.5 µm to 1.5 µm decrease in internal alumina penetration depth. The increase in grain size, and subsequently in the grain volume/grain boundaries, results in lower diffusion of the oxygen in the sub-surface, and so lower alumina penetration depth, as revealed by both internal and intergranular results.

3.6 Oxidation of the TiN phase

Nitride particles are mainly composed of titanium and nitrogen as revealed by SEM-EDS analysis in figure 2.35. The size and distribution were introduced in section 2.30. Intermetallic phases TiN are stable up to relatively high-temperatures (up to 650 °C according to Alexandre in 718 alloy [216]). TiN transformation to TiO_2 rutile appends with a volumetric expansion coefficient δ_v of 1.64 (volume ratio between the two phases according to equation 3.7). Volume expansion can be observed in cross-sectional SEM-BSE micrograph 3.24 for oxidation at 800 °C during 300 h and 600 h.

$$\delta_v = PBR = \frac{\Sigma n_{products} V_{m\ products}}{\Sigma n_{reactants} V_{m\ reactants}} = \frac{V_{m\ TiO_2}}{V_{m\ TiN}} \tag{3.7}$$

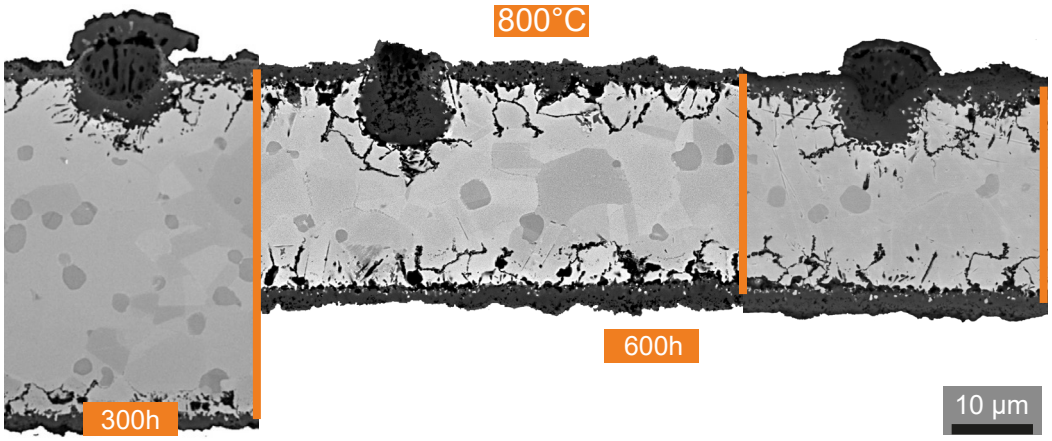

Figure 3.24: Oxidized TiN particles after 600 h exposure at 800 °C

Oxidized TiN SEM-EDS analysis resulting from wedged polished coupons at 800 °C for 600 h is exposed in figure 3.25. The nitride presents external intergranular alumina oxidation, a thin TiO_2 and Nb shell enclosing a large Cr_2O_3 internal layer, and a TiN remaining core. This SEM-EDS analysis does reveal a minor presence of TiO_2 from the TiN exhaustion, most of the titanium (as rutile) is located above the chromia layer, which is not present in figure 3.25 due to the location of this cross-section being too deep from the surface. The relative position from the chromia layer and titania core is revealed on all SEM-BSE micrographs in figure 3.24. TiN intermetallic particles oxidize mainly into rutile TiO_2.

Emerging TiN then sees rutile protrusion at the surface due to the high volume expansion coefficient. The nitride/matrix interface acts as an oxygen shortcut path and sees similar oxidation to the surface: a chromia layer topping internal and intergranular alumina spikes. Such chromia layer and intergranular alumina spikes are the ones revealed in SEM-EDS analysis 3.25. Molybdenum and tungsten are also punctually evidenced in figure 3.25. TiN particles are often associated with carbide or boride particles containing refractory elements such as Mo and W.

Oxidation of nitrides results in the release of nitrogen into the matrix. The nitrogen front may react with titanium to form nitrides again but this has not been observed nor particularly looked for within this framework.

SEM-EDS analysis of non-oxidized TiN presented in figure 2.33 evidenced an NbC shell. SEM-EDS analyses of figure 3.25 demonstrate oxidation of the NbC shell with a

high concentration of Nb revealed in the surroundings of the TiN particles with a high presence of oxygen but not associated with carbon segregation.

Connolley and Govaere reported oxidation of the NbC shell of nitrides according to equation 3.8 [9, 217]. NbC shell was reported for temperatures starting from 550 °C by Alexandre [216] with cracking of the TiN particle due to the high volume expansion of the shell from oxidation.

$$2\frac{2}{9}NbC + O_2 = \frac{2}{9}Nb_2O_5 + 2\frac{2}{9}CO_2 \tag{3.8}$$

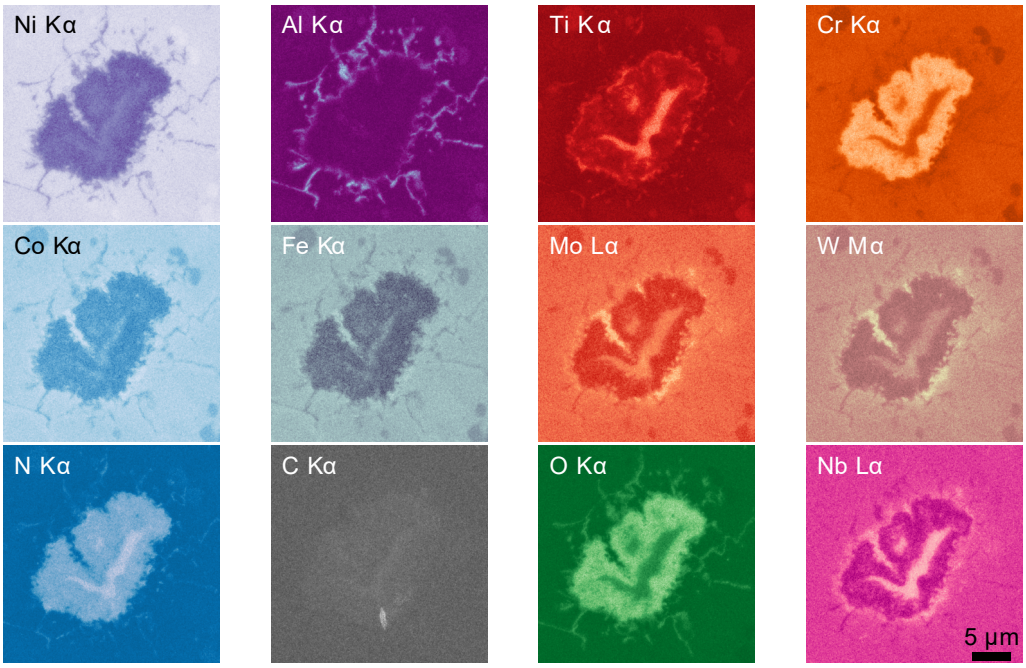

Figure 3.25: TiN oxidized at 800 °C during 600 h from wedge polished coupon

Analysis

The following conclusions were evidenced by the focus on the TiN particles:

- Oxidation of the emerging or close to the surface nitride demonstrates the extensive development of rutile oxide. The penetration depth of oxidized nitrides exceeds the intergranular alumina spikes and serves as a diffusion shortcut. The oxidation products and penetration depth of the sub-nitride alloy reveals to be similar to the surface ones.

The initial relative dimension of nitrides compared to the microstructure associated with the volume expansion due to oxidation processes exposed in this section draw special attention to these intermetallic particles into crack initiation from surface default (acting as notch effect). Such TiN particles, from their relative size compared to the microstructure, can be compared to Govaeres' findings on carbides and carbonitrides on AD730^{TM} [9]. Their presence can impair the fatigue behavior of the material and act as preferential crack initiation sites. TiN particles maximal equivalent diameter was evaluated at values of 15 µm, as exposed in table 2.4.

3.7 Thickness effect onto the oxidation behavior

Oxidation at 650 °C, 700 °C and 800 °C for durations of 10 h, 30 h, 100 h, 200 h, 600 h and 1000 h was performed on different sample thicknesses to document the reservoir effect of chemical entities involved in the oxidation processes. Such reservoir effect aims at "complete" starvation of the chromium in the bulk of the thinnest samples (chromium being the major entity involved in the oxidation processes with chromia formation). Thicknesses of 20 µm, 30 µm, 40 µm, 50 µm, 75 µm, 150 µm and 500 µm were investigated for the three temperatures and all oxidation durations.

3.7.1 Effect on the mass gain

The mass gain for all conditions is presented in figure 3.26 with distinction between the thicknesses using a color scale (darkest colors being the thinnest samples). Experimental values are presented with empty circles while the parabolic behavior modeling using equation 1.6 is presented with dashed lines. The oxidation kinetics behavior at 700 °C and 800 °C differ from the results at 650 °C.

The mass gain at 650 °C was found independent of the sample thickness investigated with less than 18 % variation on the constant rate k_p, as aforementioned in section 3.3.2. The modeling to pure parabolic kinetic using equation 1.6 does not take into account the early stage of oxidation tests as revealed by the mass gain experimental data in figure 3.26 being above the parabolic modeling (dashed lines). Better fitting of the mass gain can be obtained via modeling through Monceau and Pierraggi equation 1.8 to take into account the transient regime but the low temporal discretization of interrupted tests is too scattered (noisy) to allow a relevant fitting.

The relatively close mass gain for low oxidation durations (10 h and 30 h) between the two temperatures 650 °C and 700 °C let us think of a similar transient regime. Such an observation complies with the oxidation processes to be diffusion rate controlled (in the sub-surface matrix and/or through the oxide scale). Oxidation of the chemical entities present at the surface happens at the same rate. Once the surface is depleted of the oxidizing elements (*i.e.* Ti and Cr), diffusion of those entities from the sub-surface is temperature dependent as diffusion is thermally activated. A lower temperature induces slower diffusion as revealed by the lower mass gain after 30 h for the temperature 650 °C than for the temperature 700 °C. Such comparison is made possible by the constant oxidation mechanisms observed at both temperatures.

The oxidation kinetics at 700 °C and 800 °C was found thickness dependent, as illustrated in figure 3.27. The parabolic rate constant is plotted as a function of the samples' thickness. An increase in mass gain of 160 % and 80 % is reported for temperatures 700 °C and 800 °C respectively between 500 µm and 20 µm thick samples. Both temperatures reveal a parabolic kinetic with a minor (for 700 °C) to no (for 800 °C) influence of the transient regime. The 650 °C oxidation kinetics variations from samples' thickness reveal no significant variation (or below the mass measurement precision) contrary to the temperatures 700 °C and 800 °C.

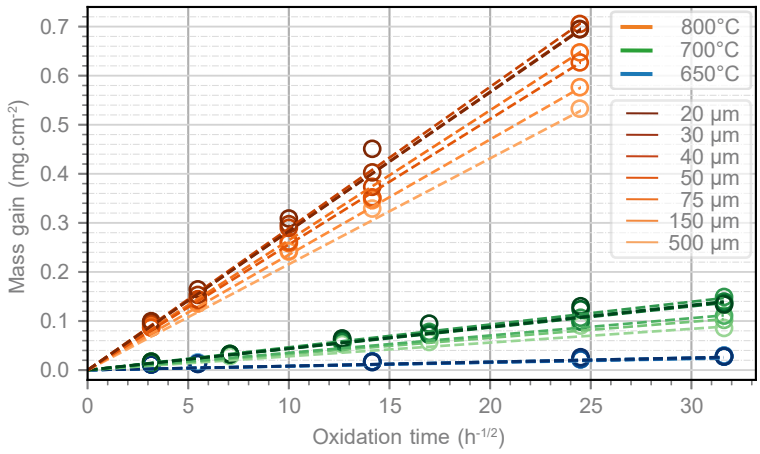

Figure 3.26: Mass gain ($g\,cm^{-2}$) vs. thickness of the sample (µm) for oxidation times of 10 h, 30 h, 100 h, 199 h and 598 h at 650 °C. Dots represent experimental values and dashed lines the parabolic fitting

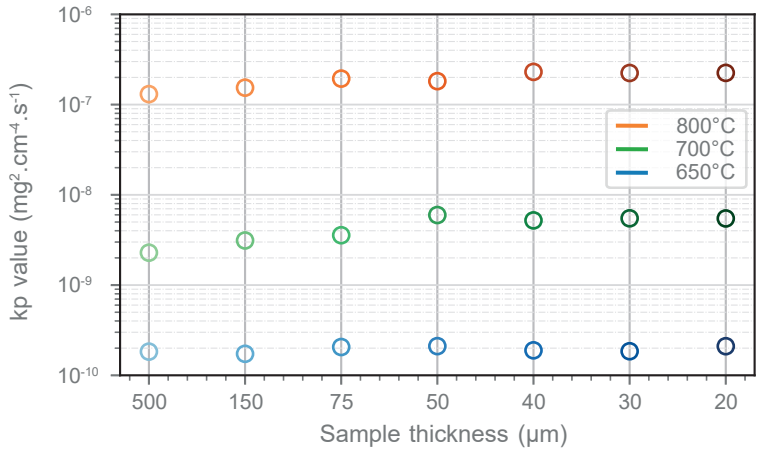

Figure 3.27: Parabolic constant rate k_p versus thickness of the samples for temperatures 650 °C, 700 °C and 800 °C

3.7.2 Investigation of the oxides layers

The origin of such thickness effect was investigated by analyzing SEM-BSE cross-sectional micrographs to document the differences in oxidation features and products as a function of the sample thickness. Two different SEM-BSE cross-sectional micrographs of thicknesses 20 µm (left) and 75 µm (right) after 600 h of exposure at 800 °C are given in figure 3.28. The 20 µm-thick sample demonstrates a thicker external chromia scale associated with lower intergranular alumina penetration depth.

The external oxide thickness (chromia + titania), intergranular equivalent thickness, and maximal penetration depth (alumina) were estimated via image analysis following a similar methodology as exposed in figure 3.17. The results for thicknesses 20 µm and 75 µm are presented in figures 3.29 to 3.31. All statistics are based on four SEM-BSE micrographs at x1000 magnification (100 nm/px resolution).

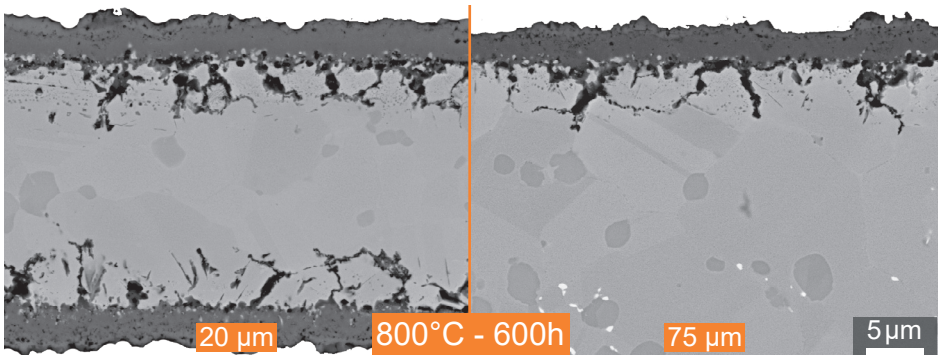

Figure 3.28: SEM-BSE cross-sectional micrographs of oxidation coupons of thicknesses 20 µm (left) and 75 µm (right) after 600 h exposure at 800 °C

Figure 3.29 reveals a thicker external oxidation layer for thinner samples with up to 1 µm difference in mean value equivalent to a 35 % increase for 600 h exposure at 800 °C. The external oxidation layer appears to grow at the same rate up to 100 h of oxidation with an increase of the oxidation rate starting from 200 h for thinner samples.

Figure 3.30 informs on the internal and intergranular (GBO for Grain Boundary Oxidation) alumina using the equivalent thickness of a uniform layer having an identical area to the identified alumina. Minor variations are revealed from the two investigated thicknesses of 20 µm and 75 µm. Such low variations are of second order on the mass gain changes from thickness variation.

Figure 3.31 presents the maximal intergranular penetration depth of alumina on both thicknesses 20 µm and 75 µm. The tendency is opposed to external oxide thickness with higher penetration depth (up to 1 µm for 600 h oxidation duration) for thicker samples. Such an observation is in agreement with the external oxide layer thickness, the intake of oxygen for internal oxidation is likely slowed down via the formation of an external oxide layer. A larger external oxide layer induces then less oxygen penetration into the material resulting in shallower intergranular alumina formation.

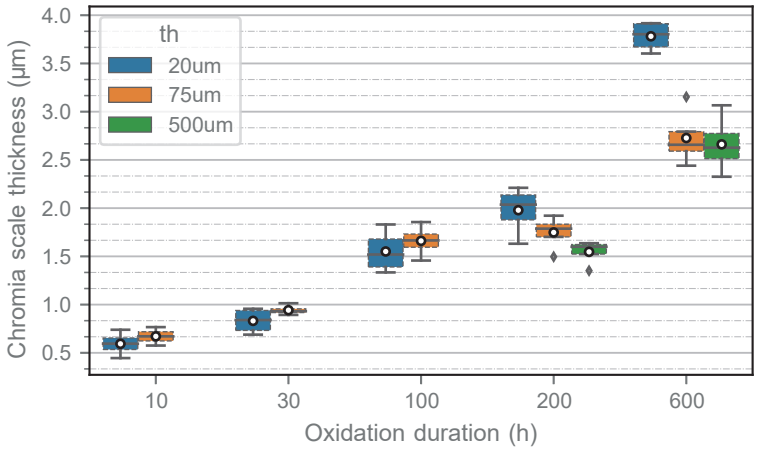

Figure 3.29: Chromia scale equivalent thickness (rectangle with identical area) for samples of 20 µm, 75 µm and 500 µm initial thickness after oxidation at 800 °C during 600 h

Figure 3.30 revealed nevertheless a similar alumina formation on both thicknesses. The shallower depth penetration of 20 µm is then accompanied by larger intergranular alumina spikes close to the metal/oxide interface as revealed by figure 3.28.

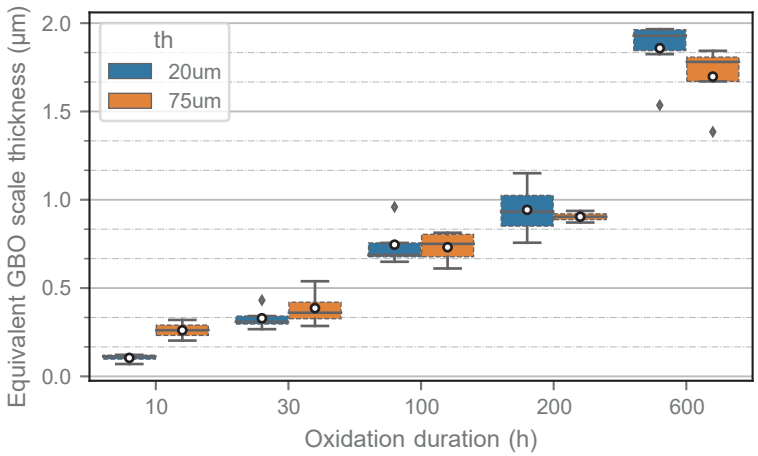

Figure 3.30: Intergranular (GBO) alumina equivalent thickness (rectangle with identical area) for samples of 20 µm and 75 µm initial thickness after oxidation at 800 °C up to 600 h

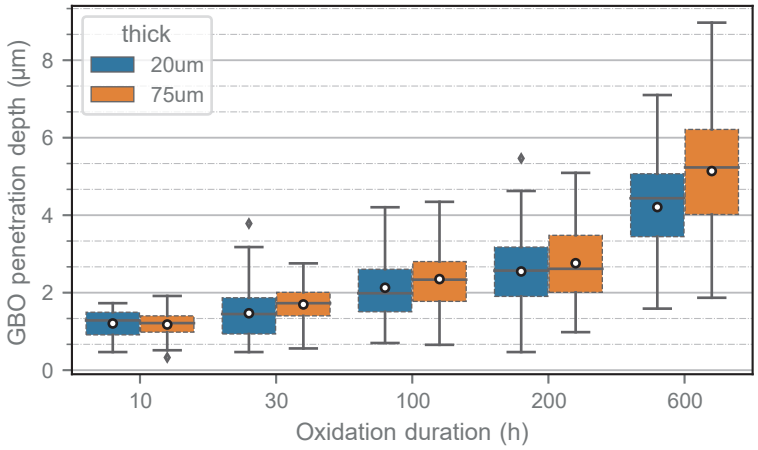

Figure 3.31: Intergranular (GBO) alumina maximal penetration depth for samples of 20 µm and 75 µm initial thickness after oxidation at 800 °C up to 600 h

3.7.3 Oxidation kinetic of the intergranular alumina: activation energy

The parabolic oxidation rate constant estimated via the maximal intergranular penetration depth was compared to similar alloys after the study of Sanviemvongsak *et al.* in figure 3.32 [211]. René 65 intergranular maximal penetration depth complies with the observations of Cruchley on RR 1000 alloy [212] with parabolic rate constants going from $2.7 \times 10^{-1}\,\mu m^2\,h^{-1}$ to $4.1 \times 10^{-1}\,\mu m^2\,h^{-1}$ for sample thicknesses of 20 µm and 75 µm, respectively. The René 65 parabolic rate constant of the intergranular oxidation

is also in good agreement with Sanviemvongsak *et al.* observations in Alloy 718 (but lower due to the lower temperature investigated for René 65).

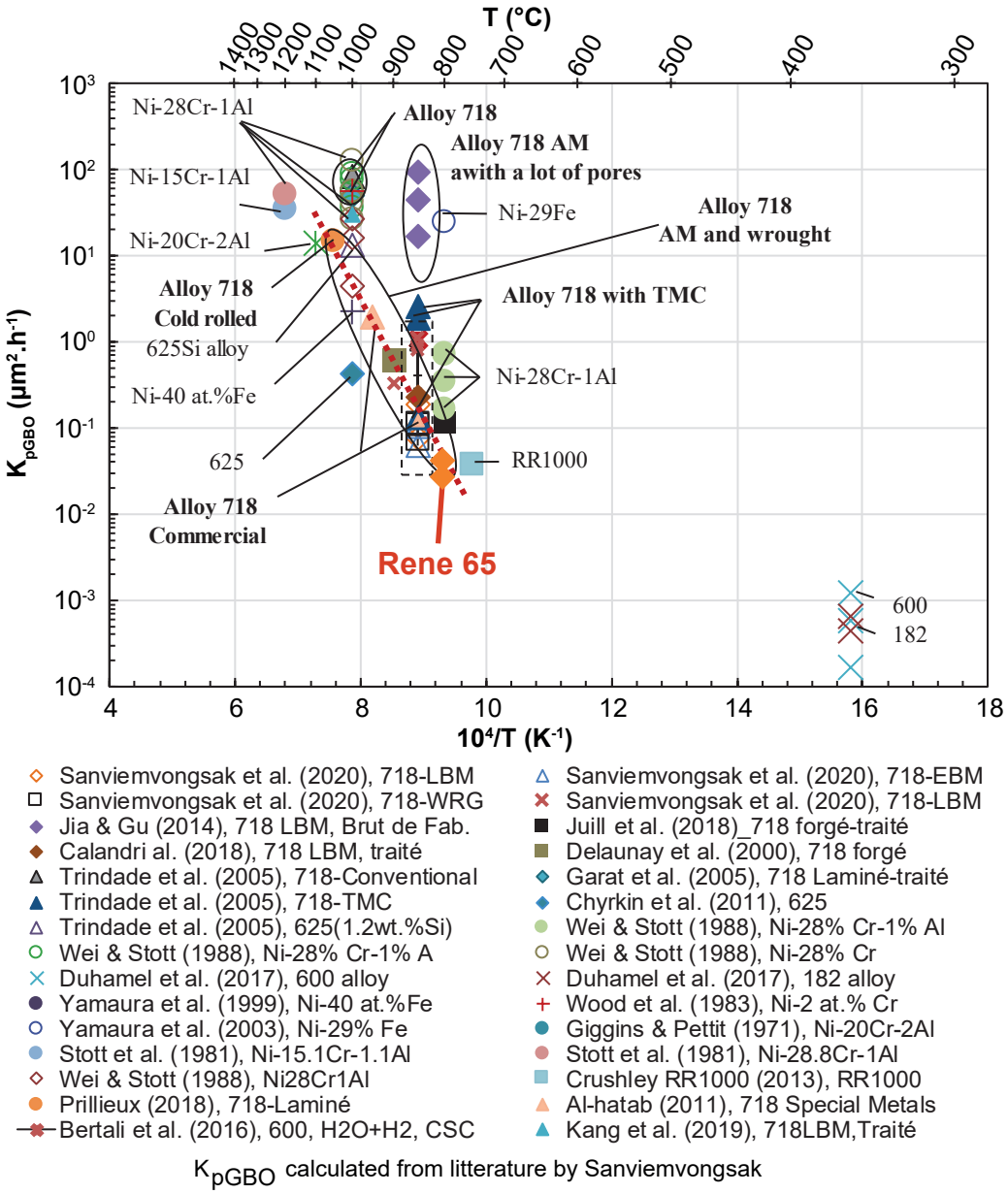

Figure 3.32: Parabolic oxidation rate constant of René 65 compared to similar alloys based on the work of Sanviemvongsak *et al.* [211]

Sanviemvongsak conclusions on the intergranular oxidation kinetic should be in agreement with the René 65 intergranular oxidation behavior (taking into consideration the differences in chemical composition, microstructure, and intergranular oxidation). The oxidation kinetics are mainly controlled by the diffusion of aluminum through the alumina/alloy interface (limiting factor compared to the diffusion of oxygen through grain boundaries).

3.7.4 Investigation of the oxidation products

The XRD diffractograms of all the samples involved in figures 3.26 to 3.31 are presented in figure 3.33.

Oxidation products developing at 700 °C are similar on all sample thicknesses with identification of chromia (especially the 33.5° peak), titania (especially the 28.5° peak), alumina (especially the 43.5° peak) and minor traces of $CoCr_2O_4$ spinels (especially the 30.5° peak). The γ and γ' phases are both identified on all durations despite close diffraction angles to the alumina.

The 800 °C oxidation behavior reveals similar oxidation products as the 700 °C oxidation. Peaks are more prominent due to the thicker oxide scales with temperature increase. The evolution of the oxidation product as a function of the samples' thickness is observed for the oxidation temperature of 800 °C. Indeed, thinner samples developed a thicker chromia layer, development of the rutile above the primary γ' precipitates and grain boundaries, and the presence of $CoCr_2O_4$ spinels and NiO.

The external and internal/intergranular oxide layers' effect on the mass of samples of different thicknesses has been discussed above while the presence of spinels being more developed in thinner samples can complete their more important mass gain at 800 °C. The lack of spinels at 700 °C associated with a more pronounced mass gain variation from samples thickness than at 800 °C assumes the minor impact of spinels in the mass gain increase with samples thickness.

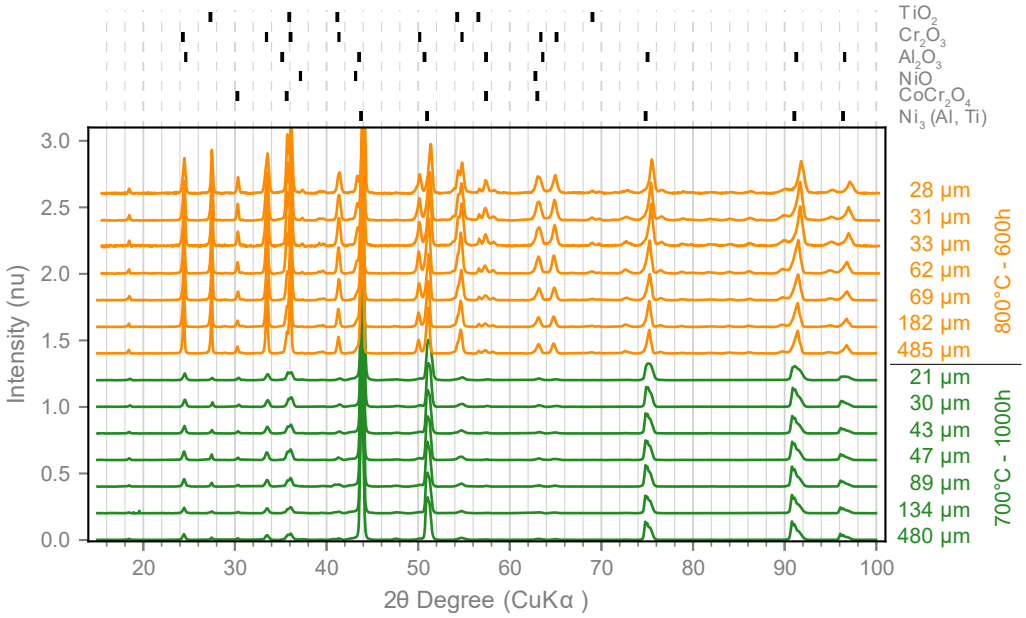

Figure 3.33: XRD diffractograms

Analysis

The following conclusions were evidenced in thin samples oxidation process:

- The sample thickness plays a role in the oxidation kinetics as demonstrated by the differences in external oxide layer thickness but also the total amount of intergranular alumina between thick and thin samples. The alumina demonstrated a total surface higher for thinner samples but a lower penetration depth. A thicker external oxide scale associated with a higher total surface of alumina results in up to 160 % of increase of mass gain for thin samples at 700 °C compared to thick/conventional samples.
- The nature of the oxidation products also evolves with the samples' thickness as observed in XRD analyses. Spinel formation is more pronounced on thinner samples.
- No important mass gain increase was observed even on low thicknesses samples. The spinel and NiO formation are then associated with InCF and not breakaway mechanism.
- The intergranular parabolic oxidation kinetics were studied and demonstrated rates in agreement with similar alloys such as RR1000.

A first idea to explain the thickness effect on the oxidation kinetics relies on the thickness of the samples themselves. Thinner samples are expected to best accommodate any stresses generated by the oxides' development compared to thicker samples due to their higher compliance. For instance, a 100 MPa compressive stress present at the surface of samples from oxide growth results in a higher tensile strength of the substrate for thinner samples (smaller section) compared to thicker samples (higher section).

The oxide formation at the surface of the metal may induce compressive stresses. The external chromia layer is assumed to grow cationically in this framework oxidation condition, as reported by Mrozowski observations on AD730^{TM} with similar oxidation conditions to this study [213]. The chromia should then grow at the free and unconstrained oxide/environment interface and so not involve any oxide growth strain [70]. The intergranular alumina formation is, nevertheless, constrained in the sub-surface grain boundaries. Kofstad demonstrated lateral stress development from chromia formation in grain boundaries [218]. A similar impact of intergranular alumina formation can be expected with internal tensile stress development within the metal not affected by oxidation. This steady-stress can indeed generate specimen creep.

The differences in accommodation of such stresses generated from the development of the external and internal oxides should result in geometrical changes in the samples with dilatation being more pronounced for thinner samples. The difference in mass gain observed, with 160 % and 80 % increase on the k_P for oxidation temperatures of 700 °C and 800 °C respectively, if only explained by dilatation of thin samples, should involve up to 43 % and 30 % increase in the wet surface of the material (surface in contact with the environment). The increase in dimensions of the samples from such increase in wet surface is in the order of 18 % (11.8 mm × 17.7 mm of final dimensions) for the initial oxidation coupons of 10 mm × 15 mm.

The wet surface of the oxidation coupons was then monitored (before and after oxidation) using an optical and laser confocal microscope to report any thickness impact on the mass gain increase and so variations in the samples' dimensions. The optical

bench, with a resolution of 4 µm pixel^{-1}, did not reveal any trend of projected geometrical evolution with the samples' thickness. Thin samples reveal to be sensitive to the stresses generated by the oxide scales, which can induce asymmetric bending. The optical bench only allows for in-plane geometrical evolutions, any bending of the specimens can alter the measurement of the samples' dimensions. The confocal microscope was then used to investigate such an out-of-plane effect, with an excellent resolution of 0.6 µm in XY and sub-micro-metric resolution in z. Similar conclusions from the optical bench were drowned with no apparent developed geometrical evolution of the wet surface from the samples' thickness.

The previous assumption relies on observation of the samples dilatation at high-temperature to remain observable at room temperature. But material provided with an oxide layer demonstrates stresses and so potential geometrical evolutions from the significantly different coefficients of thermal expansion between the oxide scale and the material. Chromia reports values of thermal expansion coefficient $8.5 \times 10^{-6}\,\mathrm{K}^{-1}$, a Poisson's ratio of 0.29, a Young Modulus of 283 GPa in the literature [179]. René 65 thermal expansion coefficient was considered to the value of $13.4 \times 10^{-6}\,\mathrm{K}^{-1}$ from Govaere in AD730^{TM} [9]. Compressive stress from the cooling of the samples can be assessed via equation 3.9 [70].

$$\sigma_{xx} = \frac{-E_{OX}\Delta T\left(\alpha_M - \alpha_{OX}\right)}{\left(1-\nu_M\right)\left(1+\frac{E_{OX}}{E_M}\frac{\xi_{OX}}{\xi_M}\right)+\left(1+\nu_{OX}\right)} \tag{3.9}$$

with E the Young Modulus, α the thermal expansion coefficient, ν the Poisson's ratio, ξ the thickness of scale and substrate metal, with $_M$ for the metal and $_{OX}$ for the oxide scale.

The 800 °C HT oxidation demonstrates internal stresses from thermal expansion mismatch of 47.4 MPa and 55.5 MPa for 20 µm and 500 µm-thick samples, considering the measured experimental values of the oxide scale presented in figure 3.29. The impact of such stress onto the section of the material, even in the thickness range 20 µm to 500 µm is negligible in the final dimensions of the oxidation coupons.

3.8 Intrinsic Chemical Failure (InCF) and breakaway mechanisms on René 65

3.8.1 Introduction

The initial idea of using samples with different thicknesses is aiming at the exhaustion of chemical entities involved in the parabolic oxidation regime. Two types of chemical exhaustion are possible:

Intrinsic Chemical Failure (InCF) results from the partial sub-surface depletion of the chemical entities due to diffusion-controlled regime up to its activity passing under the second most active entity. The most favorable oxide to form afterward does not necessarily result in a significant mass gain increase. The new oxide to form can be protective or not, the reaction is still kinetically limited by the diffusion of entities through the oxide scale.

Breakaway results in complete or partial starvation of the chemical entities involved in the protective oxidation reaction. Such starvation induces the development of fast-growing oxides with an exponential increase in mass gain. Breakaway oxidation is accompanied by loss of the external protective oxide scale integrity from cracking, spallation, or pores.

The time to complete exhaustion estimated in this work is based on the assumption that chromium is the main chemical element being oxidized (according to equation 1.10). It is based on a simple mass balance between the oxygen uptake to form the outer chromia oxide layer with parabolic kinetics and the total amount of chromium available in the material. This equation is a simple form of equation 20 in Refs. [96, 97], for a full depletion of Cr neglecting the diffusion of Cr in the alloy (equivalent to a high diffusion of chromium). Hence, it leads to an overestimation of the time to breakaway.

3.8.2 Theory on the full chromium consumption

The mass gain was considered as following a parabolic oxidation behavior in the stationary oxidation regime for 500 µm-thick samples in the temperature range 650 °C to 1000 °C (figure 3.16), but also for 20 µm to 500 µm thick samples in the temperature range 650 °C to 800 °C, as depicted in figure 3.26. The mass gain conforms with equation 1.6.
The mass balance from equation 1.10 is:

$$m_O = \frac{3}{2}\frac{m_{Cr} M_O}{M_{Cr}} \tag{3.10}$$

$$S_{wet} = 2 \cdot Area + Perimeter \cdot Thickness \tag{3.11}$$

assuming the term $Perimeter \cdot Thickness$ of equation 3.11 is negligible compared to the $Area$ of the sample (with oxidation coupons of 10 mm × 15 mm area compared to 50 mm × 0.02 mm perimeter surface), one can assume:

$$S_{wet} = 2 \cdot Area \tag{3.12}$$

The chromium available in the material is defined by equation 3.13:

$$m_{Cr} = \rho_{Cr} \cdot V \tag{3.13}$$

with ρ_{Cr} the volumetric mass of chromium and V the total volume of material ($Area \cdot \xi$)

$$m_{Cr} = \rho \cdot W_{Cr} \cdot Area \cdot \xi_m \tag{3.14}$$

$$t_{InCF} = \frac{1}{k_w} \cdot \left(\frac{3 \cdot M_O \cdot \rho \cdot W_{Cr} \cdot \xi_m}{4 \cdot M_{Cr}} \right)^2 \tag{3.15}$$

where t stands for time to full-Cr consumption (hours), k_w is the parabolic constant rate ($\mathrm{g\,cm^{-2}}$), Mi the molar mass of the i element ($\mathrm{g\,mol^{-1}}$), ρ the density of the alloy ($\mathrm{g\,cm^{-3}}$), Wi the weight percent of the i element ($\%_{\mathrm{wt}}$), and ξ_m the thickness of the sample (cm).

Figure 3.34 models the time to full-Cr consumption expected for sample thicknesses in the range 20 µm to 100 µm. The dots represent experimental points investigated, and the lines model the couple thickness/time for the studied temperatures according to equation 3.15. Experimental points located above the model lines are supposed to reach breakaway. Samples experiencing spinel and NiO formation are represented as full dots.

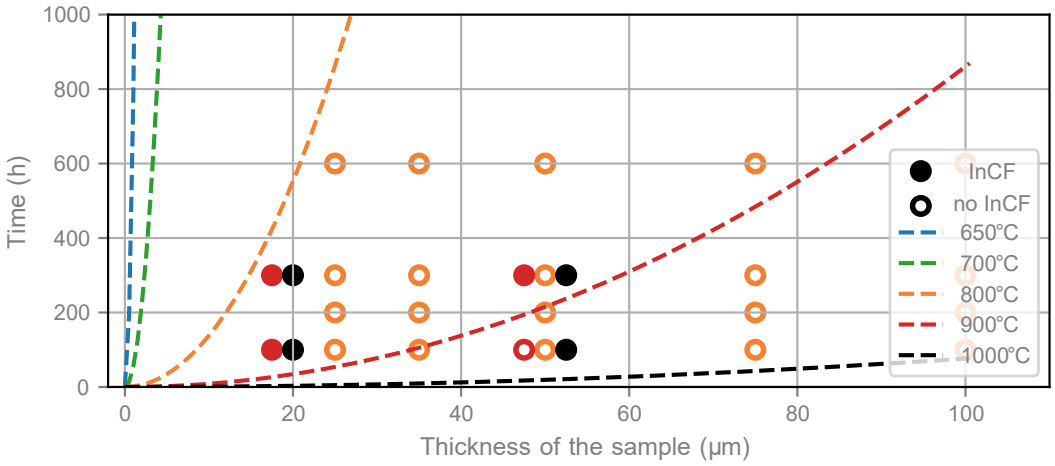

Figure 3.34: Time to full-Cr consumption as a function of the thicknesses for different temperatures ranging from 650 °C to 1000 °C

3.8.3 Experimental observations of InCF

SEM-EDS line scans analyses were performed on several oxidation conditions on the cross-section of samples in order to quantify the thickness of material affected by oxidation from metal/oxide interface to 99 % nominal composition of the elements participating in the oxidation process.

The chromium depletion ensues from supplying the chromia reaction. The γ' precipitates provide aluminum and titanium to the external titania and internal alumina formations but also participate in the chromia reaction as a non-negligible chromium concentration can be found onto the primary γ' precipitates, and thus present a different activity in chromium from the matrix [31]. Although chromium depletion of tens of micrometers is observed for bulk specimens, thin specimens with an initial thickness of 20 µm manifest bulk concentration depletion in chromium. The γ matrix reveals a Cr concentration of 18 ± 1 weight percent. A bulk concentration reduction down to

50 % can be observed in the 20 µm thick sample exposed at 800 °C for 300 h. The Cr depletion does not yet affect the chromia layer thickness nor the internal intergranular oxidation depth and primary γ' precipitates depletion width, as corroborated by the figure 3.35. No external spinel was observed above the chromia layer for oxidation temperature of 800 °C up to the critical duration of 600 h due to samples being not thin enough (the lowest value of samples in such oxidation condition is 25 µm).

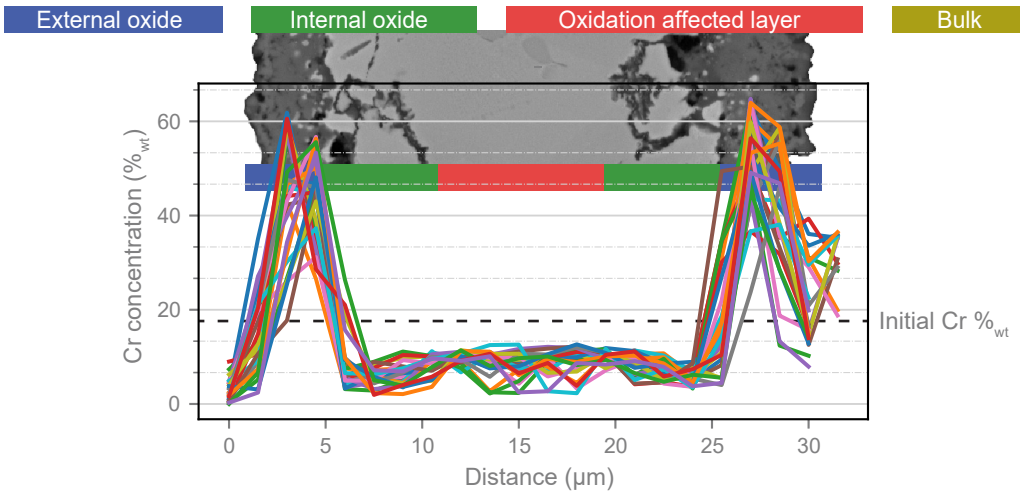

Figure 3.35: Chromium concentration profile $\%_{wt}$ from cross-sectional SEM-EDS analysis on oxidation condition 800 °C during 600 h with a sample thickness of 25 µm

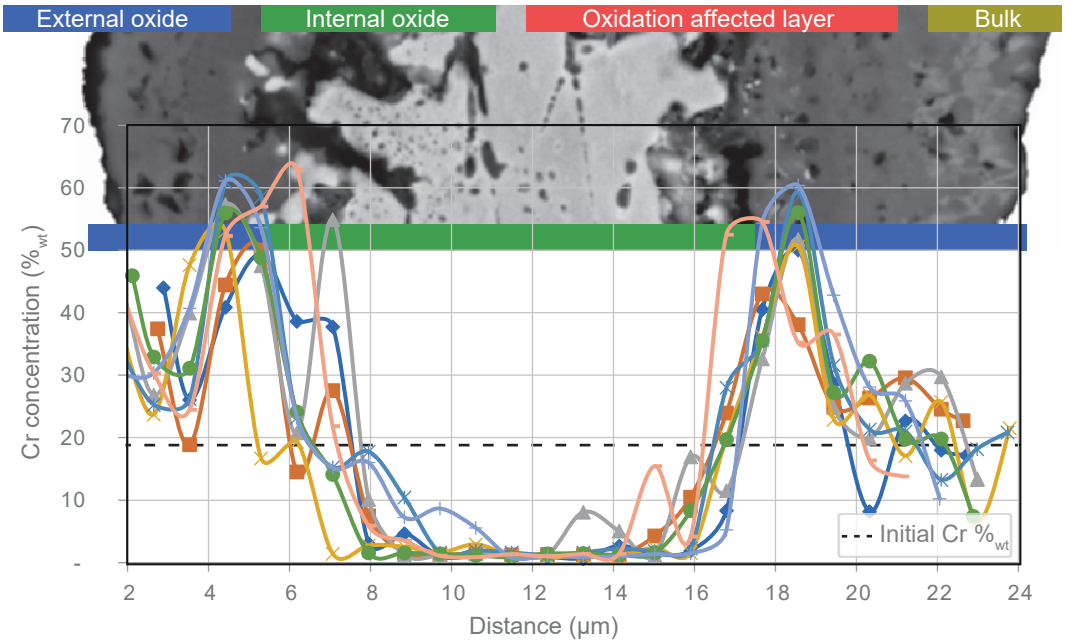

Figure 3.36: Chromium concentration profile $\%_{wt}$ from cross-sectional SEM-EDS analysis on oxidation condition 900 °C during 100 h with a sample thickness of 20 µm

The bulk chromium concentration was experimentally confronted to figure 3.34 using SEM-EDS analysis. The experimental parabolic rate constant corresponding to the intake of oxygen according to equation 3.15 leads to a bulk weight concentration of 6 % for oxidation condition of 800 °C during 600 h for a 30 µm thick sample. Such concentration is in agreement with the SEM-EDS weight percent chromium profile presented in figure 3.35 with an average chromium concentration of $7 \pm 1\,\%_{wt}$. Similar conclusion is observed in oxidation condition 900 °C during 100 h for 20 µm thick samples with close to 0 % chromium left in the bulk.

The mass gain observed on all temperatures and sample thicknesses revealed no major increase despite the almost complete core depletion in chromium. The mechanism involved the change of oxide formation then complies with InCF.

Spinel formation was reported for 900 h after 100 h in 20 µm thick samples as reported in figure 3.37. The InCF mechanism is initiated with spinel formation yet controlled via diffusion of entities through the chromia layer leading to no apparent increase in oxidation rate (*i.e.* breakaway) as observed by Fedorova *et al.* on AM1 alloy and confirmed with the mass gain of figure 3.16 [219]. Local fast-growing spinnels were observed with a maximal oxide thickness of 45 µm for 900 °C - 300 h on a 20 µm-thick sample (see Fig. 3.37)). As 1.5 w% is very small in comparison to the initial content, and because there is almost no Cr concentration gradient when breakaway occurs, using the simplified approach of equation 3.15 to determine the time to breakaway is justified.

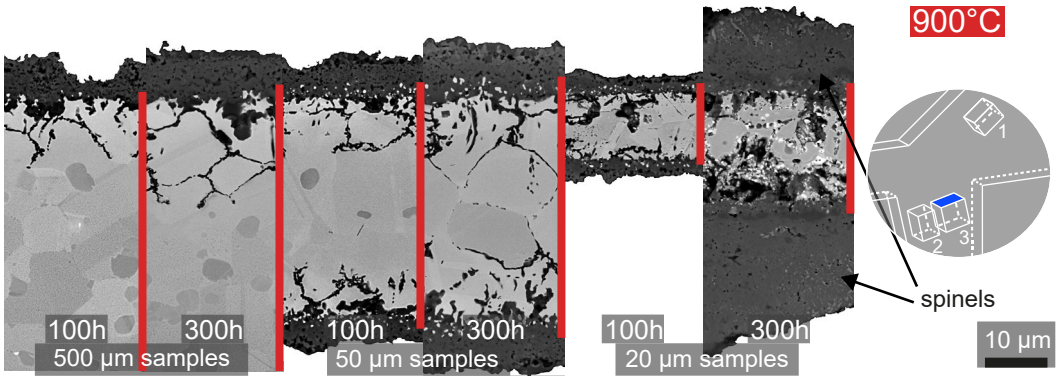

Figure 3.37: BSE micrographs of 500 µm, 50 µm and 15 µm-thick samples oxidized during 100 h and 300 h at 900 °C

Cross-section SEM-EDS analyses were performed on the 900 °C-100 h oxidation HT in 20 µm-thick sample. Such analyses expose spinel and NiO layers formation located above the chromia layer, as depicted in figure 3.38.

The oxidation behavior at 1000 °C, while being out of René 65 application scope (even the temperature 900 °C), was briefly analyzed to investigate extreme oxidation conditions. The 20 µm-thick samples did not survive the oxidation procedure due to the complete oxidation of the samples, leaving only two oxide scales and sparkles. Such fragments were analyzed via XRD as presented in figure 3.40. The 50 µm-thick samples present internal and external oxidation subsequently thinner than for the 500 µm-thick samples due aluminum and chromium depletion, in agreement with equation 3.15 for both oxidation durations of 100 h and 300 h.

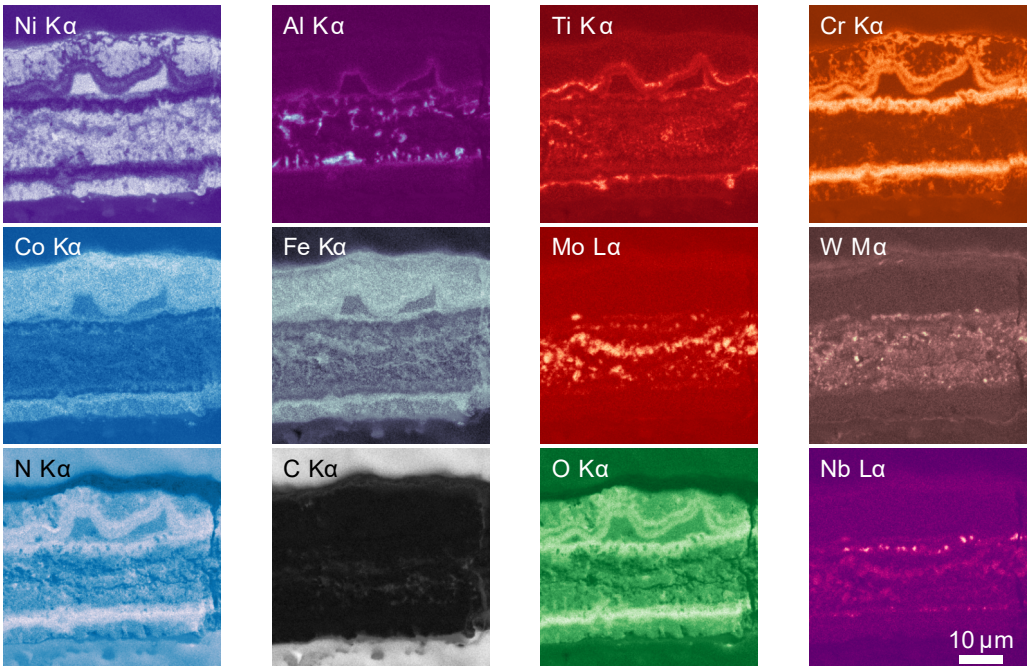

Figure 3.38: SEM-EDS analyses of cross-section of 20 µm-thick sample oxidized at 900 °C during 100 h

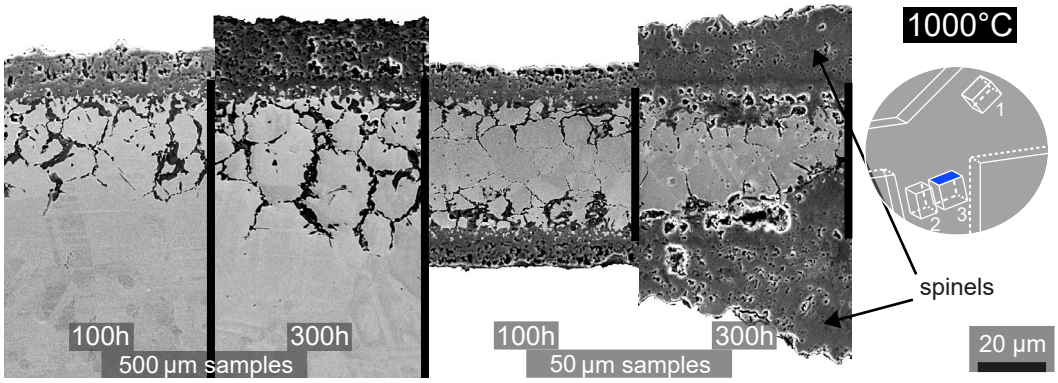

Figure 3.39: BSE micrographs of 500 µm and 50 µm-thick samples oxidized during 100 h and 300 h at 1000 °C

The oxides resulting from oxidation at 900 °C and 1000 °C temperatures were identified via XRD analysis, as presented in figure 3.40. The thin samples of 20 µm at 900 °C during 100 h and 300 h formed several oxidation products such as NiO and spinels (of type $CoCr_2O_4$) oxide, similarly to the 20 µm and 50 µm-thick samples oxidized at 1000 °C during 100 h and 300 h. Such conditions were identified as complete chromium depletion from the InCF estimation using equation 3.15.

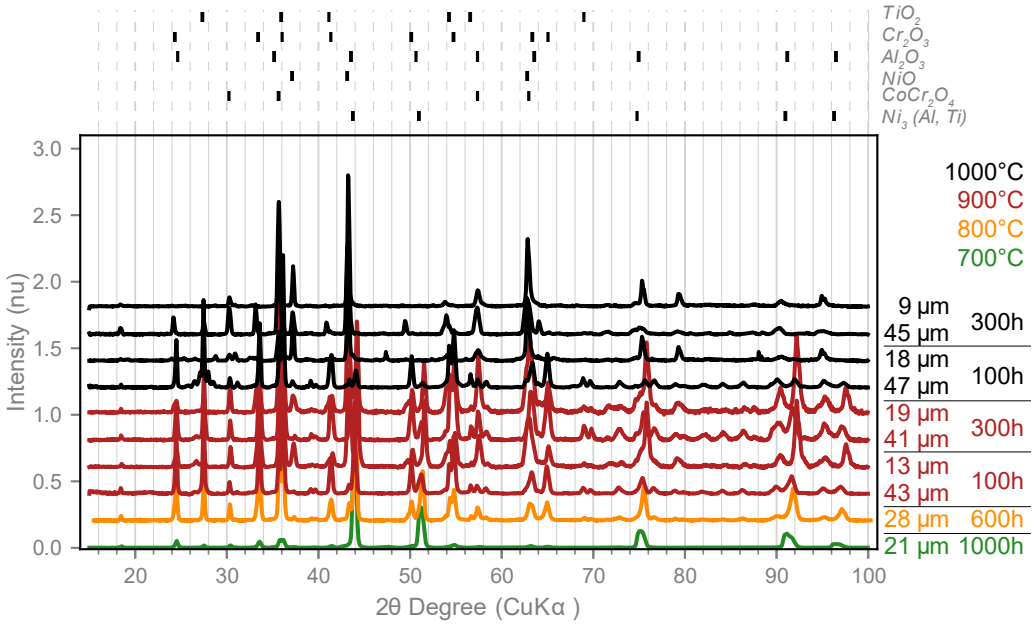

Figure 3.40: XRD analysis of the thin samples oxidized at temperatures of 700 °C and 800 °C compared to 900 °C and 1000 °C

Analysis

The following conclusions were evidenced from the study of the aged thin microtensile specimens:

- Oxidation at higher temperatures (900 °C and 1000 °C) of thin samples revealed the presence of spinels ($CoCr_2O_4$) or NiO due to InCF of the material. Such an oxidation behavior was modeled from the full depletion of chromium in the bulk of specimens and experimentally verified.

The time to InCF was experienced by Texier et al. in MCrAlY APS coatings with logarithmic and power-law mass gain regimes [96]. The InCF was experimentally observed with a change in oxidation products after almost complete starvation of the initially most active chemical entity (Al) present in such a coating. The change in oxidation behavior was not associated with major mass gain changes, as observed in this study. The mechanically intact external alumina layer in MCrAlY APS coatings, similarly to the external chromia layer in René 65, retained a beneficial role in limiting the diffusion rate of the elements involved in the oxidation process after InCF.

Thin samples reveal interesting advantages in the breakaway or InCF investigation. Typical experimental methods in achieving the breakaway consist of a temperature increase to limit the required HT duration. But increasing the temperature potentially induces side effects such as modification of the oxidation kinetics and/or products, volatilization or sublimation of elements, modification of the oxide-induced stresses, or oxides layers' spallation. One potential solution to achieve breakaway at the temperature of interest is via thinning down samples, as illustrated in this framework. Thin samples are, nevertheless, prompt to oxidation specifications external and internal oxides kinetics variations, as demonstrated in section 3.7, but also reported in the literature by several authors [96, 191, 220].

Chapter 4

Mechanical behavior

This chapter presents the experimental data resulting from tensile and fatigue tests to achieve a mechanical characterization of René 65. The mechanical conditions investigated in terms of thicknesses, oxidation/aging temperatures, and durations within this framework are assessed as a prelude in **section** 4.1.

The tensile behavior is firstly presented through **sections** 4.2 to 4.6. Particularities from the use of thin tensile specimens are introduced in the size effect **section** 4.2. The minor bulk microstructural evolutions resulting from the high-temperature exposure and their effects on the tensile behavior are presented in **section** 4.3. The oxidation impact is then addressed in **section** 4.4. The AlbiSolvus metallurgical state is then exposed in **section** 4.5. The impact of the oxides layers on the effective section of the specimens is presented in **section** 4.6

The fatigue behavior and identification of its damaging processes are discussed in **section** 4.7.

4.1 Introduction

The tensile behavior of René 65 has been explored, starting with the As-Received (AR) metallurgical state, to establish a database on such γ/γ' polycrystalline material across specimen thicknesses. The tensile behavior is quantified from the onset of plasticity with the YS to the rupture of specimens with the UTS and ductility of the specimens. The strain hardening dependency to the specimen thickness observed by Keller in pure nickel is considered using a similar methodology in **appendix** A [120].

Investigating the surface interactions and damaging consequences through the use of ultra-thin microtensile specimens imposes strong experimental limitations (strain monitoring, solicitation mode, etc.). The most adapted mechanical solicitation mode with the use of thin specimens is the tensile test, as denoted by the scientific interest found in the literature. Ultra-thin microtensile specimens aim at exacerbating the surface evolutions resulting from the high-temperature exposure. To help in analyzing the surface effects from the bulk evolution (as demonstrated with the microstructural changes in **section** 3.2.2), aged specimens, deprived of any residual oxidation-affected layer after Heat Treatment (HT), were machined and tested. The temperatures of both oxidized and aged states are of 700 °C and 800 °C for HT durations of both 200 h and 600 h.

A proof of concept is then given in the fatigue testing of ultra-thin microtensile specimens. The extended time required from fatigue testing limits the experimental conditions investigated, the metallurgical states are then: AR, oxidized at 700 °C during 200 h and 600 h, and 800 °C during 200 h. Surface evolution monitoring is performed with ex-situ full-field high-resolution SEM-SE-based DIC in interrupted fatigue tests to evidence strain localization induced from microstructural features affected (or not) by oxidation.

4.2 As-Received metallurgical state and thickness effect

This section exposes the tensile test results at room temperature for the as-received condition. Emphasis on the thickness effect of the specimens on the material response is performed with specimen thicknesses ranging from 500 µm to 20 µm.

The tensile behavior is then introduced via the stress-strain curves revealing the material response to a monotonous solicitation. The main tensile properties (Yield Stress YS, Ultimate Tensile Stress UTS, and Ductility) were identified as a function of the specimens' thickness to reveal any thickness effect.

4.2.1 As-Received stress-strain curves by thickness range

All the stress-strain curves of the As-Received (AR) state are gathered by thickness range, as defined in table 4.1:

Reference	20	35	50	75	100	250	500
Range	18-28	28-41	46-57	64-79	84-132	200-274	450-550

Table 4.1: Thickness ranges (µm) on the AR state

The tensile results by thickness range are presented in figure 4.1. The two extraction zones (Flank Zone FZ and Core Zone CZ) are distinguished in figure 4.1 using two colors: FZ in blue and CZ in red, similarly to section 2.2.3.

The stress-strain curves are presented by thickness range with a subplot emphasis on the elastic-to-plastic transition between 950 MPa to 1200 MPa and 0.4 % to 1 % of total strain. Significant evolution of the maximal total strain is revealed between the different thickness ranges, with an increase of the ductility (maximal total strain) for thicker specimens. Such a conclusion induces variations in the UTS due to the earlier rupture of thin specimens (less strain to failure is correlated to less stress at the rupture when having similar behavior). The YS also increases with the specimens' thickness.

Specimens thicker than 40 µm reveal minor superiority of the FZ specimens compared to the CZ specimens as introduced for 500 µm-thick specimens in figure 2.42 in section 2.2.3. A reproducibility of 2 to 3 specimens per condition (thickness) per extraction zone can be observed in figure 4.1, and is performed on all the tensile tests presented in this chapter. The scattering of material response (YS and UTS) at iso-thickness reports variations in the magnitude of 75 MPa to 200 MPa for specimens of thickness lower than 50 µm, while a lower magnitude variation(in the range 20 MPa to 100 MPa) is observed for thicker specimens.

The YS evolution is difficult to apprehend by presenting the stress-strain curves according to the thickness range. One stress-strain curve per thickness, chosen to be representative, is then presented in figure 4.2 for all the specimen thicknesses.

An important drop in ductility with specimen thickness is also evidenced with almost up to 3 times reduction for thin specimens in comparison with thick specimens (from 8 % to 28 % respectively). The UTS follows the same trend due to the earlier failure of the thin specimens and the true stress representation.

The elastic-to-plastic transition emphasis reveals a similar transition for specimens of thicknesses 20 µm, 30 µm, 40 µm, 50 µm, 75 µm and 100 µm which seems to differ from the similar transition of the 250 µm and 500 µm-thick specimens. The YS increases

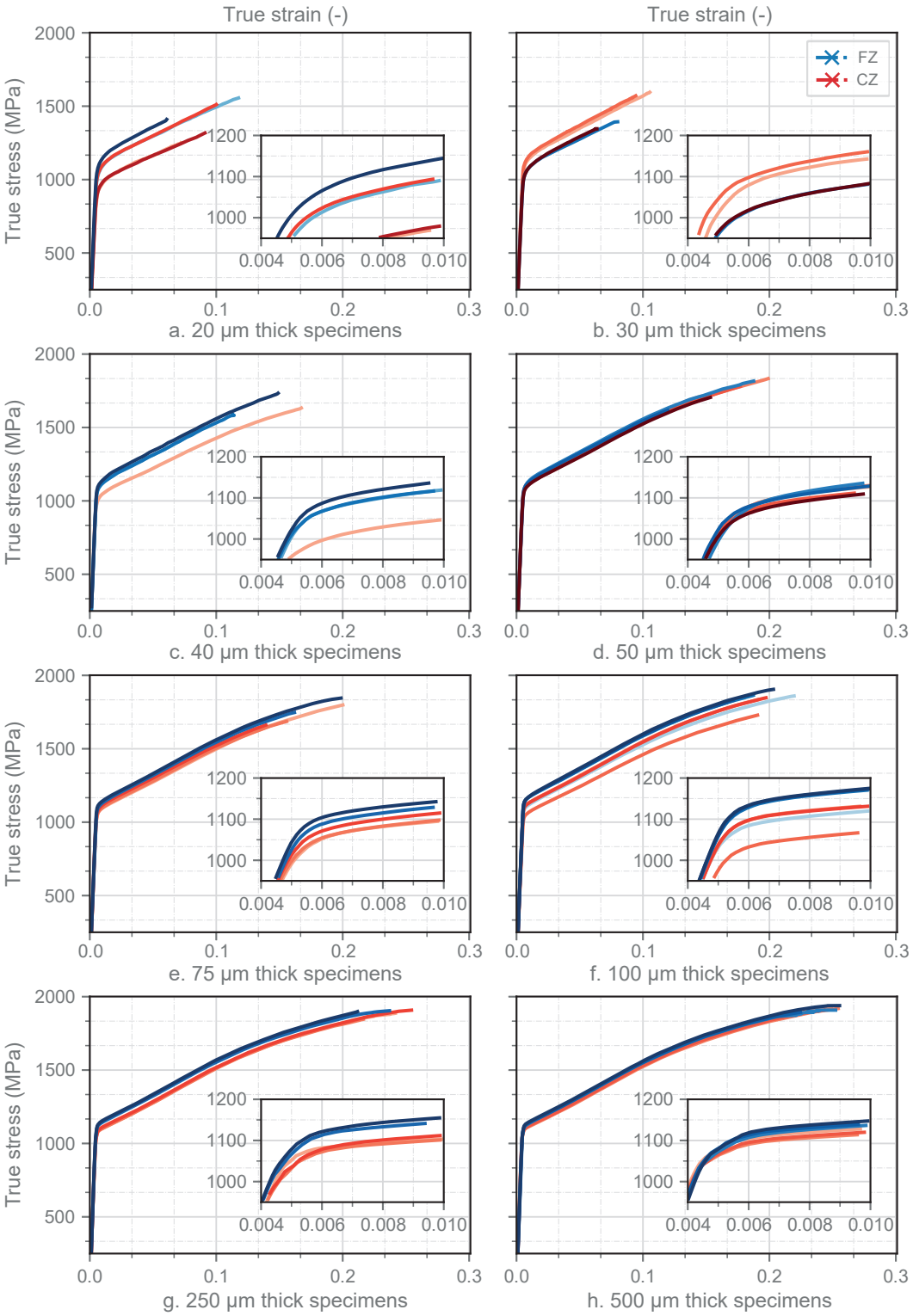

Figure 4.1: Stress-strain curves of the AR state of RT tensile tests on all thicknesses ordered by thickness range. Subplot for each thickness range emphasizing the elastic-to-plastic transition

with specimen thickness up to 100 µm, whereas the 250 µm and 500 µm-thick specimens reveal similar YS, the highest YS being experienced for the 100 µm-thick specimens. The mean value of YS for each thickness range is between 950 MPa to 1200 MPa.

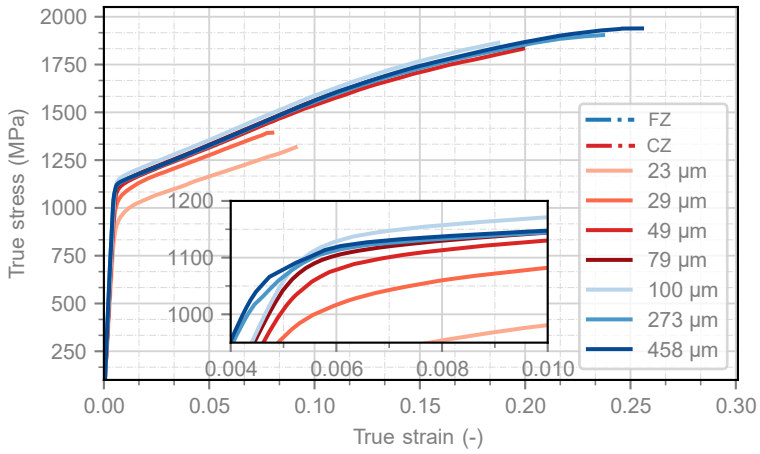

Figure 4.2: true stress versus true strain for the AR metallurgical state with thicknesses of 23 µm, 29 µm, 49 µm, 79 µm, 100 µm, 273 µm and 458 µm. The insert highlights the elastoplastic transition

4.2.2 As-Received tensile properties versus the thickness of specimens

The evolution of the macroscopic tensile properties as a function of the specimen thickness for all the specimen variants has been estimated from the stress-strain curves. All the points taken into account (only for valid tests, *i.e.* no plasticity in the radius of the specimens) are presented in the appendix section in figure D.1. The mean values of the tensile properties per thickness range of 500 µm to 20 µm are presented in figure 4.3. The black dots represent the overall average YS, UTS, and ductility of the specimens; regardless of the extraction zone. The blue and red colors are representative of the extraction zone (FZ in blue, CZ in red). The standard deviation is presented with vertical lines for each thickness range; it gives the statistical dispersion of the several tensile tests performed for each condition.

The thickness (x-axis) is plotted logarithmically to highlight the thin specimen effect and optimize the results display. The purple vertical line informs on the conventional cylindrical specimens values for the YS, UTS, and ductility as given in section 2.2.3.

While negligible evolution of the Yield Stress (YS) is observed for specimens thicker than 100 µm, the YS of the as-received material dropped down for thinner specimens, as illustrated in figure 4.3. This size effect is typical of the polycrystal-to-multicrystal transition due to the presence of the free surface [113]. Similar trends are evidenced for the evolution of the ductility and the UTS as a function of the thickness, with a transition thickness of 250 µm. YS drops down by 15.6 %, UTS down by 32.3 % and ductility down by 67.5 % for 20 µm-thick specimens compared to the reference polycrystalline properties (500 µm-thick microtensile specimens).

The free-surface grains are reported to respond differently compared to core grains due to changes in grain confinements. The absence of grain boundaries to pin dislocations

favors dislocation escapes. This subsequently delays the dislocation cells and networks to form, participating in strain-hardening [124, 221, 222].

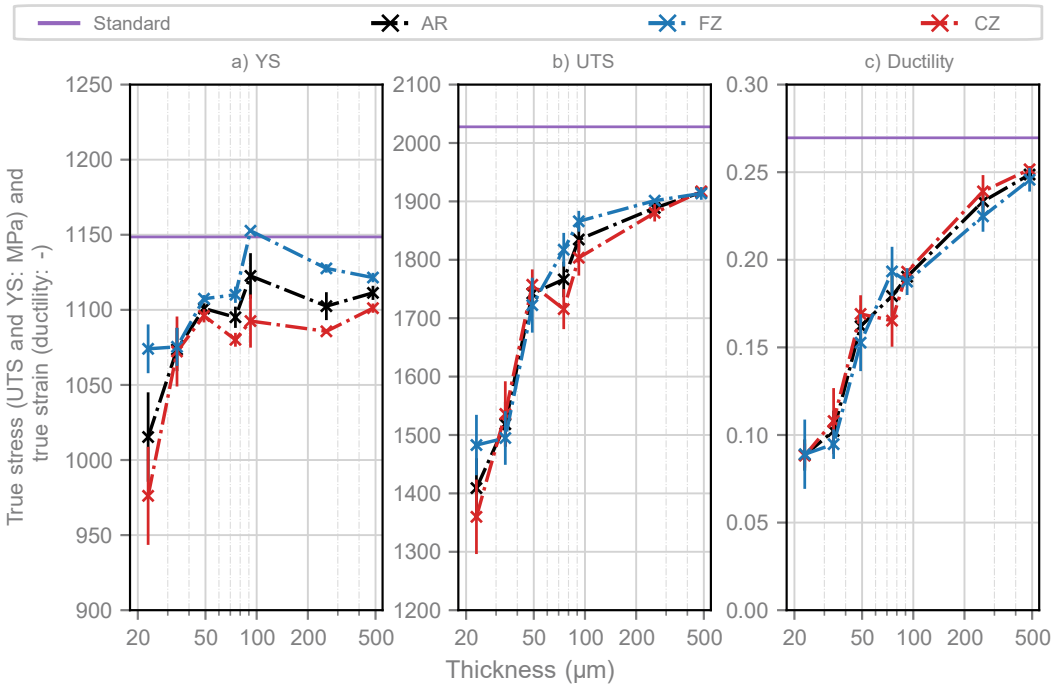

Figure 4.3: Summary of the YS, UTS, and ductility as a function of the specimens thickness of AR state for different thickness ranges

4.2.3 Fracture surface analysis

The fractographs presented below (figure 4.4 to figure 4.6) are the result of the room temperature tensile tests presented above in section 4.2.1.

The fracture surface of the AR state - 20 µm-thick specimens is presented in figure 4.4. The fracture orientation is highly dependent on the microstructure according to the change of failure plane due to a change of grain and so of crystallographic orientation in the right micrograph. Decohesion from the matrix of the primary γ' precipitates can be observed by the necking of the matrix highlighting primary γ' precipitates at the surface.

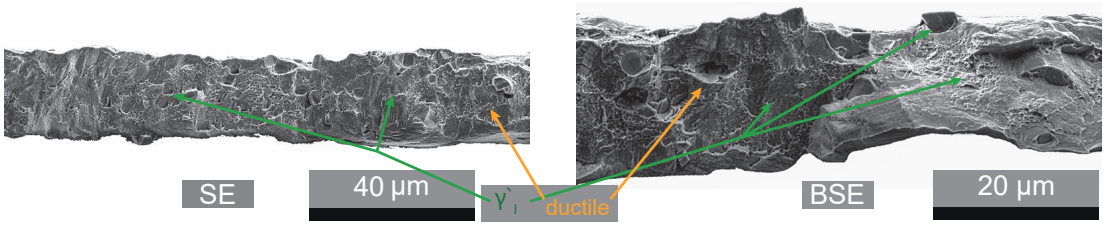

Figure 4.4: SEM fractographs of AR 26 µm-thick specimens after room temperature tensile test

The analysis of the fractography gives information about the different failure mechanisms and helps identify the failure mode. The presence of micro-voids in the

micrographs 4.5 and 4.6 confirms the ductile behavior of the material with transgranular failure mode. No change in failure mode is observed from 20 µm to 50 µm-thick specimens. The γ' particles demonstrate shearing as expected from the room temperature solicitation of such alloys, as demonstrated in 1.29. The punctual presence of borides at the sub-surface of the specimens might be of interest in the location of the failure. Both thicknesses demonstrate low necking at the specimens' surface.

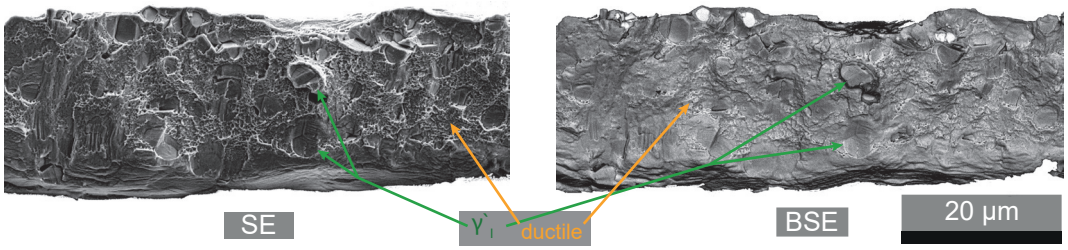

Figure 4.5: SEM fractographs of AR 26 µm-thick specimen after room temperature tensile test

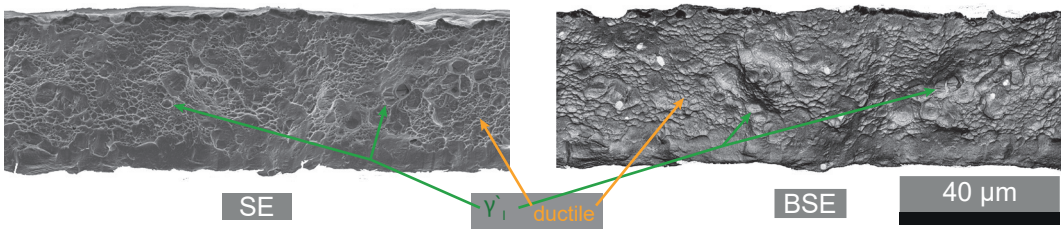

Figure 4.6: SEM fractograph of AR 50 µm-thick specimen after room temperature tensile test

Analysis

The following conclusions are obtained from the study of the AR state of thin microtensile specimens:

- A drop in YS, UTS, and ductility is observed mainly due to free-surface effect. The multicrystal-to-polycrystal transition is observed at 100 µm for the YS and UTS. The ductility demonstrates a logarithmic evolution up to 500 µm-thick specimens.
- A surge in YS is observed for the 100 µm-thick specimens. No further investigation was pursued to explain such behavior.
- AR specimens present a ductile behavior from the fractograph analysis on all specimen thicknesses, regardless of the specimen's thickness.
- The thick microtensile specimens (500 µm) demonstrate a 5 % drop in tensile properties compared to standard cylindrical specimens (on YS, UTS, and ductility).
- The strain-hardening rate demonstrates variations in the domain I, due to a more progressive elastic-to-plastic transition on thinner specimens, as presented in appendix A. The strain-hardening rate exhibits similar behavior in domains II and III due to the participation of the γ' precipitates in the hardening process of the material.

- The P2400 surface finish demonstrates no residual stresses from the grinding sequence as exposed in the appendix analysis B. The UTS and ductility are improved in the finer surface finish due to less crack initiation site, leading to less premature damage of the material.

- The use of microtensile specimens arises with technical limitations, especially to ensure the perfect planeness of the specimens. The impact of the specimens' planeness was investigated in appendix C. Not perfectly plane specimens demonstrate variations being mainly focused on the YS measurement (up to 20 % of thickness variation in thin specimens).

Very limited differences between the two extraction zones are evidenced. Minor variations are revealed on the YS with up to 50 MPa, but both UTS and ductility reveal similar values. CZ and FZ extraction zones demonstrated differences mainly in the secondary precipitates' equivalent diameter with a 10 nm decrease for the FZ zone. A decrease in secondary precipitates should induce a higher critical resolved shear stress (CRSS, down to 50 µm according to figure 1.24), which induces a higher hardening of the material and thus results in an increase in the YS. In this case, the FZ zone, with a finer secondary precipitation population, demonstrates a higher YS. The YS increase then agrees with the lowering of secondary precipitates size.

A different extraction orientation may induce variations in the specimens' texture but also in the carbides path orientation (and presence of such path) from the specimen as given in figure 2.31. No variations in the tensile RT properties from carbides paths were, nevertheless, reported in the literature. The impact of such intermetallic particles on the room temperature tensile behavior of the AR state was not investigated in this framework.

The strain-hardening rate of specimens is compared to Keller's work on pure nickel [120]. The γ/γ' polycrystal René 65 material highlights the impact of the γ' phase on the strain-hardening phenomena. Minor to no impact of the specimens' thickness is demonstrated on the strain-hardening of the specimens. Panella's work on the hardening origins in AD730^{TM} demonstrated up to 70 % contribution of the secondary and tertiary γ' precipitates onto the yield stress of the material (in fine grain microstructure, close to the one of René 65 in this framework) [223]. René 65 is less prone to strain-hardening rate modification from the specimens' thickness than of the pure nickel due to the presence of γ', the main hardening phase of René 65.

The multicrystal to polycrystal transition was measured at a t/d ratio value of about 6. Such value is close to Keller's measurements with a reported transition value of 12 to 13, as depicted in figure 1.21; but also from Texier's work on Alloys 718, in its precipitation hardened fine grain version (the closer metallurgical state to René 65 investigated), with a transition in the same range as Keller's one, as depicted in figure 1.22.

4.3 Aging effect

The aged metallurgical state for temperatures of 700 °C and 800 °C and heat treatment durations of 200 h and 600 h are presented in this section. The aging heat-treatment (HT) was performed concomitantly to the oxidized state, but having the grinding sequence after the heat treatment to ensure the complete removal of any oxidation-affected layer. Indeed, it has been verified that aged material is deprived of any oxidation-affected layers. Furthermore, the microstructural evolutions are then present in the entire volume of the specimen.

4.3.1 Stress-strain response of the aged state

The tensile behavior of the aged specimens at temperatures of 700 °C and 800 °C is given in figure 4.7 and figure 4.8, respectively. The 200 h and 600 h of heat treatment durations are exposed for specimen thicknesses of 20 µm, 50 µm, 100 µm and 500 µm with distinction on the HT duration via a lighter color for the 200 h duration. The distinction from all thicknesses is performed via a line-style chart given in the legend. Both aging temperatures are given alongside the AR behavior (from the figure 4.2). Each stress-strain curve for each temperature/time/thickness trio is chosen as the most representative for each condition (the closest to the mean behavior from the 6 specimens tested on each condition, 3 specimens per extraction zone). No distinction from both extraction zones (FZ and CZ) is performed from now on. Such consideration assumes a minor influence of the extraction zone on the microstructural changes due to the aging HT.

700 °C aged HT stress-strain response of René 65

The 700 °C HT on both durations reveals an increase in the tensile behavior of René 65, as exposed in figure 4.7. Such an observation is time-dependent with an increase of the tensile behavior with heat treatment duration in the investigated duration range. All the thicknesses stress-strain curves of the condition 700 °C-200 h present a higher YS and UTS compared to the AR state, while the 700 °C-600 h condition is higher than both metallurgical states at iso-thickness. Such an increase in tensile properties is introduced by considering the mean value of tensile properties per thickness range in figure 4.9.

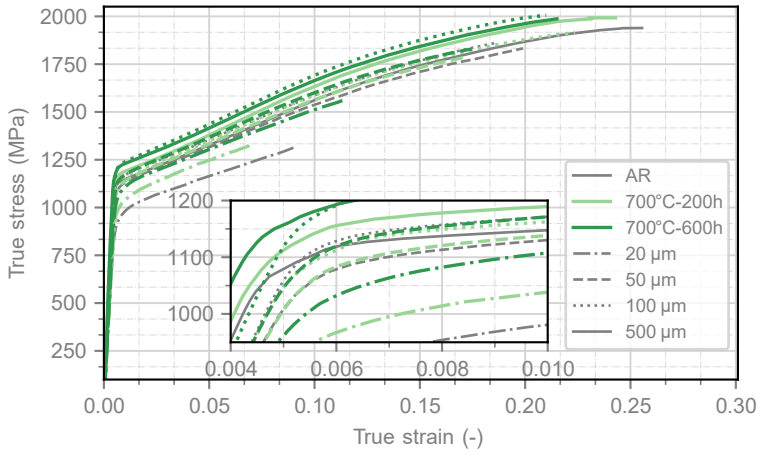

Figure 4.7: Effect of the aging heat treatment at 700 °C for 200 h and 600 h on the tensile behavior for specimens of thickness 20 µm, 50 µm, 100 µm and 500 µm compared to the AR state. The insert highlights the elastoplastic transition zone

The elastic-to-plastic transition given in the insert indicates no major modification of the strain-hardening rate from the aging HT despite the γ'_{II} and γ'_{III} evolution reported in section 3.2.2.

800 °C aged HT stress-strain response of René 65

The 800 °C HT on both durations reveals a minor decrease in all tensile properties from the AR state for specimens below 100 µm, as depicted in figure 4.8. The tensile behavior of the 20 µm-thick specimens are located above the AR state due to a higher thickness (around 35 µm instead of 20 µm). A minor decrease in tensile properties is still observed for thin specimens (as given in the summary detailed figure D.2). A 100 µm-thick mechanical properties increase observed in the AR and 700 °C aged states is not observed in the 800 °C HT temperature.

The elastic-to-plastic transition is impacted from the 800 °C aging HT on all specimens thicknesses, and especially visible on the 500 µm-thick specimens. From the early signs of plasticity to the activation of cross-slip (transition of the strain-hardening domain I to II), the strain-hardening exhibits a lower rate than that of the AR state. The strain-hardening rate then increases more over plastic strain accumulation (from 2 % to 3 %).

The analysis of γ'_{II} and γ'_{III} particles from section 3.2.2 resulted in almost complete consumption of the γ'_{III} particles in the 800 °C-600 h condition associated to 100 % increase of the γ'_{II} equivalent diameter. Such microstructural changes may be responsible for the tensile behavior evolution reported in this section.

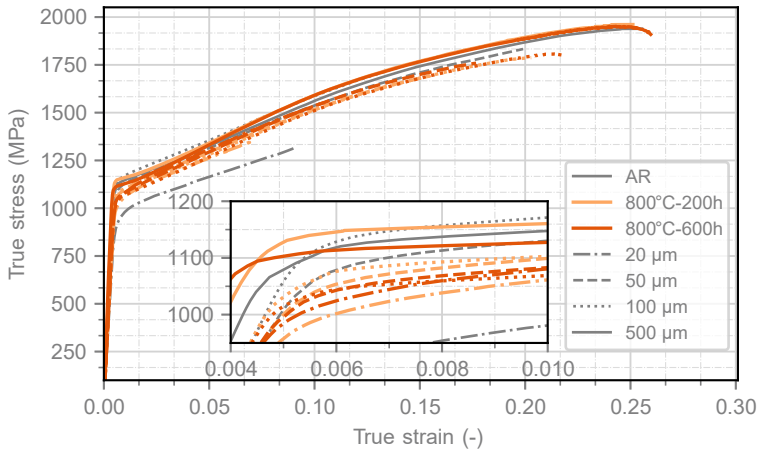

Figure 4.8: Effect of the aging heat treatment at 800 °C for 200 h and 600 h on the tensile behavior for specimens of thickness 20 µm, 50 µm, 100 µm and 500 µm compared to the AR state. The insert focuses on the elastoplastic transition

4.3.2 Summary of the tensile properties versus the thickness of aged specimens

The tensile properties after both aging (SV abbreviation) temperatures 700 °C and 800 °C and both durations of 200 h and 600 h as a function of the thickness are summarized in figure D.2 (appendix section) and figure 4.9 for the detailed and average results, respectively.

700 °C aging HT tensile behavior: summary of the tensile properties as a function of the specimens thicknesses

The 700 °C aged specimens demonstrate a higher YS and UTS from the AR state on both HT durations (200 h and 600 h) in the entire specimen thickness range. The superiority of the 600 h is observed on both the AR and the 200 h HT. The conclusions given in this section are then valid until 600 h of oxidation HT duration.

The YS presents an increase of 20 MPa to 100 MPa depending on the specimens' thickness compared to the AR state, with a maximal value on the 100 µm-thick specimens after 600 h HT. The increase in YS from the 200 h HT is in the range of 10 MPa to 70 MPa.

The UTS presents an increase in the range 40 MPa to 150 MPa for both HT durations compared to the AR state, with a 20 MPa to 40 MPa superiority on the 600 h HT.

The ductility of the specimens is nevertheless close to that obtained in the AR state up to 100 µm and then shows a decrease for 500 µm-thick specimens after 600 h of oxidation HT.

The multicrystal-to-polycrystal transition is more difficult to apprehend regarding the YS evolution due to strain-hardening lowering for low-thickness specimens on both HT temperatures. The multicrystal-to-polycrystal transition is, nevertheless, similar to the AR state with at a thickness value of 100 µm for the UTS. The ductility is still evolving up to 500 µm.

The comparison from the cylindrical standard specimens given via the dark green horizontal lines exposes similar results as for the 500 µm-thick specimens for the YS, UTS, and ductility with variations less than 1 % for the YS and UTS. The ductility is, yet, more affected by the aging HT in the cylindrical standard specimens than in the rectangular microtensile specimens. The increase in YS and UTS is observed to be of nearly the same extent in the standard tests as in the thickest microtensile specimens (500 µm).

800 °C aging HT tensile behavior: summary of the tensile properties in function of the thickness of specimens

The 800 °C HT reveals a behavior closer to the AR state than the one of the 700 °C HT.

The YS decrease down to 50 MPa might be due to a more sudden elastic-to-plastic transition leading to a lower value of YS as depicted in figure 4.8. The 600 h aging reveals a lower YS than the 200 h one due to a lower strain-hardening rate at the onset of plastic strain.

The UTS and ductility reveal a very similar behavior to the AR state on both HT durations. The strain-hardening rate of domains II and III is closer to the AR state than of the I domain, leading to a similar UTS and ductility.

The multicrystal to polycrystal transition is well established around 100 µm-thick specimens with a pronounced improvement of the YS and UTS at this thickness. The 800 °C aged specimens reveal a similar elastoplastic transition to the AR state.

The cylindrical standard specimens given via the dark orange horizontal lines expose a drop in all the tensile properties in comparison with the standard AR state (5 % drop in YS, 7.2 % drop in UTS and 26 % drop in ductility). The AR and 800 °C HT thin specimens behavior is, nonetheless, closer to the 800 °C-600 h cylindrical specimens tests in YS and UTS due to the higher tensile properties of the AR standard tests. The drop in tensile properties observed in the standard tests is subsequently less present in the thin specimens up to 500 µm with variations less than 2 % on both HT durations. A similar drop in ductility to the one observed for the 700 °C specimens is reported for the aging condition of 800 °C from the two specimens' geometries.

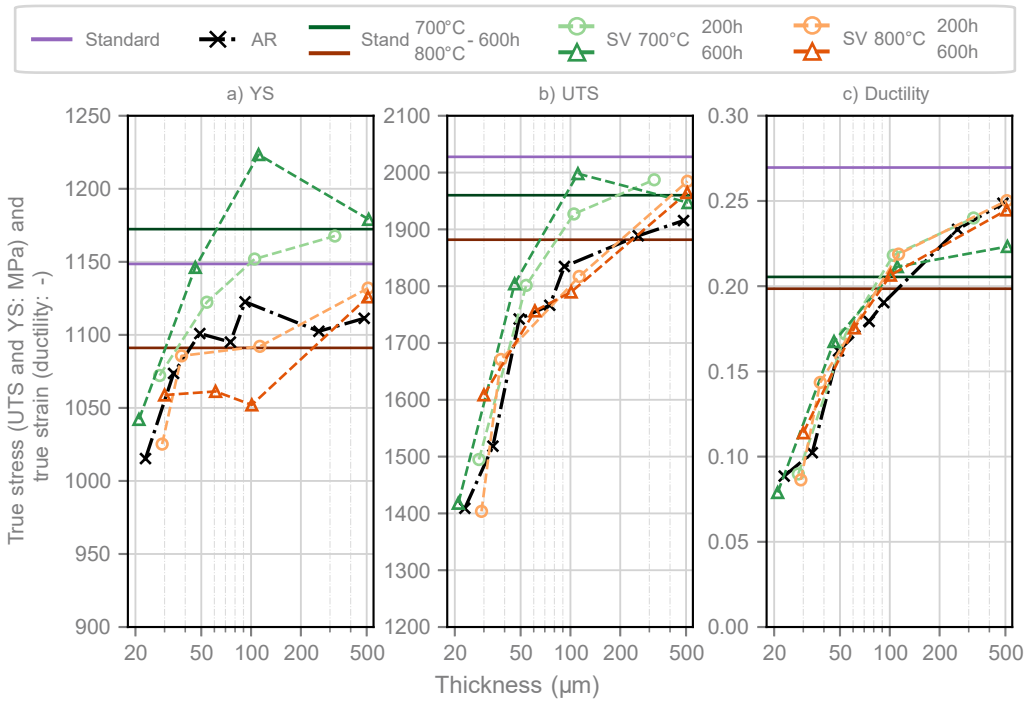

Figure 4.9: Summary of the YS, UTS, and ductility as a function of the specimen thickness for the aged conditions for different thickness ranges with regards to the AR state and the standard tests. Each point represents the average on 3 to 6 specimens

4.3.3 Fracture surface analysis

Aged specimens reveal microstructural evolutions, especially for the extreme aging condition investigated within this project, as denoted by the strong presence of TCP particles on the BSE fractographs in figure 4.10 and figure 4.11 (20 µm-thick specimens

aged at 800 °C for 200 h). The necking is more pronounced on aged specimens compared to as-receives ones. The transgranular fracture mode is, however, unchanged from the as-received specimens with the presence of voids in both fractographs.

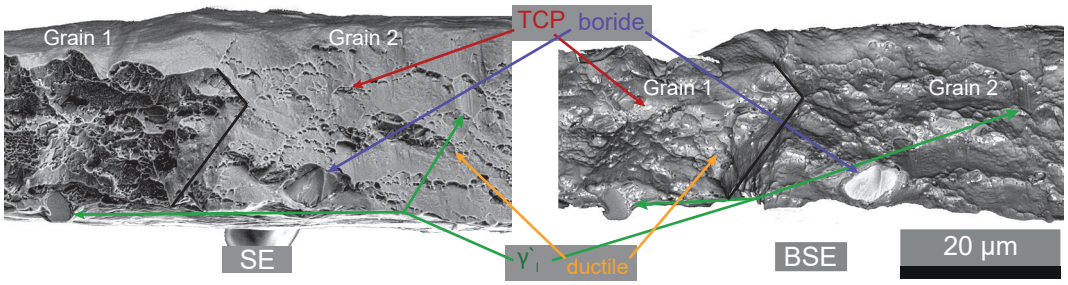

Figure 4.10: SEM fractographs of aged at 800 °C during 600 h for 20 µm-thick specimen after room temperature tensile test. TCP particles appear as small white dots on the BSE fractograph

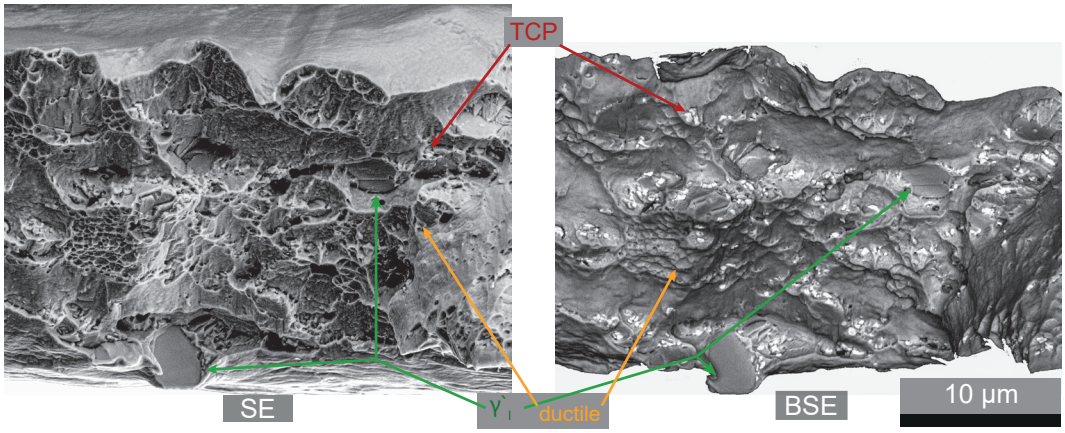

Figure 4.11: SEM fractographs of aged at 800 °C during 600 h for 20 µm-thick specimen after room temperature tensile test. TCP particles appear as small white dots on the BSE fractograph

Analysis

To dissociate any effect of the aging HT from the oxidation impact onto the tensile behavior, aged specimens evidenced:

- The aging HT at 700 °C - 200 h and 600 h induces an increase of the tensile behavior, in both microtensile and standard specimens. Such an increase evolves according to the HT duration. The 700 °C HT induces beneficial microstructural evolutions from a tensile behavior point of view with γ'_{II} and γ'_{III} equivalent diameter changes.
- The 800 °C - 200 h and 600 h aging HT demonstrate a similar tensile behavior to the AR state, but a 5 % to 10 % decrease for the standard specimens. The more important microstructural changes, especially in terms of γ'_{III} precipitates dissolution, resulting in the loss of mechanical properties for the 800 °C aging.
- The fractographs of both HT temperatures are in agreement with the AR state.

The 700 °C aged specimens demonstrate evolution of the γ'_{II} (64 nm - 35 % for AR to 51 nm - 25 % on both durations) and γ'_{III} (reduction in area fraction with HT duration) precipitates. Such evolutions may be responsible for the increase in tensile behavior as illustrated in both figures D.2 and 4.9. Such a trend has already been observed by Thebaud in AD730^{TM} but also Wessman in René 65, as depicted in figure 1.25 [34, 41]. Wessman reported an optimal size of the secondary γ' precipitates to maximize the YS of 50 nm, close to the conditions observed in the present aged conditions. The predicted room temperature YS in René 65 from Wessman modeling reports increase of 40 MPa for secondary γ' precipitates evolution of 64 nm to 51 nm, as depicted in figure 1.25 [34]. The increase in tensile properties from the 200 h to 600 h HT mainly results from the γ'_{III} evolution, as depicted in figure 3.4. The intermetallic phases (nitrides, borides, and carbides) evolution was not characterized as their impact on the room temperature tensile behavior was reported negligible from the literature analysis [8, 224].

Secondary and tertiary γ' precipitates both reported major evolution on the equivalent diameter and area fraction for aging at 800 °C. γ'_{II} precipitates revealed a 39 % increase in equivalent diameter along with 4 % decrease in area fraction. The γ'_{III} precipitates encounter almost complete dissolution with 0.3 % of remaining area fraction for the 600 h aging HT. These evolutions result in a decrease of the tensile properties from the beneficial 700 °C aging HT. The increase in tensile properties resulting from the bimodal presence of secondary γ'_{II} and tertiary γ'_{III} precipitates was experimentally evidenced and numerically demonstrated by Panella [223]. Wessman observed similar behavior on René 65 with an increase of the YS with a secondary precipitates size decrease at room temperature [34]. The decrease in tertiary precipitates population (size and area fraction) then agrees with the decrease in tensile properties at 800 °C from the beneficial evolution of the 700 °C specimens.

The γ'_{II} and γ'_{III} evolutions conclusions are temperature-dependent due to the changes in deformation mechanisms with temperature increase, as exposed in figure 1.29. The misfit from the two γ/γ' phases is also evolving with temperature increase and thus modifies the strain-hardening contribution of the γ' phases [21, 29, 225].

Another metallographic evolution between the 200 h and 600 h aged states is the presence of TCP phases. TCP particles appear along grain boundaries and primary γ' precipitates interfaces for 600 h heat-treated specimens as denoted in figure 4.11. TCP particles are known to play a deleterious role in the creep life of superalloys but demonstrate a minor impact on their tension behavior, especially at RT according to Laurence and Wessman [8, 224].

4.4 Oxidation effect

The tensile behavior of the oxidized specimens at 700 °C and 800 °C for durations of 200 h and 600 h is exposed in this section. The methodology presented in the aged section is also applied to the oxidized state. All the stress-strain curves presented in this section were computed considering the initial section value (thickness prior to oxidation). The impact of the external and internal/intergranular oxide scales is discussed on a second hand. The results for the pre-oxidized specimens are then re-evaluated by considering the whole external oxide scale as having no load-bearing capacity.

4.4.1 Stress-strain response of the oxidized states

The tensile behavior of the oxidized specimens at temperatures of 700 °C and 800 °C is given in figure 4.12 and figure 4.13, respectively. The 200 h and 600 h heat treatment durations are depicted for specimen thicknesses of 20 µm, 50 µm, 100 µm and 500 µm with distinction on the HT duration via a lighter color for the 200 h duration. The distinction from all thicknesses is performed via a line-style chart given in the legend. Both temperatures are given alongside the AR behavior for comparison (from figure 4.2). Each stress-strain curve for each temperature/time/thickness trio is chosen as the most representative for each condition (the closest to the mean behavior from the 6 specimens tested for each condition, 3 specimens per extraction zone).

Stress-strain response of René 65 oxidized at 700 °C

The improvement in tensile behavior for 700 °C observed on all thicknesses of the aged specimens is also observed in the oxidized specimens. The 700 °C condition exhibits a higher YS than that of the AR state on all thicknesses. Contrary to the aged state, the 200 h HT duration sees the highest increase in tensile behavior compared to the 600 h HT. Such an observation is particularly encountered for the thinnest specimens, with the stress-strain curve of the 20 µm-thick specimens in the same range of the 100 µm-thick AR specimens.

A spectacular drop in ductility and UTS is, however, observed with thickness reduction and HT-increased duration. The thin specimens oxidized for 600 h reveal a rupture at the onset of plastic strain (0.9 % of total strain for 9 % on the AR state). The decrease in ductility, and subsequently the UTS, is the manifestation of the premature damage caused by the external and intergranular oxide formation.

The strain-hardening of the 700 °C oxidized state is impacted to the same extent as the 800 °C aged condition. The elastic-to-plastic transition is sharper at the onset of plastic strain compared to the AR state but also the 700 °C aged state. The strain-hardening rate then increases to match the rate of the AR state in the II domain of strain-hardening.

Stress-strain response of René 65 oxidized at 800 °C

Specimens oxidized at 800 °C do not reveal the improvement observed for the 700 °C HT specimens; the tensile behavior is similar to the AR state for thicknesses above 100 µm. A major decrease of the stress-strain curve for thin specimens (below 100 µm) is observed on both oxidation durations. The 20 µm-thick specimens on both durations presents a quasi-brittle behavior with rupture in the elastic domain, or at the onset of plastic strain. The maximal stress measured on the most extreme oxidation condition (800 °C - 600 h - 20 µm) is 510 MPa.

The ductility, and subsequently the UTS, are also affected by the 800 °C oxidation, a decrease of both values being observed. The increase in oxidation duration results in a more affected stress-strain response on all thicknesses. The growth of the oxide layer (internal or external) is then responsible for the decrease in tensile behavior.

The consequences of oxidation on the microstructure evolution and the damaging processes are affecting the tensile behavior of thin specimens. The oxidation-affected layer reveals its impact on thin specimens as the ratio of affected layer versus bulk grows with the thickness reduction.

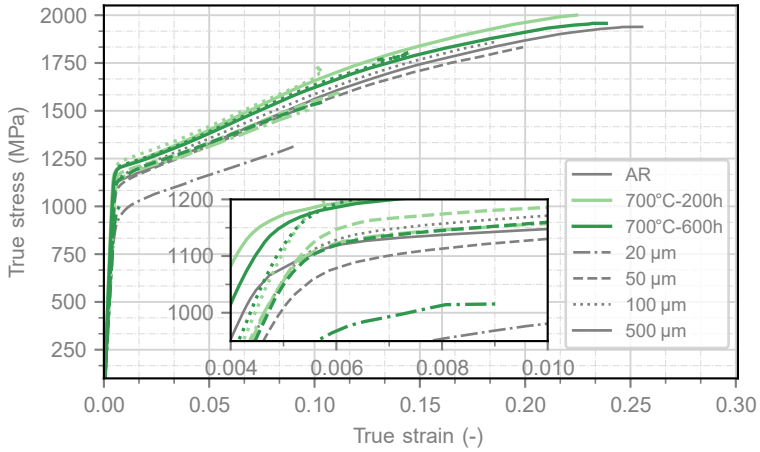

Figure 4.12: Stress-strain curves for specimens of thickness 20 µm, 50 µm, 100 µm and 500 µm oxidized at 700 °C for 200 h and 600 h compared to the AR and standard state. The insert focuses on the elastic-plastic transition

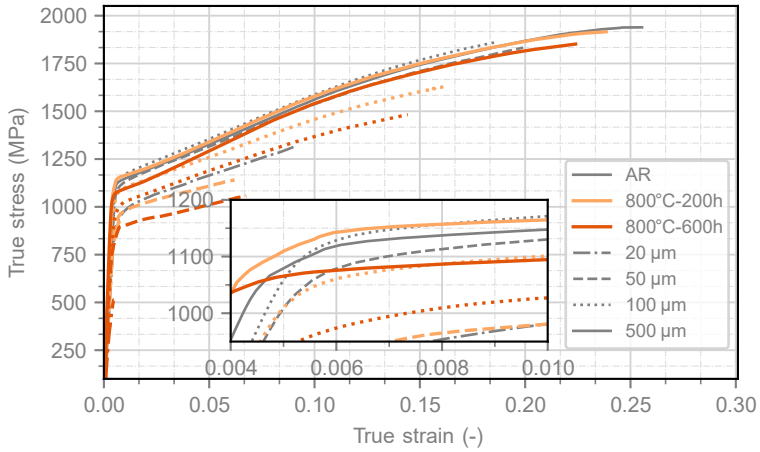

Figure 4.13: Stress-strain curves for specimens of thickness 20 µm, 50 µm, 100 µm and 500 µm oxidized at 800 °C for 200 h and 600 h compared to the AR and standard state. The insert focuses on the elastic-plastic transition

4.4.2 Summary of the tensile properties as a function of the specimen thickness

The evolution of tensile properties of oxidized specimens is compared to the AR state but also to the corresponding temperature aged state in figure D.3 and figure 4.14 for the 700 °C temperature and figure D.4 and figure 4.15 at 800 °C.

700 °C oxidation: summary of the tensile properties as a function of the specimen thickness

The effect of oxidation at 700 °C for 200 h and 600 h on the tensile behavior is similar for both durations on 100 µm and 500 µm-thick specimens. Thin specimens (below 100 µm) oxidized 200 h reveal an increase in YS, UTS, and ductility compared to the 600 h ones. The detailed analysis of each tensile property is:

The YS demonstrates a very similar behavior for all thicknesses for the 600 h aged and oxidized conditions. The external and intergranular oxide scale does not induce any modification of the elastic-to-plastic transition. The 200 h oxidized thin specimens are nevertheless located above the 600 h ones, and still 30 MPa to 80 MPa above the 200 h aged results. The 200 h oxidized specimens of thickness 100 µm and 500 µm present similar YS compared to the 600 h oxidized specimens. The 100 µm-thick "peak" in YS is observed on both oxidized durations with an increase of 50 MPa compared to the 500 µm-thick specimens.

The UTS is impaired by the oxidation process with up to a 350 MPa decrease reported for thin specimens oxidized during 600 h. Both oxidation durations reveal lower values of UTS for specimens thinner than 500 µm, while both oxidation durations of the thick specimens are in agreement with the AR, standard-aged, and aged states.

The ductility reports a major decrease for all specimen thicknesses with an average 7 % value below the aged and AR state. Specimens of thicknesses inferior to 35 µm relate all a ductility below 5 %, with a minimal value of 1 % for the 600 h oxidized condition. Both oxidation durations are in agreement despite disparities in the 100 µm-thick specimens.

The multicrystal to polycrystal transition is still explicit at 100 µm for the YS but the UTS and ductility gradually evolve up to the 500 µm-thick specimens.

No standard tests were performed on the oxidized state. The dark green horizontal line represents the 700 °C - 600 h aged condition. The comparison between the standard and the microtensile specimens was performed in the aged section 4.3.2.

The precipitation state of the oxidized specimens with the core being similar to the one in the aged state, disparities in tensile behavior observed are hence due to surface reactivity. Conclusions have to be established from fractographic analyzes presented in section 4.4.4.

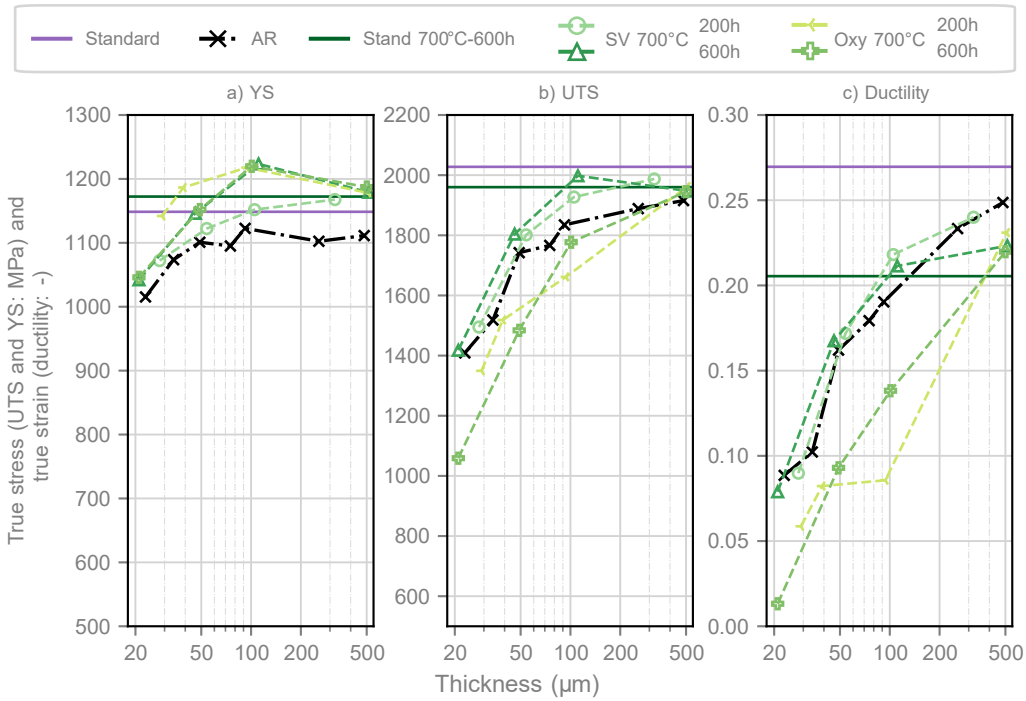

Figure 4.14: Summary of the YS, UTS, and ductility versus the thickness of the specimens for the oxidized at 700 °C condition for different thickness ranges and corresponding AR and standard behavior

800 °C oxidation: summary of the tensile properties as a function of the specimens' thickness

All tensile specimens thicknesses on the 200 h and 600 h oxidation conditions exhibit lower mechanical properties in YS, UTS, and ductility, especially for thin thicknesses. 20 µm-thick specimens broke at the onset of plasticity, around 0.8 % and 0.5 % of total strain for the 200 h and 600 h oxidation durations respectively, resulting in a major drop down in YS, UTS, and ductility. The 600 h oxidation results in a significant drop down in tensile properties compared to the 200 h oxidation HT. The detailed analysis of each tensile property is:

The YS , in the 200 h oxidation HT, demonstrates similar behavior to the ones of the equivalent aged state for 100 µm and 500 µm-thick specimens. The thinnest specimens are impacted with a 200 MPa and 100 MPa decrease for the 20 µm and 50 µm-thick specimens respectively (20 % and 10 % decrease). The 600 h oxidation leads to a decrease in YS on all specimens' thicknesses. Such a decrease is ranging from 5 % for 500 µm specimens up to 50 % for 20 µm specimens taking the equivalent aged state as a reference.

The UTS is impaired by the oxidation process with up to 40 % and 60 % decrease for 20 µm-thick specimens for oxidation times of 200 h and 600 h, respectively. The 200 h and 600 h oxidation presents lower values on all thicknesses compared to the aged results. The UTS of the 600 h oxidation HT is located below the 200 h one, the oxidation process impairs more the UTS with oxidation HT duration.

The ductility conclusions are similar to the UTS ones exposed above. The oxidation impairs the maximal strain endured by specimens due to the premature damage initiated by the oxidation products. The thin specimens present a close to null ductility as introduced above. The ductility drawback from oxidation is in the range of 10 % to 2 % in the thickness range of 20 µm to 500 µm respectively. The 600 h oxidation HT presents a 1 % to 3 % decrease compared to the 200 h one.

The multicrystal to polycrystal transition is less discernible in the 800 °C oxidized specimens due to the major impairments on all the tensile properties due to the oxidation embrittlement. A change in slope in the YS versus thickness is still noticeable at 100 µm. The UTS and ductility evolve almost logarithmically with the specimen thickness from the drop of properties in the finest specimens due to premature damage from the oxidation products, with an even greater impact regarding oxide layer depth/specimen thickness ratio (more important for thinner specimens).

No standard tests were performed on the oxidized state. The dark orange horizontal line represents the 800 °C - 600 h aged condition. The comparison between the standard and the microtensile specimens was performed in the aged section 4.3.2.

The precipitation state of the oxidized specimens being similar at their bulk from the aged state, the disparities in tensile behavior observed are likely due to surface reactivity matters. Conclusions are to be established from the fractographic analyzes presented in section 4.4.4.

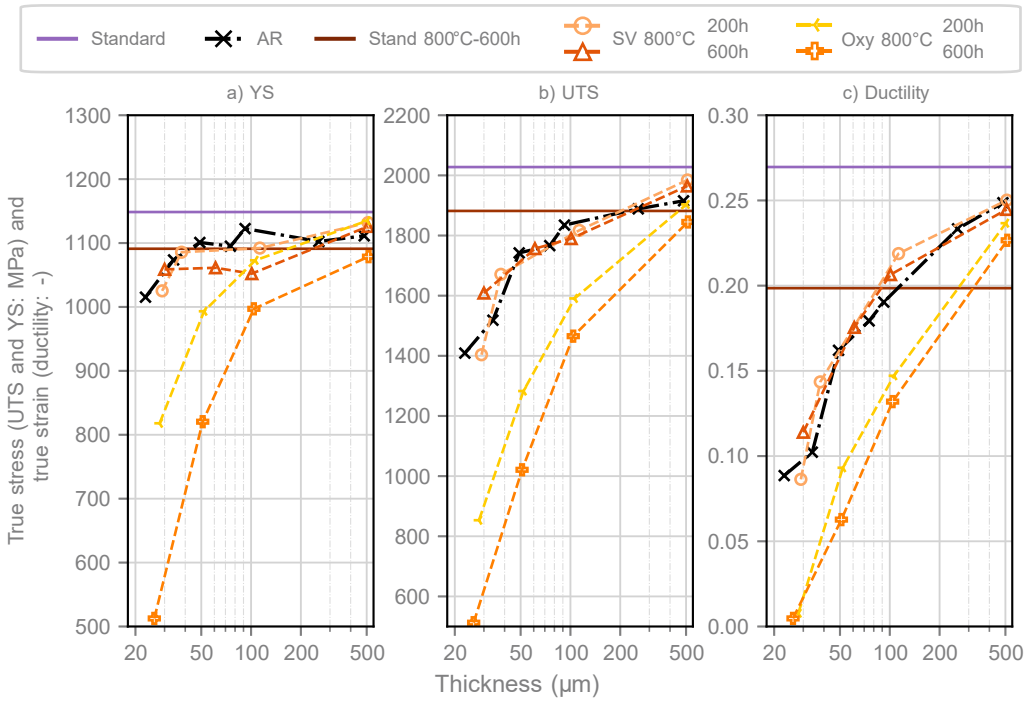

Figure 4.15: Summary of the YS, UTS, and ductility versus the thickness of the specimens for the oxidized states at 800 °C for different thickness ranges and corresponding AR and standard behavior

4.4.3 Impairments from the oxide scale - gradient-extraction of thin specimens

Methodology

To apprehend the impact of oxidation on the mechanical behavior, the JIG grinding methodology was used to extract ultrathin (20 µm and 50 µm) specimens from oxidized microtensile ones of initial thickness 250 µm. Two types of extraction are performed to investigate the contribution of the external chromia and the intergranular alumina layers or the contribution of the intergranular alumina layer only. To ensure such characterizations, the "grad Cr" specimens are ground on side A down to the core of the specimen by preserving the chromia and alumina layer on side B. The "grad Al" specimens are ground on side A down to the core of the specimen and then removed from the chromia layer on side B. Both denominations are used in figure 4.17 for the 700 °C oxidation HT and figure 4.18 for the 800 °C oxidation HT. Both gradient-extracted specimens' cross-sections are given in figure 4.16.

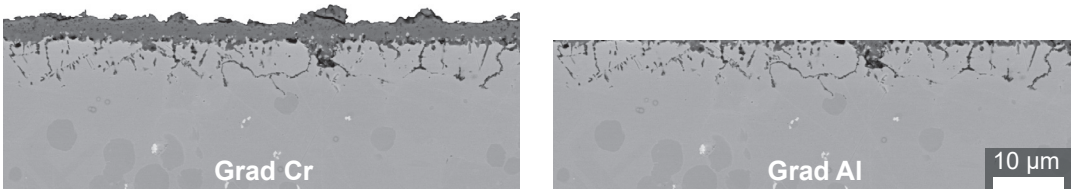

Figure 4.16: SEM-BSE cross-section micrographs representative of the grad Cr and grad Al, microstructures

700 °C oxidation HT behavior

The 700 °C oxidized gradient-extracted specimens demonstrate a similar behavior to the AR state in terms of YS for the 200 h duration on both grad Al and grad Cr specimens. Grad specimens YS results are below the oxidized specimens YS for the equivalent duration (100 MPa below) but also compared to the equivalent aged state (50 MPa below). No discernible trend is observed for both extraction methods (with and without the external chromia layer). The decrease in YS is furthermore observed on the 600 h oxidation HT of the grad Cr specimens compared to the AR, aged and oxidized states. Even though the oxide layers (external and internal) are relatively thin compared to the thickness of specimens for the 700 °C oxidation HT up to 600 h, the section of the gradient-extracted specimens is updated after the final grinding (which includes the oxide layer), that differs from the pre-oxidation measurement performed on the oxidized specimens. Post oxidation measurement takes into account the maximal value of the specimen thickness, *i.e.* above the titania island topping the γ'_I precipitates. The thickness is then overestimated (up to 3 µm) compared to the oxidized specimens (pre-oxidation measurement), leading to a lower value of YS.

The UTS and ductility are, however, closer to the AR and aged state than those measured in the oxidized state. Thin specimens reveal a UTS and ductility halfway from the oxidized and the aged states, which is coherent with the composition of the graded specimens. Only one side of the specimen sees premature damage from the presence of the oxidized layers, which induces a tensile behavior above the fully-oxidized specimens, but below the aged or AR states.

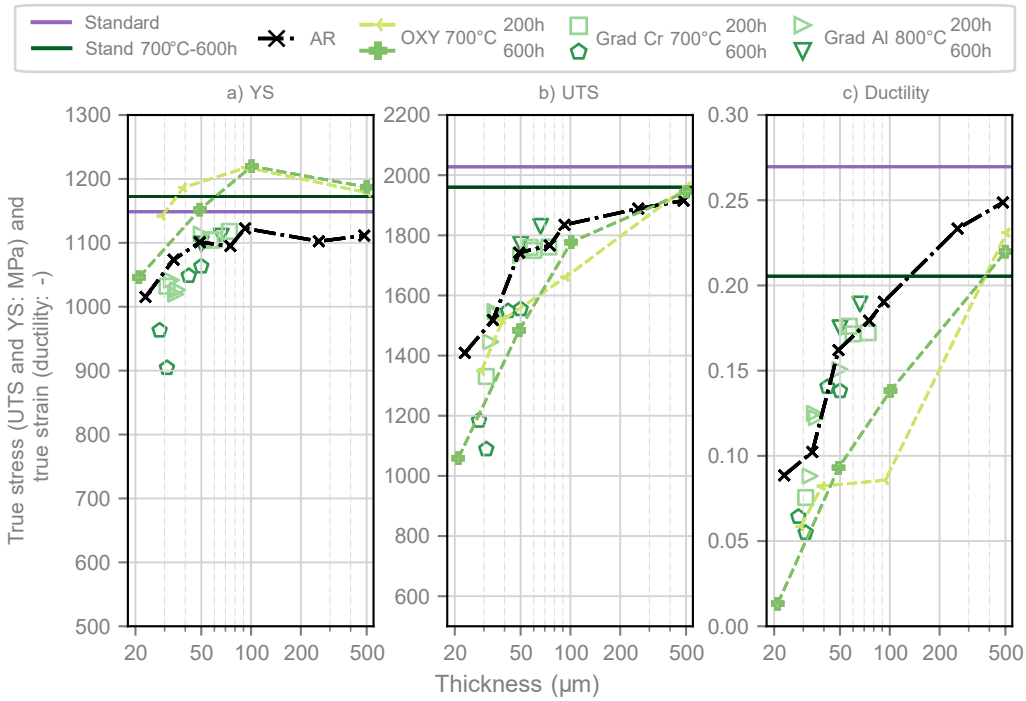

Figure 4.17: Detailed summary of the YS, UTS, and ductility versus the specimen thickness of gradient extracted specimens oxidized at 700 °C, corresponding AR and standard behavior

800 °C behavior

The 800 °C grad Al and Cr specimens present fewer experimental data due to the extreme difficulties and sensitivity in extracting 20 µm-thick specimens made of oxidation-affected layers of almost half their thickness. Interestingly, their tensile behavior reveals a YS, UTS, and ductility halfway between the oxidized and aged specimens.

The major impact of oxidation on the mechanical properties drop at 800 °C is exacerbated by the oxidized layers removal of one of the two sides. The grad Cr is far more impacted by the oxidation process compared to the grad Al specimens, despite its 5 µm to 10 µm-thinner specimen thickness. The 2 µm to 3 µm external chromia layer seems to be one of the driving factors of the mechanical properties drop and premature damaging of the 800 °C oxidation HT. Such a result differs from the 700 °C HT certainly due to the thicker external oxide.

The intergranular alumina spikes are, nevertheless, also responsible for the mechanical degradation, as demonstrated by the 200 MPa drop in YS, 300 MPa drop in UTS and 5 % drop in ductility compared to the aged and AR states (similar on both).

No fractography was performed on the gradient-extracted specimens as the oxidation impact is not supposed to differ from the fully oxidized specimens.

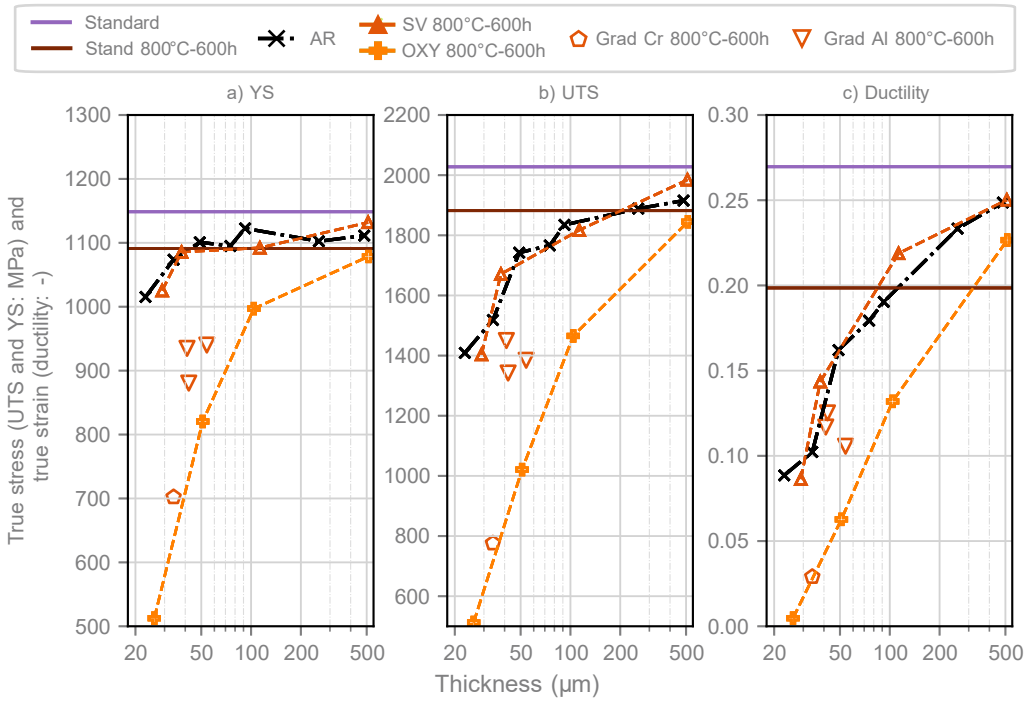

Figure 4.18: Detailed summary of the YS, UTS, and ductility versus the specimen thickness of gradient extracted specimens oxidized at 800 °C, corresponding AR and standard behavior

4.4.4 Analysis of the rupture and fractographs

The surface reactivity and sub-surface microstructural evolution gradually impact the failure mode, as exposed in figure 4.20 to figure 4.22.

The external oxide layer (Cr_2O_3) presents a typical brittle behavior at both temperatures.

The primary γ' precipitates reveal oxidation differences for both oxidation temperatures. At 700 °C, the intra-precipitates and matrix precipitates are decorated by alumina spikes demonstrating the decohesion of the γ'_I from the matrix, as depicted in figure 4.19. At 800 °C, the complete oxidation and so consumption of the primary γ' precipitates reveals similar brittle behavior as expressed by the external chromia layer.

The oxidation-affected layer presents an intergranular failure mode. The 800 °C fractographs reveal the presence of TCP particles which appear to affect the brittle to ductile transition with the lack of TCP particles in the oxidation-affected layer, *i.e.* the Cr-depleted layer (evidenced in figure 4.20 and 4.22).

The bulk of specimens demonstrate ductile failure mode similar to a coherent facies to the AR state ductile behavior with the presence of voids.

The rectangular section of the specimens did not present either any obvious initiation site or strain localization phase from the tensile fractographs. The oxidation-affected

layers are nevertheless exacerbated with different failure modes from the bulk of the specimens.

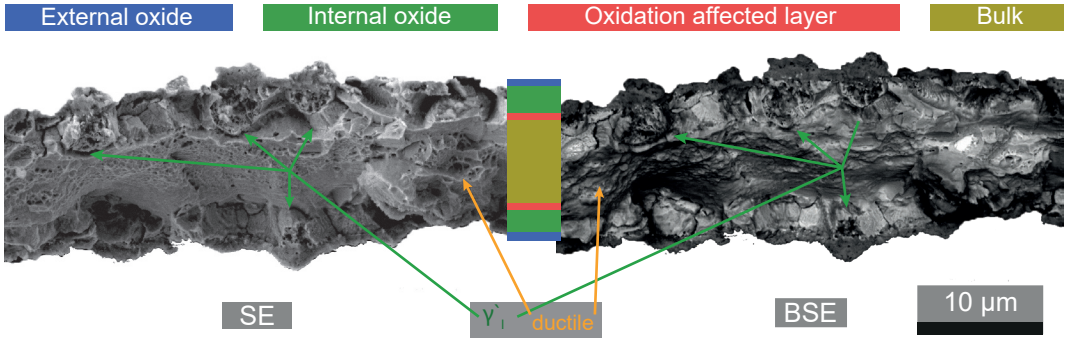

Figure 4.19: SEM fractographs of 20 µm-thick specimen oxidized at 700 °C during 600 h after room temperature tensile test

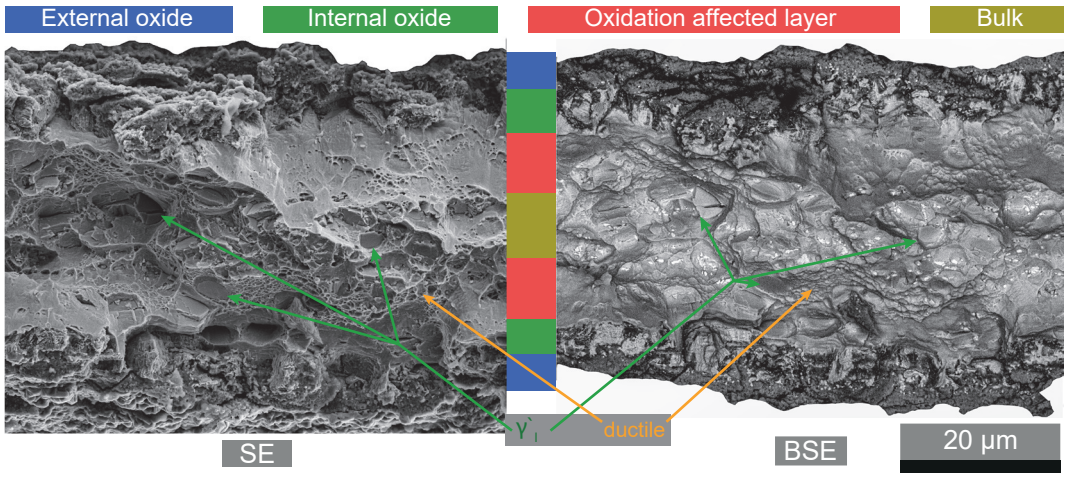

Figure 4.20: SEM fractographs of 50 µm-thick specimen oxidized at 800 °C during 200 h after room temperature tensile test

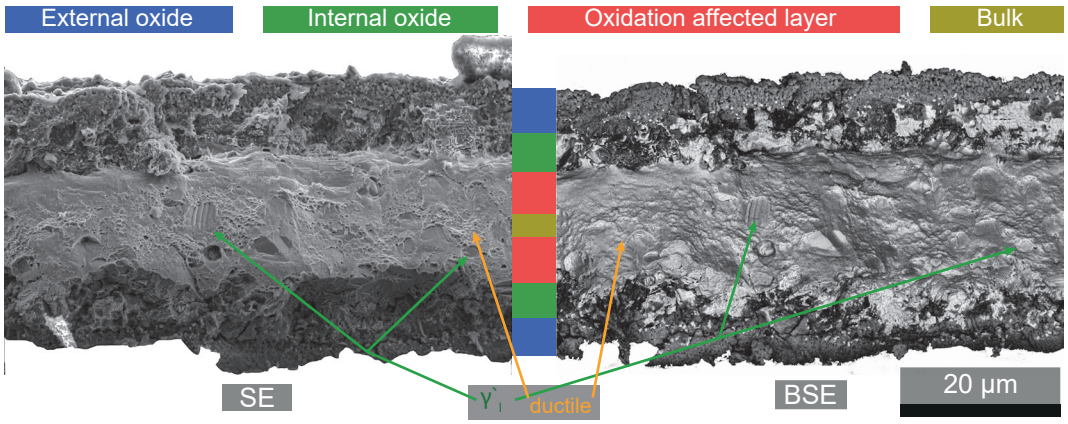

Figure 4.21: SEM fractographs of 45 µm-thick specimen oxidized at 800 °C during 600 h after room temperature tensile test

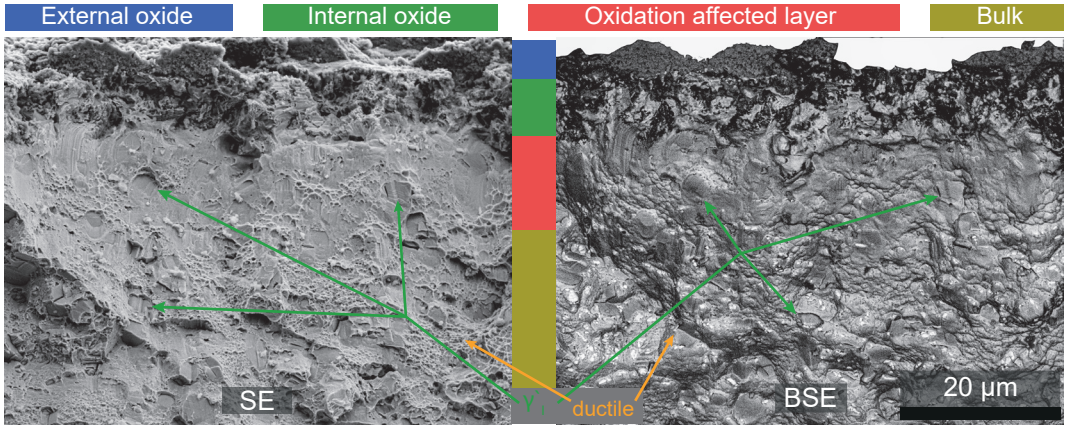

Figure 4.22: SEM fractographs of 101 µm-thick specimen oxidized at 800 °C during 600 h after room temperature tensile test

Mechanical properties drop after oxidation due to the brittle external chromia layer, the presence of internal alumina spikes, and a ductile primary γ' precipitates-free layer. This observation is enhanced with an increase in the oxidation-affected thickness versus the total thickness ratio. External and internal intergranular oxidation along with the Cr- and TCP-depleted layers demonstrate the critical role of surface reactivity in the mechanical properties, as revealed by the drop in YS, UTS, and ductility from aged to oxidized results.

The lowering of the tensile characteristics of the specimens oxidized during 600 h compared to the ones oxidized during 200 h arise from the extension of the oxidation-affected layer increasing with the oxidation duration due to premature damage within this layer. Such low ductility on thin specimens could emanate from the damaging of grain boundaries on the entire thickness from oxidation, as observed in the 800 °C - 600 h oxidized sample for which the initial thickness was 10 µm as shown of SEM-BSE micrograph in figure 4.23 [11].

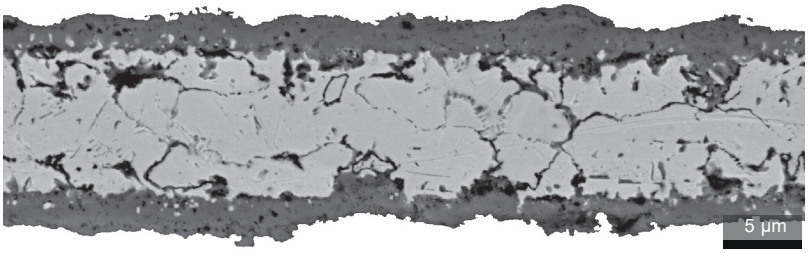

Figure 4.23: SEM-BSE cross-sectional micrograph of a René 65 10 µm-thick specimen oxidized at 800 °C during 600 h

Interrupted tensile tests and analysis of the surface

Interrupted tensile tests were performed between 0.35 % and 2 % plastic strain to document the damaging process occurring at the surface of oxidized specimens. Both temperatures of 700 °C and 800 °C report oxidized emerging γ'_I precipitates cracking at low strain values as depicted in figure 4.24. The oxidation condition 700 °C - 200 h reported only a few γ'_I cracked in the entire specimen gage with an imposed plastic strain of 2 % (assessed via HR-DIC technique). The oxidation condition 800 °C - 200 h

reported a high fraction of cracked γ'_I precipitates with an imposed plastic strain of 0.35 %. Such an oxidation condition also revealed propagation of the cracks into the chromia layer.

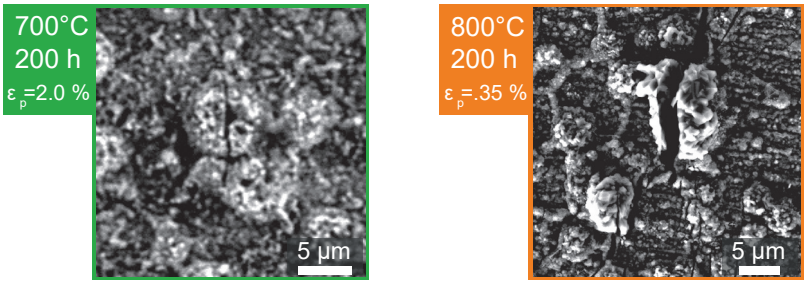

Figure 4.24: SEM-SE micrograph of a surface oxidized γ'_I on at 700 °C - 200 h (left) at plastic strain of 2 % and 800 °C - 200 h (right) at plastic strain of 0.35 %

Analysis

The oxidation impact on the room temperature tensile behavior of René 65 demonstrated the following conclusions:

- Oxidized specimens at 700 °C demonstrate a slight increase in the YS compared to the aged and AR states, especially for very thin specimens ($e \leq 100\,\mu m$). The external chromia layer appears to enhance the strain-hardening of the material due to non-free surface effect. The oxidation impact, nevertheless, results in premature damage of the specimens, as demonstrated by the drop in UTS and ductility (especially visible on thin specimens). Such conclusions are in agreement with the high resistance to cracking of thin oxide layers exposed in figure 1.31.
- Oxidized specimens at 800 °C demonstrate a drop in YS, UTS, and ductility, evolving accordingly to the HT duration. A 50 % decrease in YS is observed on the critical oxidation condition 800 °C - 600 h compared to the AR state, with specimen rupture nearly in the elastic regime. The low thicknesses are especially impacted by the oxidation processes due to the important oxidation-affected layer/total specimen thickness ratio.
- The external chromia layer and the intergranular alumina spikes induce mechanical degradation, as demonstrated via the gradient-extracted specimens.
- Oxidized specimen fractographs comfort a brittle behavior of the external chromia layer. The 700 °C inter-precipitate and intergranular oxidation results in oxidation-affected primary γ' precipitates decohesion. The 800 °C intergranular oxidation demonstrates a brittle behavior on the oxidation-affected behavior. The brittle to ductile transition progressively takes place in the oxidation-affected layer below maximal intergranular penetration depth (γ'_I-free layer, chromia diffusion layer, TCP-free layer).
- Interrupted tensile tests reveal cracks in the oxidation-affected γ'_I precipitates at the surface on both temperatures at relatively low plastic strain levels.

The decrease in YS at 800 °C, especially in 20 µm-thick specimens, is not only caused by the oxidation impairments, but by the sub-surface primary γ' precipitates free depleted zone inducing a reduction in the strain hardening of the material. Such depletion depths compared to the total thickness of "intact" material at the specimens' core ensure the participation of the solid solution layer in the decrease in YS of the material, as depicted in figure 4.19.

The cracking of the primary γ' precipitates at a stress level close to the YS was also evidenced by Cruchley on RR1000 alloy. Cruchley demonstrated apparition of cracked oxidized primary γ' precipitates starting from 800 MPa [212, 226]. The stresses associated to the 2 % and 0.35 % of plastic strain in presented in figure 4.24 are of 1200 MPa to 1250 MPa, respectively.

The FG region, with smaller primary γ' precipitates but with a constant area fraction from the MG region, exposes a smaller inter-particle distance. The cracking of those primary γ' precipitates, and the relative interconnection from their proximity to each other, should be monitored in analyzing the damage process of the material.

4.5 Primary γ' precipitates and grain size contribution

4.5.1 Stress-strain curves of the AlbiSolvus state

The AlbiSolvus (AS) state, with an average grain size of 52.3 µm, and the punctual presence of primary γ' precipitates (0.89 % area fraction) is expected to behave differently from the AR state (grain size: 7.8 µm; primary γ' precipitates equivalent diameter and area fraction: 2.03 µm - 11.8 %). The stress-strain response of the AS state compared to the AR state is presented in figure 4.25, along with the oxidized AS state at 800 °C during 200 h and 600 h.

The AS state exhibits a lower YS, UTS, and ductility on all specimen thicknesses compared to the AR state. The elastic-to-plastic transition is much more progressive compared to the AR state, especially on the 500 µm-thick specimens. The strain-hardening rate exposes minor differences from the AR state, particularly in the total strain range of 0 % to 5 %. Specimens with thicknesses 20 µm, 50 µm and 100 µm exhibit a similar strain-stress response in terms of YS and strain-hardening rate, but exhibit a drop in ductility and a corresponding drop in UTS.

The AS oxidized state presents a decrease in mechanical behavior on all thicknesses, with a more important drop with the oxidation duration. The 200 h AS oxidized specimens exhibit a drop in YS, UTS, and ductility while the 600 h AS oxidized state is located below both AS and 200 h AS oxidized specimens. The strain-hardening rate is in agreement with the AS state. The extreme oxidation condition of 800 °C - 600 h oxidation on the AS state of thickness 20 µm failing in the elastic domain due to the severe degradation from the oxidation process. The 200 h specimens present a failure in the early plastic regime (less than 1 %).

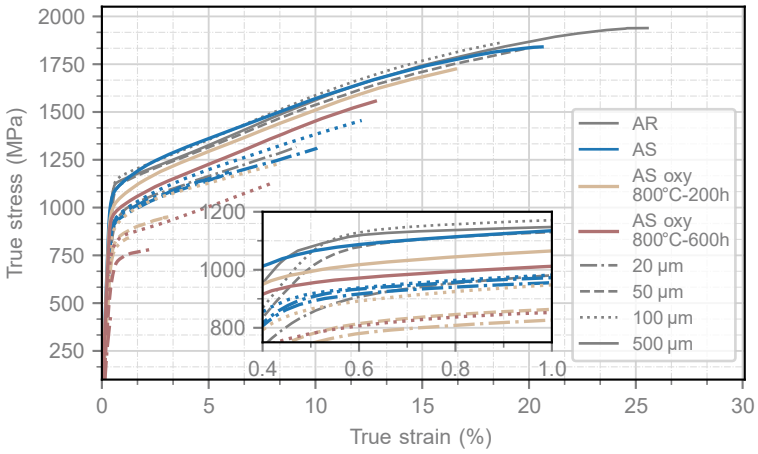

Figure 4.25: Stress-strain curves of the AS state with and without oxidation at 800 °C for 200 h and 600 h for specimen thicknesses of 20 µm, 50 µm, 100 µm and 500 µm compared to the AR state. The insert highlights the elasto-plastic transition

4.5.2 AS and 800 °C AS oxidized HT tensile behavior: summary of the tensile properties as a function of the specimen's thickness

The AS state is to be first introduced and compared to the AR state. The AS-oxidized state is then to be compared to the AS and AR-oxidized state for all tensile properties:

The YS of the AS state demonstrates a stable value up to 100 µm-thick specimens, which represents a t/d ratio of around 2 (t for specimen thickness and d for mean grain size). Such a result is in agreement with Keller's observations, as exposed in figure 1.21, but with a higher value of t/d (1 in pure nickel reported by Keller) [120]. The 500 µm-thick specimen in the AS state reports lower values than those in the AR state. The drop in YS of the thick specimens is in agreement with the drop of YS of the standard specimens from the AR to the AS state due to the grain size increase.

The YS of the AS-oxidized state does not present a similar stable plateau as compared with the AS state for the lower samples thicknesses. The effective section reduction inherent to the oxidation process does induce a logarithmic evolution of the YS as a function of the specimens' thickness on both oxidation durations of 200 h and 600 h at 800 °C. The oxidation duration accelerates this deleterious impact on the YS, as shown by the 600 h oxidized specimens being 50 MPa to 100 MPa below the 200 h ones. The 100 µm to 500 µm YS evolution of the AS-oxidized specimens follows the same trend as the AS-not-oxidized ones. The low t/d ratio of the AS-oxidized specimens reveals a different behavior from the AR-oxidized ones.

The UTS of the AS and AS-oxidized states exposes a similar behavior for all thicknesses with a drop due to oxidation phenomena. The oxidation duration increase results in a UTS drop-down due to premature damage and rupture of the specimens. The UTS evolution of all AS states rate versus the specimens' thickness demonstrates a logarithmic behavior.

The ductility reveals similar conclusions to the UTS on all AS conditions (not oxidized and oxidized at 800 °C during 200 h and 600 h.)

The multicrystal-to-polycrystal transition of the AS state reveals a lower limit of t/d ratio (2, equivalent to 100 µm) for which the YS shows a quasi-monocrystalline domain. The AS oxidized YS does not demonstrate any transition on the YS certainly due to the oxidation impairment of the effective section. Both UTS and ductility demonstrate a logarithmic behavior on all AS conditions.

AS standard tests were performed and reported with the blue horizontal line in figures D.5 and 4.26. The AS standard tests demonstrate a drop in YS, UTS, and ductility compared to the AR specimens. A similar drop is also observed from the AR and AS microtensile specimens on all properties. No oxidation tests were performed on oxidized standard specimens as this point was judged out of the scope of the present project.

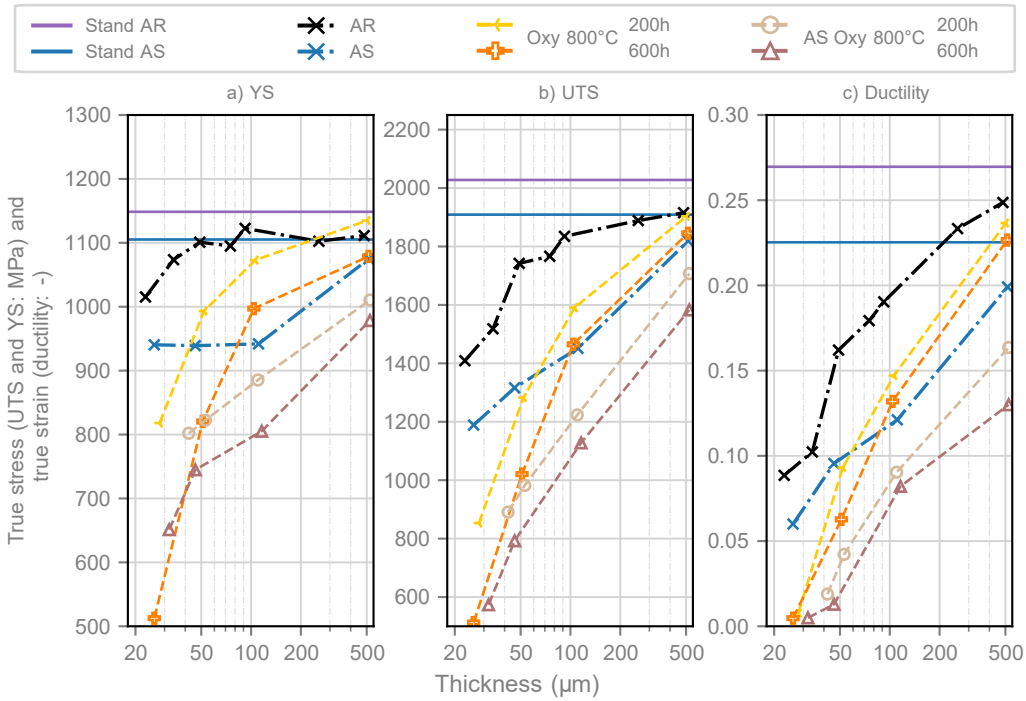

Figure 4.26: Summary of the YS, UTS, and ductility versus the specimens' thickness in the AR state (in black), AR oxidized (yellow and orange) at 800 °C for 200 h and 600 h, AS state (blue) and AS oxidized at 800 °C (light brown and brown) during 200 h and 600 h

4.5.3 Fractographic analyzes

The AS state fractographs given in figure 4.27 reveal the quasi-monocrystalline behavior of the 50 µm-thick specimen (t/d ratio of 1). The crystallographic orientation of the grains appears to control the failure of the specimens whereas remaining still ductile with the presence of voids observed in the SEM-BSE fractographs.

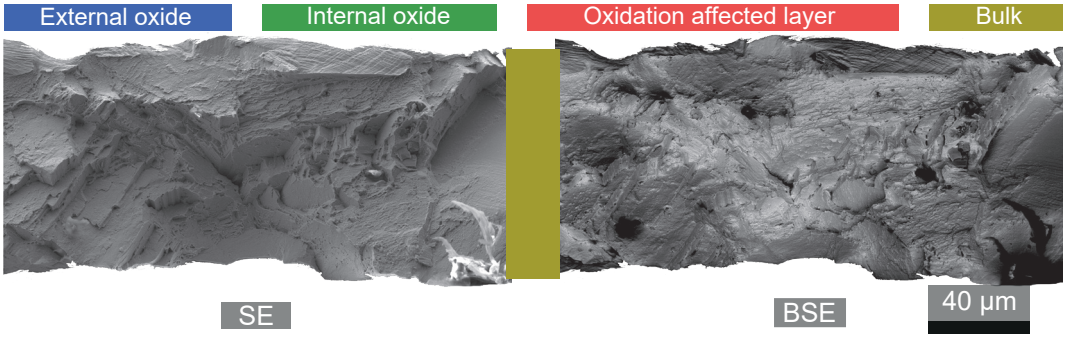

Figure 4.27: SEM fractographs of 50 µm-thick AS specimen after room temperature tensile test

The difference in oxidation mechanism from the AR state with mainly internal alumina stings reveals the presence of voids in the internal oxidation-affected layer. The external chromia layer reveals a very low adhesion to the surface of the specimens, as depicted in figure 4.29, with a brittle behavior similarly to the AR oxidized state.

A transition is observed from the oxidation-affected layer (presence of voids) to the bulk of specimens being crystallographically driven. Such transition is noticed with the appearance of white TCP particles in the SEM-BSE fractographs 4.28, 4.29 and 4.30 from 200 h HT at 800 °C.

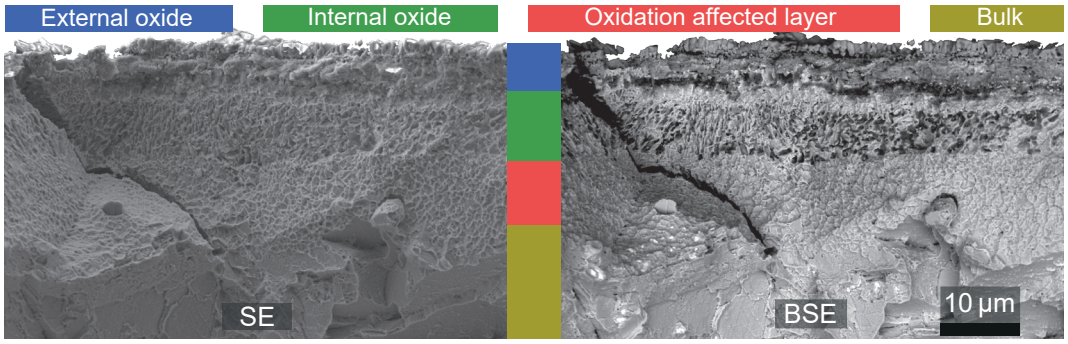

Figure 4.28: SEM fractographs of 108 µm-thick AS specimen oxidized during 200 h at 800 °C after room temperature tensile test

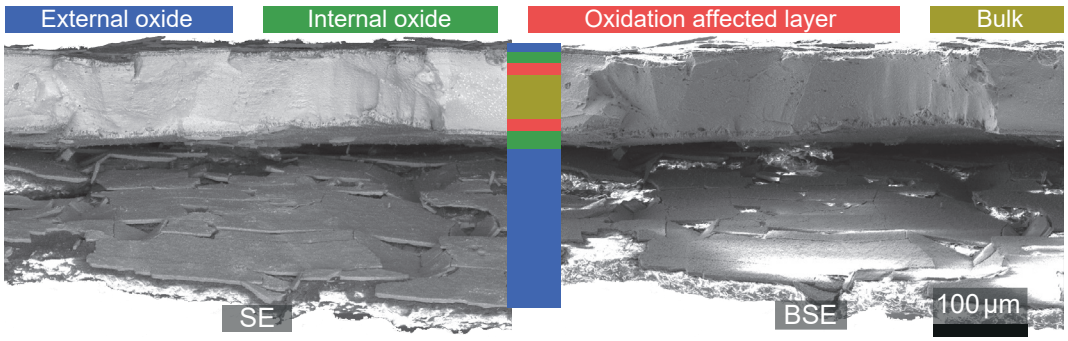

Figure 4.29: SEM fractographs of 104 µm-thick AS specimen oxidized during 600 h at 800 °C after room temperature tensile test

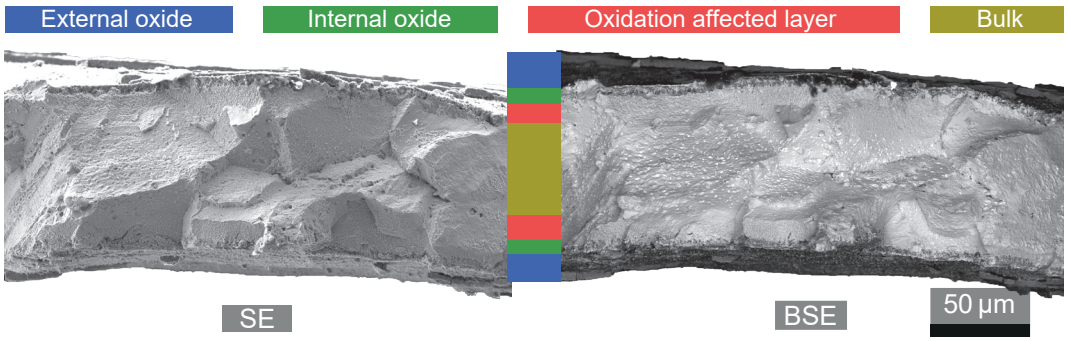

Figure 4.30: SEM fractographs of 104 µm-thick AS specimen oxidized during 600 h at 800 °C after room temperature tensile test

Analysis

The following conclusions were evidenced from the study of the AS and AS-oxidized thin microtensile specimens:

- The AlbiSolvus (AS) state exposes a constant YS for t/d ratio below 2 indicative of a quasi-monocrystal to multicrystal transition. The AS state demonstrates a drop in tensile properties (YS, UTS, and ductility) due to the grain size increase but also the decrease in secondary (40.3 nm - 30 %) and tertiary (19.7 nm - 1.2 %) precipitates size.

- AS-oxidized specimens at 800 °C show a drop in tensile behavior in agreement with the oxidation duration. No quasi-monocrystal to multicrystal transition in the YS is observed on the oxidized-AS specimens. The tensile properties decrease is less prominent from the AR-oxidized state due to the changes in internal oxidation (in %, considering the thickness of specimens). AS state reveals mainly internal oxidation due to the higher grain size resulting in fewer grain boundaries volumetric fraction in the material.

The effect of both: decrease in secondary precipitates, and increase in grain size diminish the hardening capacities of the material, as revealed by the 50 MPa decrease in YS observed on standard AS specimens compared to the AR ones. The contribution to the YS of the secondary precipitates is supposed to induce a 25 MPa decrease according to Wessman computations exposed in figure 1.25. The contribution of the grain size in the YS evolution reports a decrease of 70 MPa according to the Hall-Petch relation given in equation 1.15 and assuming a value of $k = 305\,\text{MPa}\,\mu\text{m}^{0.5}$ from Panella's work [223].

The deleterious effect of the grain size increase surely induces a decrease in strain hardening of the material. The secondary γ' precipitates contribution to the strain hardening is coupled with tertiary γ' precipitates in the actual René 65 microstructure, as compared to Wessman's work [34]. The secondary and tertiary γ' precipitation states are then responsible for 25 MPa increase in YS compared to the ones in the AR state.

4.6 Impact of the oxidation process on the effective section of specimens

All the results on the oxidized specimens presented above were computed using the initial thickness of the specimens (prior to oxidation). The oxidation process nevertheless modifies the effective load-bearing section of the specimen due to the reactants' consumption from supplying the oxidation reaction. The oxide/metal interface is reported to migrate in the direction of the bulk according to the Pilling and Bedworth ratio, as reported in the literature section 1.2.2, thus leading to metal recession.

The thickness of the external chromia layer was measured lower than 1 µm at 700 °C up to 600 h and at values of 1.75 µm and 3 µm at 800 °C on the 200 h and 600 h durations, respectively. If considering the external chromia layer as providing no load-bearing capability, the effective section is reduced from the external chromia thickness divided by its PBR (2.07). The participation of the surface and sub-surface grains can also be altered by the presence of intergranular alumina or the solid solution layer due to the γ' precipitates depletion.

To document and quantify such changes in the effective section from the oxidation process, the YS of oxidized specimens is compared to the aged specimen ones. The YS reference is extracted from the average behavior of the aged state in figure 4.14 and 4.15. Linear interpolation is performed of the reference YS behavior to match the same thickness of the oxidized specimens. The difference from the aged reference YS to the oxidized state is performed on each specimen, as given in figure D.3 and D.4. Such a gap is then supposedly caused by a change in the effective section with the strong hypotheses of no load-bearing of the oxidized layer. The results are displayed in table 4.2 in terms of thickness deviation for one specimen face from the As-Received measured thickness (prior to oxidation). Negative values are a sign of thickness shrinkage while positive ones result in a thicker specimen. This gap is given in thickness shrinkage (in µm) and relative shrinkage considering the average thickness of all the specimens in the thickness range (given as header in the table 4.2). The uncertainty stems from the experimental scatter (standard deviation).

			20 µm	50 µm	100 µm	500 µm
700	200	(µm)	0.9 ± 0.9	1.5 ± 0.6	3.0 ± 0.9	− 0.6 ± 2.5
		(%)	3.2 ± 3.4	4.3 ± 2.2	3.2 ± 1.0	0.1 ± 0.5
	600	(µm)	0.0 ± 1.0	0.1 ± 0.7	0.2 ± 1.6	1.5 ± 2.9
		(%)	0.2 ± 4.7	0.4 ± 1.5	0.4 ± 1.6	0.3 ± 0.6
800	200	(µm)	− 2.7 ± 0.9	− 2.2 ± 0.6	− 0.9 ± 1.2	0.8 ± 4.0
		(%)	− 9.8 ± 3.6	− 4.3 ± 1.2	− 0.9 ± 1.1	0.2 ± 0.8
	600	(µm)	− 6.7 ± 0.0	− 5.8 ± 0.4	− 2.8 ± 0.3	− 11.0 ± 3.2
		(%)	− 25.8 ± 0.0	− 11.3 ± 1.4	− 2.7 ± 0.3	− 2.1 ± 0.6
AS 800	200	(µm)	− 3.1 ± 0.4	− 3.2 ± 0.8	− 3.3 ± 0.6	− 16.4 ± 0.5
		(%)	− 7.3 ± 0.9	− 6.2 ± 2.0	− 3.0 ± 0.7	− 3.1 ± 0.1
	600	(µm)	− 4.9 ± 3.5	− 4.8 ± 1.4	− 8.5 ± 0.4	− 24.0 ± 2.3
		(%)	− 15.4 ± 11.1	− 10.3 ± 3.1	− 7.3 ± 0.0	− 4.6 ± 0.4

Table 4.2: Effective section (difference from the initial one per face) of the oxidized specimens to match the YS of the aged specimens

The results are the following, by temperature and state:

The 700 °C oxidized YS revealed a higher YS than the one of the aged state increasing the effective section of the specimens (negative value). The increase in YS from the 200 h HT reveals higher values than of the 600 h HT, with 3.6 % thicker effective thickness up to 100 µm. The 100 µm-thick specimens "peak" in YS is particularly visible on 200 h oxidized specimens compared to the aged state due to the progressive increase in YS of the aged state. The 100 µm-thick specimens "peak" is then especially visible since it is not present in the aged state. The 600 h HT reveals no major evolution from the aged and oxidized states inducing similar effective thicknesses.

The external brittle chromia certainly participates in the YS increase on the 700 °C oxidized state due to a grain confinement effect of the emerging grains (strong adherence onto the substrate, no spallation observed, and relatively low oxide thickness) and so delays dislocation motion at the "not so free" surface. Moreover, the intergranular alumina being mainly concentrated into the γ'_I precipitates with a punctual presence at the grain boundaries (thin alumina spikes as depicted in figure 3.20) does not weaken the emerging grains. The increase in mechanical behavior from the thin external chromia layer is valid only for low strain values due to the brittle behavior of the chromia leading to the premature occurrence of cracks at the surface of the chromia layer. Cracking of the chromia layer was evidenced at 2 % of total strain for all temperatures/durations mechanically investigated (further discussed in section 4.7.4). Such behavior induces the drop in UTS and ductility observed on both temperatures / HT durations in figure 4.14 and 4.15.

The increase in effective thickness is observed in figure 4.31. The initial thickness taken into consideration is given via the thickness between the green rectangles (without including the rectangles). The effective thickness is given between the green rectangles including the rectangles (higher than the initial thickness). The 200 h oxidation HT reveals an effective section thicker than the initial section added of the chromia layer (out of the emerging γ'_I precipitates). The increase in YS arises from the non-free surface effect, participating in the materials' hardening, which is supported by the effective section being higher than the specimens' thickness.

The 800 °C HT results show a major drop in YS, especially for thin specimens, as the consequence of the oxidation impact on the surface and sub-surface integrity. The 200 h HT presents a 2.7 µm thickness reduction per face, which results in 20 % loss of effective section for a 20 µm-thick specimen. The 600 h HT presents a decrease by 51.6 % effective section loss for the 20 µm-thick specimens. Both oxidation HT durations report the evolution of the effective section (decrease of the impacted section leading to an increase in the effective section) with thickness increase. The 500 µm-thick specimens demonstrate nevertheless strong variations in effective section compared to the AR state. The differences in the elastic-to-plastic transition and in the I-domain of strain-hardening of such specimen thicknesses induce the YS decrease responsible for the high effective thickness disparities. The thinnest specimens exacerbate the surface reactivity impact with a ratio of thickness impacted versus the total thickness higher than for thicker specimens.

The intergranular alumina reveals deeper penetration at 800 °C at grain boundaries compared to the 700 °C temperature, associated with larger spikes. Such grain boundary deterioration appears to overcompensate the increase in grain confinement induced by the chromia layer, *i.e.* the "not so free surface effect". The alumina spikes seem to control the decrease in YS observed for specimens oxidized at 800 °C, as revealed by

the effective section of the 200 h and 600 h oxidation HT durations. While the 200 h thickness shrinkage takes into account the metal recession from the chromia formation, but also a minor part of the alumina penetration depth (around 20 % of the intergranular depth determined in section 3.3.1); the 600 h reveals a much more effective thickness shrinkage from oxidation, down to the emerging grains being completely surrounded by the intergranular alumina.

The AS 800 °C oxidized state was compared to the AS without aging (metallurgical state not included in this framework). The sub-surface oxidation is mainly internal (intragranular) due to the lower grain boundary fraction, its impact on the material integrity is reduced compared to the AR oxidized state. The internal oxidation of the AS state is homogeneously distributed in the sub-surface while the AR oxidized state is mainly concentrated at the grain boundaries. The impact of such internal distributed oxidation products results in 25 % and 41 % decrease in the effective section for the 200 h and 600 h respectively compared to the AR oxidized state.

The effective section was reported on the wedged-polished coupons for the impaired conditions of AR and AS states oxidized at 800 °C during 200 h and 600 h, as depicted in figure 4.34.

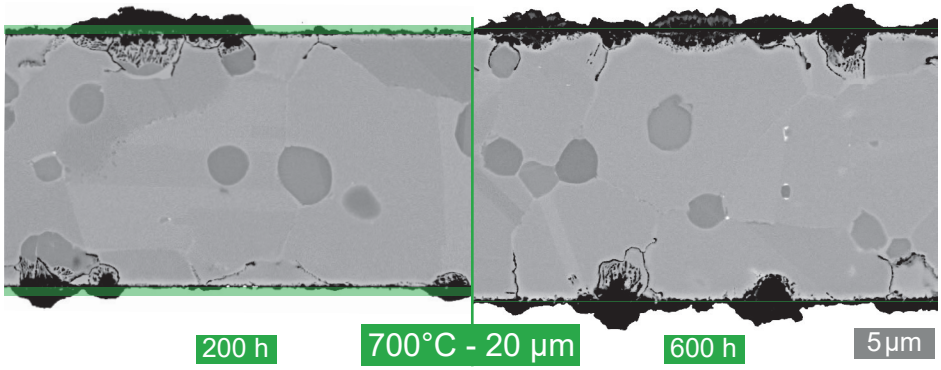

Figure 4.31: Total section and effective section (between the green rectangles) from cross-sectional SEM-BSE micrographs of René 65 oxidized at 700 °C during 166 h and 600 h on the left and right, respectively

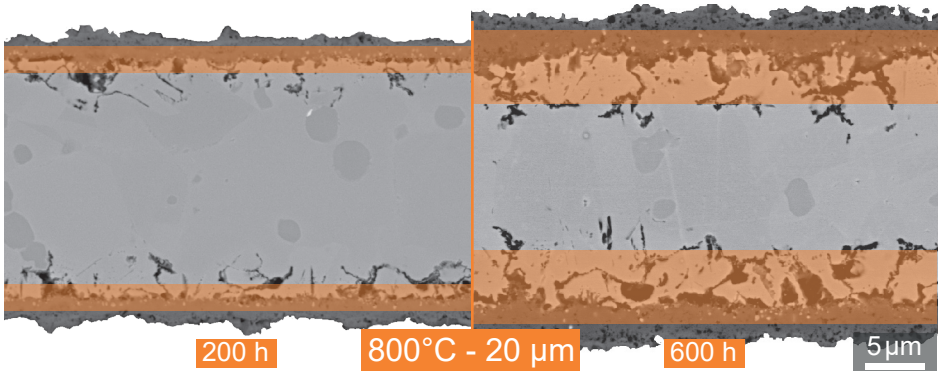

Figure 4.32: Total section and effective section (between the orange rectangles) from cross-sectional SEM-BSE micrographs of René 65 oxidized at 800 °C during 200 h and 600 h on the left and right respectively

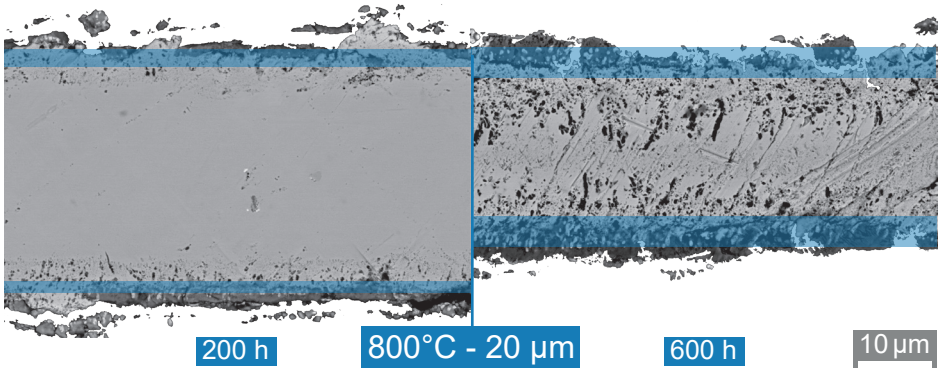

Figure 4.33: Total section and effective section (between the blue rectangles) from cross-sectional SEM-BSE micrographs of AlbiSolvus René 65 oxidized at 800 °C during 200 h and 600 h on the left and right respectively

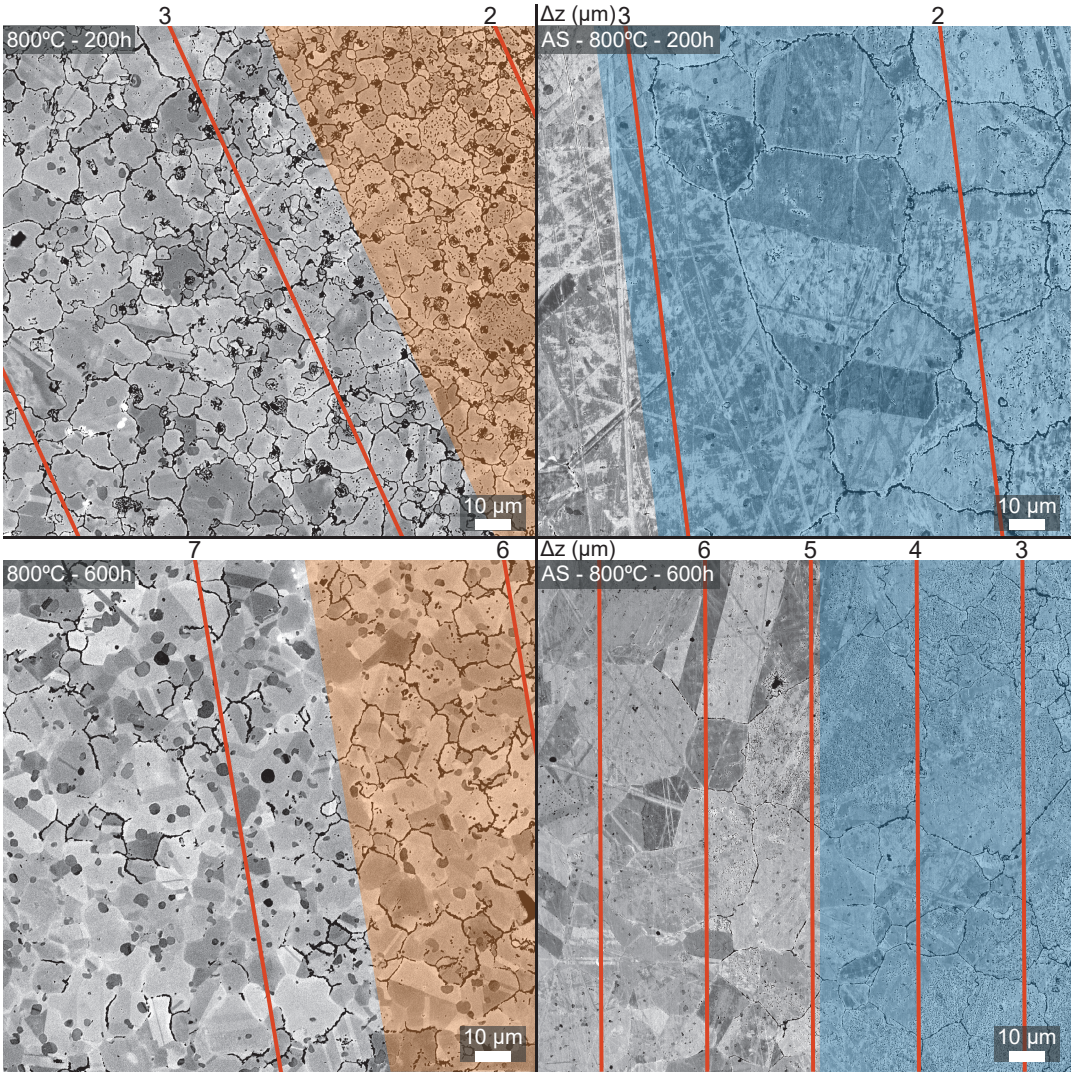

Figure 4.34: Effective section representation on the wedged-polished specimens of conditions AR and AS states oxidized at 800 °C during 200 h and 600 h

Analysis

The following conclusions can be established:

- The oxidation-affected layers at 800 °C result in a loss in the effective pegs of the specimens up to the tips of intergranular alumina formation.
- AS-oxidized specimen did not reveal any thickness transition in YS certainly due to the loss in the effective section from the oxidation-affected layers. The effective section appears to be less impacted by internal alumina than by intergranular alumina due to the different internal oxides (sparsely distributed within grains)

The effective section is supposed as a non-load-bearing region. Several authors experienced similar considerations, with a modified-load-bearing or a non-load-bearing of the oxidation-affected layers. Dreypondt *et al.* measured a non-load-bearing section in the creep behavior of MC2 alloy corresponding to the sub-surface γ' precipitates-depleted layer [227]. Bailleux *et al.* calculated the affected-layer tensile and creep properties in titanium alloys [228]. Bensch *et al.* performed creep tests on single crystal Ni-base superalloy M247LC SX having different metallurgical states (and especially γ' precipitates sizes and fractions) set to be representative of several depths-affected layers from oxidation at 980 °C [229]. Such a methodology takes into account a gradient of mechanical properties from the oxidation-affected γ'-free and γ'-reduced layers.

The former developments are based on oxidation-affected layers but located beneath any oxidized layers. The contribution to the mechanical behavior of grains being surrounded by alumina oxide is assumed negligible due to the brittle behavior of such oxide spikes. The use of thin specimens exacerbates the contribution of the oxidation-affected layers compared to the bulk behavior which allows their quantification. Such a non-load-bearing section can then be compared to the oxidation penetration depth on thick specimens as given in this section. All states oxidized at 800 °C, as depicted in figure 4.34, demonstrate such section to be closely related to the intergranular penetration depth.

4.7 Fatigue behavior

4.7.1 Introduction on the micro-fatigue testing specimens

The tensile behavior of René 65 was extensively studied up to this point, but fatigue is one of the main design criteria of the rotating parts. The tensile properties of microtensile specimens are present in various authors' research, but the fatigue response study is scarce. This section does not investigate to the same extent the fatigue behavior of microtensile specimens but intends to both serve as a feasibility study and exacerbate the surface/sub-surface impact of oxidation phenomena onto the damaging process in the fatigue life of René 65.

No specific setup was designed to perform such fatigue tests, which drove the experimental conditions to tensile-tensile fatigue tests on the same microtensile specimens geometry and the same bench as the tensile ones. The room temperature tests were displacement driven with strength threshold conditions using a ratio R_σ of 0.2 and using an input triangle signal. Strains were monitored via contactless methods (DIC techniques, similarly to the tensile tests) to a predefined number of cycles (1, 2 and 6 every 10^i cycle) through a python script. The fatigue testing frequency was set to 0.5 Hz. The maximal stress targeted on all fatigue tests is $\sigma_{max} = 0.95 Rp_{0.2}$ for each equivalent state-thickness condition (between 800 MPa and 1150 MPa depending on the thickness and state of the specimens). Fatigue testing favors surface plastic strain localization in regard to the subsequent microstructure. The surface evolution monitored via HR-DIC technics should then exacerbate the damaging process.

The AR state specimens were investigated for thicknesses of 20 µm, 50 µm, 100 µm and 500 µm to document any thickness effect on the fatigue life, similarly to tensile tests.

Interrupted fatigue tests were performed and paired microscopic strain monitoring via ex-situ high-resolution SEM-BSE micrographs. The DIC was performed on the natural speckle given by the external oxides (titania islands overhanging the emerging primary γ' precipitates). The oxidation conditions investigated here are 700 °C - 200 h, 700 °C - 600 h and 800 °C - 200 h. Fatigue interruptions and SEM-BSE micrographs were performed at predefined cycles of 0, 1, 10, 100, 1000, 5000 and 10 000.

4.7.2 Fatigue life of AR and oxidized specimens

Several fatigue conditions were performed in this framework. The total number of specimens is limited (42) due to the duration of the tests (from half a day up to 2 days). The fatigue life (total number of cycles to rupture) versus the thickness of specimens is exposed in figure 4.35 for all investigated conditions.

The AR state demonstrates a relatively steady number of cycles as a function of the specimen thickness in the range of 50 µm to 500 µm with around 45 000 cycles to failure. Only one 20 µm-thick specimen was tested and experienced half the fatigue life of thicker specimens. While only one test of thin specimen thickness does not provide a statistical representation, a transition is still observed in the fatigue life of specimens between 20 µm to 75 µm in thickness. The 90 µm-thick specimen having a 65 000 cycles life has seen a reduction in the strength applied during the fatigue test due to technical issues. Such abnormal trend in fatigue life is then not due to a material response.

The 700 °C oxidized specimens demonstrate a similar fatigue life on both oxidation durations of 200 h and 600 h. The impact of oxidation is revealed via the drop in fatigue life on thin specimens (below 100 µm). While 500 µm-thick specimens broke between 35 000 cycles to 40 000 cycles, thin specimens of 30 µm thickness only reached 5000 cycles. The fatigue life is furthermore reduced on specimens with thicknesses lower than 100 µm due to the ratio of oxidation-affected scale versus the total thickness of the specimen, as revealed by the change of slope at 100 µm.

The 800 °C fatigue life is much more affected by the oxidation process with a number of cycles to failure of 20 000 cycles on 500 µm-thick specimens. The fatigue life is stable in the thickness range of 100 µm to 500 µm, and demonstrates a similar behavior to the 700 °C oxidation HT for lower thicknesses. A clear transition is observed at 100 µm of specimen thickness.

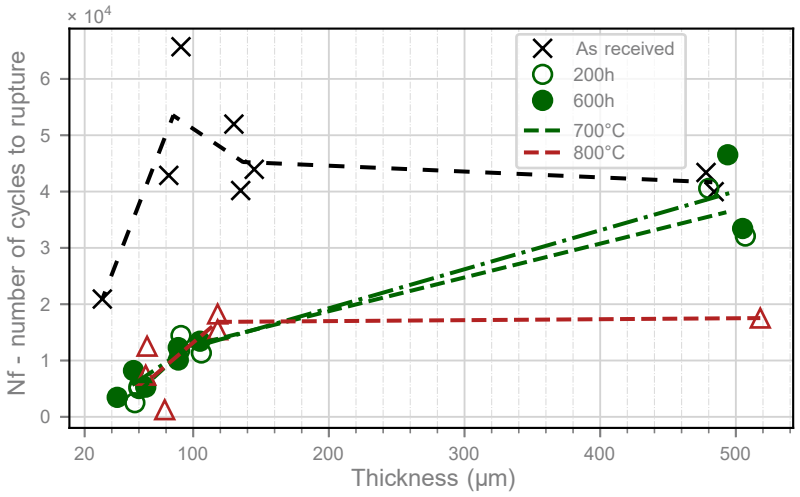

Figure 4.35: Number of cycles to rupture of thin specimens of AR and oxidized states at room temperature, $R_\sigma = 0.1$, $f = 0.5\,\text{Hz}$, $\sigma_{max} = 0.95\,\text{YS}$

The fatigue behavior of oxidized specimens in terms of total true strain as a function of the number of cycles (up to 10 000 cycles) is presented in figure 4.36. The three temperatures demonstrate a distinctive ratcheting in the first 100 cycles to 1000 cycles, as illustrated by the constant evolution of the true strain over the number of cycles. Such a phenomenon is often associated with the multiplication of crack initiation sites in those first hundreds of cycles. The material is then submitted to crack propagation with an almost steady true strain throughout the remaining fatigue tests.

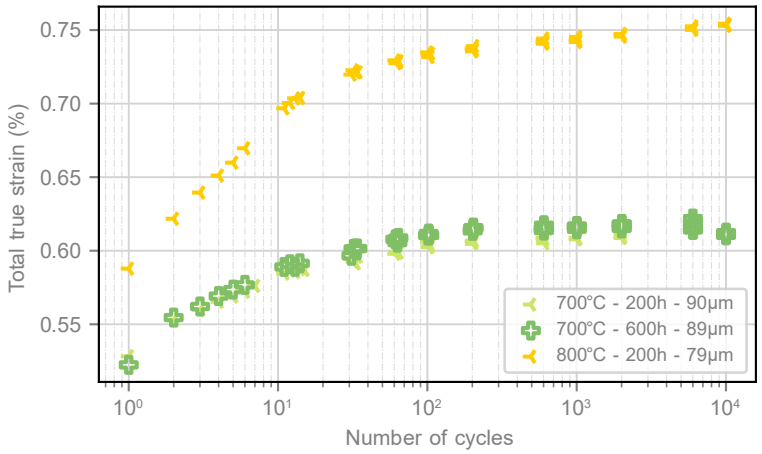

Figure 4.36: Total true strain as a function of the number of cycles (up to 10 000 cycles) of the fatigue room temperature fatigue tests on oxidation condition 700 °C - 200 h, 700 °C - 600 h, 800 °C - 200 h for 100 µm-thick specimens

4.7.3 Fractographic analyzes

The nature of the crack initiation sites on the AR fractographs was difficult to evidence due to the multitude of initiation sites. The 700 °C and 800 °C oxidized states fractographs all revealed, nevertheless, the presence of oxidized nitrides (TiN), as depicted in figure 4.37 and 4.38. Such oxidized particles were not revealed in any tensile fractograph. The important penetration depth of oxidized TiN particles associated with a brittle behavior may be responsible for their impact on the fatigue life of specimens. Such implication is to be further investigated by SEM-FIB observations presented later in this section.

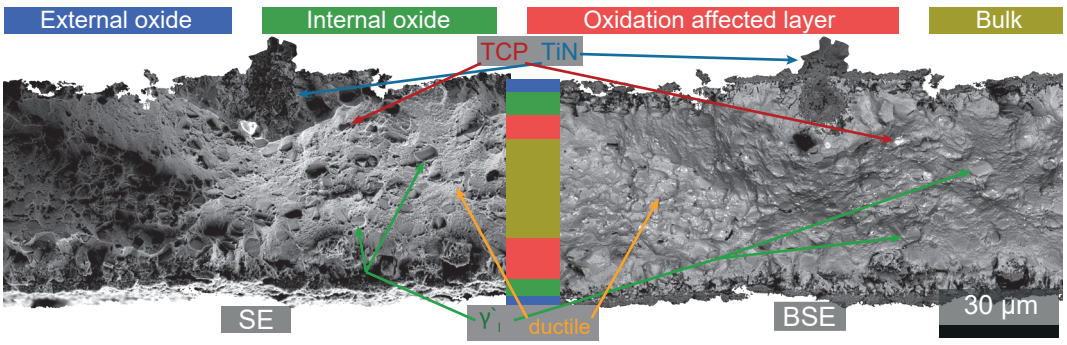

Figure 4.37: SEM fractograph of oxidized at 800 °C during 200 h for 61 µm-thick specimen after room temperature fatigue test

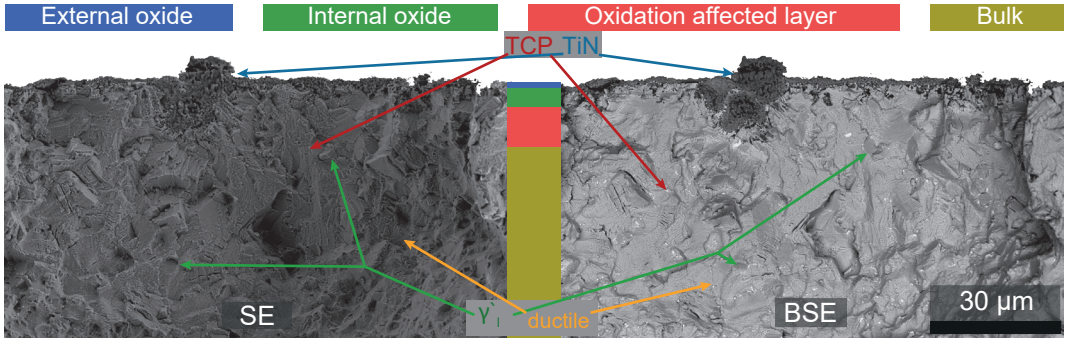

Figure 4.38: SEM fractograph of oxidized at 800 °C during 200 h for 122 µm-thick specimen after room temperature fatigue test

4.7.4 Interrupted fatigue tests for ex-situ microscopic strain monitoring

The interrupted tensile tests presented in section 4.4.4, and especially figure 4.24, demonstrated oxidized emerging primary γ' precipitates being cracked even in the low stress / low strain regime. To apprehend the impact of the titania and chromia layers overhanging the primary γ' precipitates, interrupted fatigue tests were performed using ex-situ high-resolution SEM-BSE micrographs maps (composed of 10x10 tiles at x1500 magnification) with strain determination via full-field DIC technique to monitor the surface evolutions.

The fatigue tests were performed on oxidation conditions 700 °C - 200 h as given in figure 4.39, 700 °C - 600 h as given in figure 4.40 and 800 °C - 200 h as given in figure 4.41. The strain maps at each predefined cycle are presented overlaying the SEM-BSE micrographs to ensure visualization of the strain localization in regards to the microstructure. The 800 °C strain map and the underlayed SEM-BSE micrographs are less relevant due to the higher external oxide scales leading to a more complex distinction of the oxides at the surface (titania and chromia). The strain map still reveals strain localization related to oxide cracking.

The three oxidation conditions demonstrate an early cracking of the surface with surface crack initiation within the first 100 cycles. Propagation of these cracks then occurs up to the rupture of the specimens. The high-resolution strain maps reveal initiation sites at the primary γ' precipitates - matrix interface or passing through the primary γ' precipitates (as exposed in interrupted tensile tests of figure 4.24).

The two strain maps after oxidation 700 °C at 200 h and 600 h also expose the presence of one nitride (large particle at the center of the map for the 200 h figure, darker particle at the upper center of the 600 h one). The nitrides also demonstrate crack initiation in the first cycles but are mainly located on the nitride-matrix interface.

The strain range of the three conditions demonstrates coherent boundaries with up to 8 % of local strain but a macroscopic imposed strain of $0.95 \cdot Rp_{0.2}$. Such high localization is indicative of potential cracks formation at the surface.

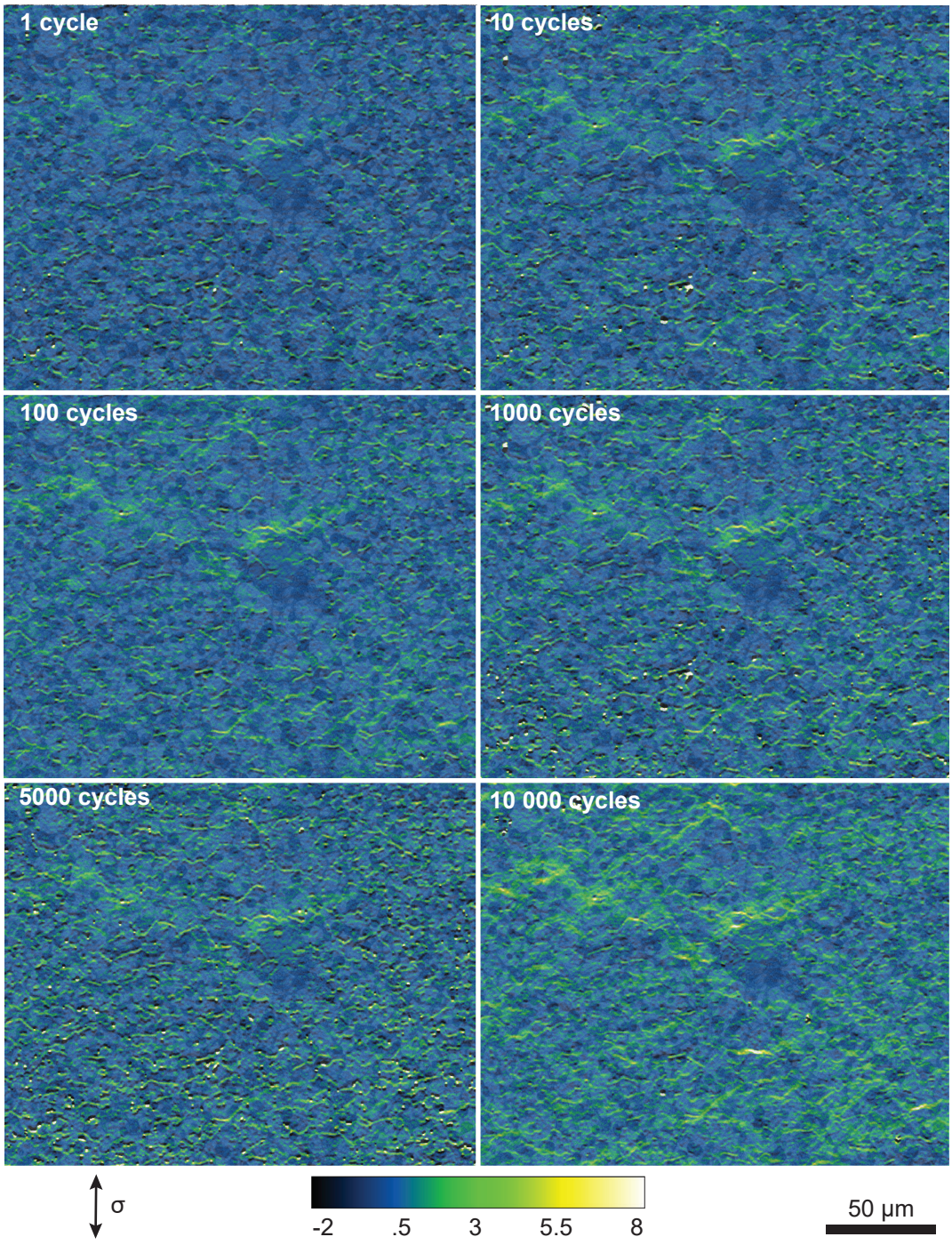

Figure 4.39: Strain cartography of interrupted fatigue test of 700 °C - 200 h oxidation condition at cycles 0, 1, 10, 100, 1000, 5000 and 10 000 overlayed with the SEM-BSE micrograph to emphasize the strain localization-microstructure relationship

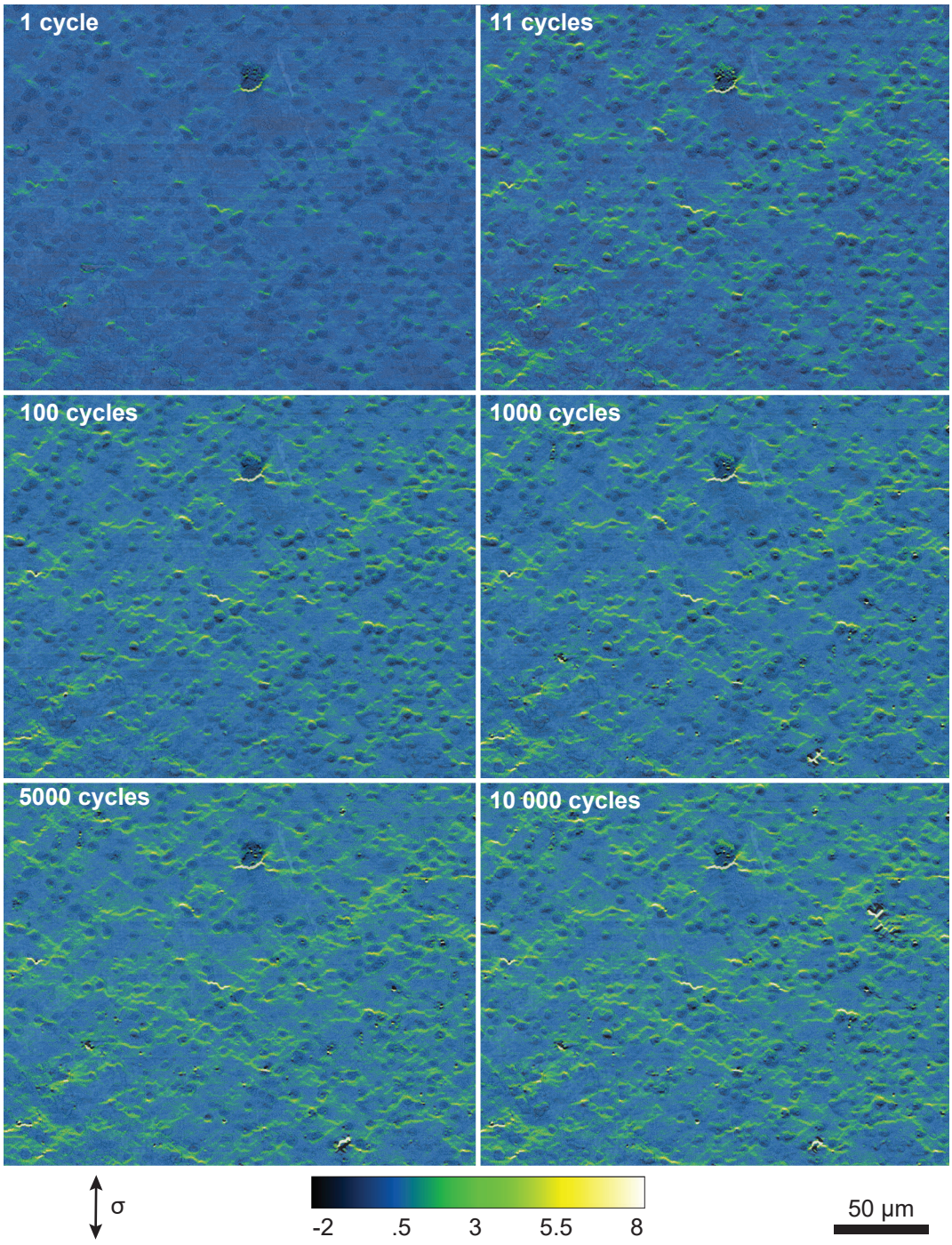

Figure 4.40: Strain cartography of interrupted fatigue test of 700 °C - 600 h oxidation condition at cycles 0, 1, 10, 100, 1000, 5000 and 10 000 overlayed with the SEM-BSE micrograph to emphasize the strain localization-microstructure relationship

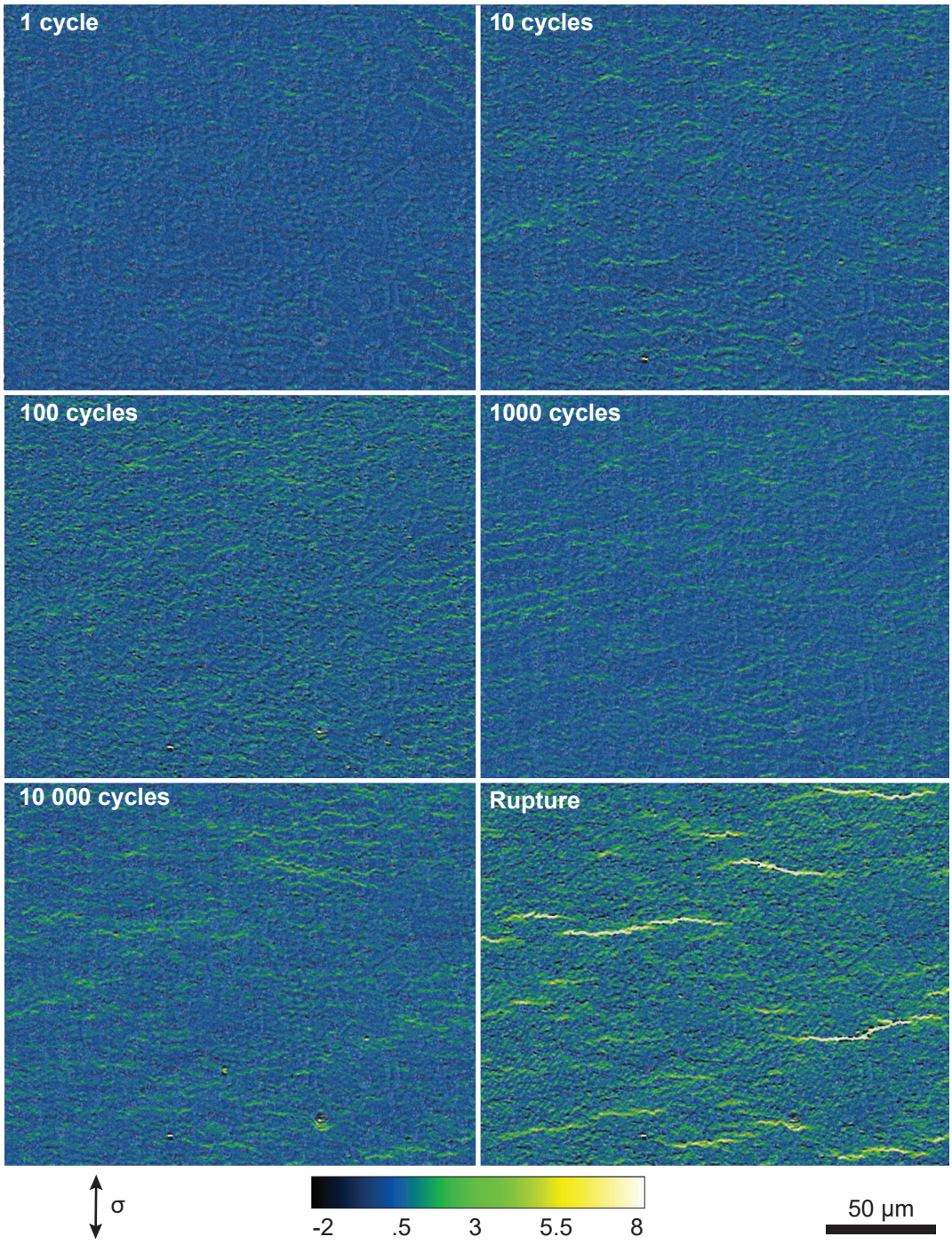

Figure 4.41: Strain cartography of interrupted fatigue test of 800 °C - 200 h oxidation condition at cycles 0, 1, 10, 100, 1000, 5000 and 10 000 overlayed with the SEM-BSE micrograph to emphasize the strain localization-microstructure relationship

The thin external chromia layer of the specimens oxidized at 700 °C ensures the underlying microstructure display. Strain localization areas were identified and directly compared to the initial SEM-SE micrograph in figure 4.42. The 200 h oxidation HT demonstrates strain localization in large grains (MG region) while the 600 h oxidation HT is localized in the fine grains region (FG).

The 600 h oxidation HT demonstrates strain localization in the primary γ' precipitates surroundings. The alignment of such particles, being normal to the applied stress, appears to play a role in the most intense strain localization.

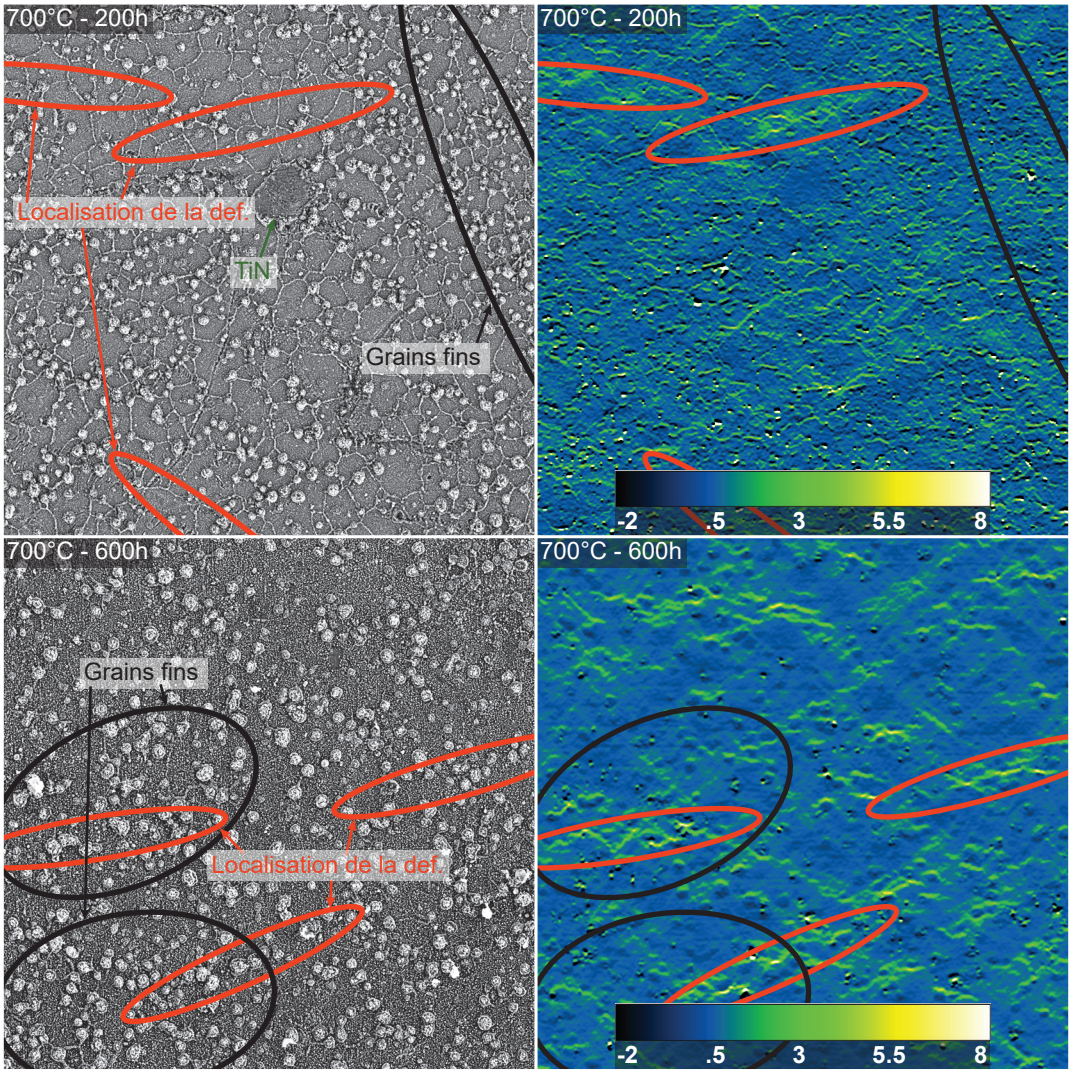

Figure 4.42: Strain cartography of interrupted fatigue test and equivalent microstructure

4.7.5 Analysis of the sub-surface premature damaging from SEM-FIB observations

A series of SEM-FIB cross-sections coupled with SEM-BSE micrographs (and SEM-EDX analysis on certain conditions) were performed to better understand the primary γ' precipitates and nitrides cracking mechanisms. The SEM-FIB micrographs were corrected of the 52° tilt angle induced from both SEM-BSE and SEM-FIB columns (specimen aligned with the SEM-FIB column).

The primary γ' precipitates cracking observations on all oxidation conditions investigated in fatigue are given in figure 4.43. The external chromia layer cracking is accompanied by subsequent intergranular alumina cracking down to the maximal penetration depth of the alumina spikes, as observed in all oxidation conditions. Primary γ' precipitates are pining grain boundaries and so ensure limited grain growth during solution heat treatments; the γ'_I are then favorably located at grain boundaries and the intergranular oxidation in the vicinity of γ' is enhanced due to Al diffusion.

Post-mortem SEM-FIB observations do not reveal any information on whether the chromia layer or the intergranular alumina spikes are responsible for the cracking. All observations of cracks in the primary γ' precipitates vicinity are however preferably located in the intergranular alumina continuation, no matter the position of the alumina spike from the primary γ' precipitate (figure 4.43 demonstrate both γ'_I-matrix interface and at the middle of the γ'_I). Such continuity of the crack path in the volume certainly indicates initiation of the cracking from the alumina spikes and propagation to the chromia scale. The strain maps revealed the interconnection of the γ'_I due to propagation and merging of the cracks. The SEM-FIB micrographs demonstrate chromia cracking propagation out of the γ'_I precipitates, in the continuity of the γ'_I cracking.

The previous observations of nitride oxidation given in section 3.6 demonstrated their potential impact on the integrity of the material from their substantial size. The strain maps revealed the presence of cracks at the nitrides/matrix interface, with a constant observation in the fatigue fractographs. Oxidized nitrides were then of interest in the SEM-FIB-BSE sequence, as given in figure 4.44.

Before assessing the nitride cracking, the SEM-FIB coupled with SEM-EDX analysis demonstrates a chromia layer, similar to the surface (thickness and morphology), at the nitride-matrix interface. The nitride oxidation results in titania formation at the two investigated temperatures (700 °C and 800 °C). The inclusion of the nitride emerging at the surface seems not to induce any changes in the oxidation regime or products of the matrix beneath it from the material surface. The nitride-matrix interface appears to favor the oxygen supply from such an interface.

The fatigue crack exposed in figure 4.44 is located at the titania / chromia interface. The incoherence of the nitride can be seen as a notch defect for the surrounding material which impairs the fatigue life and serves as a crack initiation site. The crack exposed in figure 4.44 propagates into the chromia layer and the subsequent intergranular alumina at the maximal depth of the notch.

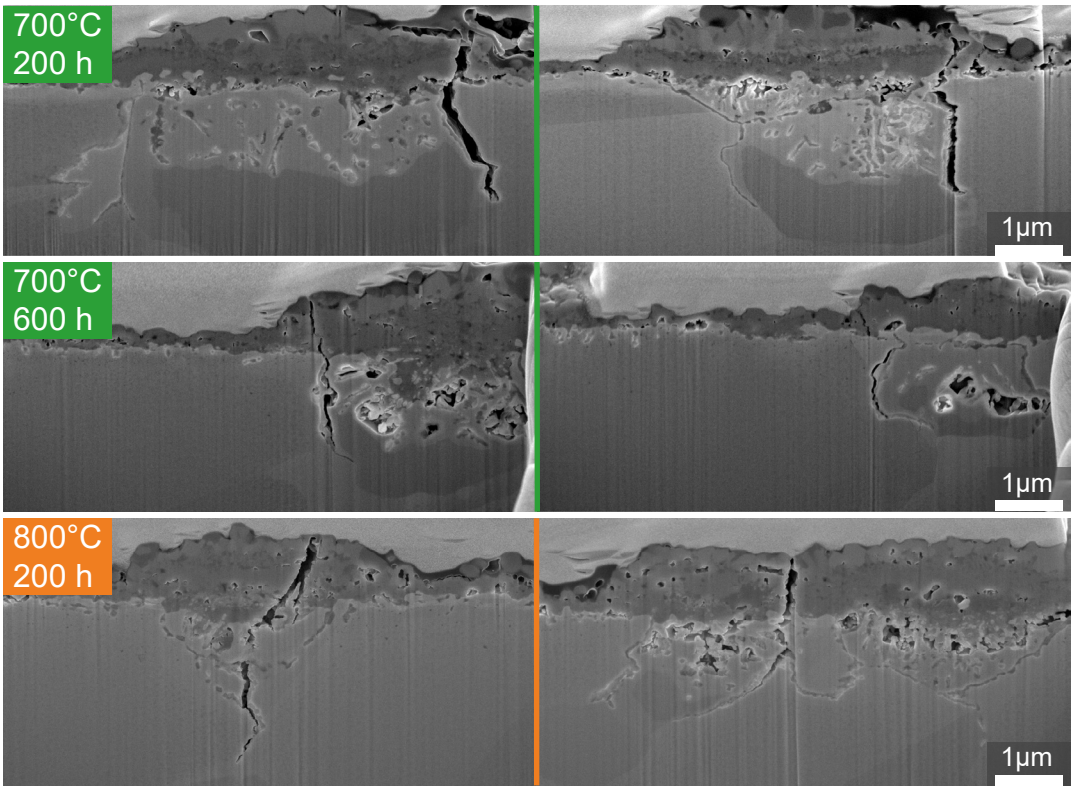

Figure 4.43: SEM-FIB-BSE micrograph of oxidized γ'_I at 700 °C - 200 h, 700 °C - 600 h and 800 °C - 200 h after fatigue testing

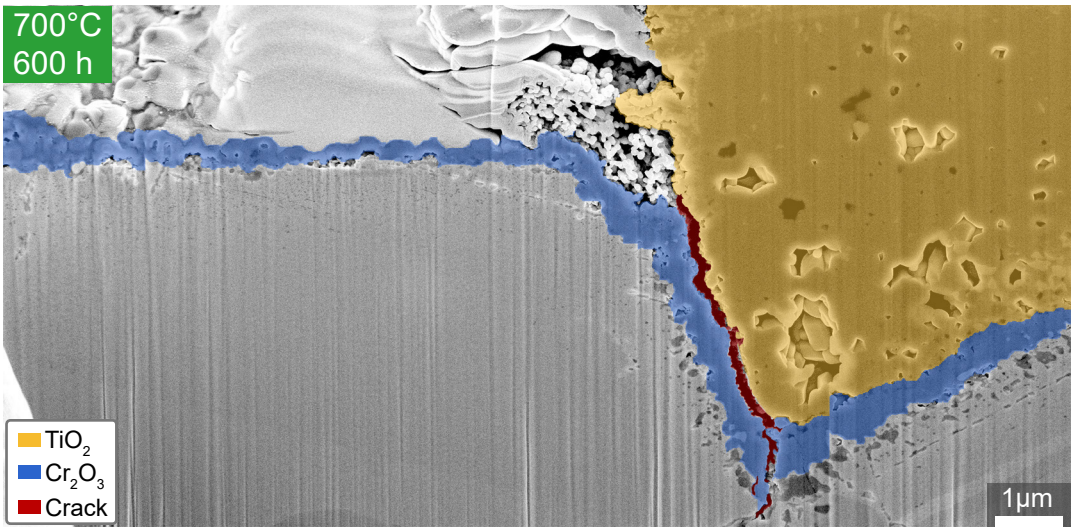

Figure 4.44: SEM-FIB-BSE micrograph of a nitride oxidized at 700 °C - 600 h after fatigue testing

Analysis

The fatigue investigation in René 65 reported the following conclusions:

- The fatigue life of thin specimens at room temperature demonstrates a drop for low thicknesses on the AR state. The multicrystal to polycrystal transition appears similar to the tensile one, close to 100 µm of specimen's thickness.

- The fatigue life of specimens oxidized at 700 °C demonstrates a major drop increasing with thickness reduction. The 500 µm-thick specimens exhibit similar fatigue life compared to the AR state. The oxidation-affected layer depths versus the total thickness of specimens are particularly visible on such a drop in fatigue life for low-thickness specimens.

- The 800 °C oxidation HT results in a major drop of fatigue life even on 500 µm-thick specimens. The impairments observed on low thicknesses specimens agree with the 700 °C oxidation behavior.

- The fractograph analyses of the fatigue specimens all demonstrate the presence of emerging oxidized nitrides as crack initiation sites.

- Interrupted fatigue tests with ex-situ full field DIC analysis from SEM-SE-BSE maps demonstrate the key role of the emerging γ'_I precipitates but also the nitrides. Crack initiation appears in the very first cycles in both particles' surroundings due to the plastic strain evolution of up to 100 cycles. Propagation then occurs up to the end of the test. Such conclusions are supported by ratcheting observation of the specimens in the firsts 100 cycles to 1000 cycles.

- A change in strain localization from large grains to primary γ' precipitates appears at 700 °C between 200 h and 600 h oxidation HT, respectively.

- SEM-FIB-BSE observations demonstrate the role of intergranular alumina present in the primary γ' precipitates vicinity onto the crack initiation. The nitrides reveal cracking at the titania / chromia (former nitride/matrix) interface.

To begin with the fatigue discussion, table 4.3 and table 4.4 summarize the maximal penetration depths of the different impairments that can occur while exposing René 65 to high-temperature.

State	Chromia scale	Intergranular alumina	$\gamma`_I$ depletion	Cr depletion	TCP depletion
700°C - 200 h	<1.0 µm	2.0 µm	N.M.	N.M.	N.A.
700°C - 600 h	1.0 µm	3.0 µm	N.M.	N.M.	N.A.
800°C - 200 h	1.5 µm	6.0 µm	7.0 µm	7.5 µm	15 µm
800°C - 600 h	2.7 µm	7.5 µm	8.5 µm	15.0 µm	20 µm

Table 4.3: Maximal penetration depth of layers from oxidation. N.M.: not monitored, N.A.: not applicable

State	Grain size	γ'_I size	TiN
AR	7.8 µm	2.0 µm	15 µm
AS	52.3 µm	1.6 µm	N.M.

Table 4.4: Average grain size and γ'_I. Maximal TiN size. N.M.: not monitored, N.A.: not applicable

The 700 °C oxidation demonstrates intergranular oxidation being mainly focused on primary γ' precipitates at 200 h while the 600 h oxidation demonstrates intergranular alumina deeper than the primary γ' precipitates. The low microstructural impact of alumina formation at 200 h induces typical LCF damaging with the formation of Persistent Slip Bands (PSB) at the surface [13]. Their location is preferably located along large grains as observed by Billot *et al.* in U720 Li alloy [162].

The oxidation-affected grain boundaries, as revealed in the 700 °C - 600 h and 800 °C - 200 h oxidation conditions, demonstrate the deleterious role of primary γ' precipitates. Laurence and Govaere reported crack initiation at the primary γ' precipitates vicinity, the matrix/γ'_I interface, or oxidized grain boundaries in AD730^{TM} on LCF and dwell-fatigue testing in the temperature range 700 °C to 800 °C [8, 9]. Govaere performed air and vacuum LCF tests to exacerbate any environmental effect in the fatigue life of AD730^{TM}. The air atmosphere demonstrated mainly primary γ' precipitates cracking while the vacuum one repented only non-metallic inclusions cracking.

Alexandre developed a crack propagation model in Alloy 718 with particle fibering effect [216]. The FG region, due to the primary γ' precipitates proximity, is more likely to react as in scenario a), while the MG region is more likely in scenario b). The oxidation-affected primary γ' precipitates, as reported in the pre-oxidation condition 700 °C - 600 h in figure 4.42, demonstrate mainly cracking in the FG region from their relatively close proximity and normality with the loading. The oxidation condition 700 °C - 200 h presented in figure 4.42 demonstrates mainly intra-precipitate oxidation that results in strain localization along PSB in large grains (MG region) and not completely related to the primary precipitates.

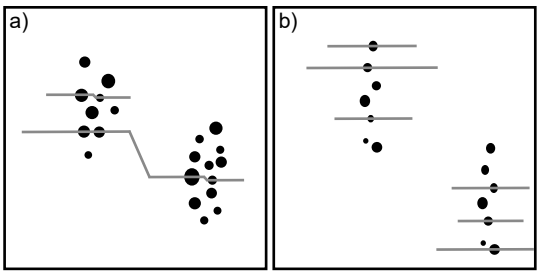

Figure 4.45: Schematic particles cracking interconnections depending on the spatial location; a) negative impact on the crack propagation with cracks coalescence; b) no coalescence of the cracks from interconnection [216]

The primary γ' precipitates oxidation induces a change in the damage mechanism as demonstrated earlier. The relatively low dimension of γ'_I compared to nitride particles, as demonstrated in table 4.3 and table 4.4, raises the question of which one of the two has the most deleterious impact on fatigue failure.

The 700 °C pre-oxidized fatigue tests demonstrate similar fatigue life from both HT durations of 200 h and 600 h. The strain localization, nevertheless, revealed differences arising from the primary γ' precipitates oxidation severity. Such a change in strain localization mechanism did not induce any differences in the number of cycles to failure of the alloy. Moreover, the presence of oxidized nitrides in all the fractographies, associated with their commensurable size compared to the γ'_I and grain size, highlight their major deleterious impact on the materials initiation mode.

Nitrides are prone to oxidation in the early stages of high-temperature exposure. The titanium itself but also the presence of an NbC shell makes of nitrides particles having high deleterious potential. Govaere reported their contribution to crack initiation mainly at low temperatures (450 °C), while the environment effect controls the intergranular cracking at higher temperature (700 °C) [9]. The results presented within this framework lead one to believe in their both concomitant effect, but are heading in the direction of a fatigue life span controlled by oxidation of the nitrides.

General conclusions and future prospects

This framework intends to understand the damage mechanisms associated with mechanically soliciting a polycrystalline nickel-based superalloy, René 65, under an oxidizing environment. The oxidation-affected layers, whether homogeneous and distributed on the surface, or localized at the grain boundaries, can induce mechanical behavior changes.

The originality of the present work arises from the use of ultrathin microtensile specimens to directly quantify the oxidation-affected layer in terms of mechanical behavior but also of breakaway consequences.

René 65

The γ/γ' nickel-based superalloy material René 65 for turbine disk application was studied in this framework. The dual microstructure is composed of insertions of fine grains (FG) in a medium-grain (MG) matrix, inheritance from the billet solidification and/or result of the forging operations. The precipitation state of the γ'_{II} and γ'_{III} is, however, similar in both regions, but demonstrates minor variations in grain and γ'_{I} size. The presence of intermetallic particles (borides, carbides, etc.) is revealed, especially nitrides that appear to play a role in the fatigue life of the material on oxidized states at both pre-oxidation temperatures of 700 °C and 800 °C.

A second microstructure was investigated, from a close-to-solvus heat treatment, named AlbiSolvus (AS). Such HT results in a near primary γ' precipitates free material but comes with a grain size increase.

Mechanical behavior

Ultrathin specimens were employed in this framework to emphasize any environmental effect of the surface and sub-surface against the bulk behavior of massive specimens. The use of thin specimens inherits particularities regarding the ratio thickness of the specimen versus grain size. While such ratio and the thin specimen behavior demonstrate a strong interest in the literature on pure or model materials (for their well-known theoretical and modeling knowledge), their application to industrial materials leads to both technical and material challenges.

The mechanical behavior of thin microtensile specimens was validated by comparing them to standard cylindrical tests. The microtensile specimens investigation required

the development of adapted characterization means, for both testing and monitoring their behavior.

The tensile behavior of the AR state of René 65 was extensively characterized in the thickness range 20 µm to 500 µm corresponding to a t/d ratio of 2.5 to 60. This database was then considered as a reference to compare the high-temperature exposure consequences on the mechanical behavior. The precipitation hardening of René 65 provides a minor influence of the thickness of specimens onto the strain hardening of the material compared to pure nickel. A decrease in macroscopic tensile properties with thickness reduction was demonstrated with a transition of multi-crystalline to polycrystalline around 100 µm-thick specimens (12.5 grains in the thickness).

The tensile behavior of the AS state was also characterized in the thickness range 20 µm to 500 µm corresponding to a t/d ratio of 0.4 to 10. The difference in t/d ratio induces a quasi-monocrystalline to multi-crystalline behavior with a transition around 100 µm (2 grains in the thickness). A decrease in tensile behavior was observed in the AS state compared to the AR state due to its intentional microstructural evolutions.

The fatigue life of René 65 was investigated in tensile-tensile solicitation using similar microtensile specimens in the thickness range 20 µm to 500 µm. A decrease in the number of cycles to rupture was observed on specimens thinner than 50 µm.

Oxidation products

The oxidation behavior of René 65 was investigated (without any mechanical solicitation). Isothermal oxidation in laboratory air follows a parabolic regime for all temperatures studied between 650 °C and 1000 °C. The oxidation kinetics are in agreement with similar types of alloys, *i.e.* chromia-forming Ni-based superalloys. Oxidation leads to the formation of several oxides: a dense external chromia layer, sparsely distributed titania islands topping the primary γ' precipitates and grain boundaries, and intergranular alumina regardless of the temperature and sample thickness. The spinel oxide phase is to occur at high temperatures, for long durations, and low thickness samples, leading to local breakaway phenomena or intrinsic chemical failure. Size effect, i.e., volume-limited effects have been here evidenced using ultrathin samples down to 15 µm.

Microstructural evolution inherent to the high-temperature exposure leads to surface and sub-surface alteration with chromium-, precipitates-, and TCP-depleted layers, whose respective depths had been determined on sample cross-section observations in order to establish the influence of sub-surface changes on the mechanical response. The impact of this microstructural gradient with regard to the thickness of the sample is of interest in the analysis of the mechanical behavior.

An effect of the thickness of samples onto the oxidation kinetics was observed on temperatures 700 °C and 800 °C. Variations in the external oxide scale and the equivalent surface of intergranular alumina were reported, and were identified as responsible for the mass gain variations measured. Thinner samples reported a thicker chromia scale and a thicker equivalent alumina scale but with lower penetration depth. The contribution of both the external chromia layer and intergranular alumina onto the total mass gain was quantified with 70 $\%_{wt}$ due to the external oxide layer. The activation energy extracted from the overall oxidation of René 65 complies with pure chromia.

The AS microstructure revealed mainly internal oxidation due to the lower grain boundary fraction. Intergranular oxidation is however present, with a penetration depth

inferior to the AR material. The external chromia was affected compared to the AR state by being non-adherent to the material surface.

Mechanical degradation and crack initiation from environmental interactions under tensile and fatigue solicitation modes

The bulk aging and oxidation impact of René 65 were both investigated at HT durations of 200 h and 600 h at 700 °C and 800 °C. Secondary and tertiary γ' precipitates evolutions were observed on both temperatures up to 10 h of HT revealing a potential microstructure homogenization. Such homogenization induces an increase in the tensile properties of the material compared to the AR state due to the increase in CRSS from shearing the smaller secondary γ' precipitates and larger tertiary γ' precipitates. The 800 °C HT microstructural evolution is much more pronounced (*e.g.* dissolution of the tertiary γ' precipitates) resulting in the loss of tensile properties and revealing a similar behavior to the AR state.

The external chromia scale appears to enhance the hardening of the material by restricting the dislocation motion for thin oxide scales, as evidenced for the 700 °C oxidized specimens. Thicker oxide scale (more than 1 µm) participates in the surface crack propagation with interconnection or cracks for high plastic strain or accumulated plastic strain. Intergranular cracking of the alumina-oxidized grain boundaries in the vicinity of primary γ' precipitates emerging at the surface of the material seems to play an important part in the damaging processes. The FG region, with primary γ' precipitates clustering, demonstrates strain localization as the result of long but shallow surface cracks interconnecting γ'_I precipitates. The loss of tensile behavior was investigated in terms of effective section supporting the mechanical stresses. Grains with completely oxidized grain boundaries from alumina formation demonstrate a very low contribution to the mechanical behavior. Thin oxidized specimens then highlight the consequences of the microstructural gradient and sub-surface embrittlement in the oxidation-affected layer.

Nitride particles revealed complete oxidation at 700 °C and 800 °C to form rutile TiO_2, associated with an important volumetric expansion. The nitride/matrix interface demonstrates similar oxidation kinetics and products as the surface of the material. Such an interface appears as an oxygen diffusion shortcut path. The fatigue fractographs revealed crack initiation in the oxidized nitride surroundings. Oxidized nitrides, from their decohesion to the matrix, but also their surface and subsurface important dimensions compared to the microstructure, appear to control the fatigue life of René 65 at room temperature.

All those conclusions are based on the room temperature characterization of René 65. The conclusions on the damaging mechanisms impairing the life of the material are only valid up to 550 °C. A change in the deformation mechanisms, and especially the γ' precipitate contribution, could induce major changes in the damaging processes, especially from $\Sigma 3$ twin boundaries.

The observations performed in this work do not allow to determine which defect is the most critical in the fatigue life of René 65 between:

- Clusters of large grains crystallographically favorably oriented
- Clusters of oxidized primary γ' precipitates associated with intergranular cracking
- Large and/or deep surface/subsurface nitrides

Future prospects

- The tensile impairments resulting from the oxidation process of the material were only considered as a non-load-bearing section. Such a discontinuous methodology could be greatly improved by considering a gradual evolution of the tensile properties from the surface of the material to the bulk behavior.

- The intergranular alumina spikes proved their contribution to the damaging of thin specimens. Complementary observations could help in setting cracking criteria for such intergranular alumina.

- All the fatigue and tensile tests of this study were performed at room temperature. The changes in deformation mechanisms occurring above 550 °C, but also the mechanical-oxidation interactions (fatigue PSB acting as oxygen shortcut path, breaking of the protective external oxide scale) that can occur during high-temperature testing can induce major differences from the conclusions drowned in this study.

  Observations of the interactions between fatigue testing and oxidation consequences were initiated within this study with 700 °C and 800 °C oxidation of specimens under cyclic loading. Such an investigation was not completed before the writing of this manuscript and intends to be presented in a further article. The formation of stress-assisted oxidation products is expected, potentially along twin boundaries.

- Specimens with gradient-extraction to target a specific layer mechanical properties were only limited to the removal of the external chromia layer, as given in section 4.4.3. The removal of the intergranular alumina-affected layer could also be of interest in order to validate the non-load-bearing section hypothesis.

- The cross-sectional SEM observations revealed a subsurface γ'-free layer, with a primary γ' precipitates-free layer but also grain boundary γ'_{II} and γ'_{III} precipitates depletion. The mechanical impact of such softened layers is of interest, as demonstrated by the current investigations of G. Burlot in his Ph.D. works (TOPAZE chair).

- The thickness effect on the oxidation kinetics was measured in terms of mass gain and oxide scale but no further explanation was given. TGA oxidation tests could improve the mass gain accuracy. In-situ monitoring of the geometrical dimensions of samples could answer any potential creep appearance.

Appendix A

Strain-hardening as a function of the specimens thickness

The elastic-to-plastic transition but also the strain-hardening behavior of specimens is of interest to document the thickness effect on the tensile response of René 65. The strain-hardening variation from thickness effect was widely documented by Keller in pure nickel [120]. The three stages of plastic deformation were introduced in section 1.3.1 (I: planar slip system activated, II: secondary and cross-slip systems activated, III: cross-slip generalized, activation of dislocation cells). The strain-hardening rate θ defined by equation A.1 was reported to evolve with the specimens' thickness in pure nickel.

$$\theta = \frac{d\sigma}{d\epsilon} \tag{A.1}$$

The strain-hardening rate was evaluated for all the tensile curves illustrated in figure 4.2. The strain-hardening was then plotted as a function of the true strain in figure A.1, and as a function of the true stress in figure A.2. Several domains are to be identified from the Crussard–Jaoul (C-J) plots (subplot focusing on the II and III domains) [120, 230, 231]:

a. Elastic domain [below 0.4 % of total strain]. The variation in strain-hardening rate confirms the variations in Young modulus reported in section 2.2.3. The YM is thickness dependent according to the variation of strain-hardening rate and evolves according to the thickness of the specimens as aforementioned in figure D.1 and 4.3.

b. The elastic-to-plastic transition [between 0.4 % to 0.5 % of total strain]. The slope of the elastic-to-plastic transition is more progressive in thin specimens in comparison with thick ones. Such a conclusion is also evidenced in the stress-strain enhancement domain in figure 4.2.

c. The I strain-hardening domain [between 0.5 % to 0.7 % of total strain - 1150 MPa]. No clear influence of the thickness between 20 µm and 500 µm specimens was found from figure A.1. The impact of the thickness onto the I domain of strain-hardening from figure A.2 arises from both a lower stress value but also the more progressive elastic-to-plastic transition.

d. Transition from I to II domain [between 0.7 % to 2 % of total strain]. This transition is also influenced by the specimens' thickness, with a more progressive slope for thinner specimens. This transition takes place at a value of 1150 MPa and

1200 MPa for all thicknesses. Keller exposed variations of up to 100 MPa onto the $\sigma \cdot \theta$ evolving according to the thickness of the specimens; no such conclusion is drowned from both strain-hardening behavior for René 65.

e. The II strain-hardening domain [between 2 % to 8 % of total strain - 1200 MPa]. No major influence of the thickness on the II plastic domain, as revealed in figure A.2 (supposed to enhance the strain-hardening domain II differences). The strain range of the strain-hardening domain II does not vary with the specimens' thickness.

f. The III strain-hardening domain [above 8 % of total strain - 1500 MPa]. Similar conclusions from strain-hardening domain II are observed in domain III. The transition from domain II to III appears at a value of 1500 MPa true stress and 8 % of total true strain for all specimen thicknesses. The strain-hardening in this domain also evidences a similar rate for all thicknesses.

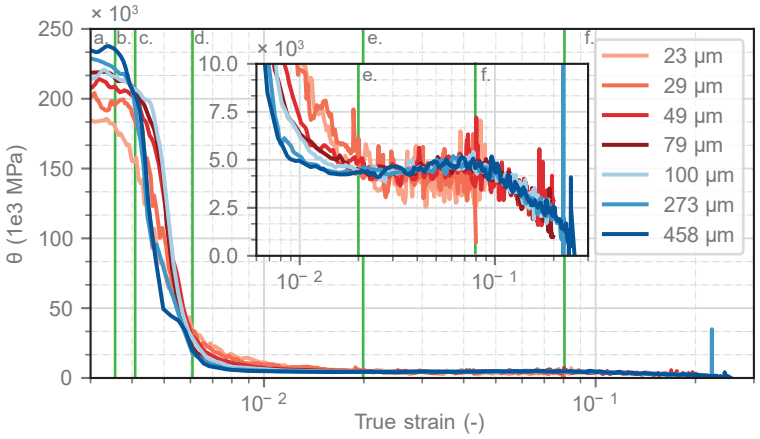

Figure A.1: Strain-hardening rate θ as a function of the true strain for different specimen thicknesses. a, b, c, d, e, and f domains are detailed above

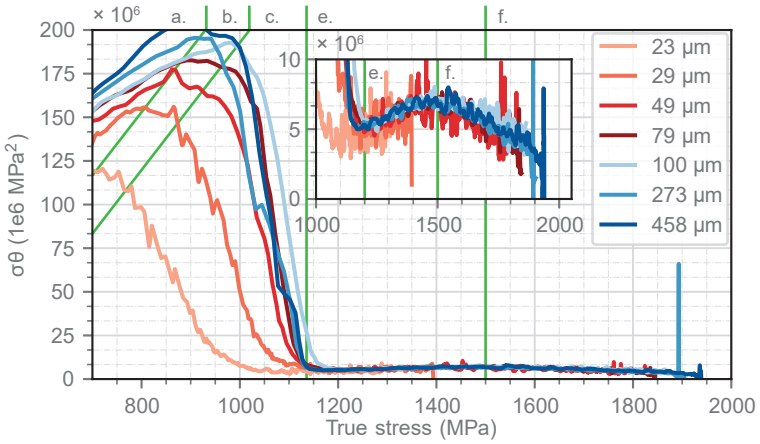

Figure A.2: True stress times strain-hardening rate $\sigma\theta$ as a function of the true stress for different specimen thicknesses. a, b, c, d, e, and f domains are detailed above

Appendix B

Impact of the surface finish on thin specimens

Specimens in the 20 µm range are expected to be more sensitive to measurement and preparation imperfection in terms of specimen planeness (and so measured section), surface finish, out-of-plane displacements, plastic strains in the jaws compared to conventional cylindrical specimens. The impact of those parameters is detailed in this section.

All the tensile tests were realized on P2400 surface finish (Ra = 0.4 µm, Rz = 3 µm, measured via laser CONFOCAL microscope), but specimens as thin as 20 µm can be seriously influenced by the surface finish resulting from the specimens' preparation. This section then aims at investigating the surface finish effect by comparing the tensile response of P2400 and 0.05 µm alumina powder OP-A (one side and two sides of specimens). The P2400 surface finish was performed via the JIG grinding machine as presented in section 2.1.3. The alumina surface finishing was additionally performed for 4 h per face sequence using a vibrotech polishing machine.

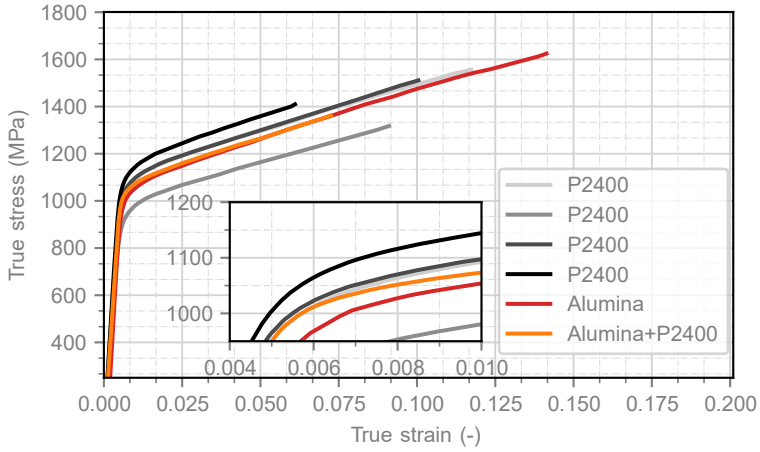

Figure B.1: True stress versus true strain with LOWESS filtering for AR metallurgical state for a 20 µm-thick targeted with a surface finish at grit P2400/800 and alumina 0.05 µm

The true strain-stress responses of the 20 µm-thick specimens and 30 µm-thick specimens are given in figure B.1 and figure B.2, respectively. The elastic-to-plastic transition and subsequently the YS demonstrate similar behavior on both surface finishes for both thicknesses. The strain-hardening is commensurable on both surface finishes for all thicknesses as well. The ductility and subsequently the UTS are the main differences as revealed by a total strain increase of 100 % on both specimen thicknesses of 20 µm and 35 µm. Such behavior might arise from the presence of fewer initiation sites on the alumina surface finish that prematurely damage the specimens and then lead to a higher elongation.

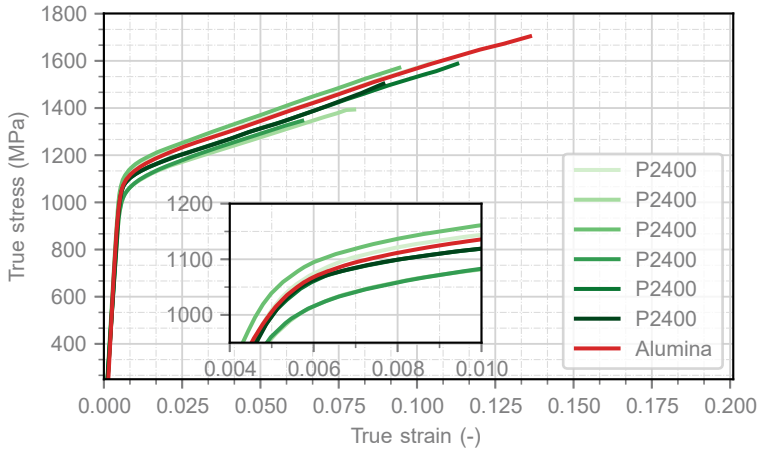

Figure B.2: True stress versus true strain with LOWESS filtering for AR metallurgical state for a 35 µm-thick targeted with a surface finish at grit P2400/800 and alumina 0.05 µm

Another idea for using the vibrotech polishing machine is to investigate the presence and impact of residual stresses resulting from the grinding process using the JIG machine. Long-term grinding sequence on such vibrotech results in almost complete removal of residual stresses from the surface of specimens. This assumption was experimentally validated by observing twin boundaries in γ' particles in SEM-BSE micrograph (very low strain-hardening from residual stresses which induce better diffraction of the crystallographic plans). The similar stress-strain responses from both surface finishes, and especially the strain-hardening rate, demonstrate the very low residual stresses induced by the JIG grinding sequence with a surface finish of P2400 for tensile testing.

Analysis

To resume the surface finish investigation onto the residual stresses of specimens: the P2400 surface finish of the tensile specimens leads to similar tensile behavior in comparison with a perfectly stress-free 0.03 µm colloidal silica surface finish. Improving the surface finish resulted in less premature damage of the specimen leading to a higher ductility and UTS of the specimens.

Appendix C

Heterogeneity of strain distribution in thin and thick specimens and planeness effect

The DIC technique used to monitor the elongation of the specimens during the tensile tests has also been analyzed in a full-field manner in the following section. Emphasis on the heterogeneity of the strain distribution in thin and thick specimens is performed before assessing the planeness effect of the specimens on the tensile response of the material.

C.1 Raw DIC results

The strain distribution in the specimen gage at different measured strain levels of 0.4 %, 0.5 %, 0.6 %, 0.8 %, 1 % and 20 % (or maximal strain if less than 20 µm), the true stress-strain curve, and the strain distribution histogram are presented in figure C.1, C.2, and C.3. The specimens tested in this section have average thicknesses of 507 ± 2 µm, 97 ± 1 µm and 25.0 µm respectively. The three-thicknesses figures present similar and homogeneous strain distribution in the specimen gage in both elastoplastic and plastic regimes. Such an observation is also supported by the commensurable stress-strain response from the mean strain and stress (blue curve) to the max strain and stress (red curve).

The strain distribution of specimens with a homogeneous thickness (relative to the total thickness) is compared to one of the biased specimens in figure C.4. The strain distribution clearly reveals a heterogeneous strain distribution with a maximal value of strain located close to a radius of the specimen, at the minimum thickness and so at the minimal section. While the strain distribution is thickness dependent, the strain-stress curves demonstrate a similar behavior from the mean and maximal values. The elastic-to-plastic transition does not seem to be affected by the 5.4 % of thickness variation present in the 5 mm-long specimen gage presented in figure C.4.

The impact of biased compared to flat specimens is further analyzed in the following section. Such a thickness deviation results from the JIG grinding process due to the not-perfect sticking of the specimens, unaligned JIG, or not-perfect flatness of the rectified glass (where specimens are stuck). Even though a thickness deviation of 2 µm is relatively negligible for thick specimens, it can result in up to 10 % thickness variation for 20 µm-thick specimens.

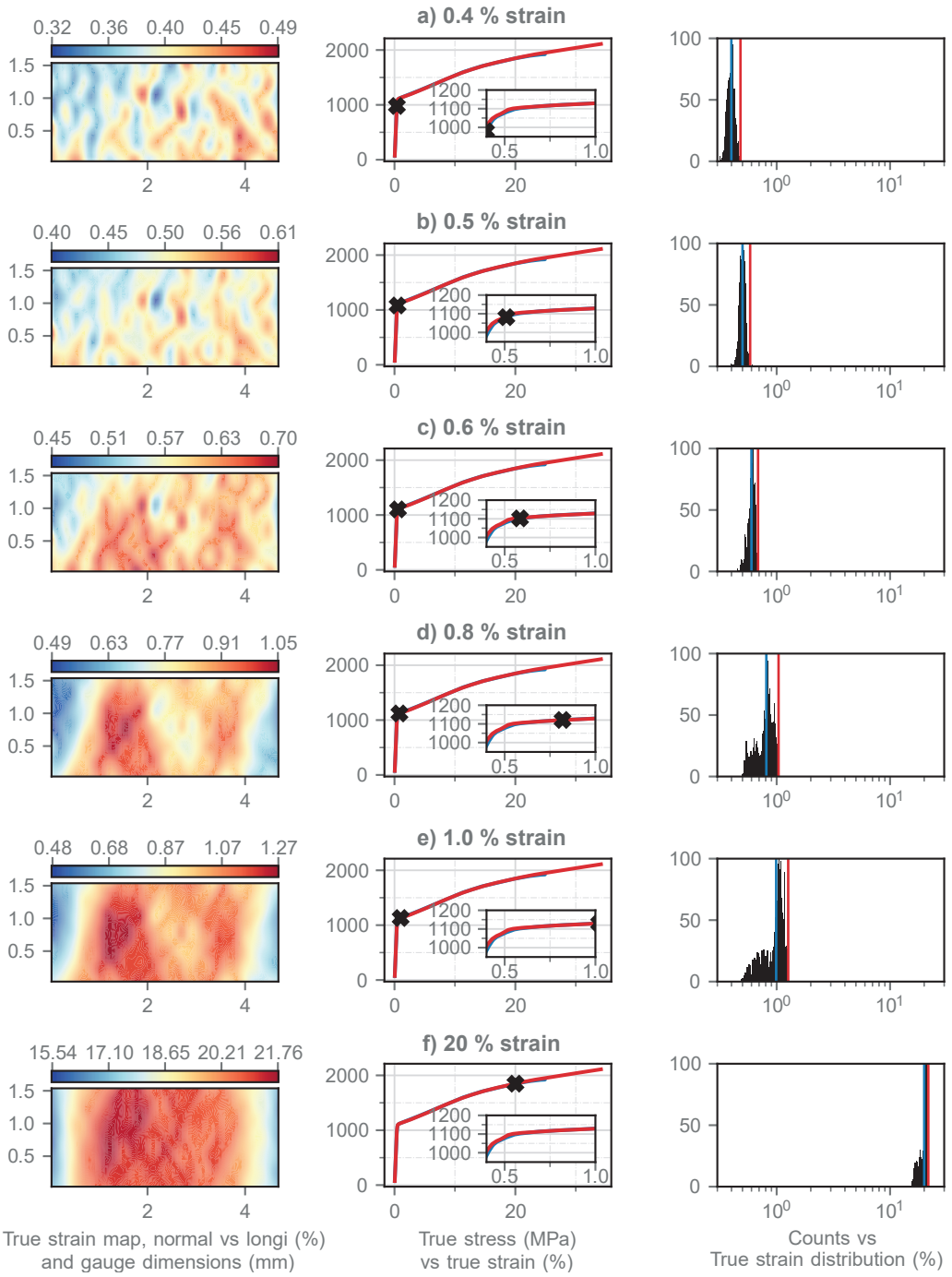

Figure C.1: Strain distribution in the specimen gage of thickness $507.0 \pm 0.7\,\mu m$ for strain values of 0.4 %, 0.5 %, 0.6 %, 0.8 %, 1 % and 20 %; corresponding true stress-strain curves with mean strain and stress in blue, max strain and stress in red; histogram of the strain distribution with mean (blue) and max (red) strain vertical line

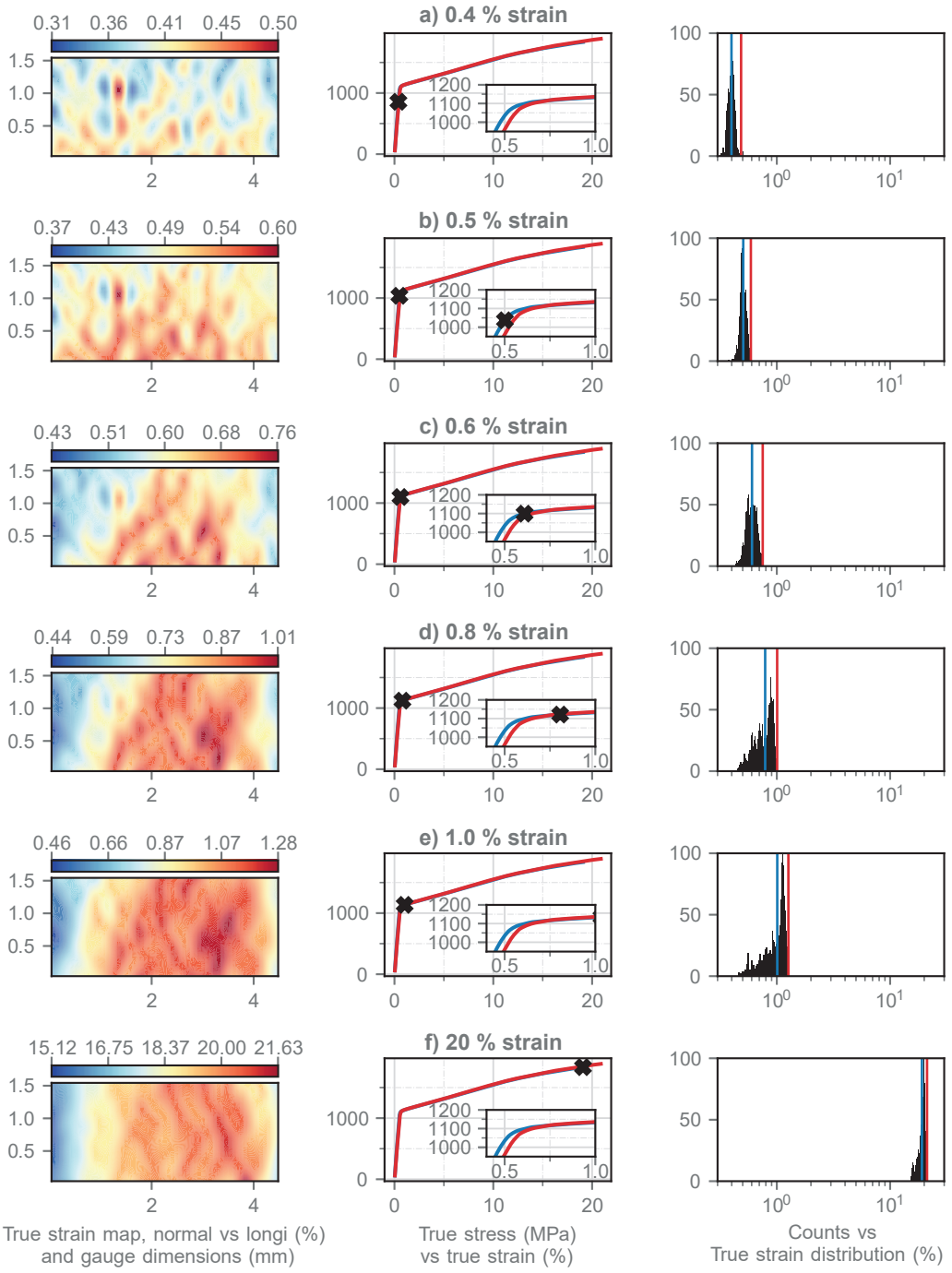

Figure C.2: Strain distribution in the specimen gage of thickness $97.0 \pm 1.0\,\mu m$ for strain values of 0.4 %, 0.5 %, 0.6 %, 0.8 %, 1 % and 20 %; corresponding true stress-strain curves with mean strain and stress in blue, max strain and stress in red; histogram of the strain distribution with mean (blue) and max (red) strain vertical line

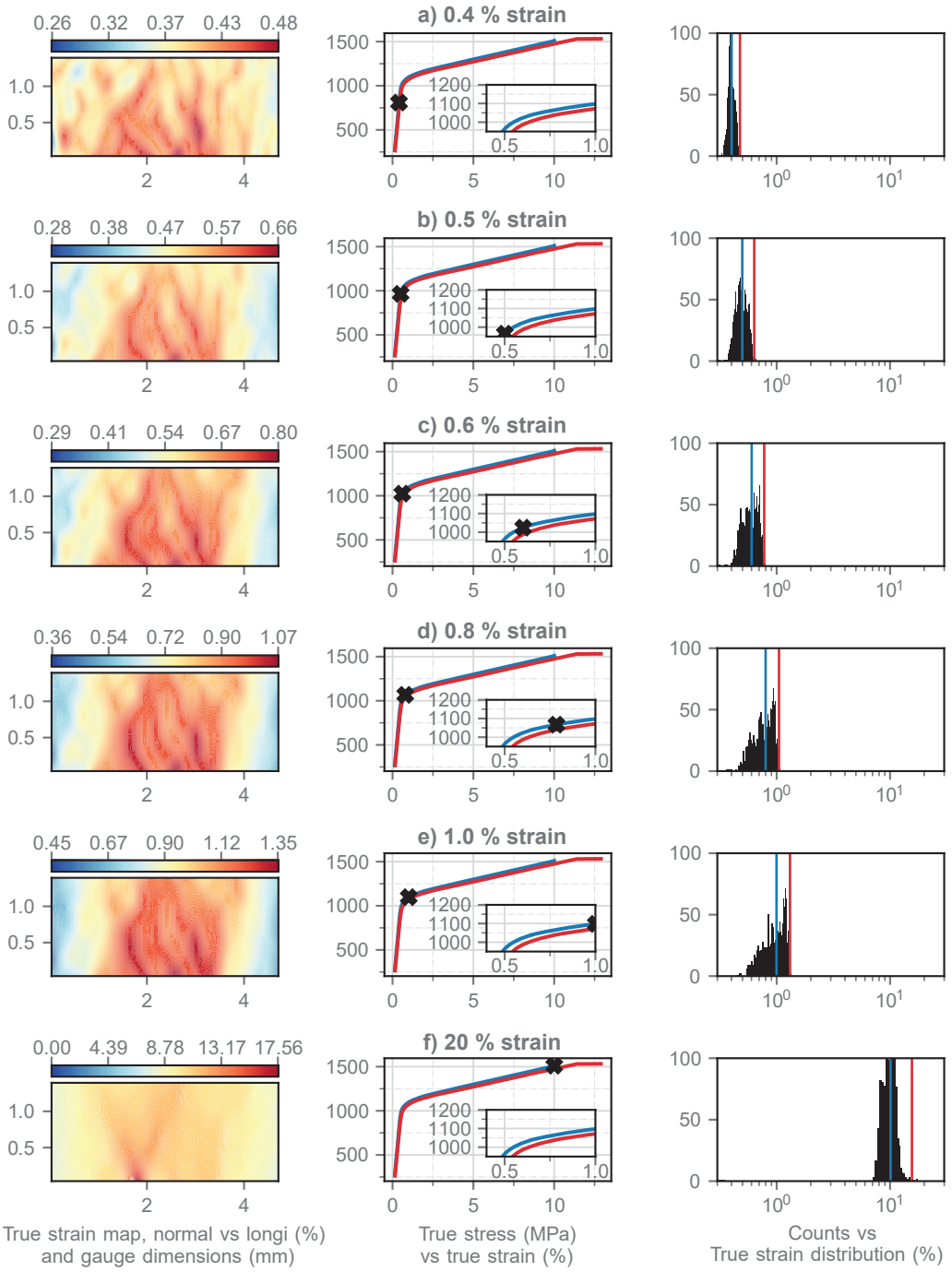

Figure C.3: Strain distribution in the specimen gage of thickness 25.0 µm for strain values of 0.4 %, 0.5 %, 0.6 %, 0.8 %, 1 % and 20 %; corresponding true stress-strain curves with mean strain and stress in blue, max strain and stress in red; histogram of the strain distribution with mean (blue) and max (red) strain vertical line

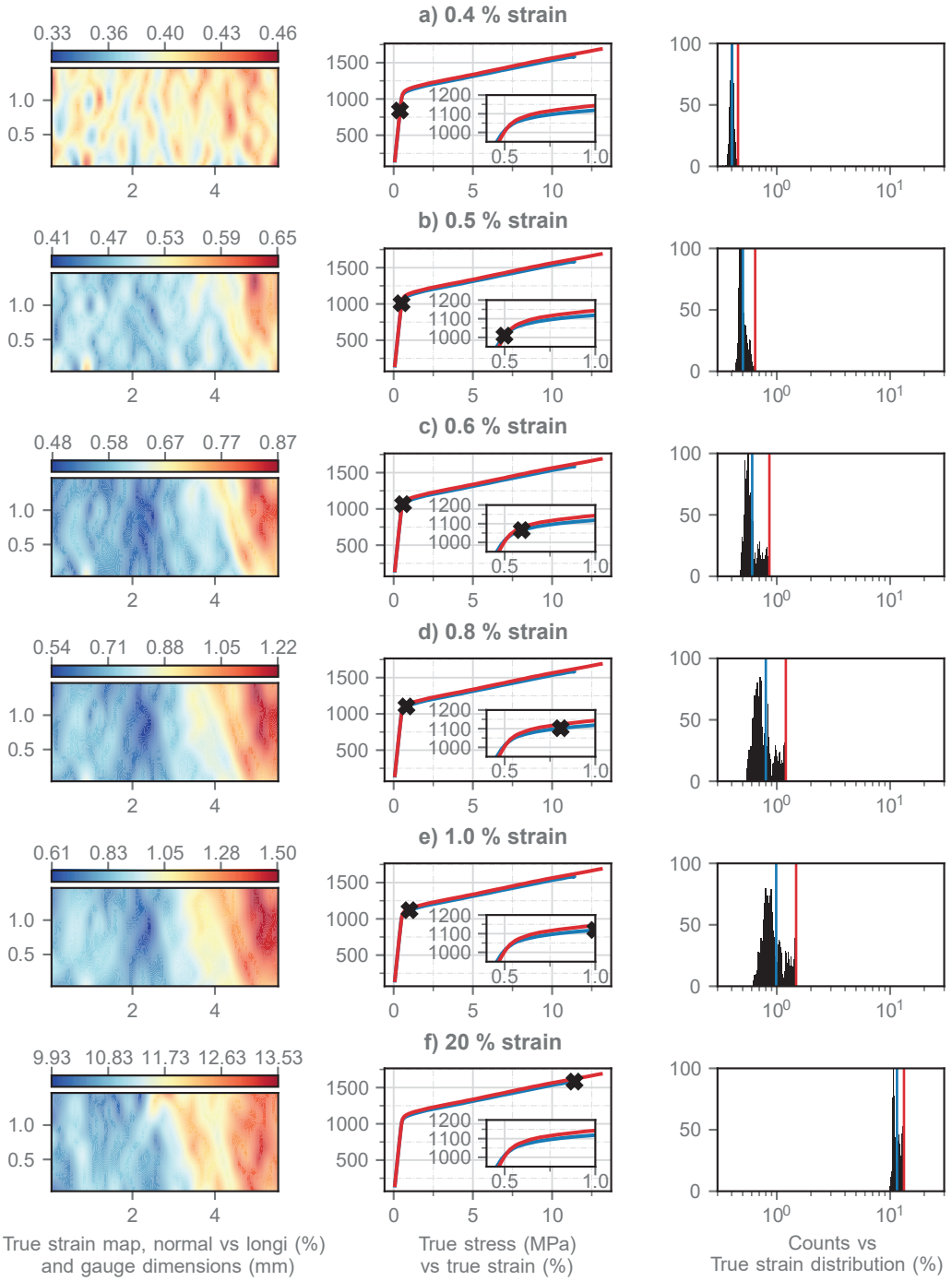

Figure C.4: Strain distribution in the specimen gage of thickness $37.0 \pm 2.0\,\mu m$ for strain values of 0.4 %, 0.5 %, 0.6 %, 0.8 %, 1 % and 20 %; corresponding true stress-strain curves with mean strain and stress in blue, max strain and stress in red; histogram of the strain distribution with mean (blue) and max (red) strain vertical line

C.2 Analysis and impact of the planeness of specimens

The impact of biased specimens in the thickness onto the mechanical response is performed via modeling the stress-strain response of biased specimens with its thickness discretized into n segments varying from the minimal to the maximal thickness, as given in figure C.5. Two specimens of similar mean thicknesses are then compared, one flat named reference (as exposed in figure C.3), and one biased named biased. The algorithm applied is the following:

1. The load measured on the biased specimen is applied on all segments. The load is the same for each segment due to its application direction (longitudinally). A matrix is created to fulfill the entire tensile test (temporally).
2. The engineering stress is computed for each segment considering the actual section of the segment. Such an event is performed for each load measured during the tensile test.
3. The engineering strain is determined by identifying the corresponding engineering stress of the reference specimen stress-strain response. Such a signal being discrete, linear interpolation is performed between the two closest values of the reference engineering stress-strain curve. Linear interpolation is relevant due to the sufficient resolution of the reference stress-strain signal.
4. The true stress is computed thanks to equation C.1.
5. The true strain is identified from the reference specimen's true stress-strain response via identification of the true stress.
6. The true stress-strain from the biased signal is then compared to the biased experimental signal in terms of mean strain and stress (similar methodology as the experimental signal), mean strain and maximal stress (minimal value of thickness and DIC technique employed as displacement gage), and maximal strain and stress (real behavior of the specimen at its minimal thickness).

$$\sigma_t = \sigma\,(1+\epsilon) \tag{C.1}$$

with σ_t being the true stress, σ the engineering stress, and ϵ the engineering strain.

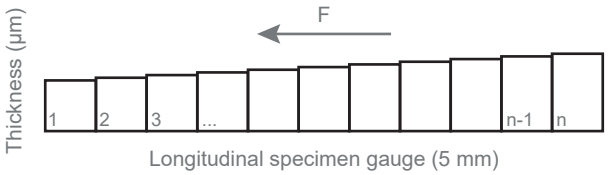

Figure C.5: Discretization of the thickness into n segments varying from the minimal to the maximal thickness

The modeling presented in figure C.6 is based on a discretization of the specimen longitude of 500 segments. The engineering and true stress and strain were smoothed using the LOWESS algorithm presented in section 2.1.2. A smoothed signal is required

to ensure proper identification of the corresponding stress and strain couple. A noisy signal is to interfere with such proper identification due to the multiplicity of strain-stress couples (multiple strain values possible for one value of stress and vice versa).

The stress-strain curves of the biased modeling algorithm are presented in figure C.6. The reference specimen behavior is the one given in figure C.3 with a flat 25 µm thickness whereas the biased specimen presents a 2 µm thickness deviation on the specimen gage. The strain distribution of the biased specimen's gage and its histogram are presented along with the modeling results in figure C.7.

The true stress-strain experimental are given in black and red dashed lines in figure C.6 for the reference and biased specimens respectively. Those curves reveal a similar behavior in terms of strain-hardening rate (similar slope) but with a 50 MPa increase in stress at iso-strain for the biased specimen. Such an increase in stress for 25 µm-thick specimen is potentially the result of a 1 µm error on the thickness measurement. The elastic-to-plastic domain (particularly visible in the sub-figure strain-hardening plot) reveals nevertheless a more progressive transition for the biased specimen (up to 3×10^3 MPa). The modeled curves are valid until 4 % of total strain (a change of slope is observed) due to the maximal stress of the biased specimens (at the minimal section) being above the reference maximal stress. The strain is then set to the maximal strain experimentally determined, and the modeled specimen then tends to an equivalent flat surface for those exceeding values of stresses. The modeled true stress-strain curves are given in solid lines:

Blue: models the true stress and strain of a perfectly flat specimen by application of the biased algorithm (but no thickness variation). Its behavior is the same as the experimental signal. Such a resemblance arises from the direct application of the stress-strain response of the reference specimen. The values are then a direct copy of the experimental values. No mean and maximal values can be determined from the invariant thickness and copy of the experimental mean strain.

Orange: gives the mean strain and stress of the modeled biased specimen. Such a curve is supposed to mimic the experimental biased specimen behavior due to the similarities in strain and stress determination. Whereas its behavior is closer to the reference specimen in terms of stress values, the strain-hardening rate is nevertheless closer to the biased specimen with a more progressive elastoplastic transition. Such progressive transition arises from the plasticity to occur step-by-step in each thickness segment. At the onset of plasticity, only the first segment of minimal thickness sees plastic deformation. The plasticity gradually propagates in all the segments with the minimal thickness segment being already in the II domain of strain-hardening (4 % of total strain for the minimal thickness segment while the largest thickness segment encounters plasticity). Such heterogeneity results in the progressive elastic-to-plastic transition while taking the mean strain and stress seen by the biased specimen.

Green: represents the maximal stress for the mean strain to take into consideration the minimal value of thickness. The strain-hardening rate of such a stress-strain determination method does not mimic the experimental behavior of both biased and reference specimens. The stress-strain curve is then located above the experimental curves.

The orange curve is directly compared to the biased experimental curve providing insight onto the elastic-to-plastic rate. The bias in the thickness of specimens is responsible for the more progressive elastic-to-plastic transition due to the strain and stress determination methodology (mean values). Such a conclusion is particularly true for thin specimens having a high ratio $\frac{\Delta thickness}{thickness}$. The maximal thickness deviation measured on the 400 specimens produced is of 5 um for 25 µm-thick specimens and 6 µm for 30 um-thick specimens. The maximal deviation ratio in thickness is of 20 %. The overall thickness deviation ratio on the 400 specimens is of 3 %.

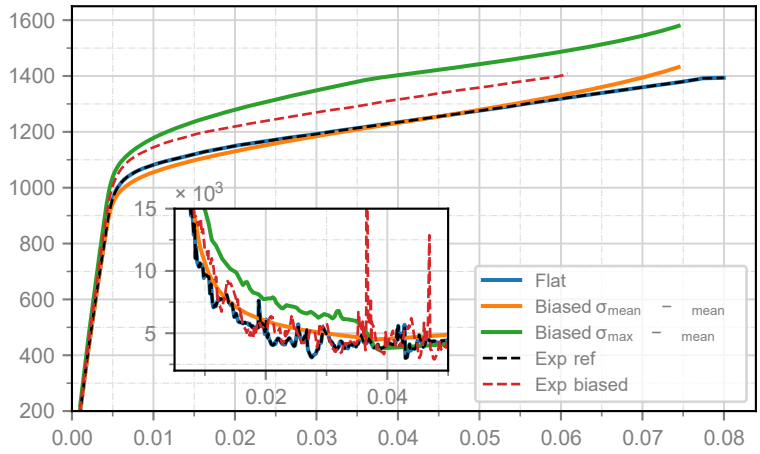

Figure C.6: True stress-strain curves of the biased specimen (red dashed curve) versus flat specimen (black dashed curve). Modeling of the bias by applying the flat specimen stress-strain response to a biased specimen (mean stress-strain of flat specimen in blue, mean stress-strain of biased specimen in orange, max stress-mean strain of biased specimen in green)

The comparison of strain distribution in the specimen gage in the experimental with the modeled biased specimen is given in figure C.7 along with the stress-strain curves and strain histogram. The blue curve and strain distribution display the experimental specimen, while the red curve is for the modeled one. The curves presented are similar to the experimental black and red curves and modeled blue and orange curves of figure C.6. The strain distribution in the specimen's gage is a correct estimation of the mean strain of each modeled segment, as exposed in both strain distribution plots on low strain levels (a, b and c). The higher strain levels (above 0.8 %) reveal higher strain values at the radius of higher thickness, sign of a thickness closer to a sinusoidal shape than a biased shape. The strain distribution histogram agrees with this conclusion on the different strain levels. Low strain demonstrates a homogeneous strain distribution while heterogeneous strain distribution with radius strain concentration is observed at higher global strain levels.

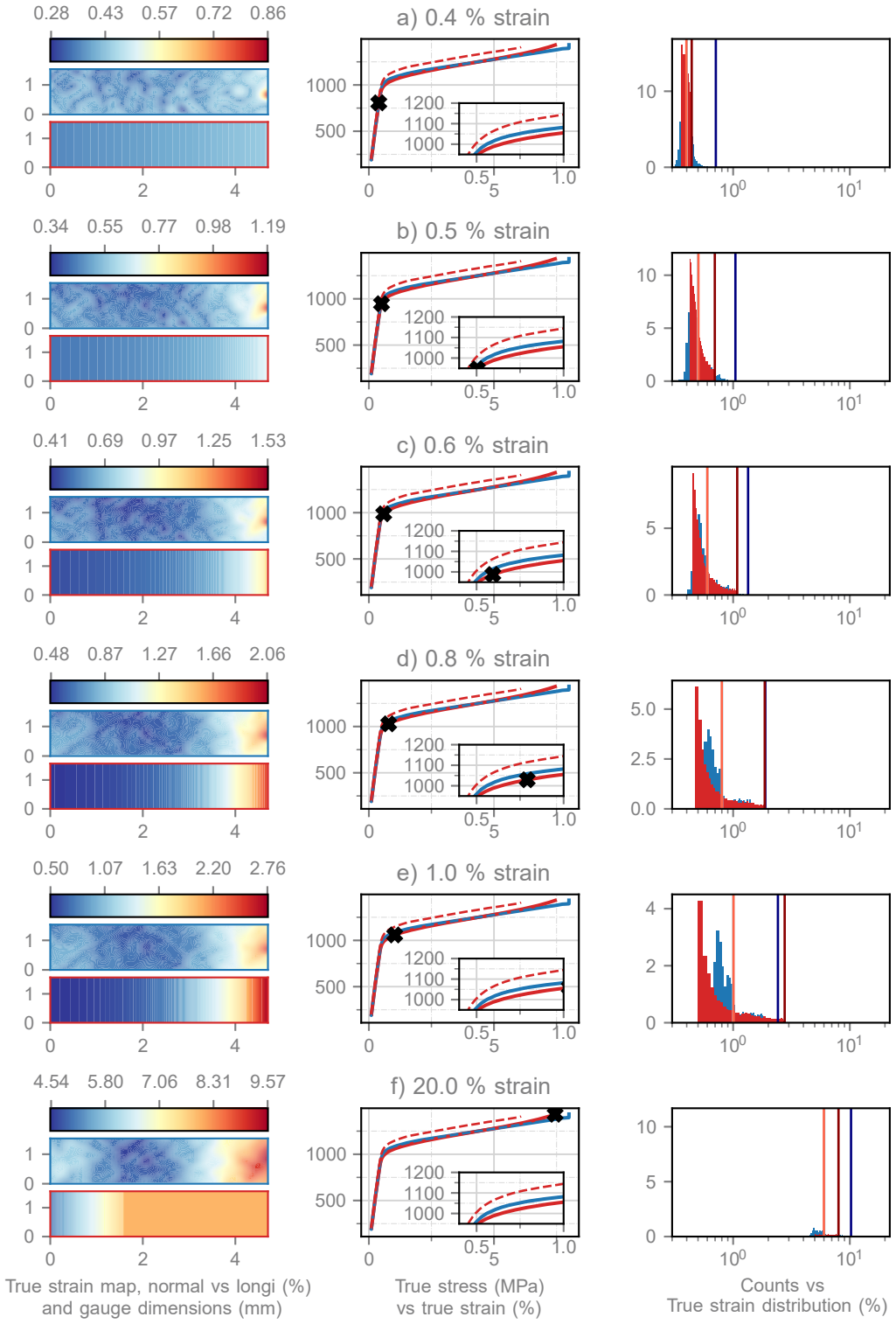

Figure C.7: Strain distribution in the gage specimen for a biased specimen of thickness $25 \pm 2\,\mu m$ (blue rectangle, stress-strain curve, and strain distribution) compared to a diagonal biased specimen with strains determined via application of a $25\,\mu m$ flat specimen stress-strain response (red color). The dashed stress-strain curves represent the modeled response, the solid curves are the experimental response

The biased specimen algorithm was implemented using several reference specimens of thicknesses 507 µm, 97 µm, 49 µm and 29 µm by keeping the same ratio of thicknesses from the experimental one. The experimental results, while observing a 50 MPa increase in stresses at iso-strain, reveal a similar strain-hardening rate from the 29 µm-thick reference specimen. The strain-hardening rate in domain I evolves along with the increase in specimen thickness, representative of the more progressive elastic-to-plastic transition for thinner specimens. Such results demonstrate that the thickness effects are unrelated to geometry specifications from thin to thick specimens but related to a material matter. The strain-hardening rate of domain II is still unrelated to any thickness effect of the specimens, as demonstrated in section A.

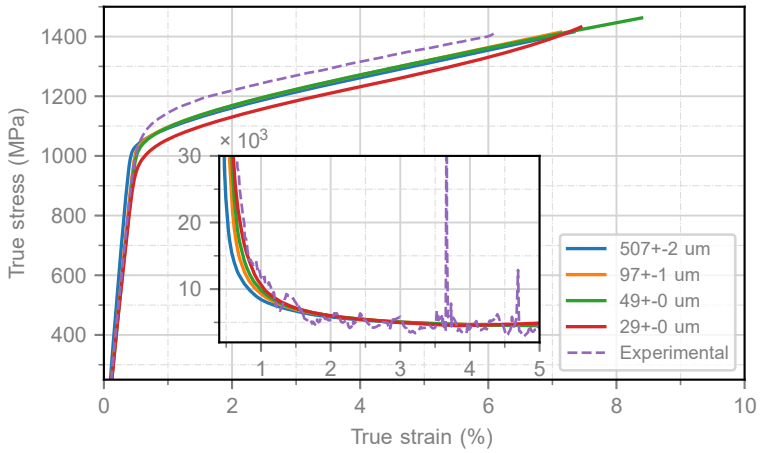

Figure C.8: Stress-strain curves (figure) and strain-hardening rate (sub-figure) of biased experimental specimen (violet) and corresponding modeling using different reference specimens of thicknesses in the range 20 µm to 500 µm

Analysis

To sum up this section: the thickness deviation consequences of thin specimens were investigated. A change in the elastic-to-plastic transition with a more progressive slope for biased specimens results from the mean thickness consideration for the stress computation.

Appendix D

Detailed plotting of the tensile properties as a function of the thickness of specimens

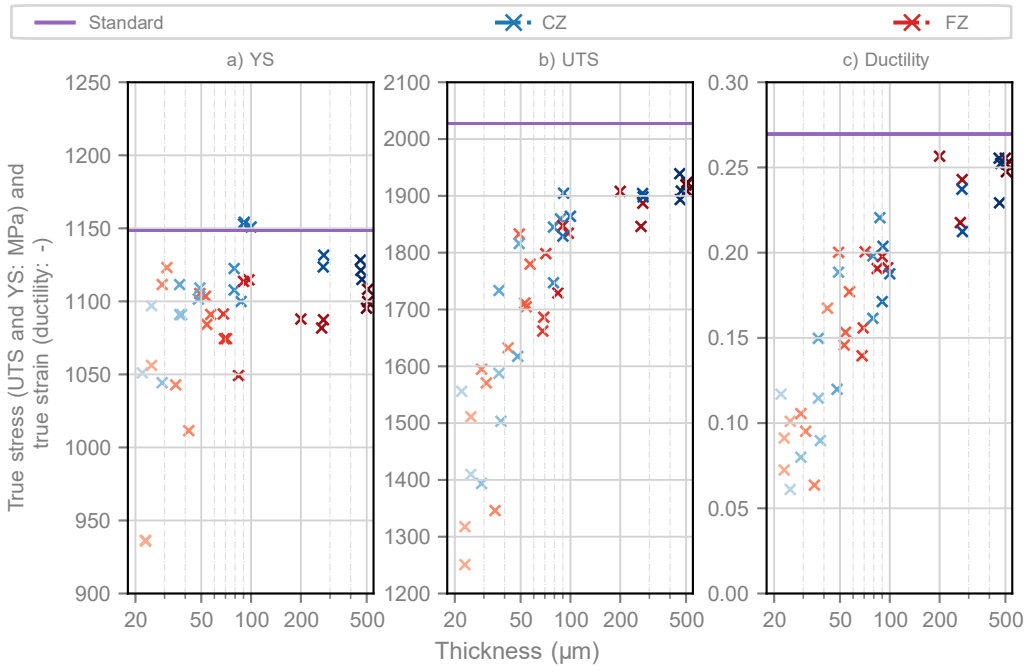

Figure D.1: Summary of the YS, UTS, and ductility as a function of the specimens thickness of AR state on all tensile tests

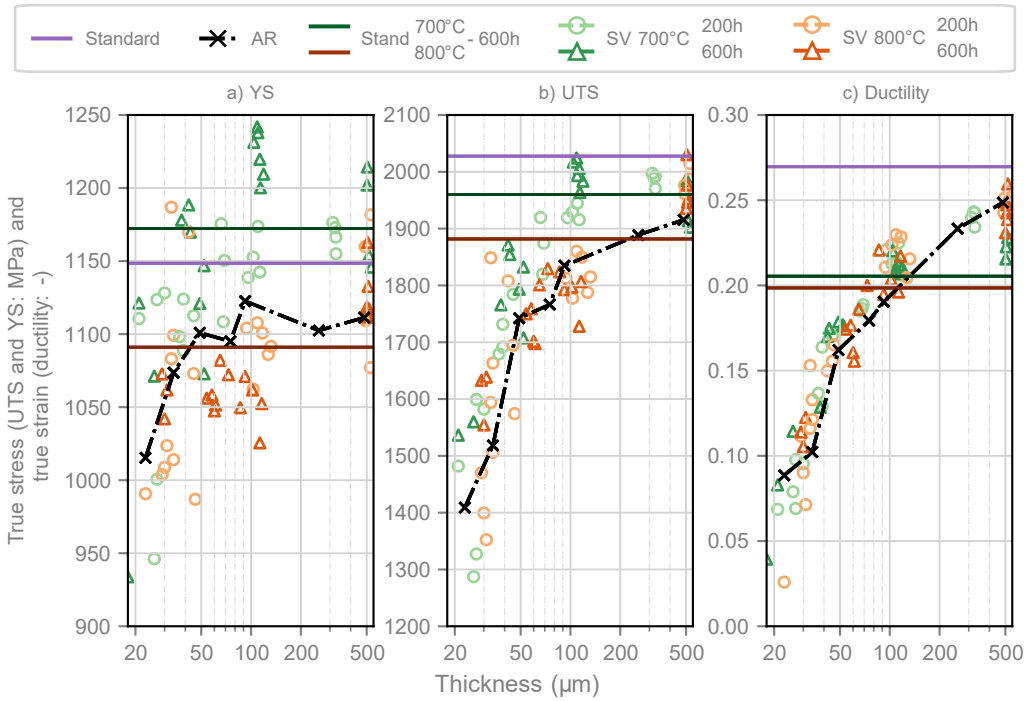

Figure D.2: Summary of the YS, UTS, and ductility as a function of the specimen thickness for the aged conditions with regards to the AR state and the standard tests

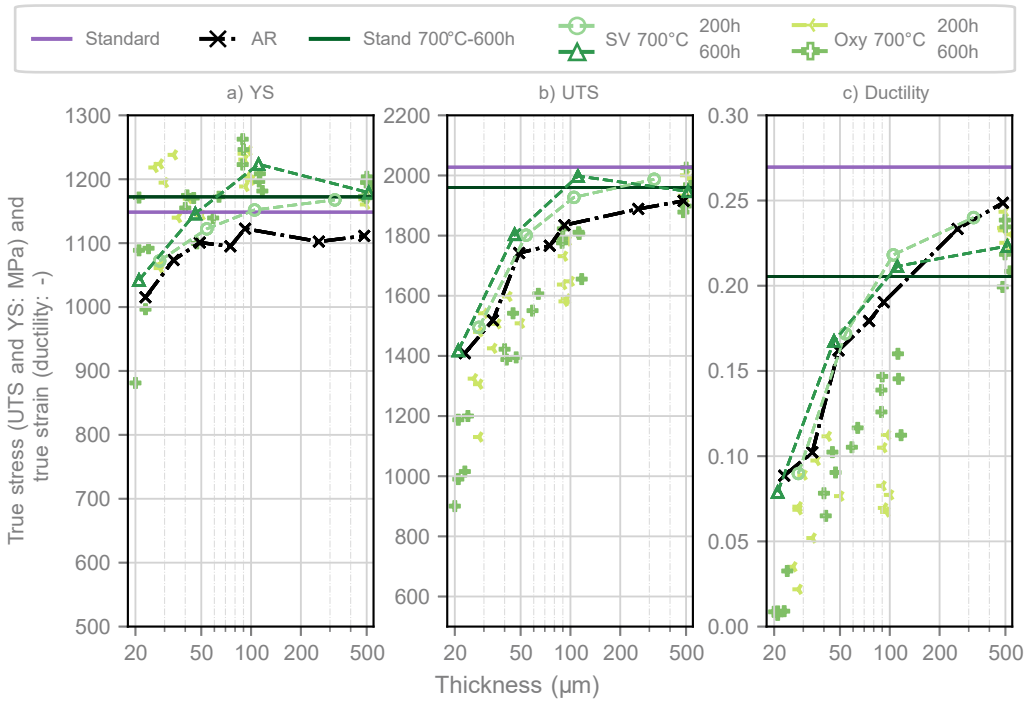

Figure D.3: Detailed summary of the YS, UTS, and ductility versus the thickness of the specimens for the oxidized at 700 °C condition and corresponding AR and standard behavior

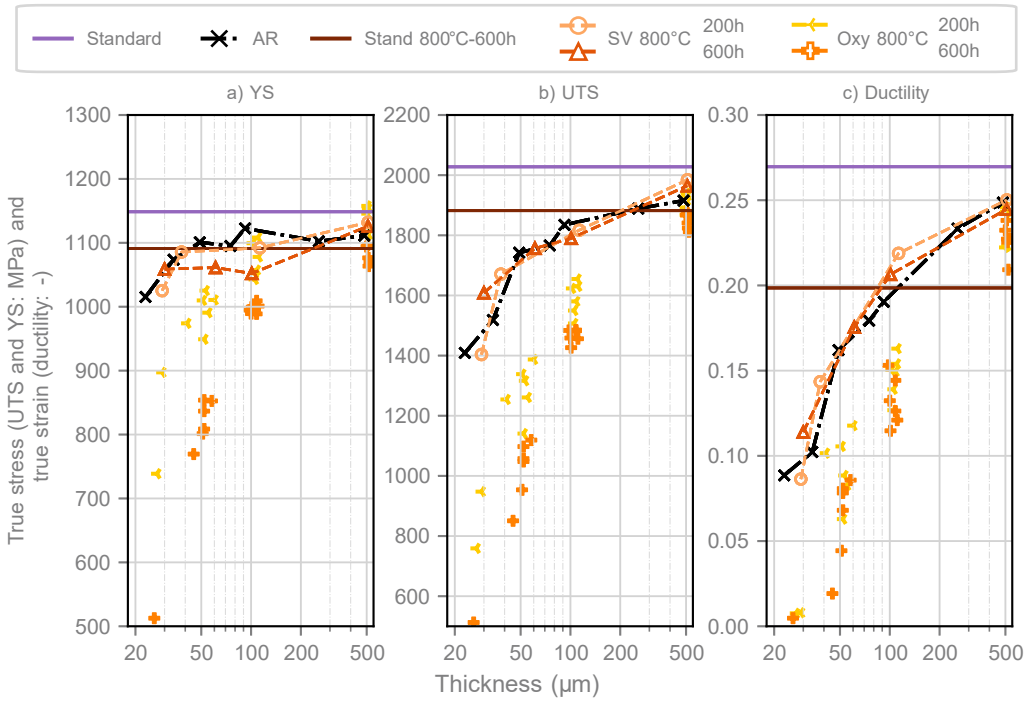

Figure D.4: Detailed summary of the YS, UTS, and ductility versus the thickness of the specimens for the oxidized states at 800 °C condition and corresponding AR and standard behavior

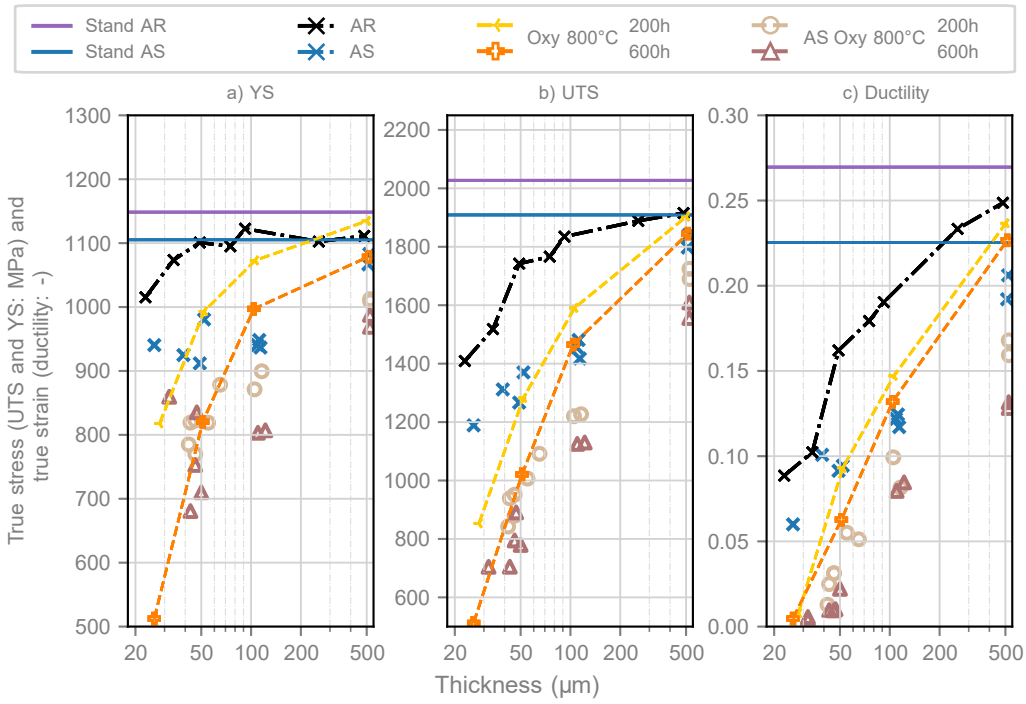

Figure D.5: Detailed summary of the YS, UTS, and ductility versus the specimens' thickness in the AR state (in black), AR oxidized (yellow and orange) at 800 °C for 200 h and 600 h, AS state (blue) and AS oxidized at 800 °C (light brown and brown) during 200 h and 600 h

Appendix E

Deep learning-based image analysis

The recent hardware evolutions, especially in the GPU field, have brought deep-learning analyses back into the foreground. The current performances allow for complex model computations with millions of internal parameters within minutes or hours. The vision area is one of the major fields in deep learning analysis, as demonstrated by the interest and developments of companies such as Google with its package TensorFlow [232].

Common image segmentation is based on edge detection algorithms such as Sobel detector [233] and Canny detector [234]. Thresholding also provides powerful segmentation on contrasted images, such as Otsu's algorithm [235]. Deep learning techniques present several advantages in terms of computation time, and integrated classification of the segmented elements (for multi-class segmentation algorithms) [236].

Deep Learning (DL) algorithms were used in this project to mimic SEM-EBSD analyses segmentation of grain boundaries without considering twin boundaries. SEM-BSE micrographs, in the case of René 65, demonstrate strong crystallographic misorientation from the neighboring grains and thus ensure the detection of the grain boundaries. Twin boundaries are also revealed from such SEM-BSE analyses. Deep learning-based algorithms allow the differentiation of grain boundaries from twin boundaries based on internal parameters and not only based on the curvature of the detected boundary (twin boundaries being mainly flat).

The present developments are based on medical image segmentation algorithms using the supervised deep learning technique Convolution Neural Network (CNN) structures. The algorithm, named DC-Unet[1], is an improved version of the Unet algorithm renowned for its predominant approach to medical image segmentation task [206]. The Unet encoder-decoder network was used to obtain binary segmentation of aluminum alloys [237]. DC-UNet uses convolutional layers to perform the semantic segmentation, as depicted in figure E.1.

Deep learning-based algorithms rely on the training of a complex model to identify and optimize the parameters (via linear regression) that best fit a training dataset and its expected output. A dataset is composed of 8-bit gray-scale SEM-BSE micrographs of various resolutions (1280 px × 1024 px to 4096 px × 3775 px) and magnification (x150 to x100 000), and their targeted mask (grain boundaries without considering twin boundaries from SEM-EBSD analyses, primary, secondary and tertiary precipitates segmentation from common image segmentation techniques). The dataset micrographs were subdivided into several tile sizes (64 px × 64 px, 128 px × 128 px, 256 px × 256 px and 512 px × 512 px) to limit the required GPU memory and expand the training dataset.

[1] https://github.com/AngeLouCN/DC-UNet

The multi-resolution tiles sizes training intends to increase the model segmentation accuracy when providing a wide range of SEM micrographs magnifications.

Image augmentation methods are used to increase the segmentation accuracy of the algorithm. Such methods consist in randomly applying to the tile and its relative mask the following operations: rotation, expansion, shrinkage, blur, and pixel degradation. All the SEM-micrographs are equalized in terms of histogram (gray-scale values going from 0 to 255). The grain boundary segmentation was performed on 10 micrographs dataset. The γ' particles segmentation training was performed on a 50 micrographs dataset, such as given in figure E.2.

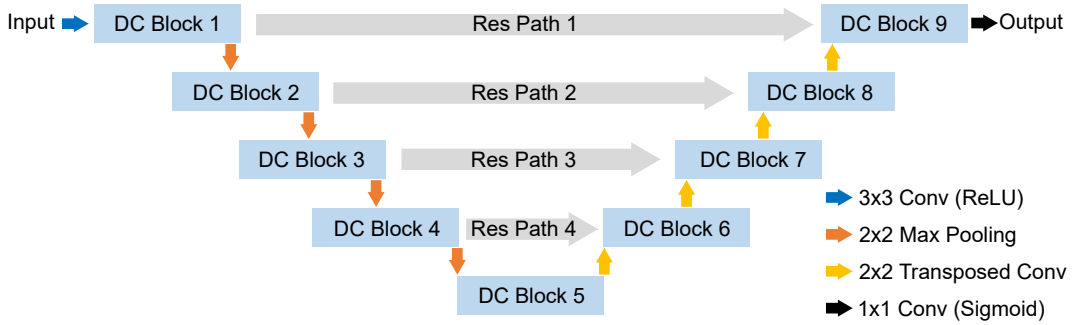

Figure E.1: DC-Unet architecture [206]

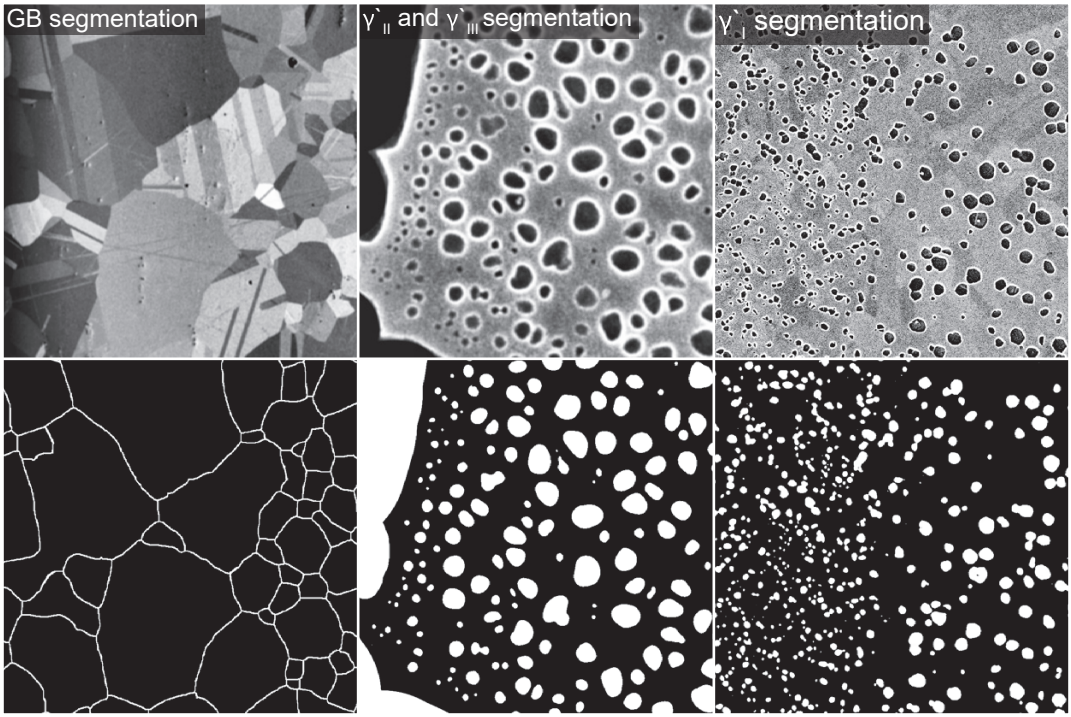

Figure E.2: SEM micrograph and equivalent mask for deep learning training

The results from image segmentation deep learning based are given in figure E.3. The grain boundary segmentation is perfectible, but the twin boundaries are not detected as grain boundaries. The main objective of such an algorithm is then met. The training was performed on a low dataset, the accuracy of the segmentation could be significantly increased by using a larger dataset. The low number of segmented

SEM-BSE micrographs from SEM-EBSD analysis composing such a dataset is due to the necessity of correcting any geometrical aberration and distortion from both experimental observation means. Authors such as Charpagne *et al.* investigated such data merging aberrations due to the large fields of view, large sample tilt required for EBSD (and the associated geometric distortions) and beam drift [238]. But such an algorithm was not implemented due to lack of time and being out of the framework scope.

The γ' precipitates segmentation demonstrates much more accurate results, with up to 96 % accuracy (according to the Jaccard Similarity (JS) coefficient, being the intersection of the input mask versus the DL based segmented one divided by their union [239]). Such accuracy was made possible after 7 training loops on a 500 micrographs dataset (approximately 2 h to 5 h of training computation time per loop on a 8 GB RTX 2080 GPU). 750 SEM micrographs were then submitted to this DL algorithm (30 min of computation time), the results are given in René 65 microstructural characterization for the AR state in section 2.2 and for the aged state in section 3.2.

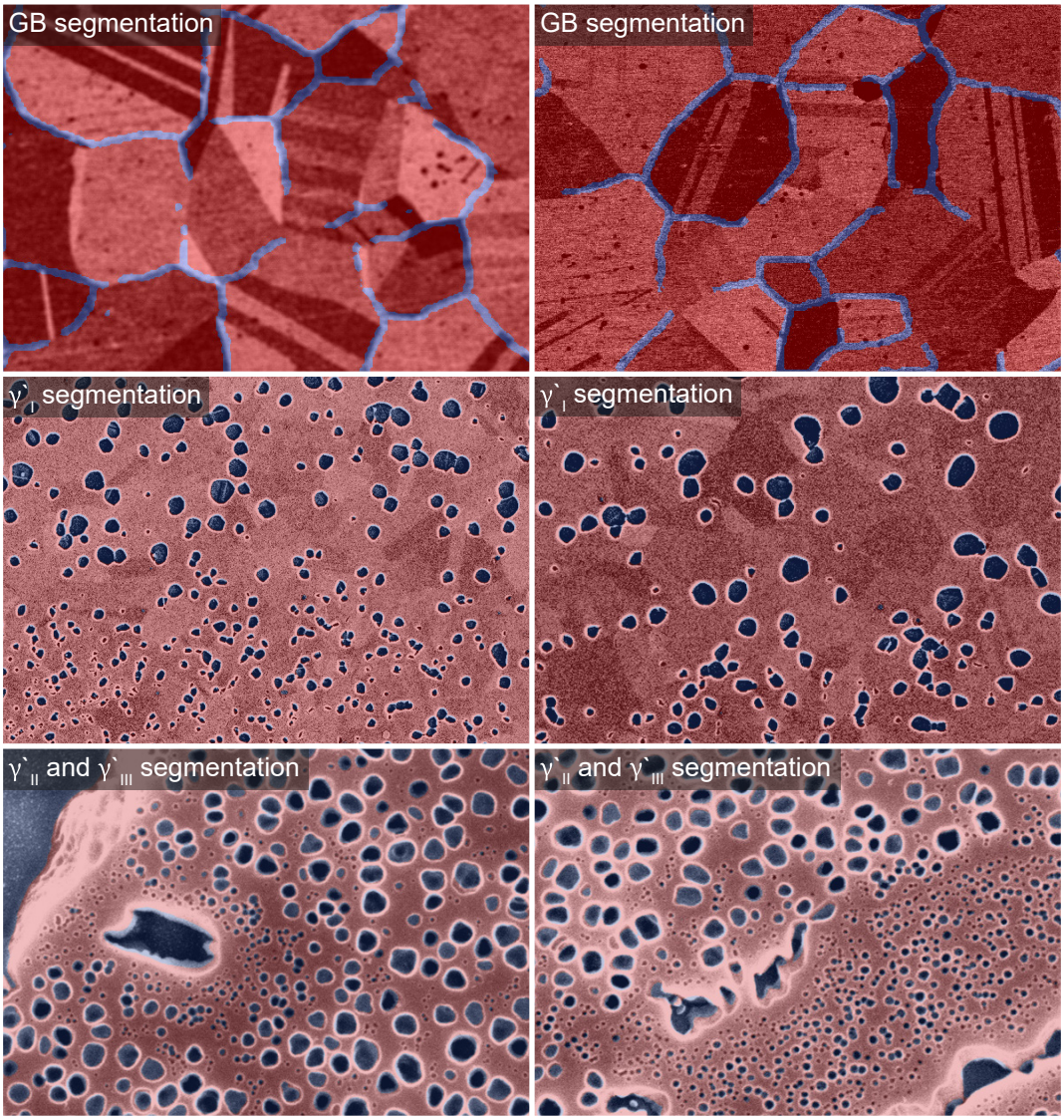

Figure E.3: Deep learning results, segmentation is overlayed to the original SEM-micrograph

List of Figures

List of Tables

Bibliography

[1] Frank Whittle. “Propulsion of Aircraft and Gas Turbines”. Pat. 2168726. Aug. 1939 (cit. on pp. 1, 11).

[2] Roger C. Reed. *The Superalloys Fundamentals and Applications*. Cambridge: Cambridge University Press, 2006 (cit. on pp. 1, 11, 12, 17–19, 21, 23, 31).

[3] S. Patel and J. deBarbadillo. “Innovation through Collaboration”. In: *Superalloys 2016*. John Wiley & Sons, Ltd, 2016, pp. 1–12 (cit. on pp. 1, 11).

[4] Shailesh J. Patel. “A Century of Discoveries, Inventors, and New Nickel Alloys”. In: *JOM* 58.9 (Sept. 1, 2006), pp. 18–20 (cit. on pp. 1, 11).

[5] Scott Delbecq, Jérôme Fontane, Nicolas Gourdain, Hugo Mugnier, Thomas Planeès, and Florian Simatos. *Référentiel ISAE-SUPAERO Aviation et Climat*. 1.1. Sept. 2021 (cit. on pp. 1, 11).

[6] C.T. Sims. “A History of Superalloy Metallurgy for Superalloy Metallurgists”. In: *Superalloys 1984 Fifth Int. Symp.* Superalloys. TMS, 1984, pp. 399–419 (cit. on pp. 1, 11).

[7] Tresa M. Pollock and Sammy Tin. “Nickel-Based Superalloys for Advanced Turbine Engines: Chemistry, Microstructure and Properties”. In: *Journal of Propulsion and Power* 22.2 (Mar. 2006), pp. 361–374 (cit. on pp. 1, 11, 21).

[8] Aude Laurence. “Impact Du Sur-Vieillissement Métallurgique Sur Le Comportement et La Durabilité Du Nouveau Superalliage Pour Disque de Turbine René 65”. PhD thesis. PhD Thesis, ISAE-ENSMA, 2015 (cit. on pp. 2, 13, 21, 22, 24–28, 46, 47, 88, 93, 101, 149, 183).

[9] Adèle Govaere. « Impact des carbures sur la variabilité des propriétés en fatigue de superalliages pour disques ». PhD thesis. ISAE-ENSMA Ecole Nationale Supérieure de Mécanique et d’Aérotechique - Poitiers, Dec. 16, 2020 (cit. on pp. 2, 3, 13, 34, 36, 90, 113, 119, 127, 183, 184).

[10] A. Encinas-Oropesa, N. J. Simms, J. R. Nicholls, G. L. Drew, J. Leggett, and M. C. Hardy. “Evaluation of Oxidation Related Damage Caused to a Gas Turbine Disc Alloy between 700 and 800°C”. In: *Mater. High Temp.* 26.3 (Sept. 1, 2009), pp. 241–249 (cit. on pp. 2, 13, 31, 34).

[11] A. A. N. Németh, D. J. Crudden, D. E. J. Armstrong, D. M. Collins, K. Li, A. J. Wilkinson, C. R. M. Grovenor, and R. C. Reed. "Environmentally-Assisted Grain Boundary Attack as a Mechanism of Embrittlement in a Nickel-Based Superalloy". In: *Acta Materialia* 126 (Mar. 1, 2017), pp. 361–371 (cit. on pp. 2, 13, 46, 48, 49, 159).

[12] *Home | Clean Aviation*. URL: https://www.clean-aviation.eu/ (visited on 03/16/2022) (cit. on p. 11).

[13] Baptiste Larrouy. "Deformation Mechanisms and Fatigue Crack Initiation in Udimet 720Li Superalloy in Relation with Microstructure". PhD thesis. ISAE-ENSMA Ecole Nationale Supérieure de Mécanique et d'Aérotechique - Poitiers, Dec. 2014 (cit. on pp. 17, 39, 45, 183).

[14] Joseph A. Heaney, Michael L. Lasonde, Andrew M. Powell, Betsy J. Bond, and Christopher M. O'Brien. "Development of a New Cast and Wrought Alloy (René 65) for High Temperature Disk Applications". In: *8th Int. Symp. Superalloy 718 Deriv.* (Rene 65 2014), pp. 67–77 (cit. on pp. 18, 21, 22, 24).

[15] Aude Laurence, Jonathan Cormier, Patrick Villechaise, Thomas Billot, Jean-Michel Franchet, Florence Pettinari-Sturmel, Muriel Hantcherli, Frederic Mompiou, and Andrew Wessman. "Impact of the Solution Cooling Rate and of Thermal Aging on the Creep Properties of the New Cast & Wrought René 65 Ni-Based Superalloy". In: *8th Int. Symp. Superalloy 718 Deriv.* (2014), pp. 333–348 (cit. on pp. 18, 21, 96).

[16] C. Zener and C. Smith. "Grains, Phases and Interfaces: Interpretation of Microstructures." In: *Trans. Metall. Soc. AIME* 175.15-51 (1948) (cit. on p. 18).

[17] R A Ricks, A J Porter, and R C Ecob. "The Growth of γ' Precipitates in Nickel-base Superalloys". In: (1982), p. 11 (cit. on p. 18).

[18] J. Tiley, G.B. Viswanathan, R. Srinivasan, R. Banerjee, D.M. Dimiduk, and H.L. Fraser. "Coarsening Kinetics of γ' Precipitates in the Commercial Nickel Base Superalloy René 88 DT". In: *Acta Materialia* 57.8 (May 2009), pp. 2538–2549 (cit. on p. 18).

[19] M. P. Jackson and R. C. Reed. "Heat Treatment of UDIMET 720Li: The Effect of Microstructure on Properties". In: *Materials Science and Engineering: A* 259.1 (Jan. 15, 1999), pp. 85–97 (cit. on pp. 18, 42).

[20] D. Locq, P. Caron, S. Raujol, F. Pettinari-Sturmel, A. Coujou, and N. Clement. "On the Role of Tertiary γ' Precipitates in the Creep Behaviour at 700C of a PM Disk Superalloy". In: *Superalloys 2004 Tenth Int. Symp.* Superalloys. TMS, 2004, pp. 179–187 (cit. on p. 18).

[21] Malik Durand. « Analyse des mécanismes métallurgiques survenant dans l'alliage AD730™ au cours du revenu de relaxation des contraintes ». In: (2021), p. 226 (cit. on pp. 18, 149).

[22] Marie-Agathe Charpagne. "Evolutions de Microstructure Au Cours Du Forgeage de l'alliage René 65". PhD thesis. PhD Thesis, Mines ParisTech, Dec. 2016 (cit. on pp. 18, 21, 22, 101).

[23] S.T. Wlodek, M. Kelly, and D. A. Alden. "The Structure of René 88DT". In: *Superalloys 1996 Eighth Int. Symp.* (1996), pp. 129–136 (cit. on pp. 19, 22).

[24] R Sharghi-Moshatghin and S Asgari. "The Effect of Thermal Exposure on the γ' Characteristics in a Ni-base Superalloy". In: *Journal of Alloys and Compounds* 368.1-2 (Apr. 2004), pp. 144–151 (cit. on p. 19).

[25] P Beardmore, RG Davies, and TL Johnston. "On The Temperature Dependence of the Flow Stress of Nickel-Base Alloys". In: *Trans. Aime* 245.7 (1969), pp. 1537–1545 (cit. on p. 19).

[26] Jean-Roch Vaunois, Jonathan Cormier, Patrick Villechaise, Alexandre Devaux, and Benjamin Flageolet. "Influence of Both γ' Distribution and Grain Size on the Tensile Properties of UDIMET 720Li at Room Temperature." In: (2010), p. 16 (cit. on pp. 19, 42).

[27] D.U. Furrer and H-J. Fecht. "Microstructure and Mechanical Property Development in Superalloy U720LI". In: *Superalloys 2000 Ninth Int. Symp.* Superalloys. TMS, 2000, pp. 415–424 (cit. on p. 19).

[28] Jian Mao, Keh-Minn Chang, Wanhong Yang, David U Furrer, Koushik Ray, and Suhas P Vaze. "Cooling Precipitation and Strengthening Study in Powder Metallurgy Superalloy Rene88DT". In: *Materials Science and Engineering: A* 332.1 (July 1, 2002), pp. 318–329 (cit. on pp. 19, 42).

[29] T. M. Pollock and A. S. Argon. "Creep Resistance of CMSX-3 Nickel Base Superalloy Single Crystals". In: *Acta Metallurgica et Materialia* 40.1 (Jan. 1, 1992), pp. 1–30 (cit. on pp. 19, 149).

[30] A. D. Sequeira, H. A. Calderon, and G. Kostorz. "Shape and Growth Anomalies of γ' Precipitates in Ni-Al-Mo Alloys Induced by Elastic Interaction". In: *Scripta Metallurgica et Materialia* 30.1 (Jan. 1, 1994), pp. 7–12 (cit. on p. 19).

[31] A. R. P. Singh, S. Nag, S. Chattopadhyay, Y. Ren, J. Tiley, G. B. Viswanathan, H. L. Fraser, and R. Banerjee. "Mechanisms Related to Different Generations of γ' Precipitation during Continuous Cooling of a Nickel Base Superalloy". In: *Acta Materialia* 61.1 (Jan. 1, 2013), pp. 280–293 (cit. on pp. 19, 129).

[32] Jean-Briac Le Graverend, Laura Dirand, Alain Jacques, Jonathan Cormier, Olivier Ferry, Thomas Schenk, Franck Gallerneau, Serge Kruch, and José Mendez. "In Situ Measurement of the γ/Γ' Lattice Mismatch Evolution of a Nickel-Based Single-Crystal Superalloy During Non-isothermal Very High-Temperature Creep Experiments". In: *Metall Mater Trans A* 43.11 (Nov. 1, 2012), pp. 3946–3951 (cit. on p. 19).

[33] Jean-Briac le Graverend and Rajendran Harikrishnan. "A Lattice-misfit-dependent Micromechanical Approach in Ni-based Single Crystal Superalloys". In: *International Journal of Mechanical Sciences* (Dec. 2020), p. 106229 (cit. on p. 19).

[34] Andrew Wessman. "Physical Metallurgy of Rene 65, a Next-Generation Cast and Wrought Nickel Superalloy for Use in Aero Engine Components". PhD thesis. PhD Thesis, University of Cincinnati, 2016. 213 pp. (cit. on pp. 20–26, 28, 42, 43, 88, 96, 101, 149, 166).

[35] James C Williams and Edgar A Starke. "Progress in Structural Materials for Aerospace Systems". In: *Acta Materialia*. The Golden Jubilee Issue. Selected Topics in Materials Science and Engineering: Past, Present and Future 51.19 (Nov. 25, 2003), pp. 5775–5799 (cit. on p. 20).

[36] Marie-Agathe Charpagne, Marie-Agathe Charpagne, Thomas Billot, Jean-Michel Franchet, and Nathalie Bozzolo. "Heteroepitaxial Recrystallization Observed in René 65™ and Udimet 720™: A New Recrystallization Mechanism Possibly Occurring in All Low Lattice Mismatch γ/γ' Superalloys?" In: *Superalloys 2016*. Hoboken, NJ, USA: John Wiley & Sons, Inc., Oct. 2016, pp. 415–426 (cit. on p. 21).

[37] Oscar R. Terrazas, Mark E. Zaun, Ramesh S. Minisandram, and Michael L. Lasonde. "Influence of Temperature and Strain Rate During Rolling of René 65 Bar". In: *Proc. 9th Int. Symp. Superalloy 718 Deriv. Energy Aerosp. Ind. Appl.* Ed. by Eric Ott, Xingbo Liu, Joel Andersson, Zhongnan Bi, Kevin Bockenstedt, Ian Dempster, Jon Groh, Karl Heck, Paul Jablonski, Max Kaplan, Daisuke Nagahama, and Chantal Sudbrack. Cham: Springer International Publishing, 2018, pp. 977–986 (cit. on p. 21).

[38] C. M. Katsari, H. Che, D. Guye, A. Wessman, and S. Yue. "Microstructural Characterization and Mechanical Properties of Rene 65 Precipitates". In: *Proc. 9th Int. Symp. Superalloy 718 Deriv. Energy Aerosp. Ind. Appl.* Ed. by Eric Ott, Xingbo Liu, Joel Andersson, Zhongnan Bi, Kevin Bockenstedt, Ian Dempster, Jon Groh, Karl Heck, Paul Jablonski, Max Kaplan, Daisuke Nagahama, and Chantal Sudbrack. The Minerals, Metals & Materials Series. Cham: Springer International Publishing, 2018, pp. 629–641 (cit. on p. 21).

[39] Oluwole A. Olufayo, Hanqing Che, Victor Songmene, Christina Katsari, and Stephen Yue. "Machinability of Rene 65 Superalloy". In: *Materials* 12.12 (June 25, 2019), p. 2034 (cit. on p. 21).

[40] Betsy J. Bond, Christopher M. O'Brien, Jeffrey L. Russell, Joseph A. Heaney, and Michael L. Lasonde. "René 65 Billet Material for Forged Turbine Components". In: *8th International Symposium on Superalloy 718 and Derivatives*. Ed. by Eric Ott, Anthony Banik, Joel Andersson, Ian Dempster, Tim Gabb, Jon Groh, Karl Heck, Randy Helmink, Xingbo Liu, and Agnieszka Wusatowska-Sarnek. Hoboken, NJ, USA: John Wiley & Sons, Inc., Dec. 12, 2014, pp. 107–118 (cit. on pp. 21, 22).

[41] Louis Thébaud. "Etude Des Relations Entre Microstructure et Propriétés Mécaniques Du Nouveau Superalliage Base Nickel AD730™". PhD thesis. PhD Thesis, ISAE-ENSMA, July 2017 (cit. on pp. 21, 31, 34–36, 88, 113, 149).

[42] François Bourdin. « Analyse des processus d'endommagement aux joints de grains dans les superalliages base Nickel ». PhD thesis. ISAE-ENSMA Ecole Nationale Supérieure de Mécanique et d'Aérotechique - Poitiers, Sept. 25, 2020 (cit. on p. 21).

[43] Madeleine Durand-Charre. *The Microstructure of Superalloys*. Routledge, 2017 (cit. on p. 21).

[44] P. Kontis, H. A. Mohd Yusof, S. Pedrazzini, M. Danaie, K. L. Moore, P. A. J. Bagot, M. P. Moody, C. R. M. Grovenor, and R. C. Reed. "On the Effect of Boron on Grain Boundary Character in a New Polycrystalline Superalloy". In: *Acta Materialia* 103 (Jan. 15, 2016), pp. 688–699 (cit. on pp. 21, 23).

[45] Paraskevas Kontis, Zhuangming Li, David M. Collins, Jonathan Cormier, Dierk Raabe, and Baptiste Gault. "The Effect of Chromium and Cobalt Segregation at Dislocations on Nickel-Based Superalloys". In: *Scripta Materialia* 145 (Mar. 1, 2018), pp. 76–80 (cit. on pp. 21, 22).

[46] Sophie Dubiez-Le Goff. « Comportement et endommagement d'un superalliage élaboré par compression isostatique à chaud ». PhD thesis. École Nationale Supérieure des Mines de Paris, Dec. 17, 2003 (cit. on pp. 21, 42).

[47] S K Jain, B A Ewing, and C A Yin. "The Development of Improved Performance PM Udimet 720 Turbine Disks". In: *Superalloys 2000* 785–794 (2000), p. 10 (cit. on p. 21).

[48] William C. Lenthe, Jean-Charles Stinville, McLean P. Echlin, and Tresa M. Pollock. "Statistical Assessment of Fatigue-Initiating Microstructural Features in a Polycrystalline Disk Alloy". In: *Superalloys 2016*. John Wiley & Sons, Ltd, 2016, pp. 569–577 (cit. on p. 22).

[49] J.C. Stinville, N. Vanderesse, F. Bridier, P. Bocher, and T.M. Pollock. "High Resolution Mapping of Strain Localization near Twin Boundaries in a Nickel-Based Superalloy". In: *Acta Materialia* 98 (Oct. 2015), pp. 29–42 (cit. on pp. 22, 23).

[50] J. C. Stinville, W. C. Lenthe, M. P. Echlin, P. G. Callahan, D. Texier, and T. M. Pollock. "Microstructural Statistics for Fatigue Crack Initiation in Polycrystalline Nickel-Base Superalloys". In: *Int J Fract* 208.1 (Dec. 1, 2017), pp. 221–240 (cit. on p. 22).

[51] Jiashi Miao, Tresa M. Pollock, and J. Wayne Jones. "Crystallographic Fatigue Crack Initiation in Nickel-Based Superalloy René 88DT at Elevated Temperature". In: *Acta Materialia* 57.20 (Dec. 1, 2009), pp. 5964–5974 (cit. on p. 22).

[52] Julien Genée. "Etude Statistique et Numérique Des Interactions Bandes de Glissement-Joints de Grains : Application Aux Superalliages de Nickel". PhD thesis. Chasseneuil-du-Poitou, Ecole nationale supérieure de mécanique et d'aérotechnique, Dec. 8, 2017 (cit. on pp. 22, 45).

[53] Paraskevas Kontis, Zhuangming Li, Mikael Segersäll, Johan J. Moverare, Roger C. Reed, Dierk Raabe, and Baptiste Gault. "The Role of Oxidized Carbides on Thermal-Mechanical Performance of Polycrystalline Superalloys". In: *Metall and Mat Trans A* 49.9 (Sept. 1, 2018), pp. 4236–4245 (cit. on p. 22).

[54] David M. Collins, Neil D'Souza, Chinnapat Panwisawas, Chrysanthi Papadaki, Geoff D. West, Aleksander Kostka, and Paraskevas Kontis. "Spinodal Decomposition versus Classical γ' Nucleation in a Nickel-Base Superalloy Powder: An in-Situ Neutron Diffraction and Atomic-Scale Analysis". In: *Acta Materialia* 200 (Nov. 2020), pp. 959–970 (cit. on p. 22).

[55] S. T. Oyama, ed. *The Chemistry of Transition Metal Carbides and Nitrides*. Dordrecht: Springer Netherlands, 1996 (cit. on p. 22).

[56] Damien Texier, Jean-Charles Stinville, McLean P. Echlin, Stéphane Pierret, Patrick Villechaise, Tresa M. Pollock, and Jonathan Cormier. "Short Crack Propagation from Cracked Non-Metallic Inclusions in a Ni-based Polycrystalline Superalloy". In: *Acta Materialia* 165 (Feb. 2019), pp. 241–258 (cit. on p. 23).

[57] Damien Texier, Jonathan Cormier, Patrick Villechaise, Jean-Charles Stinville, Chris J. Torbet, Stéphane Pierret, and Tresa M. Pollock. "Crack Initiation Sensitivity of Wrought Direct Aged Alloy 718 in the Very High Cycle Fatigue Regime: The Role of Non-Metallic Inclusions". In: *Mater. Sci. Eng. A* 678 (Dec. 2016), pp. 122–136 (cit. on p. 23).

[58] C.M.F. Rae and R.C. Reed. "The Precipitation of Topologically Close-Packed Phases in Rhenium-Containing Superalloys". In: *Acta Materialia* 49.19 (Nov. 2001), pp. 4113–4125 (cit. on p. 23).

[59] M. Simonetti and P. Caron. "Role and Behaviour of μ Phase during Deformation of a Nickel-Based Single Crystal Superalloy". In: *Materials Science and Engineering: A* 254.1 (Oct. 15, 1998), pp. 1–12 (cit. on p. 23).

[60] Yoseph Bar-Cohen. "High-Temperature Materials and Mechanisms: Applications and Challenges". In: *High Temperature Materials and Mechanisms*. CRC Press, 2014 (cit. on p. 26).

[61] A. Baldan. "Review Progress in Ostwald Ripening Theories and Their Applications to Nickel-Base Superalloys Part I: Ostwald Ripening Theories". In: *Journal of Materials Science* 37.11 (June 1, 2002), pp. 2171–2202 (cit. on p. 26).

[62] I. M. Lifshitz and V. V. Slyozov. "The Kinetics of Precipitation from Supersaturated Solid Solutions". In: *Journal of Physics and Chemistry of Solids* 19.1 (Apr. 1, 1961), pp. 35–50 (cit. on p. 26).

[63] F.S. Pettit and G.H. Meier. "Oxidation and Hot Corrosion of Superalloys". In: *Superalloys 1984 Fifth Int. Symp.* Superalloys. TMS, 1984, pp. 651–687 (cit. on p. 28).

[64] Sudhangshu Bose. *High Temperature Coatings - Second Edition.* Butterworth-Heinemann, 2017. 299 pp. (cit. on pp. 28, 29).

[65] H. E. Evans, A. T. Donaldson, and T. C. Gilmour. "Mechanisms of Breakaway Oxidation and Application to a Chromia-Forming Steel". In: *Oxidation of Metals* 52.5 (Dec. 1, 1999), pp. 379–402 (cit. on pp. 28, 33).

[66] Michael Schütze. "Mechanical Properties of Oxide Scales". In: *Oxid Met* 44.1 (Aug. 1, 1995), pp. 29–61 (cit. on p. 28).

[67] James L. Smialek and Nathan S. Jacobson. "Oxidation of High-Temperature Aerospace Materials". In: *High Temperature Materials and Mechanisms*. CRC Press, 2014 (cit. on pp. 28, 29).

[68] Etienne Marrier. « Modélisation de l'évolution de la composition du substrat au cours de l'oxydation sélective des alliages à haute température ». PhD thesis. Ecole Nationale Supérieure des Mines de Saint-Etienne, Dec. 17, 2015 (cit. on p. 31).

[69] Chunhua Xu and Wei Gao. "Pilling-Bedworth Ratio for Oxidation of Alloys". In: *Mater. Res. Innov.* 3.4 (Mar. 2000), pp. 231–235 (cit. on p. 31).

[70] David John Young. *High Temperature Oxidation and Corrosion of Metals*. Ed. by Elsevier. Elsevier, 2016. 656 pp. (cit. on pp. 31, 32, 104, 105, 114, 126, 127).

[71] NB Pilling. "The Oxidation of Metals at High Temperature". In: *J. Inst. Met.* 29 (1923), pp. 529–582 (cit. on p. 31).

[72] ST Wlodek. "The Oxidation of Rene 41 and Udimet 700". In: *Trans. Met. Sac. AIME* (1964), pp. 1078–1090 (cit. on p. 31).

[73] S. Cruchley, H.E. Evans, M.P. Taylor, M.C. Hardy, and S. Stekovic. "Chromia Layer Growth on a Ni-based Superalloy: Sub-parabolic Kinetics and the Role of Titanium". In: *Corrosion Science* 75 (Oct. 2013), pp. 58–66 (cit. on pp. 31, 113).

[74] H. E. Evans, D. A. Hilton, R. A. Holm, and S. J. Webstert. "The Influence of a Titanium Nitride Dispersion on the Oxidation Behavior of 20%Cr-25%Ni Stainless Steel". In: *Oxid Met* 12.6 (Dec. 1, 1978), pp. 473–485 (cit. on p. 31).

[75] M.P. Taylor, H.E. Evans, S. Stekovic, and M.C. Hardy. "The Oxidation Characteristics of the Nickel-Based Superalloy, RR1000, at Temperatures of 700–900°C". In: *Materials at High Temperatures* 29.2 (June 2012), pp. 145–150 (cit. on p. 31).

[76] Neil Birks, Gerald H Meier, and Fred S Pettit. *Introduction to the High Temperature Oxidation of Metals, 2nd Edition*. Cambridge: Cambridge University Press, 2006 (cit. on p. 31).

[77] Carl Wagner. "Beitrag Zur Theorie Des Anlaufvorgangs". In: *Z. Für Phys. Chem.* 21B.1 (1933), pp. 25–41 (cit. on pp. 31, 110).

[78] Carl Wagner. "Theoretical Analysis of the Diffusion Processes Determining the Oxidation Rate of Alloys". In: *J. Electrochem. Soc.* 99.10 (Jan. 10, 1952), pp. 369–380 (cit. on pp. 31, 110).

[79] Raphaëlle Peraldi. "Relations Entre Cinétiques de Croissance Des Couches d'oxyde et Leurs Microstructures Lors de l'oxydation à Haute Température Du Nickel Haute Pureté". PhD thesis. Institut national polytechnique de Toulouse, 2000 (cit. on pp. 32, 112).

[80] Daniel Monceau and Bernard Pieraggi. "Determination of Parabolic Rate Constants from a Local Analysis of Mass-Gain Curves". In: *Oxid. Met.* 50.5/6 (1998), p. 477 (cit. on p. 32).

[81] M. W. Brumm and H. J. Grabke. "The Oxidation Behaviour of NiAl-I. Phase Transformations in the Alumina Scale during Oxidation of NiAl and NiAl-Cr Alloys". In: *Corrosion Science* 33.11 (Nov. 1, 1992), pp. 1677–1690 (cit. on pp. 32, 112).

[82] Samuel Cruchley, Hugh Evans, and Mary Taylor. "An Overview of the Oxidation of Ni-based Superalloys for Turbine Disc Applications: Surface Condition, Applied Load and Mechanical Performance". In: *Mater. High Temp.* 33.4-5 (June 2016), pp. 465–475 (cit. on pp. 32, 34, 112).

[83] J. H. Chen, P. M. Rogers, and J. A. Little. "Oxidation Behavior of Several Chromia-Forming Commercial Nickel-Base Superalloys". In: *Oxid Met* 47.5 (June 1, 1997), pp. 381–410 (cit. on pp. 32, 112, 113).

[84] G. A. Greene and C. C. Finfrock. "Oxidation of Inconel 718 in Air at High Temperatures". In: *Oxidation of Metals* 55.5 (June 1, 2001), pp. 505–521 (cit. on pp. 32, 112).

[85] Yebing Hu, Tieshan Cao, Congqian Cheng, Li Zhang, and Jie Zhao. "Oxidation Behavior of a Single-Crystal Ni-based Superalloy over the Temperature Range of 850 °C–950 °C in Air". In: *Applied Surface Science* 484 (Aug. 1, 2019), pp. 209–218 (cit. on pp. 32, 112).

[86] Lei Zheng, Maicang Zhang, and Jianxin Dong. "Oxidation Behavior and Mechanism of Powder Metallurgy Rene95 Nickel Based Superalloy between 800 and 1000°C". In: *Applied Surface Science* 256.24 (Oct. 1, 2010), pp. 7510–7515 (cit. on pp. 32, 112).

[87] B. R. Barnard, P. K. Liaw, R. A. Buchanan, and D. L. Klarstrom. "Affects of Applied Stresses on the Isothermal and Cyclic High-Temperature Oxidation Behavior of Superalloys". In: *Materials Science and Engineering: A* 527.16 (June 25, 2010), pp. 3813–3821 (cit. on pp. 32, 112).

[88] Y. Shida, G. C. Wood, F. H. Stott, D. P. Whittle, and B. D. Bastow. "Intergranular Oxidation and Internal Void Formation in Ni-40% Cr Alloys". In: *Corrosion Science* 21.8 (Jan. 1, 1981), pp. 581–597 (cit. on pp. 32, 112).

[89] A Galerie and L Antoni. « Corrosion sèche des métaux - Mécanismes ». In: *Tech. L'Ingénieur* m4221 (2003), p. 18 (cit. on p. 32).

[90] Léa Bataillou, Clara Desgranges, Laure Martinelli, and Daniel Monceau. "Modelling of the Effect of Grain Boundary Diffusion on the Oxidation of Ni-Cr Alloys at High Temperature". In: *Corrosion Science* 136 (May 15, 2018), pp. 148–160 (cit. on p. 33).

[91] Léa Bataillou, Laure Martinelli, Clara Desgranges, Sophie Bosonnet, Kevin Ginestar, Frédéric Miserque, Yves Wouters, Laurence Latu-Romain, Alessandro Pugliara, Arnaud Proietti, and Daniel Monceau. "Growth Kinetics and Characterization of Chromia Scales Formed on Ni–30Cr Alloy in Impure Argon at 700 °C". In: *Oxid Met* (Feb. 19, 2020) (cit. on p. 33).

[92] Clara Desgranges. « Comprehension et prediction du comportement sous irradiation neutronique d'alliages absorbants a base d'argent ». PhD thesis. Paris 11, 1998 (cit. on p. 33).

[93] Clara Desgranges, Nathalie Bertrand, Karim Abbas, Daniel Monceau, and Dominique Poquillon. "Numerical Model for Oxide Scale Growth with Explicit Treatment of Vacancy Fluxes". In: *MSF* 461–464 (Aug. 2004), pp. 481–488 (cit. on p. 33).

[94] Clara Desgranges, Florence Lequien, Edwige Aublant, Maylise Nastar, and Daniel Monceau. "Depletion and Voids Formation in the Substrate During High Temperature Oxidation of Ni–Cr Alloys". In: *Oxid Met* 79.1-2 (Feb. 2013), pp. 93–105 (cit. on p. 33).

[95] Nathalie Bertrand, Clara Desgranges, Maylise Nastar, Gouenou Girardin, Dominique Poquillon, and Daniel Monceau. "Chemical Evolution in the Substrate Due to Oxidation: A Numerical Model with Explicit Treatment of Vacancy Fluxes". In: *Mater. Sci. Forum* 595–598 (Sept. 2008), pp. 463–472 (cit. on p. 33).

[96] Damien Texier, Maxime Ecochard, Thomas Gheno, Daniel Monceau, Mehdi Salem, and Philippe Lours. "Screening for Al2O3 Failure in MCrAlY APS Coatings Using Short-Term Oxidation at High Temperature". In: *Corrosion Science* 184 (May 2021), p. 109334 (cit. on pp. 33, 49, 50, 128, 133).

[97] D. J. Young, A. Chyrkin, and W. J. Quadakkers. "A Simple Expression for Predicting the Oxidation Limited Life of Thin Components Manufactured from FCC High Temperature Alloys". In: *Oxid Met* 77.5 (June 1, 2012), pp. 253–264 (cit. on pp. 33, 128).

[98] Brian Gleeson. “High-Temperature Corrosion of Metallic Alloys and Coatings”. In: *Materials Science and Technology: A Comprehensive Treatment*. John Wiley & Sons, Ltd, 2008, pp. 173–228 (cit. on p. 33).

[99] G. Y. Lai. *High-Temperature Corrosion and Materials Applications*. Materials Park, Ohio: ASM International, 2007. 461 pp. (cit. on p. 33).

[100] W. J. Quadakkers and K. Bongartz. “The Prediction of Breakaway Oxidation for Alumina Forming ODS Alloys Using Oxidation Diagrams”. In: *Materials and Corrosion* 45.4 (Apr. 1994), pp. 232–241 (cit. on p. 33).

[101] R. Malacarne, S. Mathieu, L. Aranda, M. Vilasi, C. Desgranges, and S. Knittel. “Long-Term Isothermal Oxidation Behavior of Two Industrial Polycrystalline Nickel Base Alloys in Air at 700 °C – Evaluation of Intergranular Oxidation Distribution and Kinetic”. In: *Corrosion Science* 188 (Aug. 1, 2021), p. 109500 (cit. on pp. 34, 113).

[102] André A. N. Németh, David J. Crudden, David M. Collins, David E. J. Armstrong, and Roger C. Reed. “Novel Techniques to Assess Environmentally-Assisted Cracking in a Nickel-Based Superalloy”. In: *Superalloys 2016*. Ed. by Mark Hardy, Eric Huron, Uwe Glatzel, Brian Griffin, Beth Lewis, Cathie Rae, Venkat Seetharaman, and Sammy Tin. Hoboken, NJ, USA: John Wiley & Sons, Inc., Oct. 28, 2016, pp. 801–810 (cit. on pp. 34, 46).

[103] E. Chateau and L. Rémy. “Oxidation-Assisted Creep Damage in a Wrought Nickel-Based Superalloy: Experiments and Modelling”. In: *Materials Science and Engineering: A* 527.7 (Mar. 25, 2010), pp. 1655–1664 (cit. on p. 34).

[104] Romain Malacarne. “Étude de l’oxydation et de La Corrosion à Haute Température d’alliages Base Nickel Polycristallins”. PhD thesis. Université de Lorraine, Dec. 13, 2021 (cit. on pp. 34, 93, 111, 113).

[105] Jean-Charles Stinville, McLean P. Echlin, Patrick G. Callahan, Victoria M. Miller, Damien Texier, Florent Bridier, Philippe Bocher, and Tresa M. Pollock. “Measurement of Strain Localization Resulting from Monotonic and Cyclic Loading at 650°C in Nickel Base Superalloys”. In: *Exp. Mech.* 57.8 (2017), pp. 1289–1309 (cit. on pp. 35, 49, 50).

[106] A Joshi and H S Hu. “Oxidation Behavior of Titanium-Aluminium Nitrides”. In: (1995), p. 9 (cit. on p. 36).

[107] V.A. Lavrenko and A.F. Alexeev. “High-Temperature Oxidation of Boron Nitride”. In: *Ceramics International* 12.1 (Jan. 1986), pp. 25–31 (cit. on p. 36).

[108] Paul C. McIntyre and Scott R. Summerfelt. “Kinetics and Mechanisms of TiN Oxidation beneath Pt Thin Films”. In: *Journal of Applied Physics* 82.9 (Nov. 1997), pp. 4577–4585 (cit. on p. 36).

[109] Naresh C. Saha and Harland G. Tompkins. “Titanium Nitride Oxidation Chemistry: An X-ray Photoelectron Spectroscopy Study”. In: *Journal of Applied Physics* 72.7 (Oct. 1992), pp. 3072–3079 (cit. on p. 36).

[110] H. Van Bui, A. W. Groenland, A. A. I. Aarnink, R. A. M. Wolters, J. Schmitz, and A. Y. Kovalgin. “Growth Kinetics and Oxidation Mechanism of ALD TiN Thin Films Monitored by In Situ Spectroscopic Ellipsometry”. In: *J. Electrochem. Soc.* 158.3 (2011), H214 (cit. on p. 36).

[111] V.B. Voitovich. “Mechanism of the High Temperature Oxidation of Titanium Carbide”. In: *High Temp. Mater. Process.* 16.4 (Oct. 1997), pp. 243–254 (cit. on p. 36).

[112] Eric Hug and Clément Keller. “Intrinsic Effects Due to the Reduction of Thickness on the Mechanical Behavior of Nickel Polycrystals”. In: *Metall and Mat Trans A* 41.10 (Oct. 1, 2010), pp. 2498–2506 (cit. on pp. 37, 40).

[113] C. Keller, E. Hug, and X. Feaugas. “Microstructural Size Effects on Mechanical Properties of High Purity Nickel”. In: *International Journal of Plasticity* 27.4 (Apr. 1, 2011), pp. 635–654 (cit. on pp. 37, 40, 140).

[114] E. Arzt. “Size Effects in Materials Due to Microstructural and Dimensional Constraints: A Comparative Review”. In: *Acta Materialia* 46.16 (Oct. 9, 1998), pp. 5611–5626 (cit. on p. 37).

[115] Damien Texier. “Mesure et Evolution Des Gradients de Propriétés Mécaniques Dans Le Système Superalliage à Base de Nickel MC2 Revêtus McrAlY”. PhD thesis. Institut National Polytechnique de Toulouse, May 2013 (cit. on pp. 37, 38, 42).

[116] P. J. M. Janssen, Th. H. de Keijser, and M. G. D. Geers. “An Experimental Assessment of Grain Size Effects in the Uniaxial Straining of Thin Al Sheet with a Few Grains across the Thickness”. In: *Materials Science and Engineering: A* 419.1 (Mar. 15, 2006), pp. 238–248 (cit. on p. 37).

[117] T. Fülöp, W. A. M. Brekelmans, and M. G. D. Geers. “Size Effects from Grain Statistics in Ultra-Thin Metal Sheets”. In: *Journal of Materials Processing Technology* 174.1 (May 25, 2006), pp. 233–238 (cit. on p. 37).

[118] E. Nakamachi, K. Hiraiwa, H. Morimoto, and M. Harimoto. “Elastic/Crystalline Viscoplastic Finite Element Analyses of Single- and Poly-Crystal Sheet Deformations and Their Experimental Verification”. In: *International Journal of Plasticity* 16.12 (Jan. 1, 2000), pp. 1419–1441 (cit. on p. 37).

[119] L. V. Raulea, A. M. Goijaerts, L. E. Govaert, and F. P. T. Baaijens. “Size Effects in the Processing of Thin Metal Sheets”. In: *Journal of Materials Processing Technology*. Containing Selected Papers from the 7th International Conference Sheet Metal: SheMet’99 115.1 (Aug. 22, 2001), pp. 44–48 (cit. on p. 37).

[120] Clément Keller. « Etude expérimentale des transitions volume/surface des propriétés mécaniques du nickel polycristallin de haute pureté ». PhD thesis. Université de Caen, July 3, 2009 (cit. on pp. 37, 38, 137, 143, 163, 189).

[121] C. Keller, E. Hug, and D. Chateigner. “On the Origin of the Stress Decrease for Nickel Polycrystals with Few Grains across the Thickness”. In: *Materials Science and Engineering: A* 500.1 (Jan. 25, 2009), pp. 207–215 (cit. on pp. 37, 42).

[122] Anthony W. Thompson. “Use of Non-Polycrystal Specimens in Mechanical Behavior Tests”. In: *Scripta Metallurgica* 8.2 (Feb. 1, 1974), pp. 145–147 (cit. on pp. 37, 40).

[123] Shuichi Miyazaki, Kenji Shibata, and Hiroshi Fujita. “Effect of Specimen Thickness on Mechanical Properties of Polycrystalline Aggregates with Various Grain Sizes”. In: *Acta Metallurgica* 27.5 (May 1, 1979), pp. 855–862 (cit. on p. 38).

[124] C. Keller, M. Afteni, M. Banu, A. M. Habraken, E. Hug, S. Castagne, L. Duchenê, F. Barlat, Y. H. Moon, and M. G. Lee. "Influence of Surface Effect On Nickel Micro Deep Drawing Process". In: NUMIFORM 2010: Proceedings of the 10th International Conference on Numerical Methods in Industrial Forming Processes Dedicated to Professor O. C. Zienkiewicz (1921–2009). Pohang (Republic of Korea), 2010, pp. 1025–1030 (cit. on pp. 38, 141).

[125] C. Keller, A. M. Habraken, and L. Duchene. "Finite Element Investigation of Size Effects on the Mechanical Behavior of Nickel Single Crystals". In: *Materials Science and Engineering: A* 550 (July 30, 2012), pp. 342–349 (cit. on p. 38).

[126] A. Couret, J. Crestou, S. Farenc, G. Molenat, N. Clement, A. Coujou, and D. Caillard. "In Situ Deformation in T.E.M.: Recent Developments". In: *Microsc. Microanal. Microstruct.* 4.2-3 (Apr. 1, 1993), pp. 153–170 (cit. on p. 38).

[127] Daniel E. Hurtado and Michael Ortiz. "Surface Effects and the Size-Dependent Hardening and Strengthening of Nickel Micropillars". In: *Journal of the Mechanics and Physics of Solids* 60.8 (Aug. 1, 2012), pp. 1432–1446 (cit. on p. 38).

[128] Damien Texier, Vincent Velay, Antonio Castro Moreno, and Daniel Monceau. "Grain Size, Precipitation State and Free-Surface Effects". In: (), p. 22 (cit. on p. 39).

[129] B. Passilly, P. Kanoute, F.-H. Leroy, and R. Mévrel. "High Temperature Instrumented Microindentation: Applications to Thermal Barrier Coating Constituent Materials". In: *Philos. Mag.* 86.33-35 (Nov. 21, 2006), pp. 5739–5752 (cit. on p. 40).

[130] Arnaud Villemiane. « Comportement mécanique d'alliages pour couches de liaison de barrière thermique par microindentation instrumentée à haute température ». PhD thesis. Institut National Polytechnique de Lorraine, Dec. 15, 2008 (cit. on p. 40).

[131] J. M. Wheeler, D. E. J. Armstrong, W. Heinz, and R. Schwaiger. "High Temperature Nanoindentation: The State of the Art and Future Challenges". In: *Current Opinion in Solid State and Materials Science*. Recent Advances in Nanoindentation 19.6 (Dec. 1, 2015), pp. 354–366 (cit. on p. 40).

[132] S. Korte and W. J. Clegg. "Micropillar Compression of Ceramics at Elevated Temperatures". In: *Scripta Materialia* 60.9 (May 1, 2009), pp. 807–810 (cit. on p. 40).

[133] C. Eberl, D. S. Gianola, and K. J. Hemker. "Mechanical Characterization of Coatings Using Microbeam Bending and Digital Image Correlation Techniques". In: *Exp Mech* 50.1 (Jan. 1, 2010), pp. 85–97 (cit. on p. 40).

[134] H. D Espinosa, B. C Prorok, and M Fischer. "A Methodology for Determining Mechanical Properties of Freestanding Thin Films and MEMS Materials". In: *Journal of the Mechanics and Physics of Solids* 51.1 (Jan. 1, 2003), pp. 47–67 (cit. on p. 40).

[135] Md Zafir Alam, S. V. Kamat, V. Jayaram, and Dipak K. Das. "Tensile Behavior of a Free-Standing Pt-aluminide (PtAl) Bond Coat". In: *Acta Materialia* 61.4 (Feb. 1, 2013), pp. 1093–1105 (cit. on p. 40).

[136] D Pan, M.W Chen, P.K Wright, and K.J Hemker. "Evolution of a Diffusion Aluminide Bond Coat for Thermal Barrier Coatings during Thermal Cycling". In: *Acta Materialia* 51.8 (May 2003), pp. 2205–2217 (cit. on p. 40).

[137] Damien Texier, Daniel Monceau, Eric Andrieu, and Georges Cailletaud. « Effet de l'état métallurgique sur les propriétés mécaniques d'éprouvettes amincies ». In: Matériaux 2010. Oct. 18, 2010, 9 p. (Cit. on p. 40).

[138] D. Texier, D. Monceau, F. Crabos, and E. Andrieu. "Tensile Properties of a Non-Line-of-Sight Processed β-γ-Γ' MCrAlY Coating at High Temperature". In: *Surface and Coatings Technology* 326 (Oct. 15, 2017), pp. 28–36 (cit. on p. 40).

[139] M. Zupan, M. J. Hayden, C. J. Boehlert, and K. J. Hemker. "Development of High-Temperature Microsample Testing". In: *Experimental Mechanics* 41.3 (Sept. 1, 2001), pp. 242–247 (cit. on p. 40).

[140] R. W. Armstrong. "The Influence of Polycrystal Grain Size on Several Mechanical Properties of Materials". In: *Metall. Mater. Trans.* 1.5 (May 1, 1970), pp. 1169–1176 (cit. on p. 40).

[141] E. Hug, P. A. Dubos, C. Keller, L. Duchêne, and A. M. Habraken. "Size Effects and Temperature Dependence on Strain-Hardening Mechanisms in Some Face Centered Cubic Materials". In: *Mechanics of Materials* 91 (Dec. 1, 2015), pp. 136–151 (cit. on p. 40).

[142] Paul A. Shade, Sang-Lan Kim, Robert Wheeler, and Michael D. Uchic. "Stencil Mask Methodology for the Parallelized Production of Microscale Mechanical Test Samples". In: *Review of Scientific Instruments* 83.5 (May 1, 2012), p. 053903 (cit. on p. 40).

[143] W.N. Sharpe, B. Yuan, and R.L. Edwards. "A New Technique for Measuring the Mechanical Properties of Thin Films". In: *J. Microelectromechanical Syst.* 6.3 (Sept. 1997), pp. 193–199 (cit. on p. 40).

[144] J. N. Florando and W. D. Nix. "A Microbeam Bending Method for Studying Stress–Strain Relations for Metal Thin Films on Silicon Substrates". In: *Journal of the Mechanics and Physics of Solids* 53.3 (Mar. 1, 2005), pp. 619–638 (cit. on p. 40).

[145] D. M. Dimiduk, M. D. Uchic, and T. A. Parthasarathy. "Size-Affected Single-Slip Behavior of Pure Nickel Microcrystals". In: *Acta Materialia* 53.15 (Sept. 1, 2005), pp. 4065–4077 (cit. on p. 40).

[146] M. G. D. Geers, M. Cottura, B. Appolaire, E. P. Busso, S. Forest, and A. Villani. "Coupled Glide-Climb Diffusion-Enhanced Crystal Plasticity". In: *Journal of the Mechanics and Physics of Solids* 70 (Oct. 1, 2014), pp. 136–153 (cit. on p. 40).

[147] D. Kiener, W. Grosinger, G. Dehm, and R. Pippan. "A Further Step towards an Understanding of Size-Dependent Crystal Plasticity: In Situ Tension Experiments of Miniaturized Single-Crystal Copper Samples". In: *Acta Materialia* 56.3 (Feb. 1, 2008), pp. 580–592 (cit. on p. 40).

[148] C. A. Volkert and A. M. Minor. "Focused Ion Beam Microscopy and Micromachining". In: *MRS Bull.* 32.5 (May 2007), pp. 389–399 (cit. on p. 40).

[149] G. P. Zhang, K. Takashima, M. Shimojo, and Y. Higo. "Fatigue Behavior of Microsized Austenitic Stainless Steel Specimens". In: *Materials Letters* 57.9 (Feb. 1, 2003), pp. 1555–1560 (cit. on p. 40).

[150] Haiming Zhang and Xianghuai Dong. "Experimental and Numerical Studies of Coupling Size Effects on Material Behaviors of Polycrystalline Metallic Foils in Microscale Plastic Deformation". In: *Materials Science and Engineering: A* 658 (Mar. 21, 2016), pp. 450–462 (cit. on p. 40).

[151] McLean P. Echlin, Alessandro Mottura, Christopher J. Torbet, and Tresa M. Pollock. "A New TriBeam System for Three-Dimensional Multimodal Materials Analysis". In: *Review of Scientific Instruments* 83.2 (Feb. 1, 2012), p. 023701 (cit. on p. 40).

[152] T. L. Burnett, R. Kelley, B. Winiarski, L. Contreras, M. Daly, A. Gholinia, M. G. Burke, and P. J. Withers. "Large Volume Serial Section Tomography by Xe Plasma FIB Dual Beam Microscopy". In: *Ultramicroscopy* 161 (Feb. 1, 2016), pp. 119–129 (cit. on p. 40).

[153] D. M. Allen. "Photochemical Machining: From 'Manufacturing's Best Kept Secret' to a $6 Billion per Annum, Rapid Manufacturing Process". In: *CIRP Annals* 53.2 (Jan. 1, 2004), pp. 559–572 (cit. on p. 40).

[154] Christoph Eberl, Xi Wang, Daniel S. Gianola, Thao D. Nguyen, Ming Y. He, Anthony G. Evans, and Kevin J. Hemker. "In Situ Measurement of the Toughness of the Interface Between a Thermal Barrier Coating and a Ni Alloy". In: *J. Am. Ceram. Soc.* 94.s1 (2011), s120–s127 (cit. on p. 40).

[155] Mats Eskner and Rolf Sandström. "Measurement of the Ductile-to-Brittle Transition Temperature in a Nickel Aluminide Coating by a Miniaturised Disc Bending Test Technique". In: *Surface and Coatings Technology* 165.1 (Feb. 3, 2003), pp. 71–80 (cit. on p. 40).

[156] D. Texier, D. Monceau, J. C. Salabura, R. Mainguy, and E. Andrieu. "Micromechanical Testing of Ultrathin Layered Material Specimens at Elevated Temperature". In: *Mater. High Temp.* 33.4-5 (June 28, 2016), pp. 325–337 (cit. on p. 40).

[157] M. F. Ashby. "The Deformation of Plastically Non-Homogeneous Materials". In: *Philos. Mag. J. Theor. Exp. Appl. Phys.* 21.170 (Feb. 1, 1970), pp. 399–424 (cit. on p. 41).

[158] D. J. Abson and J. J. Jonas. "The Hall–Petch Relation and High-Temperature Subgrains". In: *Metal Science Journal* 4.1 (Jan. 1970), pp. 24–28 (cit. on p. 42).

[159] N. J. Petch. "The Influence of Grain Boundary Carbide and Grain Size on the Cleavage Strength and Impact Transition Temperature of Steel". In: *Acta Metallurgica* 34.7 (July 1, 1986), pp. 1387–1393 (cit. on p. 42).

[160] NJ Petch. "The Cleavage Strength of Polycrystals: Journal of the Iron and Steel Institute, v. 174". In: (1953) (cit. on p. 42).

[161] K.R. Bain, M.L. Gambone, J.M. Hyzak, and M.C. Thomas. "Development of Damage Tolerant Microstructures in Udimet 720". In: *Superalloys 1988 Sixth Int. Symp.* Superalloys. TMS, 1988, pp. 13–22 (cit. on p. 42).

[162] Thomas Billot. "Fatigue and Creep-Fatigue Behaviour and Damage Processes at High Temperature of Two Different Metallurgical Structures of the Nickel-Based Superalloy Udimet 720". PhD thesis. ISAE-ENSMA Ecole Nationale Supérieure de Mécanique et d'Aérotechique - Poitiers, Mar. 2010 (cit. on pp. 43, 45, 183).

[163] E. I. Galindo-Nava, L. D. Connor, and C. M. F. Rae. "On the Prediction of the Yield Stress of Unimodal and Multimodal γ' Nickel-base Superalloys". In: *Acta Materialia* 98 (Oct. 1, 2015), pp. 377–390 (cit. on pp. 43, 45).

[164] Werner Hüther and B. Reppich. "Order Hardening of MgO by Large Precipitated Volume Fractions of Spinel Particles". In: *Materials Science and Engineering* 39.2 (Aug. 1979), pp. 247–259 (cit. on p. 43).

[165] Sonia Raujol. "Influence Du Vieillissement Sur Le Comportement En Fluage d'un Superalliage Pour Disques d'une Turbine". PhD thesis. Toulouse, INSA, Jan. 1, 2004 (cit. on p. 43).

[166] Jean Charles Stinville, Etienne Martin, Mallikarjun Karadge, Shak Ismonov, Monica Soare, Tim Hanlon, Sairam Sundaram, McLean P. Echlin, Patrick G. Callahan, William C. Lenthe, V. M. Miller, Jiashi Miao, Andrew E. Wessman, Rebecca Finlay, Adrian Loghin, Judson Marte, and Tresa M. Pollock. "Fatigue Deformation in a Polycrystalline Nickel Base Superalloy at Intermediate and High Temperature: Competing Failure Modes". In: *Acta Materialia* 152 (June 15, 2018), pp. 16–33 (cit. on p. 44).

[167] Marie Mineur. « Conditions locales d'amorçage des fissures de fatigue dans un acier inoxydable de type 316L : aspects cristallographiques (EBSD) ». Thèse de doctorat. France: Université de Poitiers, 2000. 267 pp. (cit. on p. 44).

[168] André Pineau. "Crossing Grain Boundaries in Metals by Slip Bands, Cleavage and Fatigue Cracks". In: *Phil. Trans. R. Soc. A.* 373.2038 (Mar. 28, 2015), p. 20140131 (cit. on p. 45).

[169] J.C. Stinville, W.C. Lenthe, J. Miao, and T.M. Pollock. "A Combined Grain Scale Elastic–Plastic Criterion for Identification of Fatigue Crack Initiation Sites in a Twin Containing Polycrystalline Nickel-Base Superalloy". In: *Acta Materialia* 103 (Jan. 2016), pp. 461–473 (cit. on p. 45).

[170] Yejun Gu, Jean Charles Stinville, Patrick G. Callahan, McLean P. Echlin, Tresa M. Pollock, and Jaafar A. El-Awady. "Slip Delocalization and Diffusion Mediated Carbide Formation during Fatigue of a Nickel-Base Superalloy". In: *International Journal of Fatigue* 145 (Apr. 2021), p. 106077 (cit. on p. 45).

[171] Walter W. Milligan. *Deformation Modeling and Constitutive Modeling for Anisotropic Superalloys*. National Aeronautics and Space Administration, Office of Management, Scientific and Technical Information Division, 1989. 336 pp. (cit. on p. 46).

[172] BH Kear. *Dislocation Configurations in Plastically Deformed Polycrystalline Cu3Au Alloys*. Franklin Inst Philadelphia Pa Labs for Research and Development, 1961 (cit. on p. 46).

[173] D. P. Pope and S. S. Ezz. "Mechanical Properties of Ni3AI and Nickel-Base Alloys with High Volume Fraction of γ'". In: *International Metals Reviews* 29.1 (Jan. 1984), pp. 136–167 (cit. on p. 46).

[174] M. C. Rezende, L. S. Araújo, S. B. Gabriel, J. Dille, and L. H. de Almeida. "Oxidation Assisted Intergranular Cracking under Loading at Dynamic Strain Aging Temperatures in Inconel 718 Superalloy". In: *Journal of Alloys and Compounds*. ISMANAM 2014 643 (Sept. 15, 2015), S256–S259 (cit. on p. 46).

[175] Jean-Charles Stinville, Etienne Martin, Mallikarjun Karadge, Shak Ismonov, Monica Soare, Tim Hanlon, Sairam Sundaram, McLean P. Echlin, Patrick G. Callahan, William C. Lenthe, Jiashi Miao, Andrew E. Wessman, Rebecca Finlay, Adrian Loghin, Judson Marte, and Tresa M. Pollock. "Competing Modes for Crack Initiation from Non-metallic Inclusions and Intrinsic Microstructural Features During Fatigue in a Polycrystalline Nickel-Based Superalloy". In: *Metall and Mat Trans A* 49.9 (Sept. 1, 2018), pp. 3865–3873 (cit. on p. 46).

[176] H. E. Evans. "Stress Effects in High Temperature Oxidation of Metals". In: *Int. Mater. Rev.* 40.1 (Jan. 1, 1995), pp. 1–40 (cit. on p. 47).

[177] Michael Schütze, D. R. Holmes, and Michael Schütze. *Protective Oxide Scales and Their Breakdown*. The Institute of Corrosion and Wiley Series on Corrosion and Protection. Chichester ; New York: Wiley, 1997. 165 pp. (cit. on p. 48).

[178] P. Hancock and J. R. Nicholls. "Application of Fracture Mechanics to Failure of Surface Oxide Scales". In: *Mater. Sci. Technol.* 4.5 (May 1, 1988), pp. 398–406 (cit. on p. 48).

[179] J. Robertson and M. I. Manning. "Limits to Adherence of Oxide Scales". In: *Mater. Sci. Technol.* 6.1 (Jan. 1, 1990), pp. 81–92 (cit. on pp. 48, 127).

[180] M. M. Nagl and W. T. Evans. "The Mechanical Failure of Oxide Scales under Tensile or Compressive Load". In: *J Mater Sci* 28.23 (Dec. 1993), pp. 6247–6260 (cit. on p. 48).

[181] H. E. Evans, H. Y. Li, and P. Bowen. "A Mechanism for Stress-Aided Grain Boundary Oxidation Ahead of Cracks". In: *Scripta Materialia* 69.2 (July 1, 2013), pp. 179–182 (cit. on p. 48).

[182] H. S. Kitaguchi, H. Y. Li, H. E. Evans, R. G. Ding, I. P. Jones, G. Baxter, and P. Bowen. "Oxidation Ahead of a Crack Tip in an Advanced Ni-based Superalloy". In: *Acta Materialia* 61.6 (Apr. 1, 2013), pp. 1968–1981 (cit. on p. 48).

[183] L. Viskari, M. Hörnqvist, K. L. Moore, Y. Cao, and K. Stiller. "Intergranular Crack Tip Oxidation in a Ni-base Superalloy". In: *Acta Materialia* 61.10 (June 1, 2013), pp. 3630–3639 (cit. on p. 48).

[184] U. Krupp, W. M. Kane, C. Laird, and C. J. McMahon. "Brittle Intergranular Fracture of a Ni-base Superalloy at High Temperatures by Dynamic Embrittlement". In: *Materials Science and Engineering: A*. 13th International Conference on the Strength of Materials 387–389 (Dec. 15, 2004), pp. 409–413 (cit. on p. 48).

[185] J.A Pfaendtner and C.J McMahon Jr. "Oxygen-Induced Intergranular Cracking of a Ni-base Alloy at Elevated Temperatures—an Example of Dynamic Embrittlement". In: *Acta Materialia* 49.16 (Sept. 2001), pp. 3369–3377 (cit. on p. 48).

[186] David Woodford. "Gas Phase Embrittlement and Time Dependent Cracking of Nickel Based Superalloys". In: CORROSION 2005. OnePetro, Apr. 3, 2005 (cit. on p. 48).

[187] H Pang. "Fatigue Crack Initiation and Short Crack Growth in Nickel-Base Turbine Disc Alloys?The Effects of Microstructure and Operating Parameters*1". In: *International Journal of Fatigue* 25.9-11 (Sept. 2003), pp. 1089–1099 (cit. on p. 49).

[188] H. T Pang and P. A. S Reed. "Fatigue Crack Initiation and Short Crack Growth in Nickel-Base Turbine Disc Alloys—the Effects of Microstructure and Operating Parameters". In: *International Journal of Fatigue*. International Conference on Fatigue Damage of Structural Materials IV 25.9 (Sept. 1, 2003), pp. 1089–1099 (cit. on p. 49).

[189] H.T. Pang and P.A.S. Reed. "Microstructure Effects on High Temperature Fatigue Crack Initiation and Short Crack Growth in Turbine Disc Nickel-Base Superalloy Udimet 720Li". In: *Materials Science and Engineering: A* 448.1-2 (Mar. 2007), pp. 67–79 (cit. on p. 49).

[190] H.T. Mallikarjuna, N.L. Richards, and W.F. Caley. "Effect of Alloying Elements and Microstructure on the Cyclic Oxidation Performance of Three Nickel-Based Superalloys". In: *Materialia* 4 (Dec. 2018), pp. 487–499 (cit. on p. 49).

[191] R. Orosz, U. Krupp, H.-J. Christ, and D. Monceau. "The Influence of Specimen Thickness on the High Temperature Corrosion Behavior of CMSX-4 during Thermal-Cycling Exposure". In: *Oxid Met* 68.3 (Oct. 1, 2007), pp. 165–176 (cit. on pp. 50, 133).

[192] R. Duan, A. Jalowicka, K. Unocic, B. A. Pint, P. Huczkowski, A. Chyrkin, D. Grüner, R. Pillai, and W. J. Quadakkers. "Predicting Oxidation-Limited Lifetime of Thin-Walled Components of NiCrW Alloy 230". In: *Oxid Met* 87.1-2 (Feb. 2017), pp. 11–38 (cit. on p. 50).

[193] D. Texier, Q. Sirvin, V. Velay, M. Salem, D. Monceau, B. Mazères, E. Andrieu, R. Roumiguier, and B. Dod. "Oxygen/Nitrogen-Assisted Embrittlement of Titanium Alloys Exposed at Elevated Temperature". In: *MATEC Web Conf.* 321 (2020). Ed. by P. Villechaise, B. Appolaire, P. Castany, M. Dehmas, C. Delaunay, J. Delfosse, A. Denquin, E. Gautier, L. Germain, N. Gey, T. Gloriant, J.-Y. Hascoët, S. Hémery, Y. Millet, D. Monceau, F. Pettinari-Sturmel, M. Piellard, F. Prima, and B. Viguier, p. 06004 (cit. on p. 55).

[194] Skipper Seabold and Josef Perktold. "Statsmodels: Econometric and Statistical Modeling with Python". In: *9th Python Sci. Conf.* 2010 (cit. on p. 58).

[195] William S. Cleveland. "Robust Locally Weighted Regression and Smoothing Scatterplots". In: *Journal of the American Statistical Association* 74.368 (Dec. 1979), pp. 829–836 (cit. on p. 58).

[196] J.-J. Orteu, Y. Rotrou, T. Sentenac, and L. Robert. "An Innovative Method for 3-D Shape, Strain and Temperature Full-Field Measurement Using a Single Type of Camera: Principle and Preliminary Results". In: *Exp Mech* 48.2 (Apr. 2008), pp. 163–179 (cit. on p. 62).

[197] Michael A. Sutton, Jean Jose Orteu, and Hubert Schreier. *Image Correlation for Shape, Motion and Deformation Measurements: Basic Concepts,Theory and Applications*. Springer Science & Business Media, Apr. 21, 2009. 332 pp. (cit. on p. 62).

[198] Pauli Virtanen et al. "SciPy 1.0: Fundamental Algorithms for Scientific Computing in Python". In: *Nat. Methods* 17 (2020), pp. 261–272 (cit. on pp. 63, 70).

[199] G. Bradski. "The OpenCV Library". In: *Dr Dobbs J. Softw. Tools* (2000) (cit. on pp. 66, 70).

[200] David Nečas and Petr Klapetek. "Gwyddion: An Open-Source Software for SPM Data Analysis". In: *Open Phys.* 10.1 (Jan. 1, 2012) (cit. on p. 69).

[201] Curtis T. Rueden, Johannes Schindelin, Mark C. Hiner, Barry E. DeZonia, Alison E. Walter, Ellen T. Arena, and Kevin W. Eliceiri. "ImageJ2: ImageJ for the next Generation of Scientific Image Data". In: *BMC Bioinformatics* 18.1 (Nov. 29, 2017), p. 529 (cit. on p. 70).

[202] Stefan Van der Walt, Johannes L Schönberger, Juan Nunez-Iglesias, François Boulogne, Joshua D Warner, Neil Yager, Emmanuelle Gouillart, and Tony Yu. "Scikit-Image: Image Processing in Python". In: *PeerJ* 2 (2014), e453 (cit. on p. 70).

[203] Francisco De La Peña et al. *Hyperspy/Hyperspy: Release v1.6.5*. Version v1.6.5. Zenodo, Oct. 28, 2021 (cit. on p. 70).

[204] Michael Atkinson, Rhys Thomas, Peter Crowther, Dtfullwood, João Quinta Da Fonseca, and Allan Harte. *MechMicroMan/DefDAP: V0.93.4*. Version v0.93.4. Zenodo, Mar. 11, 2022 (cit. on p. 70).

[205] F. Bachmann, Ralf Hielscher, and Helmut Schaeben. "Texture Analysis with MTEX – Free and Open Source Software Toolbox". In: *SSP* 160 (Feb. 2010), pp. 63–68 (cit. on p. 70).

[206] Ange Lou, Shuyue Guan, and Murray H Loew. "DC-UNet: Rethinking the U-Net Architecture with Dual Channel Efficient CNN for Medical Image Segmentation". In: *Med. Imaging 2021 Image Process.* Vol. 11596. 2021, 115962T (cit. on pp. 72, 207, 208).

[207] Winnie Vultos. « Influence de la microstructure sur les micromécanismes de déformation en fluage dans le superalliage AD730™ ». PhD thesis. Université Paul Sabatier - Toulouse III, Feb. 14, 2019 (cit. on p. 88).

[208] S. Shahab Naghavi, Vinay I. Hegde, and C. Wolverton. "Diffusion Coefficients of Transition Metals in Fcc Cobalt". In: *Acta Materialia* 132 (June 2017), pp. 467–478 (cit. on p. 105).

[209] Qiong Wu, Shu-Suo Li, Yue Ma, and Sheng-Kai Gong. "First Principles Calculations of Alloying Element Diffusion Coefficients in Ni Using the Five-Frequency Model". In: *Chinese Phys. B* 21.10 (Oct. 2012), p. 109102 (cit. on p. 105).

[210] C. E Campbell, W. J Boettinger, and U. R Kattner. "Development of a Diffusion Mobility Database for Ni-base Superalloys". In: *Acta Materialia* 50.4 (Feb. 25, 2002), pp. 775–792 (cit. on p. 105).

[211] Tom Sanviemvongsak, Daniel Monceau, Clara Desgranges, and Bruno Macquaire. "Intergranular Oxidation of Ni-base Alloy 718 with a Focus on Additive Manufacturing". In: *Corrosion Science* 170 (July 1, 2020), p. 108684 (cit. on pp. 111, 112, 123, 124).

[212] Sam Cruchley. "The Oxidation Damage of Ni-based Superalloy, RR1000, with Different Surface Modifications and the Role of Oxidation in Fatigue Crack Initiation". PhD thesis. University of Birmingham, July 2015. 285 pp. (cit. on pp. 113, 123, 161).

[213] Nicolas Mrozowski. « Mécanismes de propagation de fissure dans un superalliage base nickel polycristallin en régime d'interaction fatigue-fluage-oxydation-vieillissement métallurgique ». PhD thesis. ISAE-ENSMA Ecole Nationale Supérieure de Mécanique et d'Aérotechique - Poitiers, Oct. 2, 2020 (cit. on pp. 113, 126).

[214] T.P. Gabb, J. Telesman, P.T. Kantzos, J.W. Smith, and P.F. Browning. "Effects of High Temperature Exposures on Fatigue Life of Disk Superalloys". In: *Superalloys 2004 Tenth Int. Symp.* Superalloys. TMS, 2004, pp. 269–274 (cit. on p. 113).

[215] Chantal K Sudbrack, Tim P Gabb, David R Hull, Jonathan D Yu, and Timothy T Gorman. "Comparison of the High-Temperature Oxidation Behavior of Subsolvus and Supersolvus Treated Advanced Powder Metallurgy Disk Alloys". In: (2012), p. 16 (cit. on p. 113).

[216] Franck Alexandre. « Aspects probabilistes et microstructuraux de l'amorçage des fissures de fatigue dans l'alliage Inco 718 ». PhD thesis. École Nationale Supérieure des Mines de Paris, 2004 (cit. on pp. 118, 119, 183).

[217] T Connolley, P.A.S Reed, and M.J Starink. "Short Crack Initiation and Growth at 600°C in Notched Specimens of Inconel718". In: *Materials Science and Engineering: A* 340.1-2 (Jan. 2003), pp. 139–154 (cit. on p. 119).

[218] Von P. Kofstad. "High temperature corrosion." In: *Mater. Corros.* 39.7 (1988), pp. 354–354 (cit. on p. 126).

[219] E. Fedorova, D. Monceau, and D. Oquab. "Quantification of Growth Kinetics and Adherence of Oxide Scales Formed on Ni-based Superalloys at High Temperature". In: *Corrosion Science* 52.12 (Dec. 1, 2010), pp. 3932–3942 (cit. on p. 131).

[220] Charles Romain, Damien Texier, Clara Desgranges, Jonathan Cormier, Stéphane Knittel, Daniel Monceau, and Denis Delagnes. "Oxidation of Thin Nickel-Based Superalloy Specimens: Kinetics Study and Mechanical Integrity". In: *Oxid Met* 96.1-2 (Aug. 2021), pp. 169–182 (cit. on p. 133).

[221] H. Mughrabi. "Some Consequences of Surface and Size Effects in Plastically Deformed Copper Single Crystals". In: *Phys. Status Solidi B* 44.1 (1971), pp. 391–402 (cit. on p. 141).

[222] J. T. Fourie. "Sub-Surface Dislocation Structure of Deformed Copper". In: *Philos. Mag. J. Theor. Exp. Appl. Phys.* 21.173 (May 1, 1970), pp. 977–985 (cit. on p. 141).

[223] Marco Panella. "Prévision Des Propriétés Mécaniques de Superalliages Base Nickel En Relation Avec Leur Microstructure Granulaire de Précipitation". PhD thesis. ISAE-ENSMA Ecole Nationale Supérieure de Mécanique et d'Aérotechique - Poitiers, June 4, 2021 (cit. on pp. 143, 149, 166).

[224] Andrew Wessman, Aude Laurence, Jonathan Cormier, Patrick Villechaise, Thomas Billot, and Jean Michel Franchet. "Thermal Stability of Cast and Wrought Alloy Rene 65". In: *Proc. 13th Int. Symp. Superalloys.* Superalloys 2016. Ed. by Mark Hardy, Eric Huron, Uwe Glatzel, Brian Griffin, Beth Lewis, Cathie Rae, Venkat Seetharaman, and Sammy Tin. Minerals, Metals and Materials Society, 2016, pp. 793–800 (cit. on p. 149).

[225] R. S. Moshtaghin and S. Asgari. "Growth Kinetics of γ' Precipitates in Superalloy IN-738LC during Long Term Aging". In: *Materials & Design* 24.5 (Aug. 1, 2003), pp. 325–330 (cit. on p. 149).

[226] S. Cruchley, M. P. Taylor, H. Y. Li, H. E. Evans, P. Bowen, D. J. Child, and M. C. Hardy. "Effect of Prior Oxidation on High Cycle Fatigue Performance of RR1000 and Role of Oxidation in Fatigue Crack Initiation". In: *Mater. High Temp.* 32.1-2 (Jan. 1, 2015), pp. 68–73 (cit. on p. 161).

[227] Sébastien Dryepondt, Daniel Monceau, Fabrice Crabos, and Eric Andrieu. "Static and Dynamic Aspects of Coupling between Creep Behavior and Oxidation on MC2 Single Crystal Superalloy at 1150 °C". In: *Acta Materialia* 53.15 (Sept. 1, 2005), pp. 4199–4209 (cit. on p. 171).

[228] Jean Baillieux. "Effet de l'oxydation Sur Le Comportement Mécanique de Structures Minces En Alliages de Titane". PhD thesis. Toulouse, INPT, Nov. 12, 2015 (cit. on p. 171).

[229] M. Bensch, C.H. Konrad, E. Fleischmann, C.M.F. Rae, and U. Glatzel. "Influence of Oxidation on Near-Surface γ' Fraction and Resulting Creep Behaviour of Single Crystal Ni-base Superalloy M247LC SX". In: *Mater. Sci. Eng. A* 577 (Aug. 2013), pp. 179–188 (cit. on p. 171).

[230] Ch Crussard and B. Jaoul. « Contribution à l'étude de la forme des courbes de traction des métaux et à son interprétation physique ». In: *Rev. Met. Paris* 47.8 (8 Aug. 1, 1950), pp. 589–600 (cit. on p. 189).

[231] K.V.U. Praveen, G.V.S. Sastry, and Vakil Singh. "Work-Hardening Behavior of the Ni-Fe Based Superalloy IN718". In: *Metall and Mat Trans A* 39.1 (Jan. 2008), pp. 65–78 (cit. on p. 189).

[232] Martín Abadi et al. *TensorFlow: Large-scale Machine Learning on Heterogeneous Systems*. 2015 (cit. on p. 207).

[233] Samta Gupta, Susmita Ghosh Mazumdar, and M. tech Student. "Sobel Edge Detection Algorithm". In: 2013 (cit. on p. 207).

[234] Lijun Ding and Ardeshir Goshtasby. "On the Canny Edge Detector". In: *Pattern Recognition* 34.3 (Mar. 1, 2001), pp. 721–725 (cit. on p. 207).

[235] Yan Xue Dong. "Review of Otsu Segmentation Algorithm". In: *Adv. Mater. Res.* 989–994 (2014), pp. 1959–1961 (cit. on p. 207).

[236] Junfei Qiu, Qihui Wu, Guoru Ding, Yuhua Xu, and Shuo Feng. "A Survey of Machine Learning for Big Data Processing". In: *EURASIP J. Adv. Signal Process.* 2016.1 (Dec. 2016), p. 67 (cit. on p. 207).

[237] Mingchun Li, Dali Chen, Shixin Liu, and Dinghao Guo. "Online Learning Method Based on Support Vector Machine for Metallographic Image Segmentation". In: *SIViP* 15.3 (Apr. 1, 2021), pp. 571–578 (cit. on p. 207).

[238] M.A. Charpagne, J. C. Stinville, A. T. Polonsky, M. P. Echlin, and T. M. Pollock. "A Multi-modal Data Merging Framework for Correlative Investigation of Strain Localization in Three Dimensions". In: *JOM* 73.11 (Nov. 2021), pp. 3263–3271 (cit. on p. 209).

[239] Sven Kosub. *A Note on the Triangle Inequality for the Jaccard Distance*. Dec. 8, 2016. arXiv: `1612.02696 [cs, stat]` (cit. on p. 209).

Contents

Résumé

Approche multi-échelle de l'oxydation sous-contrainte appliquée aux superalliages à base de nickel : de la déformation localisée aux prémices d'endommagement mécano-chimique

Les superalliages à base de nickel sont largement utilisés pour des applications structurelles à haute température et à température intermédiaire dans des atmosphères sévères. La dégradation assistée par l'environnement, c'est-à-dire l'oxydation et la corrosion, modifie la surface des matériaux, mais également leurs propriétés à cœur en raison d'une consommation sélective et progressive des éléments réactifs impliqués dans les processus de dégradation de la surface. Le matériau situé à proximité de la surface réactive présente un gradient de composition chimique, de microstructure et de propriétés physiques. Malgré l'échelle négligeable de ces gradients (de quelques micromètres à quelques centaines de micromètres sous la surface) par rapport aux dimensions du composant structurel, la variabilité du comportement mécanique au sein du gradient entraîne souvent des dommages prématurés et la rupture progressive du composant. Afin de quantifier ces évolutions, la caractérisation micromécanique des propriétés mécaniques des matériaux du gradient est importante. En raison de la forte variabilité des propriétés mécaniques au sein des matériaux gradués, des techniques de caractérisation micromécanique sont nécessaires. La caractérisation de matériaux vieillis et pré-oxydés est réalisée à la température de 700 °C, de même qu'à 800 °C, afin d'exacerber les conséquences de l'oxydation et d'augmenter ce gradient de propriétés à iso-durée de traitement thermique. La caractérisation mécanique des éprouvettes ultraminces (quelques dizaines de micromètres d'épaisseur) en traction et fatigue est réalisée avec suivi macroscopique par corrélation d'image. En plus des valeurs macroscopiques, une investigation spécifique de la surface pour des mesures cinématiques plein champ permet d'obtenir des informations locales sur les mécanismes de déformation et d'endommagement à l'échelle de la microstructure. Le présent projet propose de s'attaquer à la dimension multi-physique complexe de l'évaluation de la déformation/de l'endommagement assisté par l'environnement en corrélant simultanément la déformation macroscopique/mésoscopique et sous-microstructure/sous-micromètre et les changements de réactivité de surface (microfissuration des oxydes, oxydes à croissance rapide, oxydation par rupture, etc.) à haute température dans diverses conditions atmosphériques. L'objectif principal de cette caractérisation expérimentale in-situ est d'apporter une nouvelle compréhension et une prédiction plus physique du comportement mécanique local et temporel des matériaux gradués à l'échelle de la microstructure en relation avec les interactions environnementales.

Mots-clés : Superalliages à base de nickel, Localisation de la déformation, Réactivité de surface, Gradient de propriétés, Micromécanique in-situ

Abstract

Multiscale approach of the stress-assisted oxidation of nickel-based superalloys: from strain localization to the onset of mechanochemical damage

Nickel-based superalloys are widely used for structural applications at high and intermediate temperatures in severe atmospheres. Environmentally assisted degradation, i.e. oxidation and corrosion, alters not only the surface of the materials but also their core properties due to a selective and progressive consumption of the reactive elements involved in the surface degradation processes. The material in a shallow region beneath the reactive surface subsequently shows a gradient in chemical composition, microstructure, and physical properties. Despite the negligible scale of those gradients (from micrometers to hundreds of micrometers beneath the surface) relative to the dimensions of the structural component, the variability in mechanical behavior within the gradient often drives premature damage and progressive failure of the component. In order to quantify these developments, micromechanical characterization of the mechanical properties of gradient materials is important. Due to the high variability of mechanical properties within graded materials, micromechanical characterization techniques are required. Materials are characterized in aged and pre-oxidized at the temperature of 700 °C, These same characterizations are also carried out at 800 °C, in order to exacerbate the consequences of oxidation and to increase this gradient of properties at iso-duration of heat treatment. The mechanical characterization of ultrathin specimens (a few tens of micrometers thick) in tension and fatigue is carried out with macroscopic monitoring by image correlation. In addition to the macroscopic values, a specific investigation of the surface for full-field kinematic measurements allows obtaining local information on the deformation and damage mechanisms at the microstructure scale. The present project proposes to tackle the intricate multi-physics dimension of the environment-assisted deformation/damage evaluation by simultaneously correlating the macroscopic/mesoscopic and sub-microstructure/sub-micrometer deformation and the changes in surface reactivity (oxide microcracking, oxide spallation, fast-growing oxides, breakaway oxidation, etc.) at high temperature in various atmosphere conditions. The main aspiration of this in-situ experimental characterization is to bring a novel understanding and a more physical prediction of the local and time-evolving mechanical behavior of graded materials at the microstructure scale related to environmental interactions.

KEYWORDS: Nickel base superalloys, Strain localization, Surface reactivity, Graded properties, In-situ micromechanical testing